Synthesis and characterization of gold shell nanoparticles for controlled enhancement of photon upconversion process

Inaugural-Dissertation
to obtain the academic degree
Doctor rerum naturalium (Dr. rer. nat.)

submitted to the Department of Biology, Chemistry and Pharmacy
of Freie Universität Berlin

by

Cynthia Elisabeth Kembuan

from Jakarta

2019

Work leading to the writing of this dissertation was performed between October 2012 to January 2019 at the Institute of Chemistry and Biochemistry (Physical and Theoretical Chemistry) under the supervision of Prof. Dr. Christina Graf.

1. Supervisor: Prof. Dr. Christina Graf
2. Supervisor: Prof. Dr. Eckart Rühl

Disputation on: 06.12.2019

Acknowledgements

I would like to thank my supervisor Prof. Dr. Christina Graf for the supervision, support and helpful discussions during the course of this thesis. Her guidance and inspiration helped me to figure out new ways in which the work could be accomplished. I also owe much gratitude to Prof. Dr. Eckart Rühl for help in reviewing this thesis.

I also wish to sincerely thank Dr. Ute Resch-Genger and her Ph.D. students, Martin Kaiser for the upconversion fluorescence measurements in the earlier stage of this thesis. I would like to thank especially Florian Frenzel, for the collaborative efforts that led to some of the data on plasmon enhancement of upconversion emissions, including all the fluorescence measurements spectra obtained with the single particle-setup and decay lifetime measurements. Their keen discussions and proposals of solutions to questions arising from our analysis have helped me tremendously.

My special thanks go to the group of Prof. Dr. Javier Garcia de Abajo and especially Dr. Lijun Meng at ICFO (Institut de Ciències Fotòniques) in Barcelona for providing the theoretical equations and calculations for plasmon-enhanced upconversion emission, including the calculations of suitable particle size and metal shell thickness. I would like to thank Dr. Madlen Schmudde for the STEM and SEM measurements, Dr. Christian Goroncy for the TEM measurements, Michael Labza at the Institute of Chemistry and Biochemistry, Freie Universität Berlin for the XRD measurements.

My deepest gratitude to Dr. Helena Oliveira at the Institute of Biology at the University of Aveiro for the help and supervisions of the cytotoxicity experiments, Dr. Fiorenza Rancan at the Department of Dermatology and Allergy, Charité Universitätsmedizin Berlin for and CLSM measurements. I would also like to thank Iris Pieper at the Institute of Ecology, Technische Universität Berlin for ICP OES measurements, Prof. Dr. Rainer Haag at the Institute of Chemistry and Biochemistry, Freie Universität Berlin for the kind permission of using the DLS device.

I also wish to acknowledge the group members of Prof. Dr. Graf (Maysoon Saleh, Dr. Madlen Schmudde, Dr. Christian Goroncy, Alkit Beqiraj, Dr. Lei Ni) for their constant and incessant support, as well as team spirit they showed me during the practical laboratory phase of this project.

I would like to thank my Master student, Sabine Eisold for the synthesis of the particles in chapter 4.1. My Bachelor students Patrick Saloga, Lucia Merkel, Antonia Herzog, Martin Hollauer and Julie Kasparian for their dedications in the research projects and hard work in the lab.

I also wish to acknowledge the collegial and moral support of Dr. Christelle Njiki-Noufele during challenging times. I also wish to thank Dr. Babila Tachu for help in editing and improving the readability of this thesis.

I would also like to thank Dahlem Research School and the Zentrales Innovationsprogramm Mittelstand of the German Ministry of Economy and Energy (BMWi) for the financial support during the laboratory work, the local women's representative and gender equality officer for the Department of Biology/Chemistry/Pharmacy of Freie Universität Berlin for financial support at IACIS conference in 2015 and the European Cooperation in Science and Technology (COST) for providing the financial possibility to complete my two Short Term Scientific Missions (STSM) at the University of Aveiro.

To my family, I owe them much gratitude for their constant support, love, and motivating words.

Abstract

In recent years, upconversion nanoparticles (UCNP) have emerged as potential inorganic NIR-fluorescence bioimaging agents. Upconversion (UC) is a non-linear optical process, where the sequential excitation of two or more lower energy photons results in the emission of photons with higher energy. Long-live emission lifetimes, defined emission peaks, high photostability, and high biocompatibility are among the advantages of UCNP. However, these particles suffer from quenching caused by crystal defects, and they have a low quantum yield. One possibility to tune and enhance the luminescence is to couple the UCNP with plasmonic metal shells such as gold or silver. The core-shell size ratio of these metal-shell particles can be tuned in such ways, so that their surface plasmon resonance varies over a wide wavelength range. A dielectric spacer such as silica between the metal shell and the UCNP can prevent direct contact between lanthanide ions and the metal shell to prevent quenching without hindering excitation or emission of light, a process also used to study the distance dependency of plasmon-modified upconversion.

Predictions of the suitable UCNP core-silica spacer-gold shell system through theoretical calculations and simulations were provided. Afterward, nanoparticles with an appropriate size and spacer/shell thickness were synthesized, based on the calculated structures where the highest emission UC luminescence enhancement could be achieved. Through a thermal decomposition method with oleate precursors, monodisperse $NaYF_4$ host crystals with Yb^{3+} ions as sensitizer and Er^{3+} ions as emitter core with size less than 50 nm diameter were synthesized, followed by a stepwise controlled growth of the silica spacer through a combination of the reverse microemulsion and Stöber method to bring the core to a suitable size. Finally the silica-coated UCNP core was coated with a gold shell. The thickness of the synthesized silica shells could be controlled between 7-149 nm on 24±2 nm diameter $NaYF_4$: Yb, Er host structures. The gold shell thickness could be varied between 30 and 68 nm, depending on the proper core-gold shell ratio for the plasmon enhancement experiments. Fluorescence decay lifetimes and the UC fluorescence intensities were obtained via single particle measurements in a confocal setup to determine the changes of the UC-luminescence emission based on variations of the gold shell thickness. In the single particle measurements, the emission intensity at 540 nm (green) and 654 nm (red) emission after gold shell coating decreased. Furthermore, an increase in the decay time was also observed, indicating a quenching occurrence. The quenching indicated an increase of the non-radiative decay rate for both emission wavelengths, due to absorption of upconversion emission energy from excited Er^{3+} ions

by the gold shell or by an energy transfer of the emission to the gold shell. A thermal quenching effect, indicated by an increase of the lifetime at different excitation energies, could be caused by high excitation power densities in the single particle measurements. A thick gold shell of 48 nm on 24 nm UCNP core with 149 nm silica shell caused stronger cavity confinement, where the thick shell obstructed the excitation photons from reaching the UCNP, thereby preventing the emitted photons from being detected.

Another UCNP application of interest in bioimaging or bioassays lies in their coupling to organic dyes. As UCNP generally have a low quantum yield, and as their use is limited in bioimaging applications, they can be coupled with organic chromophores, which can receive the upconversion emission energy through a fluorescence resonance energy transfer (FRET) process and fluoresce. Activation of contrast agents through NIR light has advantages regarding high tissue penetration and almost no auto-fluorescence compared to the activation with UV light that has photodamaging characteristics and induces background fluorescence. For this purpose, a commonly used organic dye, Rhodamine B isothiocyanate (RBITC) was coupled in various concentrations in silica shells coated on UCNP cores. After excitation of the UCNP core with NIR light and a non-radiative energy transfer from UCNP emission to the dye, emission of RBITC occurred in the 580 nm range. Further characterization of the UC fluorescence emission indicated that a slight energy transfer of the green (540 nm) emission occurred from UCNP to the RBITC dye. However, according to measurements of the decay lifetimes, the emission of the dye was mainly due to the reabsorption effect from the UC emission. The small number of erbium ions on the surface transferred their energy through the FRET process to the rhodamine dye, while the reabsorption occurred between the majority of the erbium ions inside the UCNP sphere and the dye molecules in the silica.

Next, the cytotoxicity of silica coated UCNP on human keratinocytes (HaCaT cells) and murine macrophages (RAW 264.7 cells) was investigated with an 3-(4,5-Dimethyl-2-thiazolyl)-2,5-diphenyltetrazolium bromide (MTT) assay. Microporous silica shells with various thicknesses were coated onto the UCNP $NaYF_4$:Yb, Er (d = 33±2 nm) to increase the hydrophilicity of the particles and enabled them to be dispersed in cell culture medium for biological experiments. Part of the samples was subsequently functionalized with N-(6-Aminohexyl)aminopropyltrimethoxysilane (AHAPS) that provided a positive charge on the NP surface to increase their uptake rate into cells. Generally, the non-functionalized particles show a lower degree of cytotoxicity to HaCaT than the amino-functionalized particles, due to a higher uptake of the positively functionalized particles resulting from a higher degree of initial interactions

with the negatively charged cell membranes. The thickness of the silica shells did not heavily influence the cytotoxicity of the HaCaT cells. In the flow cytometry measurements, the cells' granularity was quantitatively measured after exposure to the particles. The samples with functionalized particles caused higher changes in cell granularity compared to the non-functionalized particles, and this could be correlated to the higher cytotoxicity of amino-functionalized particles. In the murine macrophage RAW 264.7 cells, the thickness of the silica played a significant role in the degree of cytotoxicity, whereby the particles with the 7 nm silica shell were generally more cytotoxic than those with a 21 nm thick shell, due to a higher degree of lanthanide ion release. In the ion release experiments using Inductively Coupled Plasma-Optical Emission Spectroscopy (ICP-OES) measurements, it was shown that more lanthanide ions were released from thinner coated samples, which influences the degree of cytotoxicity of the particular samples. It could be shown that reductions in cell viability and an increase of macrophage granularity occurred after exposure, depending on the silica shell thickness of the particles.

Kurzfassung

In den letzten Jahren haben Upconversion-Nanopartikel (UCNP) als potenzielle anorganische NIR-Fluorophore für biologische Bildgebungsverfahren Bedeutung erlangt. Die Upconversion (UC) oder Aufwärtskonvertierung ist ein nicht-linearer optischer Prozess, bei dem die sequenzielle Anregung von zwei oder mehr Photonen mit niedrigerer Energie zu einer Emission mit höherer Energie führt. Langlebige Emissionslebensdauer, definierte Emissionswellenlängen, hohe Photostabilität und hohe Biokompatibilität gehören zu den Vorteilen von UCNP. Diese Partikel neigen jedoch zu Fluoreszenzlöschung durch Kristallstrukturdefekte und haben folglich eine geringe Quantenausbeute. Eine Möglichkeit, um ihre Lumineszenz zu verstärken, besteht in der Kopplung der UCNP mit plasmonischen Metallschalen aus Gold oder Silber. Diese Metallschalenpartikel können durch Änderung des Kern-Schale-Verhältnisses so eingestellt werden, dass ihre Oberflächenplasmonenresonanz über einen großen Wellenlängenbereich variiert. Ein dielektrischer Abstandshalter wie eine Silicaschale zwischen der Metallhülle und dem UCNP kann einen direkten Kontakt zwischen den Lanthanoid-Ionen und der Metallhülle verhindern und so eine Auslöschung der Emission vermeiden, ohne dass Anregungs- oder Emissionslicht abzuschirmen, was auch zur Untersuchung der Abstandsabhängigkeit der plasmon-modifizierten UC-Emission verwendet wird.

Es wurden erst theoretische Berechnungen und Simulationen zur Ermittlung geeigneter UCNP-Kern-Silica-Abstandhalter-Gold-Schale-Größenverhältnisse für optimale Emissionsverstärkung durchgeführt. Anschließend wurden Nanopartikel mit entsprechender Größe und passendem Kern-Schale-Abstand synthetisiert, basierend auf den berechneten Strukturen, bei denen die höchste UC-Lumineszenzverstärkung erwartet wurde. Durch ein thermisches Zersetzungsverfahren von Oleat-Präkursoren wurden monodisperse $NaYF_4$-Wirtskristalle mit Yb^{3+}-Ionen als Sensibilisator und Er^{3+}-Ionen als Emitter mit einer Größe von weniger als 50 nm Durchmesser synthetisiert. Hieran schloss sich ein schrittweises, kontrolliertes Wachstum der Silicaschicht durch Kombination eines modifizierten Mikroemulsionsverfahrens mit der Stöber-Methode an. Schließlich wurden die Silica-beschichteten UCNP-Kerne mit einer Goldschale beschichtet. Die Dicke der Silicaschale wurde zwischen 7-149 nm auf UCNP mit einem Durchmesser von 24±2 nm eingestellt, und die Dicke der Goldschale konnte zwischen 30 und 68 nm variiert werden. Das Kern-Schale-Verhältnis wurde entsprechend der obengenannten Rechnungen angepasst. Die Fluoreszenz-Lebensdauer und die Intensität der UC-Fluoreszenz wurden durch Einzelpartikelmessungen in einem konfokalen

Aufbau ermittelt, um den Einfluss der Variation der Goldschalendicke zu bestimmen. Bei den Einzelpartikelmessungen nahm die Intensität bei der Emission bei 540 nm- (grün) und 654 nm- (rot) nach dem Beschichten mit einer Goldschale ab und die Fluoreszenzabklingzeit nahm zu, was auf Fluoreszenzlöschung hindeutet. Diese Löschung könnte durch eine Erhöhung des nicht-strahlenden Abklingens der angeregten Photonen verursacht werden, in Folge der Absorption der UC-Emission der angeregten Er^{3+}-Ionen durch die Goldschale oder durch eine Energieübertragung der Emission auf die Goldschale. Ein thermischer Löscheffekt, der durch eine Erhöhung der Lebensdauer bei unterschiedlichen Leistungsdichten angedeutet wurde, sollte zudem bei hohen Anregungsleistungsdichten bei den Einzelpartikelmessungen in Betracht gezogen werden. Eine 48 nm dicke Goldschale auf einem 24 nm großen UCNP-Kern mit einer 149 nm dicken Silicaschale bewirkte einen stärkeren *Confinement*-Effekt der Lichtquanten in der Goldschale, wobei die dicke Schale das Anregungslicht daran hinderte, das UCNP zu erreichen, ebenso wie die Detektion der emittierten Photonen.

Eine andere UCNP-Anwendung, die in Bildgebungsverfahren und Bioassays von Interesse ist, ist ihre Kopplung an organische Farbstoffe. Da UCNP im Allgemeinen eine geringe Quantenausbeute aufweisen und daher ihre Anwendungen für die Bildgebungsverfahren nur begrenzt sind, können sie mit organischen Chromophoren gekoppelt werden, auf die die UC-Emissionsenergie durch einen Fluoreszenz Resonanz Energie-Transfer (FRET) übertragen wird. NIR-Licht zur Aktivierung von Kontrastmitteln bietet als Vorteile eine hohe Gewebedurchlässigkeit und erzeugt nahezu keine Autofluoreszenz im Vergleich zu der Aktivierung mit UV-Licht, das oft phototoxische Eigenschaften aufweist und Hintergrundfluoreszenz induziert. Zu diesem Zweck wurde ein häufig verwendeter organischer Farbstoff, Rhodamin B-Isothiocyanat (RBITC), in verschiedenen Konzentrationen in mit Silica beschichteten UCNP-Kernen gekoppelt. Nach Anregung mit NIR wurde die Emission von RBITC im Bereich von 580 nm beobachtet. Untersuchungen der UC-Emission und der Fluoreszenzlebensdauern zeigten, dass eine minimale Energieübertragung von der grünen Emission zum Farbstoff auftritt, die Emission des Farbstoffs jedoch hauptsächlich auf Reabsorption zurückzuführen ist. Ein geringer Anteil von Erbium-Ionen auf der Oberfläche transferierte seine Energie durch FRET auf den Rhodaminfarbstoff, während Reabsorption zwischen der Mehrheit der Erbium-Ionen im UCNP-Kern und den Farbstoffmolekülen in der Silicaschale auftrat.

Als Nächstes wurde die Zytotoxizität von Silica-beschichteten UCNP in menschlichen Keratinozyten (HaCaT-Zellen) und murine Makrophagen (RAW 264.7-Zellen) mittels eines

3-(4,5-Dimethyl-2-thiazolyl)-2,5-diphenyltetrazolium bromide (MTT) Assays untersucht. Mikroporöse Silicaschalen mit verschiedenen Dicken wurden auf 33 nm-große UCNP aufgewachsen, um die Hydrophilizität der Teilchen zu erhöhen, und dadurch das Redispergieren der Partikel im Zellkulturmedium für biologische Experimente zu ermöglichen. Ein Teil der Proben wurde anschließend mit N-(6-Aminohexyl)aminopropyltrimethoxysilane (AHAPS) funktionalisiert, das eine positive Ladung auf der NP-Oberfläche erzeugt und so deren Aufnahme in Zellen erhöht. Generell zeigen die nicht funktionalisierten Partikel eine geringere Zytotoxizität gegenüber HaCaT-Zellen als die amino-funktionalisierten Partikel. Die Ursache hierfür war eine höhere Wechselwirkung der positiv geladenen Partikel mit der negativ geladenen Zellmembran, die zu einer höheren Aufnahmerate im Vergleich zu den nicht funktionalisierten Partikeln führte. Die Dicke der Silica-Schalen beeinflusste das Ausmaß der Zytotoxizität in den HaCaT-Zellen kaum. Bei den Durchflusszytometrie-Messungen wurde die Granularität der Zellen nach Inkubation mit den Partikeln quantitativ gemessen. Die Proben mit funktionalisierten Partikeln verursachten im Vergleich zu den nicht funktionalisierten Partikeln höhere Änderungen in der Granularität der HaCaT-Zellen, was mit der höheren Zytotoxizität von Amino-funktionalisierten Partikeln in Zusammenhang stehen könnte.

In den RAW 264.7-Zellen waren die Partikel mit der dünneren 7 nm-Schale aufgrund eines höheren Lanthanoid-Ionenfreisetzungsgrades im Allgemeinen zytotoxischer als die Partikel mit den dickeren 21 nm-Schalen. In den Ionenfreisetzungsexperimenten mittels Inductively Coupled Plasma-Optical Emission Spectroscopy (ICP-OES) wurde nachgewiesen, dass mehr Lanthanoidionen aus den Partikeln mit den dünneren Schalen freigesetzt wurden, was den Zytotoxizitätsgrad der jeweiligen Proben beeinflusste. Man konnte die von Silicaschalendicke abhängige Abnahme der Zellviabilität und eine Zunahme der Granularität der Makrophagen nach Inkubation mit den Nanopartikeln beobachten.

Contents

1 Introduction and motivation

Nanotechnology is a science that studies materials at the molecular scale. According to IUPAC recommendations, the size limit of such materials (known as nanoparticles or nanomaterials) usually lies at a range of 1-100 nm.[1] A wider approach of this field includes imaging, modelling, and manipulating matters within the above-mentioned size range. Nanomaterials have distinct characteristics different from those of the same chemical at a larger scale (> 100 nm). This is due to size related effects that become dominant or significant as the material gets smaller up to the sub-atomic scale, with a consequent increase of their surface-to-volume ratio, which leads to enhanced chemical reactivity and changes in electronic, optical and magnetic properties of the materials.[2-3]

Although nanoparticles have existed in nature for thousands of years,[4-5] their practical applications in ancient civilizations were mainly as nanofibers for ceramic matrix[6] and as colour pigments for glass or other household appliances.[7-8] Nanoparticles derived from modern science laboratories were only reported in the middle of the 19th century. In recent years, nanotechnology has evolved to be one of the most important fields for the development of electronics, information technology, biomedicine, energy conversion processes, automobiles, and environmental sciences applications, as the demand for efficient, effective small-sized electronic components, chemical agents, and novel medicines increases across a broad range of industries. In biomedical applications, various nanomaterials have been utilized for disease prevention, detection, and treatment.[9]

Where superparamagnetic nanoparticles are utilized in magnetic imaging, other important biomedical imaging applications include those that run in the optical or near infrared (NIR) region. Within the 650-1450 nm of excitation/emission wavelength is the so-called *in vivo* "imaging window" where the tissue experiences minimal absorbance and hence low auto-fluorescence, allowing for deep and whole tissue imaging.[10] Efforts have been made towards finding different nanomaterials, that were suitable as contrast or imaging agent and were excitable in the NIR region.[11-14]

For this purpose, upconversion nanoparticles (UCNP) have emerged in recent years as potential inorganic NIR-fluorescence bioimaging agents. Upconversion is a non-linear optical process, where the sequential excitation of two or more photons results in emission of higher energy wavelengths. In UCNP, the excitation often occurs with near infrared (NIR) wavelength and results in higher energy wavelength emission, i.e., upconversion is an anti-Stokes process. Common

organic NIR-contrast agents have disadvantages such as low photostability,[11] comparatively low quantum yields in the NIR region,[12-13] and short fluorescence lifetimes (1-5 ns in NIR and visible range).[13] Due to their broad fluorescence emission peaks, they are not suitable for multiplexing applications. Though inorganic semiconductor structures such as quantum dots have higher quantum yields, higher photostabilities, and lifetimes than their organic NIR counterparts, their use in the life sciences and medicine is limited due to their cytotoxicity,[14-16] high aggregation probability,[13] and chemical blinking.[17]

Advantages of UCNP are long-lived emission lifetimes, defined emission peaks, photostability, and high biocompatibility. However, these particles suffer from quenching caused by crystal defects, and they particularly have a low quantum yield. As the particles grow smaller, their ability for imaging is therefore reduced due to their increasing surface-to-volume ratio and hence, increasing energy deactivation.[10, 18] One possibility to tune and enhance the luminescence is to couple the UCNP with plasmonic systems such as gold or silver. Metallic nanoshells with a wide range of plasmonic absorption bands can be tuned or coupled to UCNP systems to increase their luminescence intensities.[19-22]

Many works have been done in using various plasmonic structures to modify upconversion emission. Possible plasmonic systems that are applicable in solution for UCNP are either metallo-dielectric core-shell structures[23-25] or the coupling of UCNP with metal nanoparticles.[21-22, 26] Coupling with metal NP (MNP) requires a suitable covalent bonding between UCNP and MNP. However, the risk of quenching in this system is higher due to possible quenching interactions between the MNP and the UCNP-coupled MNP.[24, 27] Additionally, the spectral plasmonic absorption bands of small solid gold nanoparticles (diameter (d) < 40 nm) and larger solid silver and gold nanoparticles (d < 50 nm) can only be modified in a small range so that it is difficult to investigate the correlation or coherence between the plasmonic wave range and the emission characteristics of UCNP.[28] In contrast, for metallo-dielectric core-shell systems with a UCNP core, one can modify and adjust the spectral plasmonic bands so that they match with the upconversion absorption or emission by varying the nanoshell thickness and the ratio between the core-shell.[19-22] A direct coating of a UCNP core with a plasmonic metal shell however causes fluorescence quenching due to the increase of non-radiative energy transfer and cross-relaxation. Moreover, a mismatch between the donor UCNP emission and the plasmonic wavebands may occur, since, for a small core, the possibilities for the variation of the core to shell-ratio is limited. Therefore, a dielectric spacer such as silica between the metal shell and the UCNP is recommended to prevent

direct contact between lanthanide ions and the metal shell without hindering the excitation or emission wavelengths. Such structure also enables a study of the distance dependency of plasmon modified upconversion, since field enhancement, absorption, and quenching rates are all distance dependent.[24, 27] Additionally, current methods of growing metal nanoshell on particles often produce non-homogeneous coating which hinders a reliable correlative study between plasmonic nanoshell systems and upconversion modified luminescence generated.[29-31]

Until now, some initial studies have shown how plasmonic energy bands matched to either upconversion absorption or emission can increase the upconversion luminescence intensity.[22, 24, 32-33] Many plasmonic system structures that provide coupling between UCNP, and metal plasmon nanostructures have been investigated, such as periodic structures of lanthanide doped pillar arrays suspended on a gold film, glass substrate doped with lanthanide ions containing metal nanoparticles, and enhancement through localized surface plasmon resonance or coupling of UCNP with metal nanoparticles with different morphologies such as spheres or rods.[34 35] Works predicting structures of core-spacer-shell systems that deliver strong upconversion luminescence enhancement are scant.[30, 36-37] Often, the experimental conditions which lead to UC enhancement for each system are not thoroughly explained. As an example, the UC-efficiency is basically a function of excitation power; low energy pump power lead to higher enhancement compared to saturated pump power that already produced high upconversion luminescence intensity.[38] Many publications do not mention the excitation parameters used. In publications, which discussed core-shell systems of UCNP and gold or silver nanoshells, one system could bring enhancement while the others induced quenching.[30-31, 35] Thus, based on calculations that describe optimal core-shell ratios of UCNP cores with gold shells for plasmon-enhanced UC-emission, and considering the limiting conditions of dimmed pump and saturated pump excitation, experimental studies for the synthesis of suitable UCNP cores were carried out, and then silica spacers with controllable thickness were grown to a homogeneous closed gold shell on a core-spacer structure. Silica was chosen as a spacer to prevent quenching and increase the UC emission.[38]

Firstly, predictions of the suitable core-spacer-shell system using theoretical calculations and simulations were obtained through collaboration with the group of Prof. Dr. Javier Garcia de Abajo and Dr. Lijun Meng at ICFO (Institut de Ciències Fotòniques) in Barcelona. Nanoparticles with appropriate size and spacer/shell thickness were synthesized based on the proposed calculated structures for which the highest emission UC luminescence enhancement could be achieved. A stepwise growth method comprising the synthesis of monodisperse $NaYF_4$ host crystals (< 50 nm

diameter) with Yb^{3+} ions as sensitizer and Er^{3+} ions as emitter. The silica shell, synthesized by the modified reversed microemulsion method, served the purpose of surface deactivation and protection as well as bringing the cores to a suitable size. This growth was eventually combined with the classical Stöber method, before finally coating the already silica-coated UCNP core with a gold shell. The thickness varied between 5-149 nm for the synthesized silica, and 30-68 nm for the gold shell, depending on the suitable core-gold shell ratio for plasmon enhancement experiments. The thickness of the gold shell, which is formed in the last synthesis step was chosen to fit the model calculations, for which plasmon resonance can provide high UC-luminescence enhancement. Spectroscopy evaluations of decay lifetime rate and UC fluorescence measurements were done to determine in which ways and methods the UC-luminescence emission could be modified based on variations of the gold shell thickness.

Other UCNP applications that are of interest in bioimaging or bioassays are those involving coupling to organic dyes. Fluorescence resonance energy transfer (FRET) occurs when the absorption band of a dye is in the range of the UC-emission. Activation of contrast agents through NIR-light has advantages regarding high tissue penetration and low auto-fluorescence compared to activation with UV light that has photodamaging characteristics.[39-44] However, due to UCNP's low quantum yield, the possibility of using UCNP in bioapplications, where low excitation power density is required, is severely limited. There are already some publications describing the coupling UCNP as a donor with organic dyes as an acceptor to modulate emission.[45-47] However, in most articles, systematic studies of concentration-dependent UCNP donor-dye acceptor-FRET in a dielectric transparent shell such as a silica shell has not been thoroughly investigated. Silica shells serve the purpose of controlling the distance to keep the dye molecules close to the emitter ions for optimal FRET,[47-49] as FRET efficiency decreases with increasing donor-acceptor distance. For this target, a commonly used organic dye, Rhodamine B isothiocyanate (RBITC) was coupled in various concentrations in silica shells coated on a UCNP core. This particular dye was chosen since its absorption bands matched the emission of erbium-doped $NaYF_4$. As with the gold shell system, fluorescence and decay lifetime measurements were taken to study the modulation of FRET emission resulting from the coupling of UCNP and dye.

When high amounts of lanthanide ions are found on the surface of the UCNP, they are prone to surface quenching effects from solvents and other organic materials.[50] Additionally, UCNP are often hydrophobic under the commonly used synthetic conditions, making them unsuitable for biological applications.[50] It is hence necessary to protect the UCNP from surface quenchers, reduce

the surface defects, and simultaneously increase the hydrophilicity in bioassay applications. Coating of the nanoparticle core with silica is a versatile and simple approach for protecting the surface lanthanide ions while increasing the hydrophilicity[51] and optimizing the core-spacer-shell structure.[24, 52] Although the cytotoxicity of UCNP is considered low or not existent,[53] it is still necessary to investigate the possible leeching effects of rare earth metal ions in biological systems and the consequent increase of cytotoxicity. Non-toxic silica shells can provide additional protection against leeching. Silica shells, however, provide the particle with a negative charge, which hinders the particles' uptake through the negatively charged cell membrane, which instead will preferentially take up ligands with a membrane stabilising positive surface charge.[54-55] A high uptake rate into cells is desirable in this case as it facilitates investigations of the behavior and effect of UCNP after uptake.

The thickness of silica shells could also play an essential role regarding the degree of uptake into cells and the mechanism of the uptake since the shell thickness is proportional to particle size. Different sizes of particles can be taken up in cells by different uptake mechanisms.[55, 56] Thick silica shells also decrease possible lanthanide leeching, as thicker shells would prevent release of ions into the surrounding biological medium. Previous cytotoxicity studies of UCNP with silica shells usually only investigated one size of silica shell thickness with one or more types of surface charge or ligands.[39, 41-42] Hence, in this work core-shell UCNP-silica systems with two different silica thicknesses and two different surface charges (positive and negative) were synthesized, and their cytotoxicity were evaluated on human keratinocyte HaCaT and RAW 264.7 macrophage cells in *in vivo* cytotoxicity assays. The result was evaluated with the degree of aggregation, uptake rate, the surface charge of the particles, silica shell thickness, and the degree of ion release, to determine the parameters influencing the degree of cytotoxicity. In addition to the coupling UCNP with RBITC as indicated above, the silica shell was also coupled with RBITC and functionalized with a positively charged ligand. Particle uptake by cells was studied by using a confocal laser scanning microscopy.

2 State of the Art

2.1 Nanoparticles and upconversion nanoparticles

Nanoparticles are defined structures of atoms or molecules, which build a zero-dimensional structure of atoms with a size between 1-100 nm.[3, 57] Due to the increased surface area to volume ratio of nanoscopic structures, nanoparticles have different optical, electronic, and chemical characteristics from their bulk counterparts. Nowadays there are various areas of application for the use of nanoparticles; from drug delivery, cosmetics, gas sensors, gene chips to hyperthermia.[57] There are basically two approaches to create nanomaterials: the "top-down" and "bottom-up" method. In the "top-down" method the technology used to create bulk or macroscopic components are adjusted in ways to build the same components in smaller formats. Processes such as grinding, chemical vapour deposition (CVD), physical vapor deposition (PVD) are examples of "top-down" approaches.[58] For example, modern microlithography techniques in the semiconductor industries can produce circuits within nm precisions. In the "bottom-up" approach complex structures are created from small building blocks, such as atoms or molecules. Self-assembly is the process whereby the atoms or molecules undergo chemical and physical processes to form nanoparticles.[59] An example is the implementation of this technique in self-assembled monolayers of molecules to produce polymer light-emitting diodes (LED).[60]

As was mentioned, NP have size-driven distinct characteristics which makes them physically and optically different from their bulk counterparts. Small gold nanoparticles exhibit red colour when their size is between 20-50 nm, and the plasmon resonance becomes less distinct with decreasing size.[61] This effect is the result of the localized surface plasmon resonance (LSPR) (see Figure 2.1), wherein an incident photon causes collective electron oscillation relative to the positively charged core of the metal atom, i.e., plasmon resonance caused by interactions of electromagnetic radiation with the electron gas of nanoparticles.[57, 62] In Figure 2.1, the oscillation directions of the particles, which is parallel to the applied electric field, and perpendicular to the propagation direction of the light wave are shown. The oscillation energy depends on the size, shape and the surrounding medium of the nanoparticles.[62]

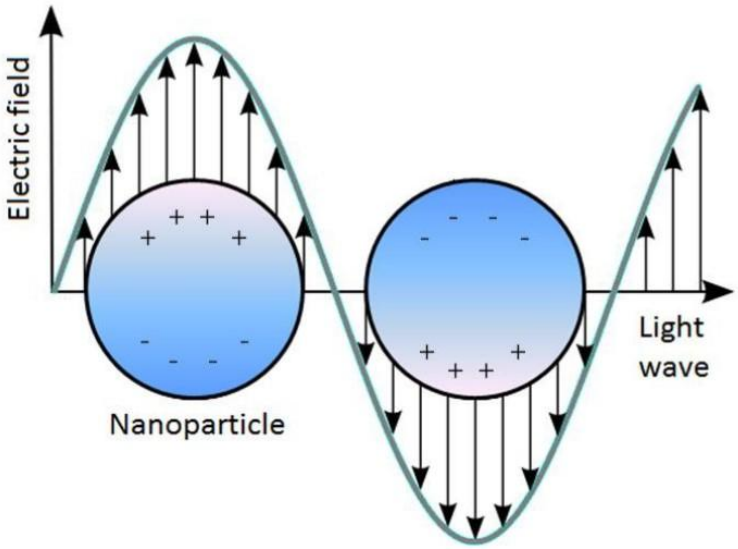

Figure 2.1: Surface plasmon resonance caused by oscillation of surface electrons due to interactions with incoming photons. (Republished from reference [63])

Noble metal nanoparticles, such as gold or silver nanoparticles, and fluorescing nanoparticles such as quantum dots can be simultaneously used in biomedicine as drug carriers and contrast agents. Especially, owing to their distinct extinction peaks and small sizes, gold nanoparticles are used as detection agents in cell detection experiments or simply as tools to investigate biological mechanisms and inner cell processes.[64-66]

2.1.1 Upconversion nanoparticles

Lately, the potential use of UCNP in bioimaging and biosensing has been widely investigated, since the near infrared (NIR) excitation wavelength has deep tissue penetration, is less photodamaging than the energy used to excite quantum dots, causes no auto-fluorescence, and is not absorbed by surrounding biological media.[67]

Upconversion is a non-linear optical process, in which two or more photons are excited by infrared radiation, leading to the emission of higher energy photons in the visible range, in a typical anti-Stokes process. The nonlinearity of the process stems from the observation that the emission wavelength depends on the incident light density.[68] This is unique in the case of upconversion, as other linear optical processes such as fluorescence or phosphorescence of materials usually are independent of the intensity of the excitation light.

There are three different mechanisms of upconversion: energy transfer upconversion (ETU), excited states absorption (ESA), and photon avalanche. The energy diagram of each mechanism is shown in Figure 2.2: [69]

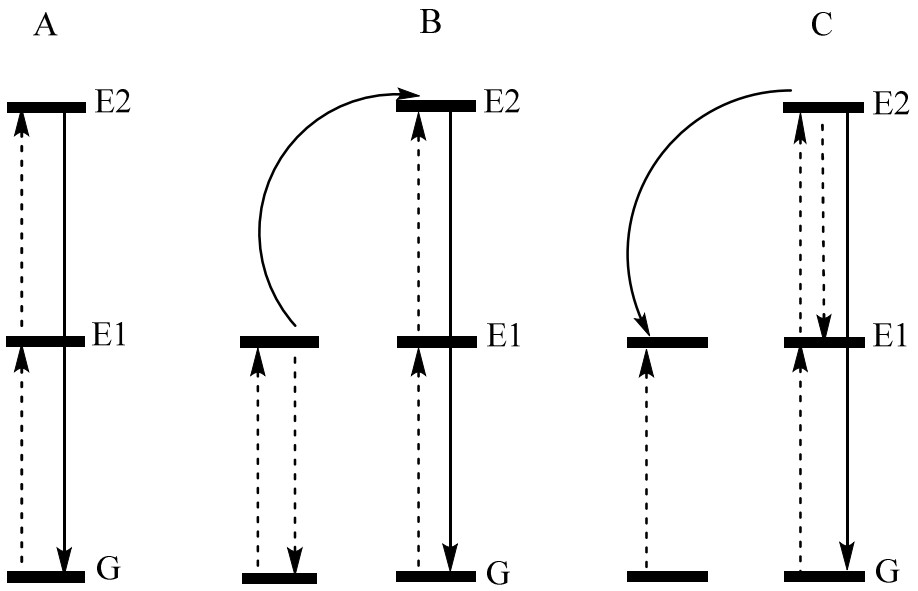

Figure 2.2: Mechanisms of upconversion processes; A: excited states absorption (ESA), B: excited state upconversion, and C: photon avalanche. G is ground state, where E1 and E2 are the first and second excited states. The dotted arrow represents photon absorption and photon emission. The curved arrows in Figure B represent photon transfer to adjacent ions, and C represents cross relaxation, while the solid straight arrows represent photon emission from the second excited state to the ground state.[69]

In excited absorption states, a photon in a single ion is excited from the ground state G to the first excitation state E1. Due to the ladder-like arrangements of the energy states between G and E1, and E1 and E2, a sequential second photon could be excited, promoting the ion to E2 due to the long lifetime state of E1, before emitting back to G. The energy released from this emission is equal to the energy difference between the levels E2 and G.

In energy transfer upconversion, there is energy transfer between two adjacent ions. Two photons from two neighbouring ions are excited to E1, and this might lead to a non-radiative energy transfer with one of the ions being excited to E2, while the other ion emits back to G. The second ion then emits this photon and falls back to G. The efficiency of this process is proportional to the concentrations of both ions, since this determines the distance between ions in solution or solid

states and the probability for energy transfer occurring. The ion that transfers its energy to the neighbouring ion in E2 is known as sensitizer or activator, while the other ion is known as emitter. In photon avalanche, photons are excited to E1, followed by further excitation to E2. A cross-relaxation of an excited photon with a photon in a neighboring ion in the ground state level occurs, causing both E1 levels to be occupied. The photons can then be excited to E2 levels, leading to high-intensity emissions that are caused by repeated cross relaxation processes, excitation to E2 and exponentially increased emission.

Upconversion nanocrystals usually consist of a host crystal and low concentrations of dopant ions. As dopants, lanthanide ions provide the most efficient and highest upconversion intensity.[18, 30, 68] The dopants that undergo the original upconversion process are called activators or emitters. Host crystals such as lanthanide/rare earth fluorides or metal lanthanide fluorides such as $NaYF_4$, $LiYF_4$ or $LiGdF_4$, having low phonon energy are able to minimize non-radiative emission, and enhance the radiative emission intensity, and are commonly used for upconversion.[18, 30, 68-69] Lanthanides or rare earth metals with an ion size close to the dopant ions are chosen as components in the host crystal to reduce lattice defects and impurities, which can promote non-radiative cross relaxation between the ions and reduce the emission.[32, 46]

Lanthanide ions have a long lifetime in the metastable excited states and ladder-like higher energy levels, which eases sequential photoexcitation to the next level, hence lanthanide ions are capable of upconversion. The most common emitters nowadays include Er^{3+}, $Tm^{3+,}$ and Ho^{3+}.[68-69] Especially Er^{3+} has high upconversion efficiency since its two adjacent energy level pairs ($^4I_{11/2}$ - $^4I_{15/2}$, and $^4I_{11/2}$-$^4F_{7/2}$) have similar energy difference. The energy level pair $^4F_{9/2}$ and $^4I_{13/2}$ is also located very close to each other. Two-photon absorptions of Er^{3+} can hence lead to three different emission wavelengths (520, 540, and 650 nm). Figure 2.3 shows the energy level scheme of Yb^{3+} as sensitizer, which under 980 nm excitation is excited to $^2F_{5/2}$ from the ground state $^2F_{7/2}$. Under an ETU process, the excited photon is transferred to neighbouring Er^{3+} or Tm^{3+} ions. The emission wavelength of Er^{3+} is as mentioned before, while the emissions of Tm^{3+} resulted from the transition $^1G_4 \rightarrow {}^3F_4$ (650 nm) and $^1G_4 \rightarrow {}^3H_6$ (475 nm).

As the electronic transitions between 4f orbitals are Laporte-forbidden, the absorption of photons to these levels are highly inefficient, causing weak absorption and emission rates of upconversion processes. Increasing the concentrations of the emitters only leads to increased non-radiative relaxation and cross-relaxation, which reduces the emission intensity.[68] To overcome this problem a sensitizer ion can be doped into the systems at a higher concentration. Ytterbium has large

absorption cross-section and energy levels that resonates with many f-f-transitions of the lanthanide ions.[18, 30, 68] Ytterbium can hence be used as an effective sensitizer, which can transfer the energy from its excited photons to neighbouring emitter ions. So far, the most efficient and well-known sensitizer/emitter ion pairs are Yb^{3+}/Er^{3+} and Yb^{3+}/Tm^{3+}.[18, 30, 68]

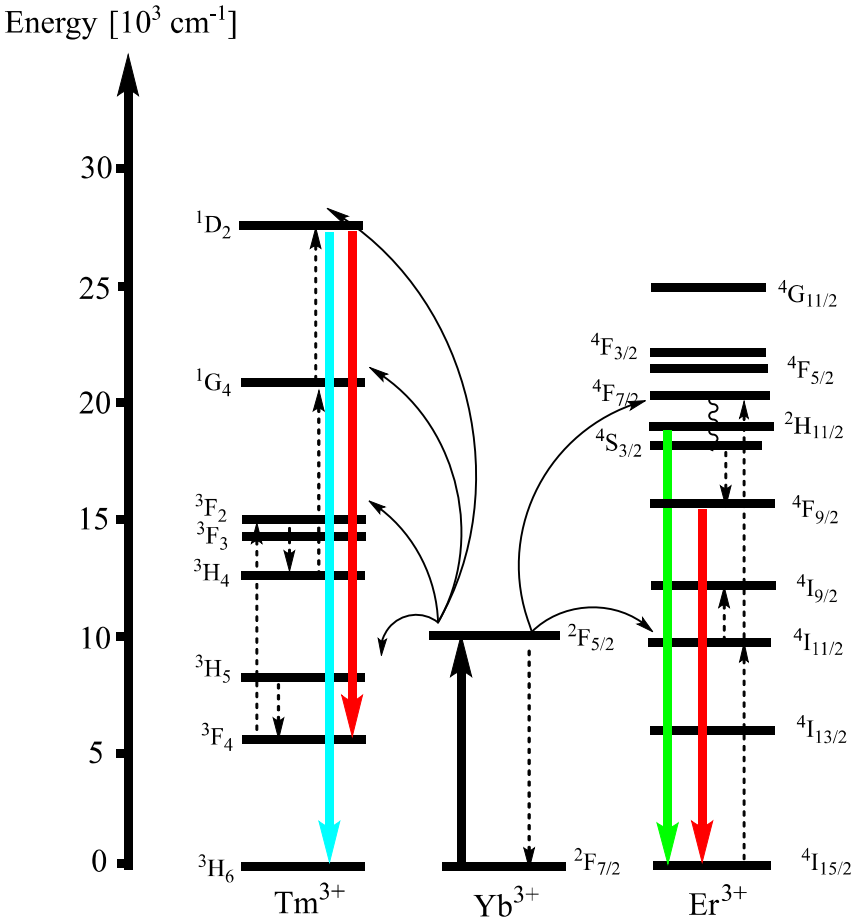

Figure 2.3: Scheme of upconversion emission process of Er^{3+} and/or Tm^{3+} as emitters, with Yb^{3+} as activator or sensitizer. (Republished from reference[70] Copyright Wiley-VCH 2019)

2.1.2 Synthesis of upconversion nanoparticles

For the synthesis of monodisperse UCNP with high UC-emission intensity and efficiency, many chemical synthesis methods have been developed and utilized. Among those, the most well-known methods are co-precipitation methods, thermal decomposition, and hydrothermal synthesis.[44, 68-69] Co-precipitation is one of the simplest means by which UCNP can be produced. The process is easy and time efficient, since it does not need difficult lab synthesis techniques. One of the earliest works of UCNP synthesis through the co-precipitation method was done by van Veggel et al.[71]

They developed the synthesis of LnF_3 doped with various lanthanide ions, such as Er^{3+} and Ho^{3+}. Yi et al. [72] reported the synthesis of $NaYF_4$: Yb, Er with ethylenediamine tetraacetic acid (EDTA). After synthesis, annealing is often used to increase the particles' size and enhance luminescence intensity.[44] The disadvantage of this method is the high hydrophobicity of the product and the low monodispersity compared to, for example, the thermal decomposition method.

In the thermal decomposition method, lanthanide trifluoracetates are usually decomposed at high temperatures to lanthanide fluorides. Zhang et al.[73] are among the first authors to develop this method. Mai et al.[74] synthesized lanthanide doped $NaREF_4$ from $Na(CF_3COO)$ and rare earth metals $(RE)(CF_3COO)_3$ by using a mix of coordinating and non-coordinating solvents. Octadecene was used as the non-coordinating solvent due to its high boiling point (T = 315 °C). Oleic acid or oleyl amine was used as a coordinating solvent to control the particles' size and prevent aggregation. According to Mai et al. once the reaction mixture reaches 250 ºC, CO_2 and fluorinated/oxyfluorinated carbon are released from the reaction solution, indicating that the CF_3COO^--ions are decomposed early in the reaction, while NaF is formed through the decomposition process of CF_3COONa and $RE(CF_3COO)_3$.[75] In a typically delayed nucleation pathway, when there is enough NaF formed, and its amount is higher than the nucleation threshold, α-$NaYF_4$: Yb, Er nuclei form and their size increases abruptly (burst nucleation). At the nucleation threshold concentration, the nucleation rate of the α-NaYF4: Yb, Er nanopolyhedra (initial morphology of the particles directly after nucleation) is high, and the particles' size decreases as more nanocrystals are formed at this high nucleation rate.

At the beginning of the reaction (delayed nucleation pathway stage) and in the second stage (size growth because of monomer supply), the monomer concentration is high, and the α-NaYF4: Yb, Er nanopolyhedra grow quickly in a monodispersed form. In this phase, the oleic acid (OA) stabilizes the particles' surface predominantly by van der Waals interactions. When the monomers are consumed completely, the α-NaYF4: Yb, Er nanopolyhedra are dissolved and reformed in the form of small cubes, where OA is strongly aligned and attached to the [100] planes. The small cubes can then grow larger in the fourth stage throughout the whole reaction, owing to some facilitating factors: firstly, small cubes having large surface energy are unstable and strive to be stable by coming together to build bigger particles with lower surface energy; and secondly, condensation of surface ligands leads to attractive forces between the smaller cubes.

The transformation from α- to β-phase $NaYF_4$: Yb, Er occurs after the delayed nucleation pathway, where at first the monomer α-$NaYF_4$: Yb, Er concentration is high, and the Ostwald ripening is

limited, causing the size to increase at first. After the redissolution of the α-phase crystals, small β-$NaYF_4$: Yb, Er are formed.

Boyer et al. [76] used a similar method to synthesize $NaYF_4$: Yb, Er/Tm nanoparticles and additionally reported a way to control the monodispersity of the particles by adding the precursors slowly in short periods to separate the nucleation and growing stages. Shan et al.[77] developed a method for synthesizing small (5-20 nm diameter) $NaYF_4$: Yb, Tm/Er/Ho by using trioctylphosphine oxide (TOPO) as solvent. They reported a lower energy barrier of cubic-to-hexagonal phase UCNP crystals compared to those obtained by using other high boiling point solvents such as oleylamine or oleic acid/1-octadecene. The hexagonal phase is known to have more efficient energy conversion than the cubic phase, resulting in higher luminescence intensity. They reported a total α → β transition at 280 °C and in a later publication reported that the building of β-phase crystal consists mainly of two stages: a kinetically controlled precipitation stage of α-phase crystals and a diffusion controlled phase of β-phase formation.[78] The disadvantage of this method lies in the toxicity of the side products, which are the oxyfluorinated compounds from the trifluoracetate precursors and the high temperature required by the reaction.

In the solvo-/hydrothermal method, precursors are sealed in an autoclave, and the reaction is run under high pressure. The advantage of using this synthesis method is that nanocrystals with high crystallinity are obtained at low temperatures.[69] The size of the particles is also controllable by adjusting the amount and ratio of the precursors. The hydrothermal method could also be used to synthesize hydrophilic UCNP directly. Wang et al. reported the hydrothermal synthesis of $NaYF_4$: Yb, Er/Tm NP with organic polymer surfactants, such as polyethyleneimine (PEI) and ethylene glycol (EG) as a surfactant.[79-80] Wang et al. also developed a solvothermal method for synthesizing $NaYF_4$: Yb, Er/Tm NP with various polymers such as PVP, polyethylene glycol (PEG) and polyacrylic acid (PAA).[81]

In this work, the thermal co-precipitation method initially developed by Park et al.[82] for the synthesis of iron oxide nanoparticles is used, with slight modifications. Briefly, the metal-surfactant complex is synthesized from their respective chloride derivatives and mixed with sodium oleate to create metal-oleate complex. In the high-temperature thermal coprecipitation method in octadecene, the first two oleate ligands dissociate at 200-240 °C (nucleation step), and the last oleate ligand dissociates at 310 °C (beginning of the growth process). For $NaYF_4$-based UCNP NaOH and NH_4F as sodium and fluoride sources are added in methanol (MeOH) in a solution containing lanthanide oleates in high-boiling point solvents such as 1-octadecene and a

coordinating agent such as oleic acid, prompting the growth of $NaYF_4$. The advantages of this method, besides the separation of nucleation and growth phases to produce highly monodisperse particles, are the lack of toxic by-products and their wide application on many materials.[46]
In Table 2-1 is a list of the most known synthesis methods of UCNP along with their advantages and disadvantages:

Table 2-1: Synthesis methods of UCNP

Synthesis methods	**Advantages**	**Disadvantages**
Co-precipitation	-Fast and simple	-Low monodispersity
Thermal decomposition	-High monodispersity -Pure crystal phase.	-Pre-synthesis of precursor -Toxic by-products -High temperature is required
Solvo-/hydrothermal	-Simple -Lower temperature than thermal decomposition -High crystalline product	- Autoclave is required -Predictions over results are difficult
Thermal coprecipitation	-High monodispersity -Pure crystal phase -Non-toxic by-products	-Pre-synthesis precursor -High temperature is required

2.1.3 Silica nanosystems on UCNP core

As UCNP have been proven to have potential applications as biomedical imaging and drug delivery agents, the essential first step to modify hydrophobic UCNP is to increase the hydrophilicity by coating the particles with silica or polymers.
Silica has many advantages when it is used as a coating agent for biomedical applications. It is transparent, chemically inert, and suitable for many surface modifications.[68] Growing a silica shell on UCNP can be done either with the well-known Stöber method or with a reverse microemulsion method.[83-85] In the Stöber method tetraethoxy- or tetramethoxysilane (TEOS or TMOS) hydrolyzed in ethanol or methanol is used, with ammonia water as a catalyst. Alkoxysilica network can be produced by a sequential process of hydrolyzation, condensation and cross-linking of TEOS (Figure 2.4).

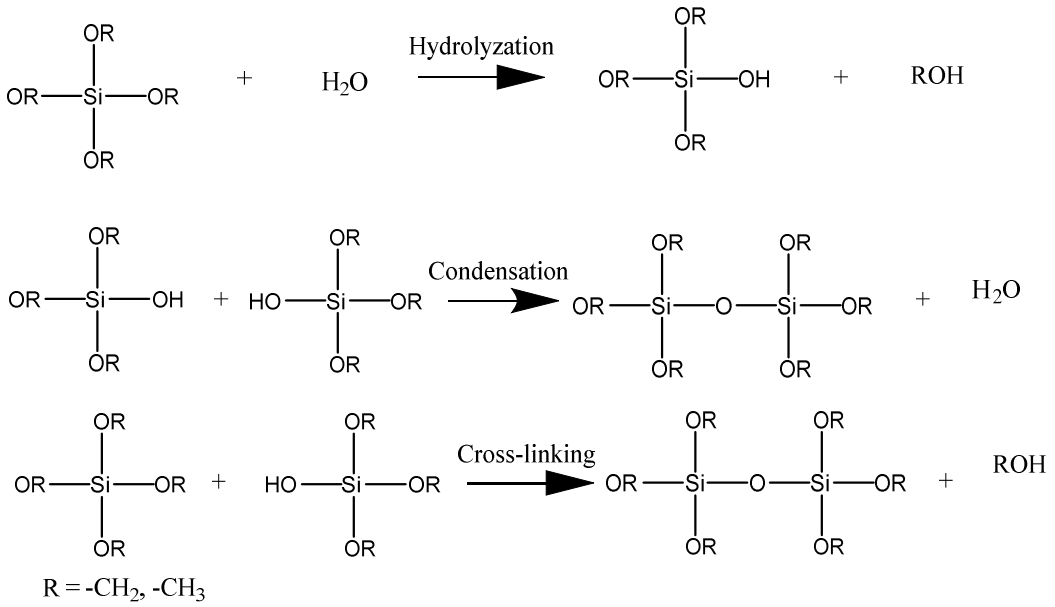

Figure 2.4: Stöber reaction mechanism in the silica particles' synthesis.[86] In the first reaction, alkyltetroxysilane are hydrolyzed first to form alkylalkoxysilanes, which react further with other hydrolyzed alkoxysilanes through condensation reaction (second reaction) and finally through cross-linking in the third reaction to form a long silica network.

Li et al.[87] coated polyvinylpyrrolidone (PVP) functionalized $NaYF_4$: Yb, Er/Tm nanoparticles with silica through the Stöber method. The shell thickness could be adjusted to 10±3 nm by controlling the amount of TEOS. However, the particles aggregated after coating. Shan et al.[88] coated oleate-functionalized $NaYF_4$: Yb, Er NP with silica by the reversed microemulsion method. The reverse microemulsion method is similar to the Stöber method, but the reactions are done in a nonpolar solvent such as cyclohexane and a surfactant such as Igepal CO-520, or Triton X, used to form micelles which contain the hydrophilic reagents of the reaction. However, the coated particles also tend to aggregate. Johnson et al. [89] did a ligand exchange on oleate functionalized $NaYF_4$: Yb, Er NP with PVP, before covering them with silica via the Stöber method. The resulting silica-coated particles had a thin (9 nm) silica shell with good stability in water. However, many core-free silica particles were produced. Since core-free silica particles are disadvantageous in the later gold-shell-growing phase, this method was not further tried in this work.

The reverse microemulsion method is described in Figure 2.5. The added surfactant Igepal CO-520 forms micelles in cyclohexane, where the hydrophobic groups are pointing outwards. When oleate-

functionalized UCNP cores are added, a ligand exchange occurs between the oleate and part of the surfactant, while the rest of the surfactant forms bigger micelles due to the addition of ammonia. The added TEOS hydrolyzes in the oil-water interphase and undergoes a ligand exchange with the surfactant. Along with a further hydrolyzation reaction, the UCNP core is brought into the water phase, and a closed silica shell is finally formed on the surface under the condensation reaction of the hydrolyzed TEOS.[90]

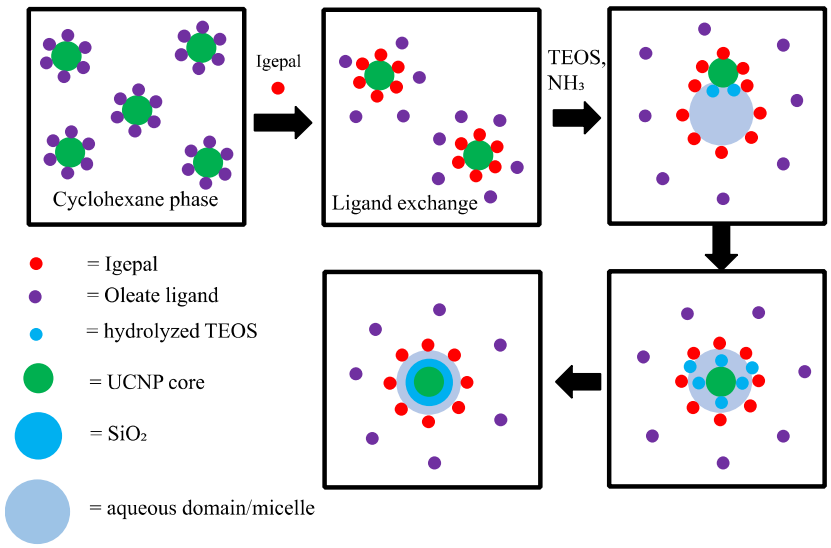

Figure 2.5: Coating of UCNP core with silica through the reverse microemulsion method. The scheme is adapted with slight modifications from the illustration of Ding et al. [90] explaining the coating iron oxide nanoparticles with silica. After adding Igepal CO-520 to oleate coated UCNP, the oleate ligands are detached and replaced by Igepal. Along with the addition of TEOS followed by the hydrolyzation, condensation, and cross-linking reaction in the water-phase to form a silica shell, the UCNP core is brought into the water phase and the silica coating is completed in the water phase.

2.2 Plasmonic enhancement of upconversion emission by noble metal nanosystems

Due to closely spaced energy levels of lanthanide ions in UCNP, they are prone to quenching by multiphonon transition.[27, 91-92] Quenching from the non-radiative decay of low energy photons or cross-relaxations due to lattice impurities additionally weakens upconversion-luminescence efficiency. As a result, UCNP have relatively low quantum yields, a key factor contributing to limitations in their practical applications.[91]

Plasmonics is, in general, the study of plasmon resonance, which arises due to the oscillation of excited free conduction electrons in metallic (mostly gold or silver) nanomaterials or

nanostructures, for example nanoparticles, nanoantennas, nanoresonators, or nanocavities.[93 94] It also refers to the manipulation of the resonant properties of these nanomaterials, which are called the plasmonic systems, in which their electron oscillations or surface plasmon can induce an electric field larger than the incident light.[93,95-96] Plasmonic systems can be used as antennas to enhance luminescence, by enhancing the radiation flux, or radiative decay rate.[27] Plasmon enhancement means, in general, the capability of plasmonic systems to enhance locally applied electromagnetic field, due to the coupling of the incoming light with surface plasmons. The enhanced electromagnetic field modifies the local density of states, which could lead to faster radiative decay rates.[27] The field enhancement is hence the ratio of the local electric field induced by the plasmonic systems relative to the incident electric field. Thus, plasmonic systems can enhance the absorption or emission of a chromophore, by adjusting the plasmonic system in such a way that plasmon resonance matches either the absorption or the emission of the UCNP.

In equation 2.1 below, the absorption cross section (σ) is the ratio between the absorbed power (P_{abs}), i.e., the part of the excitation power that leads to photon excitation, to the incident intensity (I_{inc}), i.e., total excitation pump power, which further depends on $|E(r_0)/E_0|$.[91] $E(r_0)$ is the induced electric field at the position of the ion and E_0 is the incident electric field, $\hat{n}$ is the unit vector along the direction of the induced dipole moment.

$$\sigma = \frac{P_{abs}}{I_{inc}} = \sim \frac{|\hat{n} \cdot E(r_0)|^2}{|E_0|^2} \tag{2.1}$$

Plasmon resonance can enhance upconversion absorption by increasing the local electric field. Enhancement of the local electric field can increase excitation, wherein the plasmon resonance can increase the transition rate of the lanthanide ions to the final excited state, hence increasing the final emission. The emission intensity is defined by the equation E^{2n}, where E is the electric field and n is the number of excited photons.[27] Plasmon resonance can also increase the non-radiative decay rate, and thus induce quenching.[91]

When the plasmon resonance frequency (and associated energy) is equivalent to the emission energy, it impacts the radiative decay rate directly, and the non-radiative decay rate indirectly. The quantum yield of emission (η) is defined by the following equation:

$$\eta = \frac{\gamma_{rad}}{\gamma_{rad} + \gamma_{non-rad}} \tag{2.2}$$

Where γ_{rad} and $\gamma_{non\text{-}rad}$ are the radiative and non-radiative decay rates, respectively. The value of η is indirectly influenced by the upconversion efficiency. Quantum yield only considers the decay rates of photons from the final emitting state, while upconversion efficiency (ratio of the emitted photon to the absorbed photons) considers all related processes after absorption. The maximum value of η is 1, whereas the maximum value of the upconversion efficiency is 0.5 for two-photon absorption, since only one photon will emit and fall back to the ground state, i.e., two-photon absorption process will only have a maximum upconversion quantum efficiency of 50 %. A plasmonic structure can affect both the radiative or the non-radiative decay rate, leading to either emission enhancement when the radiative rate is bigger than the non-radiative rate, or quenching for the opposite case.[91]

The quantum yield in the presence of a plasmonic system can be described as follows:

$$\eta_P = \frac{\gamma'_{rad}}{\gamma'_{rad} + \gamma'_{non-rad}} \tag{2.3}$$

The values of γ'_{rad} and $\gamma'_{non\text{-}rad}$, [27] which are the radiative and non-radiative decay rates in the presence of plasmon resonance, can be calculated by the following equation :

$$\gamma'_{rad} = \gamma^0_{rad} + \gamma^P_{rad} \tag{2.4}$$

$$\gamma'_{non-rad} = \gamma^0_{non-rad} + \gamma^P_{non-rad} \tag{2.5}$$

Where γ^0_{rad} and $\gamma^0_{non\text{-}rad}$ are the intrinsic radiative, and non-radiative decay rates, respectively, and γ^P_{rad} and $\gamma^P_{non\text{-}rad}$ are the radiative and non-radiative rates when the plasmonic system is present. Equation 2.3 can be rewritten as follows: [27]

$$\eta_P = \frac{\gamma^0_{rad} + \gamma^P_{rad}}{\gamma^0_{rad} + \gamma^0_{non-rad} + \gamma^P_{rad} + \gamma^P_{non-rad}} \tag{2.6}$$

The radiative enhancement (F_{rad}) is the ratio of γ^P_{rad}: γ^0_{rad}, and the non-radiative enhancement ($F_{non\text{-}rad}$) is the ratio of $\gamma^P_{non\text{-}rad}$: $\gamma^0_{non\text{-}rad}$. The intrinsic quantum yield (η_0) [27] is then defined as:

$$\eta_0 = \frac{\gamma^0_{rad}}{(\gamma^0_{rad} + \gamma^0_{non-rad})} \tag{2.7}$$

Hence equation 2.6 can be rewritten as:

$$\eta_P = \frac{\eta_0 \cdot (1 + F_{rad})}{1 + F_{non-rad} + \eta_0 \cdot (F_{rad} - F_{non-rad})} \quad (2.8)$$

The interactions between the parameters in equation 2.8 could be modelled as shown in Figure 2.6:

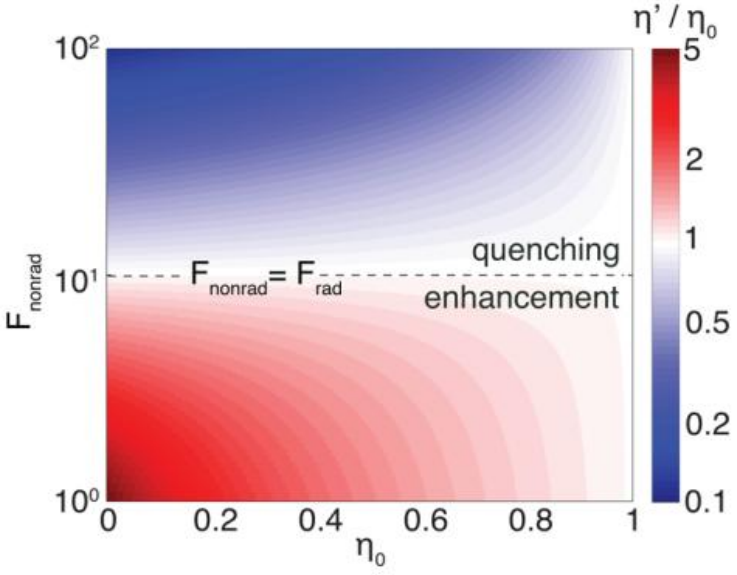

Figure 2.6: Plot describing the relation between $F_{non-rad}$, η_0, and the ratio of the plasmonic influenced quantum yield and the intrinsic quantum yield η'/η_0 (The colour bar is in logarithmic scale). (Reprinted with permission from Wu et al.[27] Copyright 2018 American Chemical Society)

Quenching is induced, when $F_{non-rad} > F_{rad}$, as described by the blue plot, whereas enhancement is induced when $F_{rad} > F_{non-rad}$. Furthermore, one can recognize from the plot, that if η_0 is already high, it is difficult to increase the enhancement further.

There are two ways of building a plasmonic metal system around a fluorophore. The first one is to bring metal nanoparticles nearby the fluorescing molecule. Luminescence intensity increases as the concentration of the metal particles increases before it decreases as quenching effects dominate. The same effect applies to the distance between the metal particles and a fluorescent molecule. The enhancement factor is first low when the UCNP molecules are close to the particles (separation distance (z) < 10 nm), and gradually increases as the distance increases, before reaching a maximum, and decreasing as the separation distances further increases.[97] Anger et al. calculated the theoretical enhancement factor for different sizes of gold particles as a dependence of z for a single molecule fluorophore.[97] They studied the fluorescence of a single molecule fluorophore (nile blue) on a glass substrate under the influence of an 80 nm gold particle on a fibre tip. At 5 nm

distance, the fluorescence enhancement is at the highest, while quenching dominates at distances < 5 nm and lower fluorescence emission occurs at larger distances.

The second type of plasmonic system involves growing a metal shell on UCNP core to better control the distance between lanthanide ions and the plasmon resonance. As mentioned before, the separation distance can cause either enhancement, quenching, or no effect on upconversion emission. The enhancement factor depends on the core-shell geometry ratio (ratio of UCNP and gold shell thickness). The plasmonic wavelength should be in resonance to the absorption or emission wavelength of the UCNP core. Fujii et al. synthesized $NaYF_4$ doped with Yb and Er with a size of 140 nm, a silica shell thickness of 15 nm and gold shell thickness of 20 nm. They observed a red (650 nm) emission enhancement at a factor of 1.36, whereas a green (540 nm) emission was decreased by a factor of 0.74 compared to silica coated UCNP.[30] The theoretical calculations in the work of Fujii et al. were based on the method of transfer-matrix solution of a dipole radiating inside and outside a stratified sphere consisting of concentric spherical shells as described by Moroz.[98] With the size parameters mentioned, the experimentally obtained enhancement factor is smaller relative to the calculated enhancement factor for the quantum efficiency. For example, for the quantum efficiency of silica coated UCNP without gold shell, the experimentally obtained enhancement factor differed from the theoretically calculated one by a factor of 1.88, owing to quenching effects. The quasi-static approximation of the square of the incident field is 0.6 for a gold shell of 17 nm with the same size of silica coated UCNP. The same value was estimated for a gold shell thickness of 20 nm obtained from the TEM measurements. This shows that the plasmon influenced upconversion emission was indeed sensitive to the core-shell geometry, and that the conditions to enhance the incident electric field, and the quantum efficiency are limiting. Additionally, excitation parameters such as excitation power density should also be further defined for upconversion enhancement of core-shell systems.

In gold nanoparticles, the localized surface plasmon resonance has defined frequencies depending on the size or thickness of the particles and shell. The oscillation frequency of the plasmon can be a dipole mode, which is the dominant mode for gold particles or gold shells with sizes smaller than the excitation wavelength, or for higher order modes such as quadrupole or octupole modes.[99] Dipole mode resonance excitation occurs when all electrons in a metal experience oscillation in the same phase as the incoming electromagnetic wave. Along with increasing particle size, higher order plasmon modes can be excited due to phase retardation of the field inside the nanoparticles. In gold shells, the oscillation frequency of the higher order modes such as quadrupole, hexapole or

octupole modes are, unlike to those of solid gold spherical nanoparticle, well separated.[99-100] Another plasmon mode of the nanoshell in dielectric core-metal shell structure is the cavity mode, which results from electromagnetic excitation on the inner interface of the metal shell, where the incoming light is confined inside the dielectric core and hence induce charges inside the nanoshell.[101]

The two plasmons in the inner shell (cavity mode) and outer shell (sphere mode) interact according to plasmon hybridization theory.[101-102] This interaction leads to a splitting of the plasmon resonances into a low energy (bonding plasmon) and a high energy bonding mode (anti-bonding plasmon). The bonding energy can be varied by varying the ratio of the shell thickness to the core radius. With increasing shell thickness, the sphere resonance of the gold shell with the dielectric core shifts to longer wavelengths, and becomes more similar to the sphere resonance of solid gold nanoparticles, due to a decreased interaction between the outer sphere resonance and the cavity mode, causing a lower separation of the energy levels of the bonding and anti-bonding plasmons.[102-103] When the size of the core is increased while the gold shell thickness decreases, the plasmon resonance peak also red-shifts, as a thinner shell leads to a stronger coupling between the sphere and cavity plasmons.[102,104] Penninkhof et al. demonstrated that the calculated field enhancement in an optimized size core-shell gold colloid is higher than that of optimized bulk gold nanoparticles, which makes the core-shell system ideal for fluorescent or Raman enhancement.[105] Hence, by varying the core-shell ratio of silica coated UCNP and the gold shell thickness, different plasmon resonance modes can be excited, since the plasmon frequency of gold nanoshells can be tuned to the visible and near infrared frequency range.

2.3 Luminescence resonance energy transfer

Luminescence resonance energy transfer (LRET) or more commonly known as fluorescence or Förster resonance energy transfer (FRET) is a non-radiative energy transfer process from an excited donor fluorophore to an acceptor, where the emission energy of the donor overlaps with the absorption energy of the acceptor. As mentioned in the introduction, coupling of a UCNP donor to a fluorophore organic dye as acceptor is used in bioimaging applications, owing to the less damaging nature of NIR radiation compared to UV-light, deeper penetration distance, and the fact that this radiation causes no auto-fluorescence in biological media..[39-44] If the absorption wavelength range of the dye is within the emission wavelength range of the UCNP, excitation of the dye can be simply achieved by using low energy density NIR-light. Electrons of the donor that

are excited to higher energy states relax back non-radiatively to the ground states, while transferring their energy to a neighboring acceptor. The excited electrons of the donor emit back to the ground state through a fluorescence process. When the emission-absorption band of both donor and acceptor resonates, energy is transferred from the donor to the acceptor, leading to a concomitant reduction in emission intensity of donor and an increase in emission intensity of acceptor.[106] Additionally, the decay lifetime of the excited photons of the donor decreases, as the photon energy is transferred to the emitter, which causes the photon to relax non-radiatively faster to the ground state. The FRET intensity depends on the distance between the donor (D) and the acceptor (A). An important parameter is the so-called Förster radius (see chapter 2.3). The Förster radius is typically around 10-55 Å.[107]

According to theory, the FRET efficiency (E_{FRET}) depends on several factors, as described by the following equation: [108]

$$E_{FRET} = \frac{k_T}{k_T + k_D + k_{Di}} = \frac{{R_0}^6}{{R_0}^6 + r^6} \tag{2.9}$$

$${R_0}^6 = \frac{9 \cdot \ln 10 \cdot \kappa^2 \cdot \Phi_D \cdot J}{128 \cdot \pi^5 \cdot n^4 \cdot N_A} \tag{2.10}$$

where k_T is the rate of energy transfer, k_D is the radiative decay rate in the absence of acceptor and k_{Di} is radiative decay rate of the acceptor, ${R_0}^6$ is the Förster distance where the probability of a fluorescing donor equals the probability of an energy transfer to its acceptor, r is the donor-acceptor distance, κ^2 is the orientation factor between the emission and absorption transition dipole moments of donor and acceptor (possible values = 1-4), Φ_D is the quantum yield of the donor within the absence of an acceptor, J is the overlap integral between the donor and an acceptor, and n is the refractive index. R_0 was defined by Förster as the donor-acceptor distance, where the energy transfer efficiency is 50 %. The efficiency decreases with increasing r and increases with increasing R_0. E_{FRET} changes rapidly when $r \approx R_0$ and slowly when $r >> R_0$ or $r << R_0$.[106]

The relation between donor lifetime and E_{FRET} is described by the following equation:

$$E_{FRET} = 1 - \frac{\tau_{DA}}{\tau_D} \tag{2.11}$$

where τ_{DA} is the lifetime of the donor in the presence of an acceptor and τ_D is a donor's lifetime in the absence of the acceptor.

UCNP can transfer its energy to a fluorophore through photon reabsorption (inner filter effect or radiative energy transfer) or non-radiative energy transfer (NRET).[109-110] Photon reabsorption occurs when the donor emits excited photons, and upon relaxation, the energy is absorbed by a fluorophore molecule in a suitable distance. As there are no interactions between the two molecules, no decrease in the donor's emission lifetime is observed. In a non-radiative energy transfer (FRET or Dexter's energy transfer), the energy is transferred between two resonant electronic excited states. This path is more efficient than photon reabsorption, as the donor experiences an additional relaxation pathway. A decrease in the donor's emission lifetime is also observable. NRET can occur in two ways, which are FRET or Dexter's energy transfer (DET). In FRET the energy transfer occurs between two resonant energy states between D and A through dipole coupling, while DET occurs via singlet-singlet or triplet-triplet states between D and A (see Figure 2.7). UCNP can be a suitable donor source as they have multiple defined emission bands over a broad spectral range, due to the multiple states of the 4f orbitals of the lanthanides.

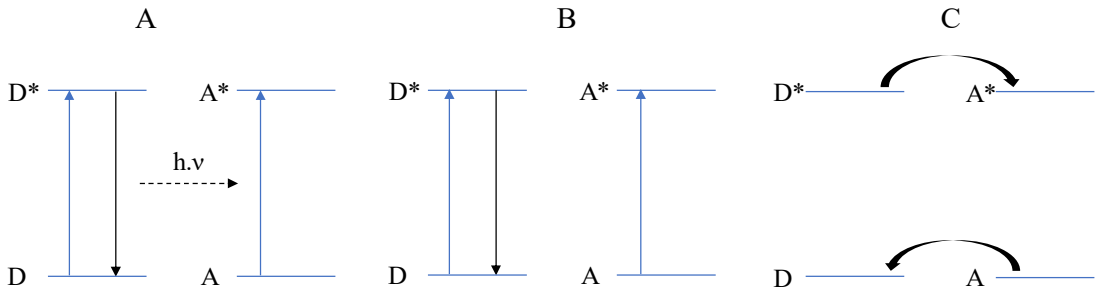

Figure 2.7 A: Radiative energy transfer scheme. The donor is excited to the first excited state D and upon relaxation transfers its energy to the acceptor A, which further excites the latter to the excited state A*; B: non-radiative energy transfer scheme in form of FRET, where the energy transfer occurs through dipole-coupling between D and A; C: Dexter energy transfer, where either a singlet-singlet or triplet-triplet transfer occurs.*

UCNP utilized for FRET effects are usually coupled with an organic dye on the surface within certain distances. Depending on the excitation or absorption wavelength of the dye, UCNP can be used as an antenna to transfer UC-emission energy to the dye or the other way round. For dyes acting as donor molecules, the excitation light excites the dye's electrons to an excited singlet state followed by several deactivation processes such as internal conversion (IC), intersystem crossing (ISC), radiation relaxation, and energy transfer to lanthanide ions.[111]

FRET occurs if the dye relaxes back to the ground singlet state while transferring its energy to an activator of the UCNP, and only if dipole transition is allowed. If the ISC process dominates over the energy transfer, the relaxed photon of the dye will go to the excited triplet state, making the transition to be spin-forbidden. The energy transfer then occurs from the triplet state of the dye to excite the activator. Thus, FRET (electronic) or Dexter (exchange) type energy transfer can be used as the explanation for such a process.

The energy transfer mechanism of FRET is described in Figure 2.8.

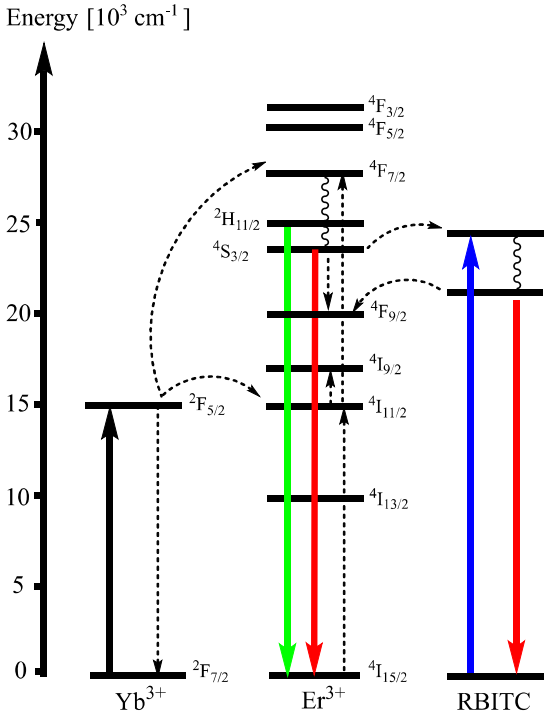

Figure 2.8: Energy level scheme of upconversion emission in Yb^{3+}/Er^{3+}-dopants system and the following energy transfer processes to RBITC.(Republished from reference.[112] Copyright 2019 with permission from Elsevier.)

Beside the common ETU and PA process of UCNP, UCNP can transfer the photon energy to RBITC from $^4S_{3/2}$ states. An energy back-transfer can occur from RBITC to $^4F_{9/2}$ for an increase of UC-red emission at 654 nm.

2.4 Scanning- and transmission electron microscopy

Scanning (SEM) and transmission electron microscope (TEM) are important tools used to characterize the size, structure, and morphology of nanoparticles through optical depiction. Both methods work by shooting a focused beam of electrons on particles that are fixed on an objective

plate or a special grid and the resulting transmitted (TEM) or backscatter and secondary (SEM) electrons after a collision with the sample are then monitored. Every atom or crystal structure scatters or diffracts the incident electrons variably and can deliver optical information about the sample. The main difference between the two methods is that SEM measurements result in the three-dimensional depiction of the particles which can be used to investigate the surface structure or topography of the particles, whereas TEM produces a two-dimensional picture of particles useful only for size measurements. Another type of TEM is the scanning-TEM (STEM), which combines the principles of TEM and SEM. Like TEM, STEM utilizes transmitted electrons for object characterizations and additionally combines other detectors that are not available in TEM, such as the backscatter electron detector, or a scattered beam detector. Like in SEM, objects in STEM mode are scanned by a highly focused electron beam. The advantage of STEM compared to SEM is in the spatial resolution. While conventional TEM provides better resolution of images, which according to modern standard equipment can depict up to 0.2±0.1 nm resolution in size,[113] STEM could provide high resolution of up to 50 pm,[114] whereas the best resolution for field emission (FE)-SEM nowadays lies at the 0.4 nm range.[115]

Electron interactions with metals, semiconductors or insulators are basically divided into two types: elastic and inelastic scattering. In elastic scattering, the electron is deflected by an elementary particle in the nucleus or an electron in the outer shell, which has the same energy as the incoming electron. The backscattered electron (BSE) is then scattered in a wide-angle direction (> 90°) relative to the arrival direction with a small energy loss.[116]

Inelastic scattering is caused by various types of interaction of the incoming electrons with the electrons or the nucleus of the samples, which result in a higher energy loss than for BSE. The amount of energy loss depends on the kind of excitation of the samples' electrons and the binding energy of this electron to the core. This energy is transferred to the sample, leading to the formation of secondary electrons that can be used to detect and characterize the sample.[116] Other types of inelastically scattered products are Auger electrons, cathodoluminescence, and characteristic X-rays as depicted in Figure 2.9. Electrons can also pass through a sample if it is thin enough. The transmitted electrons can be used to observe the internal structure of a sample. When incident electrons reach a samples' surface, they penetrate through the electron shells before they encounter the core. The primary electron beam then creates a zone of primary excitation, where the size and shape of the zone depend on the electron energy and density of the sample. The use of higher beam

energy, i.e., electron acceleration, creates a larger primary excitation region but results in the loss of surface details.[116]

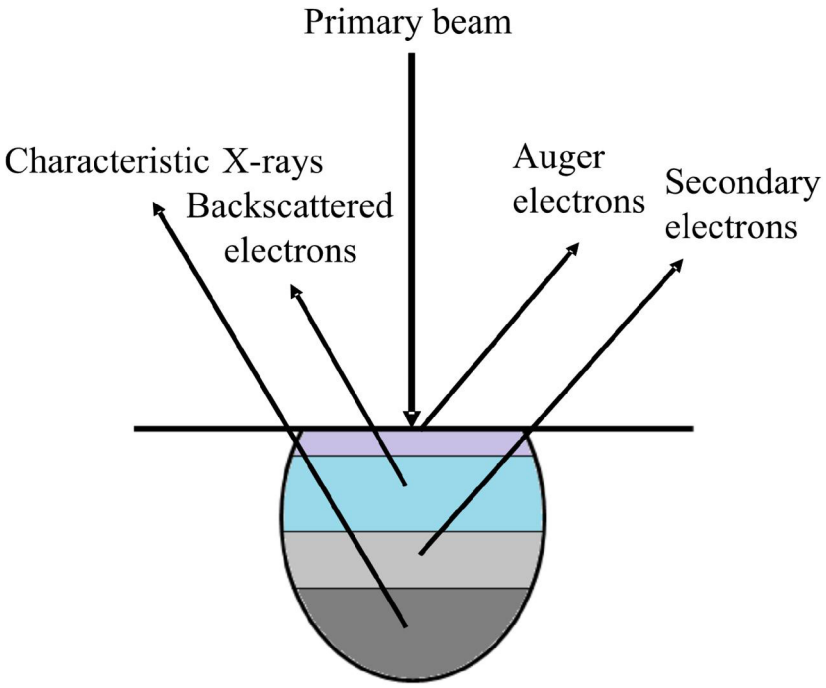

Figure 2.9: Types of electrons produced due to interactions with a primary beam. Electrons hitting the sample's surface create a primary excitation zone (oval-shaped zone). The primary beam hit the samples and electrons are either reflected or scattered and the energy from each electron depends on the depth of the reflected electrons. (Redrawn and adapted from reference[116])

Secondary electrons (SE) are used mostly for signal detections. These electrons are created from ionization of the sample surface caused by the interaction of the primary electron beam with the sample's atoms, in which weaker bounded electrons are loosened from their shell. As these electrons have relatively weak energy (3-5 eV), they can only escape a region within a few nanometers from the surface. This causes the signals to give the exact location of the beam with fine resolution. SE are mainly used to investigate the surface structure of samples. Primary beams with a high acceleration allow the ion of a deeper region of samples compared to lower acceleration beams.[116]

Backscattered electrons (BSE) have, compared to secondary electrons, a much higher energy (> 50 eV) due to elastic scattering of the primary beam after interactions with the nucleus of the atoms, which leads to a wide-angle directional change of the incoming electrons. Elements with high atomic numbers have more protons that could interact with the primary beam, causing a higher

production of BSE for signal detection. The BSE yield (percent of BSE/primary electrons) therefore depends on the atomic number, and as such BSE can provide information on what type elements are in the sample. The region where BSE are produced is larger than that of SE, owing to the high energy of the BSE that prevents them from being absorbed by the sample. The resolution from this signal is hence worse than for SE, which is effectively the same as the electron beam size, though it allows for depiction of deeper regions.[117]

Figure 2.10 shows the general construction scheme of an SEM. On the very top is the electron gun which produces and accelerates electron with a voltage acceleration between 0.1-30 keV. Older SEM machines use a tungsten filament as an electron gun, whereas a field emission source is often used nowadays.[116] Cold field emission produces electrons at room temperature simply by applying an electric field between a cathode and an anode, whereas in thermal emission a higher temperature is needed, leading to the production of gas molecules which reduces absorption and stabilizes the primary beam.

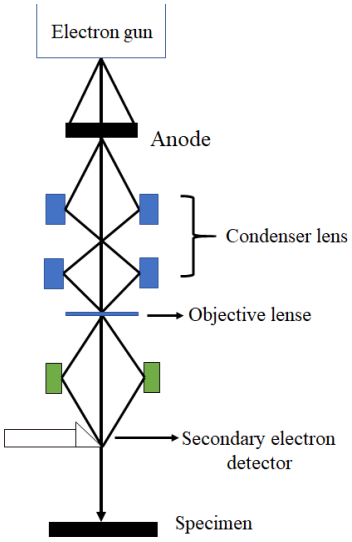

Figure 2.10: General STEM construction. (Redrawn and adapted from reference [116])

The beam from the electron gun is quite wide (~50 µm) and needs to be focused to a size of 1-100 nm by an electromagnetic field produced by electromagnetic lenses and apertures. Along the whole process, a high vacuum environment is crucial to prevent the electron beam from being scattered by air molecules. Next, electron lenses can magnify or demagnify the electron beam, as the aberration from electromagnetic lenses is still quite weak compared to normal lenses.[116] In SEM

the electron lenses always demagnify the electron beam. There are two kinds of electron lenses: condenser lenses that converge the electron beam after it passes the anode plate, and objective lenses that further focus the electron beam on the sample's surface. Lastly, there are the different detectors used to detect the signal from the SE, BSE, and other electron signals. The most well-known detector is the Everhart-Thornley detector for detecting the SE signal.[116] It consists of a scintillator, which converts the incoming electron into light, a pipe that transfers the light to a photomultiplier tube, which then converts the light back to electrons.[116]

2.5 Dynamic light scattering

Dynamic light scattering (DLS), also known as photon correlation spectroscopy or quasi-elastic light scattering, is a method of measuring the hydrodynamic diameter of macromolecules or nanoparticles in solution, i.e., studying the diffusion behavior of particles in a dispersion. Molecules in liquid move randomly through Brownian motion, and DLS correlates this movement with the size of the particles. Smaller size particles move more rapidly than bigger or heavier ones. The hydrodynamic diameter D_H is obtained from the following Stoke-Einstein equation:

$$D_H = \frac{k \cdot T}{3 \cdot \pi \cdot \eta \cdot D} \tag{2.12}$$

where D is the diffusion coefficient, D_H is the particles' hydrodynamic diameter, k is the Boltzmann's constant, T is the temperature and η is the solvent's viscosity.

The hydrodynamic diameter measurements depend on the temperature, as the viscosity changes with temperature. When laser light hits a sample solution, the particles scatter the light either in a mutually destructive phase (i.e., the scattered light cancels each other) or mutually constructive phase (scattered light enhances each other), where the intensity fluctuations can be correlated using an auto-correlator to determine how fast the light intensity fluctuates. The auto-correlator measures and correlates the signal intensity at the time t and t+τ (delay or lag time), where the period t+τ can be chosen to be shortly after t. Small particles will have a low correlation at t and t+τ, as they move quicker than bigger particles, and hence have bigger fluctuations in terms of the scattered light, while bigger particles will have lower and more persistent fluctuations at t and t+τ. Random fluctuations are depicted in the autocorrelation function in a correlogram, where the autocorrelation function is a function of the delay time.

The intensity correlation function ($G_2(\tau)$) describes the motion of particles in the dispersion and can be formulated by the following equation: [118-119]

$$G_2(\tau) = \langle I(t) \cdot I(t+\tau) \rangle \quad (2.13)$$

$$g_2(\tau) = \frac{\langle I(t) \cdot I(t+\tau) \rangle}{\langle I(t) \rangle^2} \quad (2.14)$$

where τ is the time difference between two points and $g_2(\tau)$ is the normalized electric field correlation function.

The electric field correlation function ($G_1(\tau)$) describes the movement of the particles relative to each other and can be formulated by the following equation: [118-119]

$$G_1(\tau) = \langle E(t) \cdot E(t+\tau) \rangle \quad (2.15)$$

$$g_1(\tau) = \frac{\langle E(t) \cdot E(t+\tau) \rangle}{\langle E(t) \rangle^2} \quad (2.16)$$

Again $g_1(\tau)$ is the normalized correlation function.

E(t) and E (t+ τ) are the scattered electric field at the time t and (t+τ).

$G_1(\tau)$ and $G_2(\tau)$ are connected by the Siegert relation:[120]

$$g_2(\tau) = B + \beta \cdot | g_1 \cdot (\tau)|^2 \quad (2.17)$$

B is the baseline, and β is the coherence factor, which depends on the detector's position, optical alignment and scattering properties of the particles.

For monodisperse particles, $g_1(\tau)$ has an exponential decay function and depends on a decay constant Γ: [118-119]

$$g_1(\tau) = e^{-\Gamma \cdot \tau} \quad (2.18)$$

For a polydisperse system, $g_1(\tau)$ is an integral of the distribution of the decay rates ($G(\Gamma)$): [118-119]

$$g_1(\tau) = \int_0^{\infty} G(\Gamma) \cdot e^{-\Gamma_\tau \cdot d\Gamma} \tag{2.19}$$

The decay constant can be described by the following equation: [118-119]

$$g_1(\tau) = \int_0^{\infty} G(\Gamma) \cdot e^{-\Gamma_\tau \cdot d\Gamma} \tag{2.20}$$

$$\Gamma = -D_\tau \cdot q^2 \tag{2.21}$$

Where q is the wave vector and can be formulated as:

$$q = \frac{4 \cdot \pi \cdot \eta}{\lambda} \cdot \sin\frac{\theta}{2} \tag{2.22}$$

where λ is the wavelength of the incident light and θ is the angle of the detector.
The relation between the particles' movement and the electric field correlation can be described as follows: [118-119]

$$g_2(\tau) = 1 + \beta \cdot e^{-2 \cdot D_\tau \cdot q^2 \cdot \tau} \tag{2.23}$$

The normalized intensity correlation function can be turned into a field correlation function by turning the Siegert relation into a logarithmic function and developing a polynomial for the fitting of the data:

$$\ln(g_2(\tau) - B) = \ln\beta + 2 \cdot (-\Gamma \cdot \tau + \frac{k_2}{2!} \cdot \tau^2 - \frac{k_3}{3!} \cdot \tau^3 + \frac{k_4}{4!} \cdot \tau^4 \ldots.) \tag{2.24}$$

The polynomial fitting is called the cumulant fit, where especially k_2/Γ^2 is the polydispersity index (PDI), which is the relative width of the distribution size. A PDI value < 0.05 represents very high monodispersity, 0.05 < PDI < 0.15 represents high monodispersity, 0.15 < PDI < 0.25 represents low monodispersity, 0.25 < PDI > 0.5 represents very low monodispersity, and PDI > 0.5 means the measurement is unreliable. [118-119]

Figure 2.11 shows a typical construction scheme of a DLS device.

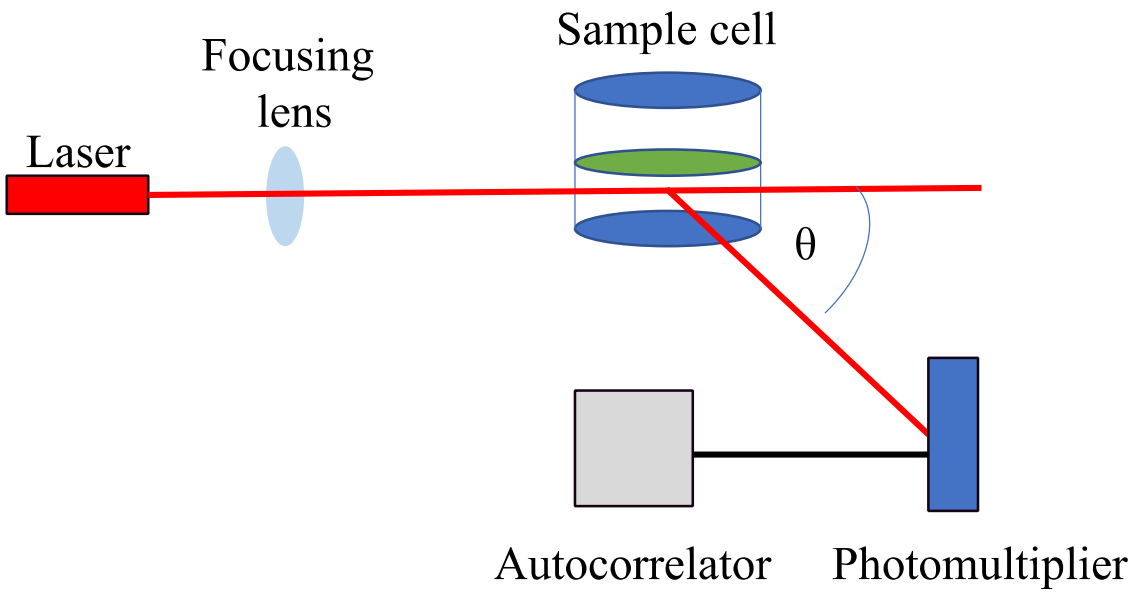

Figure 2.11: Typical construction scheme of a DLS machine. The laser light (red line) from a laser source is focused after passing through a lens. After hitting the sample cell, the scattered light intensity is enhanced by a photomultiplier and measured by an autocorrelator.

A detector can be placed at 90° to the incident light or at a wider angle (173° or 158°) for backscatter measurements. Such backscatter measurements are useful for highly concentrated samples and scattering from large particles can be avoided, as the laser light does not have to travel as far as in forward scattering measurements. This reduces the so-called multiple scattering, i.e., scattering caused by other particles. Large particles or dust mainly scatter in the forward directions, so backscatter measurements can be useful in reducing the scattering effect from larger particles.

2.6 Electrophoretic light scattering

Electrophoretic light scattering allows for the determination of surface charges of nanoparticles through measurement of the zeta potential. Charged particles in solvents have an electrostatic double layer, where counter ions form in the Stern layer. There are two parts of this double layer: the first is the inner region, the Stern layer, where the counter ions form a solid layer and are strongly coupled; the second is the outer region or diffuse double layer. When particles move, the ions in the inner region stay with the particles, whereas the ions on the outer region change

consistently with the flow of the medium. The zeta potential is the potential of the area between these two layers, called the slipping plane (see Figure 2.12).[121]

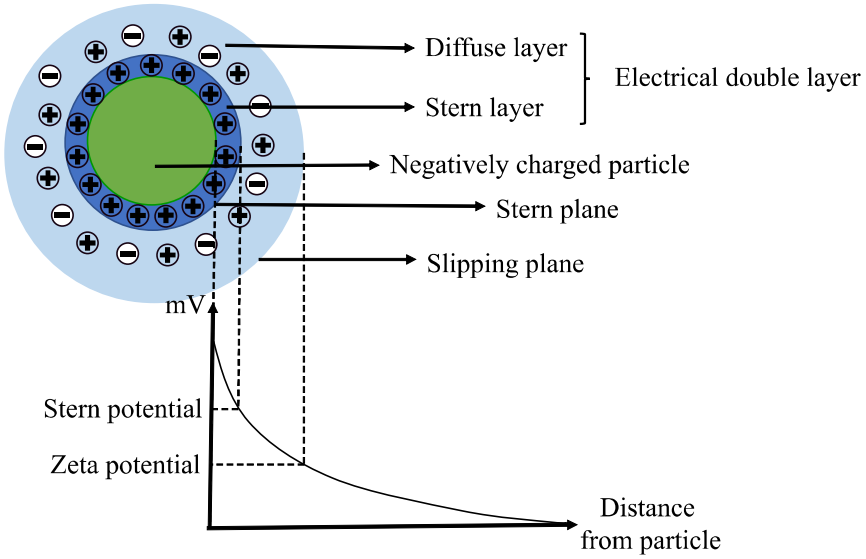

Figure 2.12: Electrical double layer of charged particles and the slipping plane which determines the zeta potential. This figure has been readapted from reference [122].

Electrophoresis is the movement of charged particles in a medium when an electric field is applied to them.[122] The electrostatic force moves the particles to the electrode with the opposite charge, but the frictional force that is caused by the viscosity of the medium slows down the particles. At the equilibrium between these two forces, the particles move with constant velocity to the electrode, and this corresponds directly to their electrophoretic mobility (μ_{ep}).[122]

According to Henry's equation, the μ_{ep} can be determined as follows:

$$\mu_{ep} = \frac{2 \cdot \nu . \zeta . f(\kappa . a)}{3 \cdot \eta} \qquad (2.25)$$

where ε is the dielectric constant, ζ is zeta potential, f (κ.a) is Henry's function, and η is the viscosity of the medium.

A laser source in the measuring device shines on the particles, and the frequency of the light scattered by the moving particles is shifted according to the Doppler effect. The electrophoretic mobility is then measured based on the frequency shift of the particles: [123]

$$\Delta f = \frac{2 \cdot \nu \cdot \sin\left(\frac{\theta}{2}\right)}{\lambda} \tag{2.26}$$

where Δf is the frequency shift, ν is particles' velocity, θ is scattering angle and λ is the laser wavelength.

2.7 Fluorescence spectroscopy

In this work, fluorescence spectroscopy is an essential tool used to determine the change of emission intensity due to the silica coating or gold shell on the surface of silica coated UCNP. Fluorescence is an electronic transition process, where a chromophore (light-absorbing molecule) emits photons during de-excitation from the excited singular state (S_1) back to the ground vibrational state, which is commonly described in a Jablonski diagram. In a common downconversion process, the absorption wavelength is shorter than the emission wavelength, since the energy needed to excite a photon from the ground state is higher than the energy released upon emission by the photon. The emission energy is independent of the excitation/absorption wavelength in a downconversion process, and emission that occurs from the excited singular state S_1 describes the electronic distribution within this state. The process is a non-linear one such that the emission wavelength depends on the excitation wavelength. A fluorescence excitation spectrum can be measured by setting the emission wavelength and running the excitation monochromator.
A spectrofluorometer is used to measure fluorescence spectra. It consists of a light source, a monochromator for the excitation and one for the emission, a filter, and a detector (see Figure 2.13).

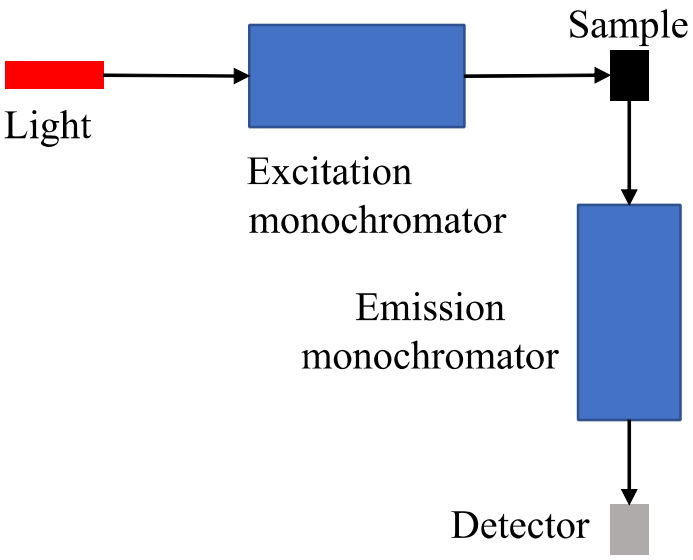

Figure 2.13: General construction of a spectrofluorometer consisting of a light source, excitation and emission monochromator and detector.

As light source, either a tungsten-halogen lamp, a mercury lamp or a xenon arc lamp can be used. A Xenon arc lamp provides a continuous spectral output of energy. For UCNP measurement a 980 nm laser diode is used. A filter is used to isolate both the excitation and emission wavelength. In modern instruments, two diffraction grating monochromators are commonly utilized to select both excitation and emission wavelength. Two diffraction grating monochromators are used to measure both excitation and emission spectra. The slit width in these monochromators can be adjusted to modulate the spectrum's resolution. Lastly, a photomultiplier is used as a detector.

2.8 Lifetime measurement spectroscopy

Changes in fluorescence emission due to energy transfer effect, whether it is a plasmonic or FRET effect, are usually accompanied by changes of fluorescence lifetime or decay rate, due to changes in the electronic transitions during a radiative decay.[124] An excited molecule stays in the excited state for a definite time before relaxing back to the ground state. The mean time spent on an excited state is called the fluorescence lifetime (τ) and can be calculated by the following equation:

$$\tau = \frac{1}{k_{rad} + k_{non-rad} + k_{isc}} \qquad (2.27)$$

Where k_{rad} is the radiative decay constant, $k_{non\text{-}rad}$ is the non-radiative decay constant, and k_{isc} is the decay constant of intersystem crossing.

In FRET there is another term called the rate of energy transfer k_T which depends on the donor lifetime (τ_D) and the Förster distance (see chapter 2.3). k_T is defined as:

$$k_T = \frac{1}{\tau_D} \cdot \left(\frac{{R_0}^6}{{r_{DA}}^6} \right) \tag{2.28}$$

Where r_{DA} is the distance between donor and acceptor.

There are basically three different methods used to measure the fluorescence lifetime: The Strobe method, Time-Correlated Single Photon Counting (TCSPC), multifrequency and cross-correlation spectroscopy.[125] The first two methods measure in the time domain, while the last one measures in the frequency domain.

In the Strobe method, the sample is excited by a pulsed light source and the fluorescence lifetime is measured during a very narrow time window. The time window is shifted after every measurement until enough data are collected and a decay intensity curve can be drawn.[126-127]

In TCSPC one photon is excited by a pulsed laser source. The time it needs to relax back to the ground state is then measured with the excitation pulse used as a reference. Repetitive excitation to detect all one-photon cycles (time from excitation to emission) is needed to provide sufficient statistics, where fluorescence intensity is plotted against time.[128] The one-photon cycle can be detected by a photomultiplier or a multi-channel plate photomultiplier.

In cross-correlation spectroscopy, the sample is excited by a light source with a sinusoidally modulated intensity. As a result, the sample also emits sinusoidally with a phase shift compared to the light source. The fluorescence lifetime is correlated to the phase shift of the emission; a large phase shift/delay corresponds to a longer fluorescence lifetime.[125]

2.9 Infrared spectroscopy

In IR spectroscopy, a sample is hit with infrared light, which causes the molecules to vibrate and rotate. IR spectroscopy is an important and widely used method used to identify molecules, as every little change in the bonding type and structure of molecules can lead to distinct changes in the IR spectrum.

Not all vibrational movements can be detected by an IR spectrometer, but rather vibrational movements that lead to a change of the dipole moment can be detected. A symmetrical vibrational movement is not detectable by IR spectroscopy, for example. Polar functional groups, on the

contrary, have strong absorption bands in the IR spectra, whereas nonpolar groups have relatively weak bands. The electromagnetic wave interacts with the vibrating molecules, which leads to the absorption of the IR energy.[129]

Commonly, the IR spectrum is measured as a function of the wavenumber $\bar{\upsilon}$ (cm^{-1}), which is the reciprocal value of wavelength and the measured region is normally between 400-4000 cm^{-1}.

As an infrared source, a Nernst lamp, which is made from ZrO_2, is heated to 1500-2000 °C to generate the necessary heat energy. In the monochromator, which is either a prism or diffraction grating, the light is filtered and passed through the sample. An IR detector is a thermoelement, which detects the changes in heat (i.e., the intensity of the IR beam) and converts it to electric signals, which can be enhanced and measured.[129]

Nowadays a Fourier-Transform-IR (FT-IR) spectrometer is commonly used for measurements, which allow for faster measurement, since all radiation frequencies can be detected at the same time and not one by one. Instead of a monochromator, a Michelson interferometer is used. An interferogram converts a mathematical operation called Fourier transformation into a detectable IR-spectrum.

2.10 X-ray diffractometry

X-ray diffractometry (XRD) is commonly used to investigate the structure or phase of crystallites. In this work, it was used to determine the crystal structure of the UCNP core since the hexagonal phase of $NaYF_4$ commonly has lower phonon energy than its cubic phase $NaYF_4$, and hence, can provide a more effective emission intensity.[68-69]

Because X-ray wavelengths and crystal lattice parameters are in the same size range, incoming X-rays can be diffracted by the crystal atoms upon interaction. The Bragg's law describes the constructive interference of X-ray diffraction from the crystal lattice as:

$$n \cdot \lambda = 2 \cdot d \cdot \sin\theta \qquad (2.29)$$

where n is the order of diffraction peak, λ is the wavelength of incident X-ray, d is the plane spacing and Θ is the diffraction angle.

Every crystal structure has a certain construction of crystal lattice plane, which reflects the incoming X-ray in distinctive reflection angles θ, caused by d value characteristic to each crystal phase (see Figure 2.14).

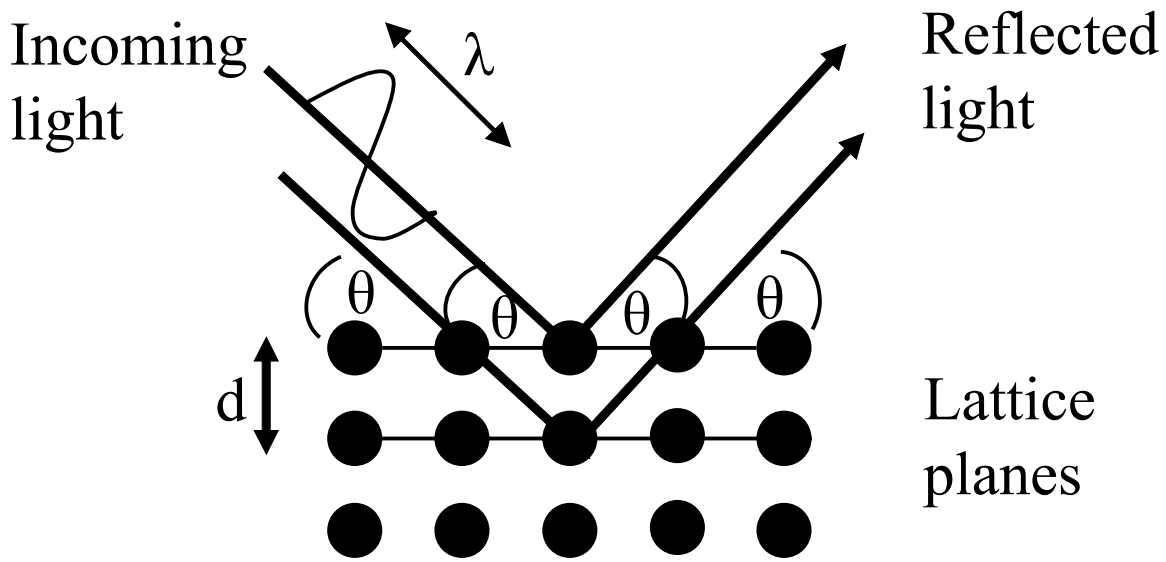

Figure 2.14: Radiation and reflection of X-ray on lattice plane based on Bragg's theory.[130]

The most well-known method of X-ray diffraction is the Debye-Scherrer technique. In this method, a powder is used as a sample. The crystals in the sample would then lie in random orientation relative to the parallel plane. By moving the X-ray light from 0° to 90° relative to the sample, all possible diffraction angles caused by the plane spacing d can be measured. A monochromatic X-ray is produced by a cathode tube that can be rotated at an angle of 0° to 90° relative to the sample. The diffracted wavelengths are then detected by a detector, which sends the signals to a computer. An instrument used to rotate the X-ray tube and the detector is called a goniometer (see Figure 2.15).[131]

XRD spectra consist of diffraction peaks of the samples. These diffraction peaks can be used to calculate the interatomic distances through the determination of Miller indices (hkl), which is the notation for describing the planes and directions of a crystal. By calculating d from Bragg's law, one can determine the Miller indices from a reference pattern. For example, for a cubic structure the hkl is calculated from the following formula:

$$d = \frac{a}{(h^2 + k^2 + l^2)} \tag{2.30}$$

where a is the unit cell of a cubic structure. After all Miller indices are identified, one can then determine the structure or phase of the crystal.

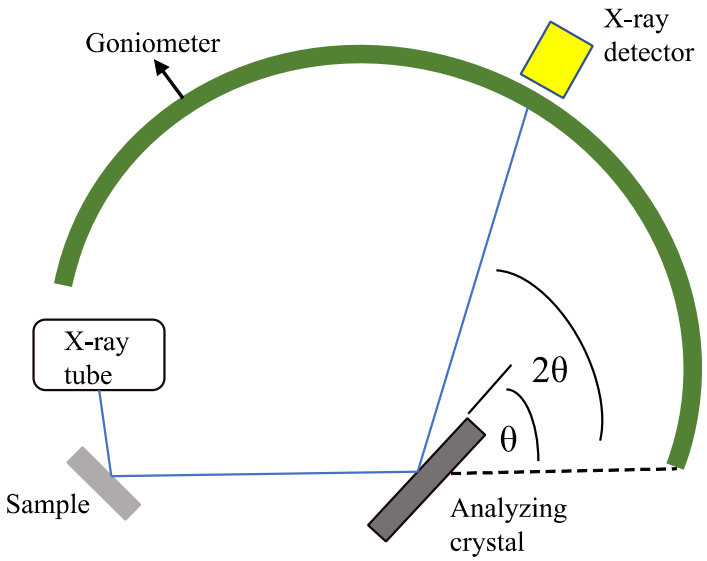

Figure 2.15: XRD instrument scheme with a goniometer.[132] This illustration has been redrawn from the reference.

2.11 UV-VIS-NIR spectroscopy

The UV-VIS-NIR spectroscopy or electron absorption spectroscopy measures the absorption energy of electrons in a molecule or atom, upon excitation to a higher energy orbital. The excited electrons are mostly valence electrons. The allowed electronic transition from one orbital to another is determined by different selection rules, such as Laporte's rule, which says that a transition is only possible when the symmetries of the transition orbitals are different. During excitation, the electrons can also vibrate as they absorb a wide range of energy. Thus, the absorption spectrum is in the form of band spectrum, and not discrete absorption energy peaks, owing to the broad range in exciting energies .[129]

A deuterium arc lamp (170-330 nm) light source as a radiation source is used for detection of the UV spectrum, while a tungsten-halogen lamp or recently a LED lamp is utilized for the visible spectrum. A monochromator is used to measure the absorption at one wavelength after the other in a manually pre-determined range. A diffraction grating or prism monochromator is used in the UV-VIS region or an optical grid for the UV-VIS-NIR region. The selection of the cuvette type is important for the accuracy of the measurements. A glass cuvette is only suitable for detecting $\lambda >$ 300 nm, whereas a quartz cuvette is suitable for down to 200 nm wavelength. As a detector, a photomultiplier, photodiode, or a charged-coupled device (CCD) is used.[129]

A UV-VIS spectrometer measures the percentage intensity of light that passes through a sample (I) relative to the incoming light intensity (I_0). This percentage is expressed in the form of the transmittance (T):

$$T = \frac{I}{I_0}.100\ \% \tag{2.31}$$

The extinction (sum of absorption and scattering experienced by a nanoparticle) is the negative logarithmic function of T, and it depends on the absorption coefficient, sample's concentration, and cuvette thickness. This relation is known as the Lambert-Beer law and can be used to determine a sample's concentration:

$$A = -\log T = \varepsilon \cdot c \cdot d \tag{2.32}$$

where A is absorption, ε is the extinction coefficient, c is the sample's concentration, and d is the thickness of the cuvette.

2.12 Inductively coupled plasma-optical emission spectroscopy (ICP-OES)

The real lanthanide doping concentrations of Er^{3+} and Yb^{3+} ions can be measured by ICP-OES, as this method can measure atomic concentrations down to the 1 ppm range.[133] This is important, as different dopant concentrations and ions can lead to different emission characteristics of particles. In an ICP-OES instrument, a sample that was nebulized into an aerosol is introduced to a plasma stream. Plasma is basically highly energized ionized gas. In ICP-OES argon gas is used as plasma source. Upon entering the plasma, there are three processes that the aerosol droplets undergo: the first is desolvation (removal of solvent from the droplet) that produces a dry aerosol in the form of particles. The particles are then vaporized and turn into gases. Finally, the gas sample is atomized due to the plasma's high temperature, and the free atoms are promoted into excited states. The energy is high enough to further turn the atoms into ions in the excited states. Each ion has characteristic energy lines upon emission to the ground state, due to discrete electronic transitions and energy states characteristic of each atom. The number of the emitted photons is directly proportional to the ion concentration. Hence, ICP-OES can be used to determine the type of atoms in a sample and the sample's concentration.[134]

An ICP-OES instrument consists of a nebulizer that turns the sample into an aerosol that is injected into the plasma chamber. There are two types of nebulizers commonly used: pneumatic nebulizers

that use high-speed gas flow to create aerosol; and ultrasonic nebulizers (USN) that use ultrasonic oscillation from a piezoelectric crystal to break down the sample.[134] Next a spray chamber is located between the nebulizer and the plasma torch. In this chamber, only fine aerosol (~8 µm diameter) can be injected into the plasma, whereas bigger droplets are sorted out.[134]

The torch to create the plasma consists of three fused silica tubes coiled with a copper coil connected with a radio frequency (RF) generator. An RF power (700-1500 W) is applied to the coil, and an alternating current oscillates inside the coil, with a frequency of the RF generator (27 or 40 MHz). The current induces an electromagnetic field on top of the torch. Argon gas is flown through the tubes, and a spark from a Tesla coil excites the electrons and produces ions inside the argon gas. These ions and electrons are accelerated by the previously created magnetic field and collide with other argon atoms, which increases the ionization rate until a high-temperature plasma (T = 7000-8000 K) is achieved.[134]

There are two torch viewing configurations: firstly, the radial view of the plasma, where the plasma operates vertically, and the optical analyzer is placed sideways to plasma; and secondly, the axial view where the plasma is turned horizontally and the optical view faces the end of the plasma (Figure 2.16).

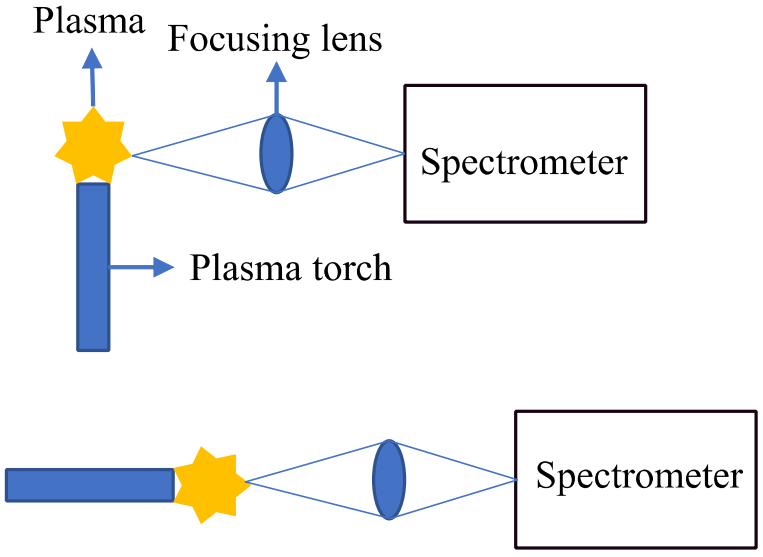

Figure 2.16: Top image: radial view of plasma. Lower image: axial view of plasma relative to the spectrometer. (Redrawn and adapted from reference [134])

In modern instruments, the emission light enters the echelle monochromator through a collection mirror and a slit. It is then diffracted by a collimating mirror, before reaching the echelle grating

and a prism, which selects the wavelengths and turn them into a two-dimensional spectrum.[135] A charged-coupled device (CCD) detector turns the wavelengths into electrical signals and amplifies the signals to be recorded on a computer.

2.13 Toxicity of upconversion nanoparticles

A lot of research has been done on exploring the potential applications of UCNP as biomedical imaging agents, biosensing or drug delivery agents. [40, 136] Whether the UCNP becomes useful in these applications is largely based on its intrinsic toxicity. It is therefore mandatory to carry out extensive toxicity tests to ensure the safety of UCNP bound for use in biological systems.

In a cytotoxicity test, a series of concentrations of UCNP are dispensed into a pre-calculated number of cells cultured in wells of a plate for a defined exposure time. Other experimental conditions such as temperature, pH, nutrients, and waste concentrations are tightly controlled since cell cultures are sensitive to changes in the environment.[137] Multiple cytotoxicity assays are also done simultaneously to reduce variability since nanoparticles can adsorb dyes and are often redox active. The most common cytotoxicity assays measure the changes of mitochondrial activity of cells after being exposed to NP. The MTT 3-(4,5-Dimethyl-2-thiazolyl)-2,5-diphenyltetrazolium bromide test is the most well-known method, where pale yellow MTT can be reduced to dark purple formazan by the mitochondrial dehydrogenase enzyme of active mitochondria in live cells (see Figure 2.17). Other cytotoxicity assays measuring the mitochondrial activity of cells are (4-[3-(4-iodophenyl)-2-(4-nitrophenyl)-2H-5-tetrazolio]-1,3-benzene disulfonate) (MTS), 2,3-Bis-(2-methoxy-4-nitro5-sulfophenyl)-2H-tetrazolium-5-carboxanilide salt (XTT) or Cell Counting Kit-8 (CCK-8), which uses WST-8 (2-(2-methoxy-4-nitrophenyl)-3-(4-nitrophenyl)-5-(2,4-disulfophenyl)-2H-tetrazolium, monosodium salt) as dye reagent. Another common method to measure cytotoxicity is by lactate dehydrogenase (LDH) monitoring, where LDH release from damaged cells oxidizes lactate to pyruvate, which further turns tetrazolium salt into formazan.[138]

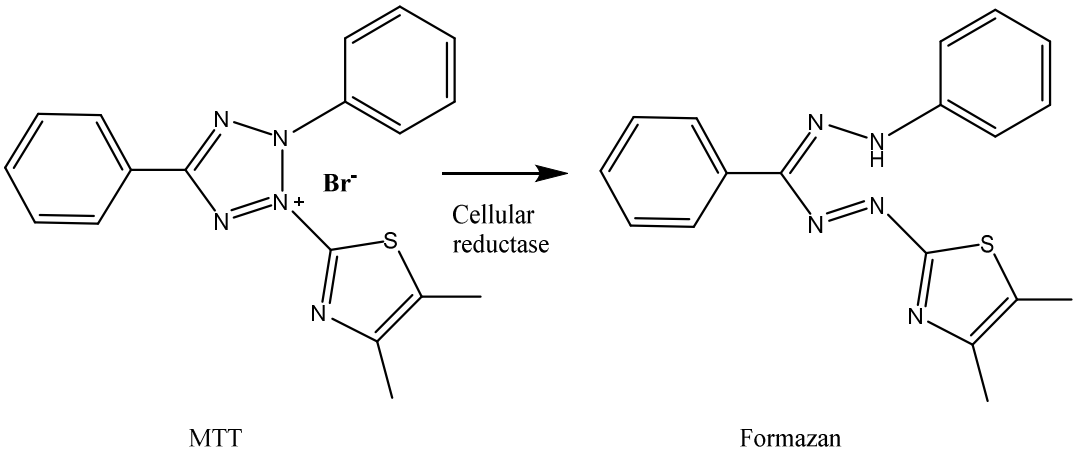

Figure 2.17: Reduction of MTT to formazan by mitochondrial dehydrogenase.[139]

Nanoparticles are commonly internalized through endocytosis. The uptake rate and way depend on the surface functionalization and size of the particles; the particles can be taken up via phagocytosis or more commonly through pinocytosis. In pinocytosis, there are four processes involved, the occurrences of which depend on particle size. Macropinocytosis involves the uptake of nanoparticles bigger than 1 μm; other processes are receptor-mediated endocytosis, such as clathrin-mediated endocytosis, which commonly internalizes NP less than 120 nm in diameter. Caveolae-mediated endocytosis, on the other hand, involves the uptake of NP up to 60 nm size.[140-141] The uptake of NP, however, depends strongly on surface charge and the varying response of each cell type.[122] Positively charged nanoparticles are usually taken up at a higher rate than neutral or negatively charged particles, due to increased interactions with the negatively charged cell membrane. After uptake, the particles are commonly stored in the endosomes and lysosomes and are not transferred to the cytosol.[140] Figure 2.18 shows the uptake mechanisms of molecules into cells.

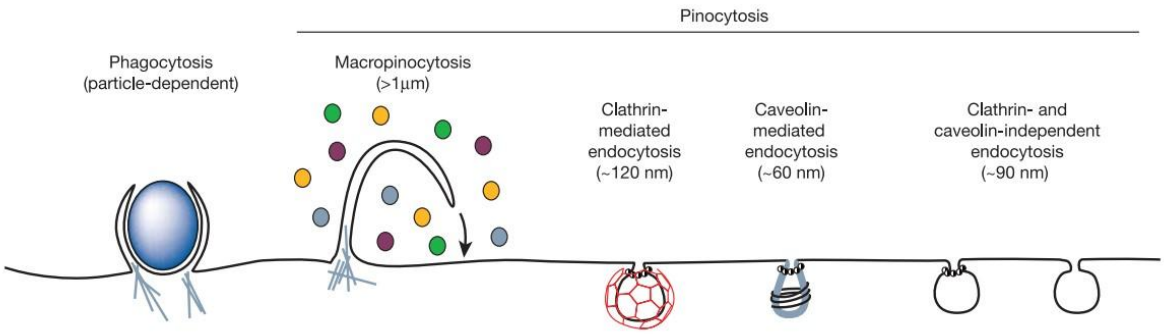

Figure 2.18:Uptake mechanisms of molecules into cells. (Reprinted with permission from Springer Nature License on behalf of Cancer Research UK: Springer Nature, Conner, S. D.; Schmid, S. L., Regulated portals of entry into the cell. Nature 2003, 422, 37.Copyright 2019)[140]

The cytotoxicity of nanoparticles depends on their concentrations and the length of time the cells are exposed to them. Up to now some publications investigating the cytotoxicity of UCNP *in vitro* have been published, and the reports showed that UCNP have relatively low toxicity and the cytotoxicity is concentration dependent.[41, 142-143] The degree of cytotoxicity can almost be pre-determined by the uptake rate of the UCNP into the cells; the uptake rate depends heavily on surface charge. Wong et al. investigated the uptake rate of $NaYF_4$: Yb, Er nanoparticles functionalized with polyethyleneimine (d = 50 nm; zeta potential (ZP) = 51.1 mV) into HeLa cells, human breast carcinoma MCF-7 cells (HTB-22, ATCC), and human glioblastoma U87MG cells and compared these to the uptake rate of polyvinylpyrrolidone (PVP) and polyacrylic acid functionalized $NaYF_4$ nanoparticles with ZP of 10.2 mV and -18.1 mV, respectively.[144] They found that positively functionalized UCNP had the highest uptake rate, whereas negatively functionalized UCNP had the lowest uptake rate. Additionally, the uptake is also concentration dependent, with more concentrated particles have higher uptake rates.

Zhang et al. investigated the cytotoxicity of silica coated $NaYF_4$ crystals on skeletal myoblasts and bone marrow-derived stem cells (BMSC) for particle having a concentration of 1-100 μg/mL and found the cell viability of both cell types after exposure to be 80±1 % and 90±1 %, indicating low toxicity.[39] Li et al. reported a higher half maximal inhibitory concentration (IC_{50}) value of $NaYF_4@Fe_xO_y$ in human nasopharyngeal epidermal carcinoma (KB) cells compared to iron oxide NP but a lower value compared to gold NP.[145-146] Since iron oxide and gold NP are considered as non-toxic to organisms, it can be concluded that UCNP have low cytotoxicity indeed. Kalas et al.

reported, however, that $NaGdF_4$ were cytotoxic to NIH3T3 fibroblasts and RAW 264.7 cells, but this cytotoxicity could be reduced by PEGylation or coating with silica shells.[147]

All these results showed that UCNP have a relatively low *in vitro* cytotoxicity. However, the results can vary under different experimental conditions, surface functionalization, and cell culture type.

2.14 Flow cytometry

Flow cytometry (FC) is an optical and fluorescence characterization method for measuring size, internal complexity, and granularity of single cells, particles or microorganisms.[148] In FC, particles or cells are brought in a sheath fluid stream to a laser interception point. Upon radiation with the laser the particles scatter light or fluoresce. The scattered lights or the fluorescence emission are then collected by optical lenses and passed through beam splitters and filters before reaching detectors.[148]

Ideally, the stream that is transporting the particles should be positioned in the center of the laser beam and additionally there should be only one particle measured at a time. The fluid is placed in a so-called flow chamber that is designed in such a way, that the sample flow is centered in the middle of the sheath fluid at the contact point with the laser. This is called hydrodynamic focusing, and the width of the sample flow can be adjusted by setting the flow sample pressure. A high sample pressure increases the width of the sample flow, allowing more particles being detected at a given time. This method is usually used for quantitative measurements such as immunophenotyping, a method used for identifying proteins expressed by cells. A low sample pressure decreases the width of the sample flow and is usually used to get higher resolutions. [148] Both schemes of high and low sample pressure in a flow cytometry device are depicted in Figure 2.19.

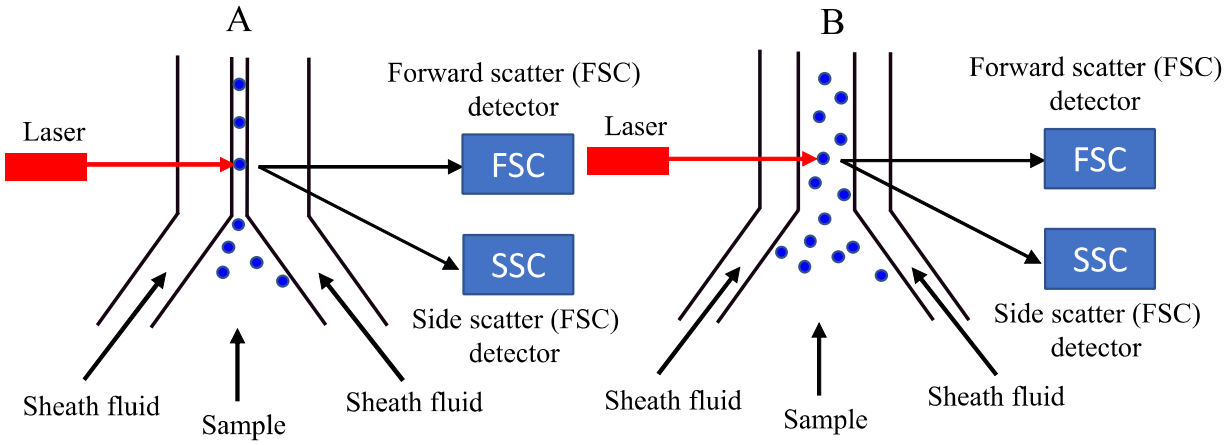

Figure 2.19: Scheme of a flow chamber in a flow cytometry instrument. A: FC measurements on high sample flow pressure and B: FC measurements on low sample flow pressure.(Redrawn and adapted from reference [148])

There are two methods of measuring scattered lights in FC: The forward-scattered light (FSC) method measures mostly the diffracted light and the detector is located on the same axis as the incident light in the forward direction. FSC measurement helps to define the cell surface and charge. In side-scatter light (SSC) mostly refracted and reflected lights are measured. This method can detect the change in the refractive index and yield information on the cell granularity or internal complexity. The SSC is collected at 90 ° to the laser beam and then redirected by a beam splitter to the detector.

In the optical system, there are excitation and collection lenses. The excitation optics consist of laser and lenses to center and focus the laser beam. SSC and fluorescence light are diverted to a photomultiplier (PMT) through collection lenses by a series of dichromatic mirrors before being brought to an SSC detector or fluorescence emission detectors, whereas FSC signals are collected by a photodiode. PMT and photodiode convert the light signals into electronic signals that can be analyzed by a computer.[148-149]

2.15 Confocal laser scanning microscopy

Contrary to a normal wide-field fluorescence microscope, where the whole sample is illuminated evenly at the same time, in a confocal laser scanning microscope (CLSM) the laser scans the sample, and the fluorescence light is emitted from the interaction between the incident beam and a very small illumination volume of the sample behind the objective lens.[150] This illumination volume is as small as the wavelength of light. The light emitted from a light source is converged by a lens on a confocal plane and passed through a source pinhole aperture. The passed light is

reflected by a beam splitter, focused by an objective lens and scans across the sample. The focal plane of the instrument can be moved gradually along the depth of the sample (scanning), and the optical fluorescence is then measured in small optical sections.[150] The fluorescence from the sample is collected by the objective lens, then passed through the beam splitter and a second pinhole before reaching the detector. The second pinhole placed before the detector only let excited lights from the focal point to pass. Thus, three-dimensional pictures with high resolution can be produced, due to the small and filtered illumination volume of the sample. Either the sample or the laser beam can be moved to provide a point-by-point scanning of the sample (Figure 2.20).

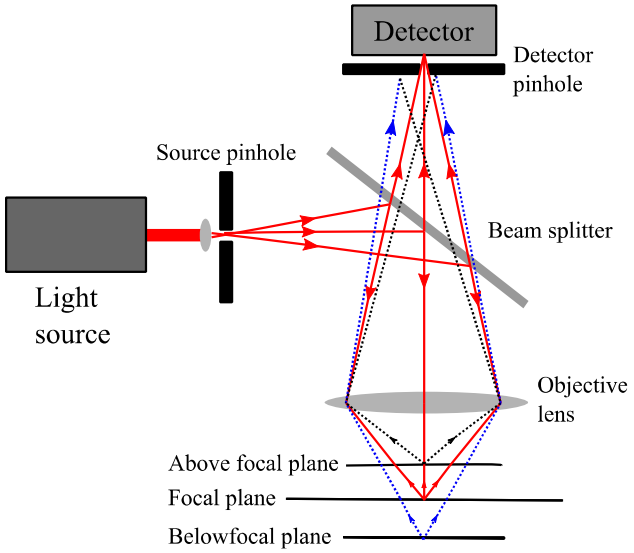

Figure 2.20: Scheme of a confocal microscope. The lights coming from a light source is focused by a lens, go through a source pinhole, are reflected by a beam splitter, subsequently focused by an objective lens and scan the sample. The reflected excited lights are focused by the objective lens, pass through the beam splitter and a second pinhole before reaching the detector. The blue and black lines represent out of focus lights or lights that do not come from the focal plane, which are sorted out by the detector pinhole . (Reprinted and adapted with license obtained from Elsevier) [151]

3 Experimentals

3.1 General synthesis methods

All syntheses were carried out in standard glass equipment previously cleaned with 8 % hydrofluoric acid. For all syntheses involving gold nanoparticles, the glass flasks were cleaned additionally with aqua regia.

All samples were centrifuged using a Rotina 380R or a Universal centrifuge from Hettich or a Compact Star CS4 from VWR.

Redispersion of samples was done using an ultrasonic bath Sonorex RK512H (215 W, 35 kHz) from Bandelin. Alternatively, a sonotrode UP200H (200 W, 24 kHz) from Hielscher was used.

Ultrapure water (Millipore; filter size = 0.22 μm, ρ = 18.2 MΩ cm) was used for all syntheses.

3.2 Characterization methods and instruments

3.2.1 Transmission electron microscopy (TEM)

The TEM images were taken using a Zeiss EM CR transmission electron microscope with an electron acceleration voltage of 80 kV. Alternatively, STEM images were recorded using a Hitachi SU 8030 scanning electron microscope in the STEM mode with an electron acceleration voltage of 30 kV and a current of 20 μA. For both approaches, a droplet of the particles (c = 0.5-1 g/L) dispersed in either cyclohexane for UCNP core or ethanol for silica coated UCNP, and water for gold-coated UCNP, was dried on a carbon-coated copper grid (Cu 400 mesh, Quantifoil®: 100 carbon support films). Image analysis was done using FIJI Image J (https://imagej.net/Fiji).

3.2.2 Scanning electron microscopy (SEM)

SEM images were taken using a Hitachi SU 8030 scanning electron microscope in the SE mode with a 30-kV voltage, and an amperage of 20 μA for surface investigations of gold clusters and gold coated particles and BSE mode for UCNP core and silica-coated UCNP investigations. The samples were prepared the same as for the TEM measurements.

3.2.3 Dynamic light scattering (DLS) and electrophoretic light scattering

The DLS measurements were carried with a Zetasizer Nano ZS from Malvern Instruments at 25 °C at a wavelength of 633 nm. The particles were dispersed in suitable solvents and filtered with a

sterile syringe (pore size: 0,2 µm; materials: nylon, polytetrafluorethylene (PTFE), regenerated cellulose, polymethylmethacrylate (PMMA); Rotilab).
Zeta potential measurements were carried out with a Zetasizer Nano ZS in capillary zeta cells DTS 1070 from Malvern Instruments.
Sample concentration was between 0.5-1 mg/mL.

3.2.4 UV-VIS-NIR-spectroscopy

UV-VIS-Spectra were recorded using a UV-VIS/NIR spectrometer from Perkin Elmer Lambda 950 UV-VIS/NIR spectrometer in a 1.5 mL PMMA half micro plastic cuvette from VWR or a quartz glass cuvette (QS Suprasil, 10 mm or 5 mm thickness) from Hellma or VWR.
The extinction spectra in chapter 4.2.3.2 were measured with a Cary 5000 spectrometer from Agilent.

3.2.5 Fluorescence spectroscopy

The fluorescence spectra were recorded with a FluoroMax-4 from Horiba Jobin Yvon in a quartz glass cuvette (QS Suprasil, 5 mm, Hellma or VWR). The excitation and emission slit width was 1 nm. For erbium doped samples the excitation wavelength was 378 nm (detection range = 400-700 nm), whereas for thulium-doped samples the excitation wavelength was 360 nm (detection range = 390-700 nm).
Sample concentration was 1-2 g/L for UCNP in cyclohexane, silica coated UCNP in ethanol and gold-coated UCNP in water .

3.2.6 Upconversion fluorescence spectroscopy

The upconversion measurements for the samples in chapter 4.1 were carried out using an Ulbricht-Labsphere in the group of Biophotonics of Dr. Ute Resch-Genger at Bundesanstalt für Materialforschung (BAM) by Martin Kaiser. The excitation wavelength was 980 nm with a laser excitation power density (P) of 800 W/cm^2. A CCD camera from Andor was used to detect the emission. Fluorescence lifetime measurements were done with an FLSP 920 Edinburgh Instrument spectrometer. The laser excitation power density at the excitation wavelength of 980 nm was 2 W/cm^2 and emission was detected at 90° to the excitation beam.

Additionally, the upconversion and the following lifetime measurements for samples in chapters 4.2 and 4.3 were done by Florian Frenzel in the same group as mentioned above with an FLS 980 Edinburgh Instruments spectrofluorimeter with an excitation wavelength of 980 nm.

For upconversion fluorescence measurements of samples in chapter 4.3, the same apparatus and cuvettes as for standard fluorescence spectroscopy (see 3.2.5) were used, and as an excitation source, an externally attached laser diode (P = 2 W/cm^2) from Insaneware-Robert Nowak was used. The excitation wavelength was 980 nm.

3.2.7 Confocal fluorescence microscopy for single particle measurement

The confocal setup for single particle measurement in chapter 4.2.4.2 is a self-made construction in the Biophotonic group at BAM (see the above sub-chapter) constructed by Florian Frenzel. The components are from Pico-Quant. The components and the set-up are similar to the commercially sold model of MicroTime 200 from Pico Quant. The single particle measurements were also done by Florian Frenzel. Below is a scheme of the confocal setup device:

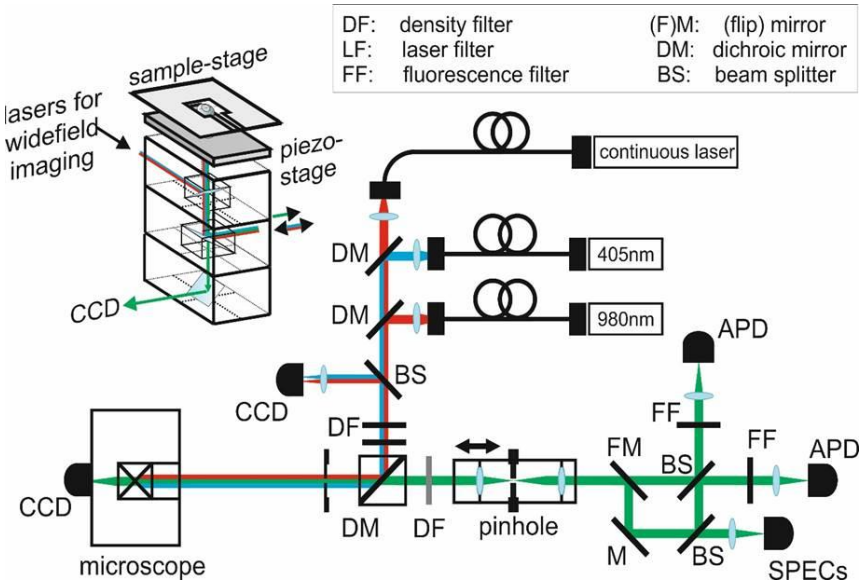

Figure 3.1: Confocal setup device scheme

3.2.8 Inductively coupled plasma-optical emission spectroscopy (ICP-OES)

For the determination of the elemental composition of the UCNP samples, 1 mL of dispersions (concentration = 5 g/L UCNP core in cyclohexane or same concentration for silica coated UCNP in ethanol for) was dried and dissolved in aqua regia and diluted to a minimum of 5 mL with

ultrapure water. The measurements were carried out using an iCAP 6000 Series ICP Spectrometer from Thermo Scientific with a radial optical approach.

A series of solutions with different concentration for calibrations was prepared separately from $YCl_3.6H_2O$ or Yttrium standard for ICP (c Y^{3+}-ion = 10, 20 and 40 ppm), $YbCl_3.6H_2O$ or Ytterbium standard for ICP (c Yb^{3+}-ion= 10, 20, 40 ppm) and $ErCl_3.6H_2O$ or Erbium standard for ICP (c Er^{3+}-ion = 1, 5, 10 ppm). The rare earth metal chlorides were treated with aqua regia and diluted to the intended concentration with ultrapure water.

3.2.9 X-ray diffraction spectrometry (XRD)

For XRD measurements, a minimum of 10 mg dried samples were used. The XRD device was a STOE Stadi P from STOE. As a Cu Kα1 radiation source, a Cu anode was used with a radiation wavelength of 1.5405 Å. The measurement angle was between 10-90° and with a measurement time of 120 s/0.2°. The reflexes of the UCNP core crystals are compared to the reflexes in a database provided by The International Centre for Diffraction Data (ICDD).

3.2.10 Cell culture of HaCaT cells and RAW 264.7 cells for cytotoxicity assay

Non-tumorigenic immortalized human keratinocyte cells (HaCaT) were bought from Cell Line Services, and the RAW 264.7 cells were provided by the group of Dr. Philipp Seib at the University of Strathclyde, Glasgow, UK.

The cells were grown in Dulbecco's modified Eagle medium (DMEM) supplemented with 10 % fetal bovine serum (FBS), 2 mM L-glutamine, 100 U/mL penicillin, 100 µg/mL streptomycin, and 250 µg/mL fungizone at 37 °C in 5 % CO_2 humidified atmosphere.[152] The cell medium, FBS, the antibiotics, and phosphate buffer saline (PBS) were purchased from Life Technologies.

The T-75 and T-25 flasks used to grow the cells and the 12- and 96-well plates were from Corning®.

Cell scrapers used to scrape off the RAW 264.7 cells attached to the surface of T-culture flasks were from PLC Labclinics.

For cell confluency and viability observations, an Eclipse TS100 microscope in inverted phase contrast-mode was used. An orbital Mini Shaker from Kisker Biotec was used for the preparation of samples for MTT measurements.

3.2.11 3-(4,5-Dimethyl-2thiazolyl)-2,5-diphenyltetrazolium bromide (MTT) assay

The optical density of reduced MTT in cell cytotoxicity experiments was measured at 570 nm in a microtiter plate reader (Synergy HT from BioTeK Instruments Inc.). The MTT assay steps are further described in chapter 3.8.4.

3.2.12 Flow cytometry

Exposed HaCaT cells and RAW 264.7 cell granularity were characterized using an Attune NxT acoustic focusing cytometer (Thermo Fischer Sci.). The steps and preparations for flow cytometry measurements are further described in chapter 3.8.6.

3.2.13 Confocal laser scanning microscopy

The exposed HaCaT cells were visually characterized with the confocal laser scanning microscope (CLSM) FluoView FV 1000.

3.3 Chemicals

The following table lists the chemicals used in this project.

Table 3-1: Chemicals

Chemicals	**Chemical formula**	**Supplier**	**Purity (%)**
Acetone	C_3H_6O	Stockmeyer	99.5
Ammonia water	NH_3	Roth	25[1]
Ammonium fluoride	NH_4F	Sigma Aldrich	99.8
Ascorbic acid (AA)	$C_6H_8O_6$	Sigma Aldrich	99
Chloroauric acid trihydrate	$HAuCl_4.3H_2O$	Acros	49[1]
Cyclohexane	C_6H_{12}	Roth	99.5
Dichormethane (DCM)	CH_2Cl_2	VWR	99
Dimethylformamide (DCM)	C_3H_7NO	Acros	99.9
Erbium chloride hexahydrate	$ErCl_3.6H_2O$	ABCR	99.9
Erbium standard for ICP	Er	Sigma Aldrich	1000 mg/L in nitric acid
Ethanol (EtOH)	C_2H_6O	Berkel AHK	100
Hydrochloric acid	HCl	Roth	37
Hydrofluoric acid	HF	Riedel de Haën	30
Hydroxylamine hydrochloride	$(NH_3OH)Cl$	Sigma Aldrich	99.999

[1] Concentration

Hexadecyltrimethylammonium bromide (CTAB)	$C_{19}H_{42}BrN$	Sigma Aldrich	99
n-Hexane	C_6H_{14}	VWR	95
N- (6- Aminohexyl)aminopropyl trimethoxysilane (AHAPS)	$C_8H_{22}N_3O_3Si$	Sigma Aldrich	97
Nitric acid	HNO_3	Grüssing	65
Nitrosyltetrafluoroborate	$NOBF_4$	Sigma Aldrich	95
1-Octadecene	$C_{18}H_{36}$	Sigma Aldrich	95
Oleic acid (OA)	$C_{18}H_{34}O_2$	ABCR	90
Polyacrylic acid (1,8 kDa; PAA)	$(C_3H_4O_2)_n$	Sigma Aldrich	99
Polyethylene imine (25 kDa; PEI)	$(C_2H_5)_n$	Sigma Aldrich	99
Potassium carbonate	K_2CO_3	Riedel de Haën	99
Rhodamine B-isothiocyanate (RBITC)	$C_{29}H_{30}ClN_3O_3S$	Sigma Aldrich	≥95
Sodiumborhydride	$NaBH_4$	Sigma Aldrich	96
Sodium hydroxide	NaOH	Grüssing	99
Sodium oleate (Na-oleate)	$NaO_2C_{18}H_{33}$	Sigma Aldrich	82
Ytterbium chloride hexahydrate	$YbCl_3.6H_2O$	ABCR	99.9
Ytterbium standard for ICP	Yb	Sigma Aldrich	1000 mg/L in nitric acid
Ytterbium chloride hexahydrate	$YbCl_3.6H_2O$	ABCR	99.9
Yttrium chloride hexahydrate	$YCl_3.6H_2O$	ABCR	99.9
Yttrium standard for ICP	Y	ABCR	1000 mg/L in nitric acid

3.4 Synthesis of nanoparticle precursors

3.4.1 Synthesis of rare earth metal trifluoracetates

Rare earth metal trifluoracetates were synthesized either from their chloride compounds or corresponding rare earth oxides.[76, 153] Sodium trifluoracetate was synthesized from sodium carbonate. Rare earth metal chloride hexahydrates were mixed in a predetermined molar ratio (Y: Yb:Er/Tm = 80:18: 2/1) and dissolved in 5 mL ultrapure water before precipitation with ammonia. The product was centrifuged (3354 g, 7 min) and washed three times with water. After product separation by extraction using a separating funnel, Na_2CO_3 (1 mmol) and trifluoroacetic acid (TFA) (0.7 mL; 9 mmol) were added, and the product was dried in vacuum ($p = [3\pm1] \times 10^{-3}$ mbar) and could be used without further cleaning.

Typical IR bands for products are: 1679, 1466, 1206, 1143, 1020, 914, 856, 794, 723 cm^{-1}.

Alternatively, rare earth metal oxides in a predetermined ratio (Y:Yb:Er/Tm = 80:18:2/1) were mixed with TFA (50 %, 8 mL) and heated under reflux until a clear solution developed. Finally, water and non-reacted TFA were removed under vacuum (p = [5±1] × 10^{-3} mbar). Separately, Na_2CO_3 (10 mmol) was mixed with TFA (50 %, 80 mL) to synthesize sodium trifluoracetate. In the end, water and TFA residues were removed under reduced pressure (p = [5±1] × 10^{-3} mbar), and the product was dried in vacuum with the same pressure.

Typical IR bands for the different products are:

$Na(CF_3COO)$: 2362, 2331, 1717, 1673, 1445, 1204, 1143, 845, 796, 717 cm^{-1}.

$Y(CF_3COO)_3$: 3730-3600, 2366, 2336, 1743, 1660, 1480, 1203, 1151, 850, 796, 717 cm^{-1}.

$Yb(CF_3COO)_3$: 3694, 3611, 2363, 2337, 1762, 1651, 1592, 1490, 1207, 1143, 851, 800, 715 cm^{-1}.

$Er(CF_3COO)_3$: 3668, 3638, 2361, 2338, 1717, 1668, 1617, 1479, 1203, 1143, 851, 796, 719 cm^{-1}.

3.4.2 Synthesis of rare earth metal oleates

The synthesis was done as described before for the preparation of precursors for the synthesis of iron oxide nanoparticles,[82, 154] with slight modifications. As an example, the synthesis of 1 mmol of $NaYF_4$ nanoparticles doped with 18 % Yb and 2 % Er is described: A mixture of yttrium- (0.242 g; 0.78 mmol), ytterbium- (0.069 g; 0.18 mmol), and erbium chloride (0.02 mmol; 0.006 g) hexahydrate was dissolved in 3 mL ultrapure water, 7 mL ethanol (EtOH) and 7 mL hexane. Sodium oleate (1.22 g; 4 mmol) was dissolved in 2 mL ultrapure water and 3 mL ethanol in a 50 mL one-necked flask, then the solution of the mixed chlorides was added to this. Hexane (7 mL) was finally added, and the solution was heated under reflux and kept at 70 °C for 4 h. The solution was cooled down to room temperature and extracted three times with ultrapure water. Subsequently, the organic phase was separated, and the waxy white product was dried under vacuum (p = [5±1] × 10^{-3} mbar) in a 100 mL three-necked flask at room temperature before being used in a high-temperature synthesis (see chapter 3.5).

3.5 Synthesis of upconversion nanoparticles

3.5.1 Synthesis from rare earth chlorides

The synthesis is based on the work of Zhang et al.[155] Lanthanide chloride hexahydrates were mixed with the intended lanthanide ratio (Y:Yb:Tm:Gd = 65:18:2:15), so that the amount of rare earth ions was 1 mmol in total. The mixture was poured into a three-necked 100 mL glass flask dissolved in 1-octadecene (15 mL) and oleic acid (6 mL) and stirred. The solution was heated to 80 °C and

evacuated. Under vacuum, this solution was further heated to 160 °C and stirred for 30 min. After cooling to 50 °C under argon, NaOH (2.5 mmol) and NH_4F (4 mmol) in 10 mL methanol was added, and the solution was stirred for 30 min at this temperature. After removal of methanol, the solution was heated to 300 °C (T = 12 K/min) and stirred for 1.5 h. After, the mixture was cooled down to room temperature, the product was precipitated with ethanol, centrifuged (1207 g, 15 min) and washed through redispersion in 10 mL cyclohexane and precipitated with 5 mL ethanol for three times. The particles were stored in cyclohexane or hexane (sample: UC_Gd_1).
Table 3-2 shows variations of UCNP synthesis from lanthanide chlorides.

Table 3-2: Variations of the synthesis from lanthanide chlorides

Samples	Yb (%)	Gd (%)	Tm (%)		Er (%)	Solvents	Reaction conditions
UC_Gd_2	18	15	2		-	1-Octadecene	T= 300°C, 2 h
UC_Gd_3	18	4	2		-	1-Octadecene	similar to UC_Gd_1
UC_1	18	15	-		2	Trioctylamine	similar to UC_Gd_1

3.5.2 Synthesis from rare earth trifluoracetate precursors

A mixture of rare earth trifluoracetates from 1 mmol rare earth oxides was dissolved in 6 mL oleic acid and 15 mL 1-octadecene along with 2 mmol sodium trifluoracetate in a three-necked flask with an argon flow joint and temperature controller. The mixture was stirred at room temperature and heated to 100 °C under vacuum. After evacuating all air and vapor at this temperature, the mixture was stirred under an argon atmosphere and heated further to 300 °C (ΔT = 12 K/min) and stirred for 1.5 h. After that the mixture was cooled down, the nanoparticles were precipitated with ethanol and cleaned three times by centrifugation (1207 g, 20 min) with repeated redispersion with 10 mL cyclohexane or hexane and precipitated with 5 mL ethanol. Table 3-3 shows variations of synthesis parameters.

Table 3-3: Variation of the UCNP synthesis from lanthanide trifluoracetates

Sample	Yb (%)	Gd (%)	Er (%)	Na:RE-TFA ratio*	Reaction condition
UC_Gd_4	18	15	2	1:1	T = 300 °C, 1 h
UC_Gd_5	18	4	2	1:1	T = 300 °C, 1.5 h

** RE-TFA = rare earth trifluoracetates

3.5.3 Synthesis from rare earth oleate precursors

The following method describes a typical synthesis of 1 mmol UCNP from rare earth oleates.[156] The rare earth oleates (see chapter 3.4.2) were dissolved in a mixture of 1-octadecene and oleic acid (15:7 v/v) in a three-necked flask with an argon flow joint and a temperature controller, heated under vacuum (pressure = 1×10^{-3} bar) until the reaction mixture reached 100 °C and kept at 100°C for 1 h to evaporate all water and hexane. The mixture was cooled down to 50 °C under argon flow. NaOH (100 mg; 2.5 mmol) and NH_4F (148 mg; 4 mmol) were dissolved in 5 mL MeOH and added drop wise to the oleates with a syringe while stirring. The mixture was further stirred for 30 min at 50 °C, and MeOH was evacuated (p = [5±1] × 10^{-3} mbar). After alternately vacuum degassing and flushing with argon for 3 times to ensure that all MeOH has evaporated, the reaction was heated to 300 °C and stirred at this temperature under argon for 1.5 h. After the reaction was cooled down, 15-20 mL EtOH was added until the particles precipitated. The white powder was washed three times with 5-10 mL EtOH and redispersed in 10 mL cyclohexane.

3.5.4 Synthesis of undoped $NaYF_4$ shell

Coating of the UCNP core with undoped $NaYF_4$ was done by redispersion of yttrium oleate precursor in a 1-octadecene/oleic acid mixture followed by the addition of UCNP under high temperature described in chapter 3.5.3. As an example, yttrium oleate (0.2 mmol) was dissolved in 1.2 mL oleic acid and 3 mL 1-octadecene in a three-necked flask with an argon flow joint and temperature controller. The mixture was heated to 150 °C under vacuum and stirred for 30 min. Afterward, the solution was cooled to 80 °C and flushed with argon. The UCNP cores dispersed in cyclohexane (c=20 g/L; 0.2; 0.4; or 0.6 mmol) were injected into the flask. The solvent (cyclohexane or hexane) was removed at 50 °C under reduced pressure (p = [5±1] × 10^{-3} mbar). Afterward, NH_4F (0.8 mmol) and NaOH (0.5 mmol) in 2 mL methanol were added, and the whole reaction was stirred for 30 min. The flask was heated to 80 °C to remove methanol, and after washing with argon a few times, the mixture was heated to 300 °C (T = 12 K/min) and stirred for 1.5 h. The white product was precipitated with ethanol, centrifuged for 3 times (1207 g, 15 min), redispersed in 10 mL cyclohexane, precipitated again with 5 mL ethanol, and finally dispersed in cyclohexane or hexane after washing in an ultrasonicator.

3.6 Synthesis of silica-coated upconversion nanoparticles by the layer-by-layer method

3.6.1 Silica-coating with microemulsion

The synthesis of the silica coating is based on a modified microemulsion method.[84, 157] In the following, a typical microemulsion synthesis for the silica coating of UCNP is described. For the first silica shell, the amount of tetraethylorthosilicate (TEOS) was calculated so that a shell thickness of 5 nm could grow if the full conversion of the available TEOS is assumed (see TEOS calculation in Attachment A.)

As an example, for the first silica shell growth with a calculated thickness of 5 nm, a dispersion of UCNP (UC_Er_4, d_{TEM} = 24±1 nm, c = 25 g/L in cyclohexane) was diluted to 3 g/L by adding 11 mL cyclohexane. Afterward, 0.154 mL Igepal CO-520 co-surfactant was added. After sonication for 10 min, 1.213 mL Igepal CO-520 was added, and after brief mixing, 0.159 mL 30% NH_3 was added, and the dispersion was sonicated for 20 min. Finally, 0.159 mL TEOS were added, and the whole mixture was sonicated in an RK512H (215 W, 35 kHz) sonicator from Bandelin Sonorex for at least 1 h. Generally, a volume concentration of 12 weight percent (wt%) was used for Igepal CO-520, and a maximal water concentration of 2-3 wt% was maintained in the dispersion. After that, the suspension was stirred overnight at 1200 rpm at room temperature. The particles were precipitated with 5-10 mL EtOH and washed three times with 10 mL ethanol through centrifugation (1207 g, 1 h) and finally redispersed in 10-15 mL EtOH.

For the further stepwise growth of silica shells with this microemulsion approach, additional cyclohexane, Igepal CO-520, and ammonia were added to the dispersion to maintain a surfactant concentration of 11 wt% and a water concentration of a maximum of 2-3 wt%. The initial particle concentration was set to 20-25 g/L. It was important that the microemulsion was not broken during the entire synthesis process; i.e., the last layer of silica was grown before the particles were precipitated with ethanol.

Table 3-4 shows an example of typical solvent and reactant amounts for multi-step silica shell synthesis with the microemulsion method. The UCNP cores (UC_Er_4; d_{TEM} UCNP = 24±1 nm, c = 25 g/L, m = 32.5 mg) were already coated with a silica shell with a calculated thickness of 5 nm as described in the previous paragraph. The total concentration of Igepal CO-520 was 12 wt%. TEOS was added dropwise through a peristaltic pump with a speed of 20.8 µL/min. Finally, the particles were precipitated with 5-10 mL ethanol and washed several times by centrifugation (1207 g, 15 min). The particles were dispersed in ethanol before further silica growth.

Table 3-4: Amount of reactants for a stepwise silica coating of UCNP core by the microemulsion method. Values are given for the sample UC_Er_4 core (m = 32 mg, d_{STEM} = 24±1 nm, c = 25 g/L)

Layer	Thickness of the existing SiO_2 shell (calculated) [nm]	Calculated growth of the SiO_2 shell [nm]	Total thickness of the SiO_2 shell [nm]	Volume of initial dispersion [mL]	Added volumes			
					Cyclohexane [mL]	Igepal [mL]	Ammonia water [mL]	TEOS [mL]
1	0	7	7	0.781	11.00	1.364	0.159	0.159
2	7	11	18	13.463	16.85	1.850	0.674	0.674
3	18	14	32	33.511	66.05	7.29	1.887	1.887
4	32	11	43	97.162	93.10	10.272	2.660	2.660

Table 3-5 shows the surfactant concentration (c Igepal), ammonia concentration (c NH_3) and NH_3-to Igepal weight ratio in each synthesis for each given sample:

Table 3-5: Surfactant concentration (c Igepal), ammonia concentration (c NH_3) and NH_3-to Igepal weight ratio for each synthesis

Sample	Shell	c (Igepal) [wt% in cyclohexane]	c (ammonia water) [wt% in cyclohexane]	Ammonia water-to Igepal weight ratio
UC_Er_4@SiO_2_38	1st	15.90	1.67	1:9.5
UC_Er_4@SiO_2_60	2nd	14.79	3.45	1:4.3
UC_Er_4@SiO_2_94	3rd	14.32	3.34	1:4.3
UC_Er_4@SiO_2_112	4th	14.22	3.31	1:4.3

3.6.2 Silica coating by the Stöber method

The growth of silica shells on UCNP via the Stöber method[83] was done after a multistep growth of silica shells (r SiO_2 = ~ 40-50 nm) using the microemulsion approach if the zeta potential reached a value above -30 mV. Ammonia and ethanol were added to an ethanolic dispersion of silica-coated UCNP (c = 1-10 g/L) (see Table 3-4). Subsequently, TEOS is added dropwise (v = 20.8 µL/min) to this mixture (see Table 3-4) while stirring. After the addition was completed, the particles were washed three times by centrifugation (3354 g, 1 h), washed with 10-20 mL EtOH and finally redispersed in 10 mL EtOH.

Table 3-6: Amount of reactants for the silica shell growth via the Stöber method

Batch	Diameter SiO_2-coated UCNP (nm)	Mass of SiO_2-coated UCNP (mg)	Dispersion concentration (g/L)	Calculated thickness of the additional SiO_2 shell (nm)	Added volume		
					EtOH (mL)	Ammonia (mL)	TEOS (mL)
1	93±4	100	19	14	5.00	1.0	0.423
2	93±4	100	19	14	10.00	1.5	0.423
3	93±4	100	19	14	20.00	2.5	0.423
4	112±4	16	16	15	15.25	2.0	1.100
5	112±4	16	16	15	15.25	3.0	1.100 in 2 mL EtOH

3.6.3 Synthesis of dye-coupled silica coated upconversion nanoparticles

The synthesis is based on the method of van Blaaderen et al.[158]

For the growth of a silica shell with covalently bound RBITC, the dye was first coupled with 3-aminopropyltrimethoxysilane (APS). For this, 2.7 mg (5×10^{-3} mmol) RBITC was diluted to 1 mM in EtOH and 10 µL (5×10^{-2} mmol) APS was added and the solution was stirred overnight at room temperature. The dye coupling product was called RBITC-APS.

To grow a silica shell on UCNP coupled with different dye concentrations, the previously made coupling product was given to the microemulsion dispersion after the first silica coating was grown onto the UCNP through a reverse microemulsion method (core: UC_Er_4; see chapter 3.6.1). In this case, the ammonia was added as the last reagent after the addition of RBITC-APS and TEOS. Typical amounts and conditions are given in Table 3-7 (sample: UC_Er_4; d_{TEM} = 24±1 nm, c = 25 g/L, m = 32.5 mg).

Table 3-7: Amount of reactants for the synthesis of RBITC-coupled-silica coated UCNP

Sample name	**Calculated thickness of the dye-doped SiO_2 shell (nm)**	**Vol. of added)**	**Added volume**			
		Cyclohexane (mL	**Igepal (mL)**	**Ammonia (mL)**	**RBITC-APS (c = 1 mM in EtOH) (µL)**	**TEOS (mL)**
UC_Er_4@RBITC_1	5	11	1.367	0.159	52	0.159
UC_Er_4@RBITC_2	5	11	1.367	0.159	78	0.159
UC_Er_4@RBITC_3	5	11	1.367	0.159	104	0.159
UC_Er_4@RBITC_4	5	11	1.367	0.159	130	0.159
UC_Er_4@RBITC_5	5	11	1.367	0.159	157	0.159

To determine the real amount of dye embedded in the silica shell, 1 mL of the dispersion particle was treated with an equal volume of 0.43 M NaOH (EtOH:NaOH = 1:1 v/v), and the released dye was measured by UV-VIS-absorption. The concentration of silica coated nanoparticles was 4.5±0.5 mg/mL.

For the determination of dye concentration, a calibration curve, where the absorption of RBITC at 547 nm was plotted against the concentration, was obtained from a series of concentrations of RBITC in an EtOH/NaOH (1:1 v/v) mixture. The gradient of the curve was calculated and this gave the extinction coefficient value (ε), which can be used to determine the amount of dye (see Attachment E). The calibration curve of RBITC absorption at 547 nm as well as the absorption spectra of RBITC in various concentrations for the calibration calculations are shown in Attachment E. The RBITC concentrations were 0.001, 0.002, 0.004, 0.008 and 0.01 mM in an ethanol/0.43 M NaOH-mixture (1:1 in volume).

The amount of theoretically calculated RBITC/L SiO_2 is shown in Table 3-8.

Table 3-8: TEOS, RBITC-APS amount and theoretically calculated amount of RBITC/particles given for RBITC-doped silica coated UC_Er_4

Sample	**TEOS**	**RBITC-APS 1 mM**	**Calculated amount of RBITC/L SiO_2**
	mmol	**10^{-4} mmol**	**mmol/L SiO_2**
UC_Er_4@ RBITC_1	0.71±0.08	[0.52±0.05]	2.44±0.10
UC_Er_4@ RBITC_2	0.71±0.08	[0.78±0.08]	3.66±0.20
UC_Er_4@ RBITC_3	0.71±0.08	[1.05±0.11]	4.93±0.30
UC_Er_4@ RBITC_4	0.71±0.08	[1.31±0.13]	6.15±0.30
UC_Er_4@ RBITC_5	0.71±0.08	[1.57±0.16]	7.37±0.40
UC_Er_4@ Ref	0.71±0.08	-	-

3.7 Synthesis of gold nanoshells on silica coated UCNP

For all reactions involving gold, the flasks and stirring bars were first washed with aqua regia and 8 % HF, and the reactions were conducted in an argon atmosphere without exposure to light.

3.7.1 Synthesis of gold clusters

The first step for the formation of a closed gold shell synthesis was the growth of small gold nanoclusters as seeds. The synthesis was done before the gold nanocoating processes as described by Graf et al.[159]

An attachment process for gold nanoclusters onto silica-coated UCNP is described below. As examples, two samples of silica-coated UCNP with different sizes and silica shell thickness were used. The first sample was UCNP coated with a thick silica shell (sample: UC_Er_4@SiO_2_321; d UCNP = 24±2 nm, d_{total} = 321±16 nm, SiO_2 thickness = 149±8 nm). The second sample was UCNP with a thinner silica shell (sample: UC_Er_4@SiO_2_120; d UCNP = 24±2 nm, d_{total} = 120

±4 nm), for which a two-step process of gold nanocluster deposition was used to provide a more dense surface covering of gold nanoclusters according to the method of Zhang et al.[160]

For the synthesis of gold nanoclusters and gold nanoshells, a gold stock solution of $HAuCl_4.3H_2O$ ((c = 24.9 mM) in ultrapure water) was prepared. For the synthesis of the gold clusters, a mixture of 136.5 ml ultrapure water, 4.5 ml of a 0.2 M NaOH-solution, 3 mL tetrakis(hydroxymethyl)phosphonium chloride (THPC) (1.2 ml aqueous solution of 80% THPC diluted with 98.8 mL ultrapure water) and 6 mL of an aqueous solution of chloroauric acid trihydrate (c = 24.9 mM) was prepared. The NaOH solution was added first to the water, followed by the THPC solution. The chloroauric acid solution was added after 2-3 minutes, after all NaOH and THPC had been well dissolved, under vigorous stirring (1200 rpm). The solution turned dark brown immediately. The solution was stirred for another 5 min and could be used immediately.

The silica-coated upconversion nanoparticles were functionalized with aminopropyltriethoxysilane (APS) to create a positive surface charge, to couple the negatively charged gold nanoclusters. For this purpose, 1 mL (c = 32 g/L in ethanol) of UC_Er_4@SiO_2_321 was diluted with ethanol to c = 10 g/L. 1 mL APS and 134 µL ammonia water (30% v/v) was added and the mixture was stirred overnight, followed by heating under reflux for 1 h.

To attach the gold clusters, 1 mL of a dispersion of APS-functionalized UC_Er_4@SiO_2_321 (c = 32 g/L) in ethanol was diluted with 18.5 mL EtOH and 70.5 mL ultrapure water in a 250 mL round-bottomed glass flask and stirred vigorously (v = 1200 rpm) for at least 12 h. 23.5 mL chloroauric acid were added to this dispersion under stirring (v = 1200 rpm). The solution was further stirred overnight. Three further centrifugation (a = 34 g) steps and three washing steps with water were required to remove any non-attached gold clusters.

For the attachment of gold clusters onto the second sample (UC_Er_4@SiO_2_120), 50 mg of these particles were functionalized with APS (see chapter 3.7.1) and subsequently used for the first gold cluster deposition (the same method as for UC_Er_4@SiO_2_321; the amount of reactants was calculated according to the particles' total surface area in the sample and compared to the total surface area of the UC_Er_4@SiO_2_321). For the first gold cluster attachment procedure, 208.25 mL chloroauric acid solution was mixed with the second sample for 30 min and left overnight at 4 °C in the dark.

For the second gold cluster solution, a reaction mixture consisting of 277 mL ultrapure water, 9.13 mL of 0.2 M NaOH solution, and 6.08 mL of an 80 % aqueous solution of THPC, and 12.17 mL 1

wt% aqueous solution of $HAuCl_4.3H_2O$ was used. The mixture was stirred for 5 min, and the dispersion turned to dark brown. It was then left at 4 °C for at least 12 h in the dark.

For the second gold deposition, the gold clusters functionalized UC_Er_4@SiO_2_120 had to be once again functionalized with APS. For this purpose, 110 mL ultrapure water, 1.332 mL APS, and 1.106 mL 37 % HCl were mixed and stirred for 1 h under argon at RT. Afterward, 20 mg of the particles with the attached gold clusters were added to the sol-gel APS mixture and stirred for 20 min. Afterward, the particles were washed once in water by centrifugation (34 g, 12 h).

For the second deposition of gold clusters, 10 mg of the sol-gel APS functionalized sample 2 was mixed and stirred (RT, 1200 rpm, 30 min) with 16.66 mL of the gold cluster solution. The mixture was kept overnight in the dark at 4 °C, and subsequently washed three times by centrifugation (34 g, 12 h). The particles were stored in the dark at 4 °C until further use.

3.7.2 Synthesis of closed gold nanoshell

For the synthesis of gold nanoshells on gold cluster-functionalized, silica-coated UCNP, a gold growth solution (AUW) was prepared at least 3 days prior to the coating process. A typical gold growth solution was prepared from 2,955 mL ultrapure water, 45 mL chloroauric acid solution (c = 24.9 mM), and 747 mg K_2CO_3. The mixture was stirred for 5 min (1200 rpm) and kept in the dark at RT for at least 3 days.

In a typical synthesis process, a gold shell with a thickness of 30 nm was grown onto 11±1 mg of gold cluster-functionalized UC_Er_4@SiO_2_321 (referred to as sample UC_321@Au) by stepwise mixing and adding certain amounts of AUW and an aqueous solution of hydroxylamine hydrochloride ($NH_2OH.HCl$; c = 0.8705 mM).[159] First, UC_321@Au was added under stirring (1200 rpm) to a certain amount of AUW (see Table 3-9) before the first amount of $NH_2OH.HCl$-solution was added. The colour turned from transparent to muddy reddish brown, indicating the growth of the gold shell. After the first reaction was terminated, this procedure was repeated twice.

Table 3-9: Amount of AUW solution and aqueous NH_4Cl solution for a stepwise gold nanoshell growth

Thickness of gold shell (nm)	AUW (mL)	NH_4Cl (mL)
10	270	81
20	310	93
30	340	102

After the gold coating process was completed, the dispersion was stored in the dark until the particles sedimented at the bottom of the flask. The supernatant was carefully removed using a 10-mL piston-operated pipette or a 50-mL syringe. The particles were cleaned three times with ultrapure water without centrifugation since the particles precipitated easily.

3.8 Cytotoxicity assay of upconversion nanoparticles

3.8.1 Incubation and cell passaging of biological cells

All cell passages and cultures were done under sterile bench conditions at room temperature. The cells were cultured and grown at 37 ºC in 5 % CO_2 humidified atmosphere (see chapter 3.2.10).

3.8.2 Cell culture and cell passaging of HaCaT cells

HaCaT cells were grown in a Dulbecco's modified Eagle's medium (DMEM, high glucose) supplemented with 10 % fetal bovine serum (FBS), 2 mM L-glutamine, 100 U/mL penicillin, 100 µg/mL streptomycin, and 250 µg/mL fungizone. The cells were used at 70-80 % confluency (after ca. 48 h).

A typical procedure for passaging HaCaT cells grown in a 75 cm^2 (T-75) flask is described below. Supplemented DMEM was removed following washing for 1 min with 5 mL phosphate buffer saline (PBS). After PBS was removed, 5 mL 0.05 % ethylenediaminetetraacetic acid (EDTA) in PBS were added, and the cells were incubated for 10 min at 37 °C in 5 % CO_2 humidified atmosphere. Afterward, EDTA was removed, 1.3 mL 0.25 % Trypsin-EDTA was added, and the cells were incubated again under the same condition for 5 min, leading to their detachment. After the cells were detached from the flask, 6 mL DMEM was added, and the cells were passed through a syringe to separate cell clumps. The cells were counted using a Neubauer chamber before seeding them in a new flask until they reached 70-80 % confluency (t = ~48 h) before using them for further cell growth or next cell passaging.

3.8.3 Incubation and cell passaging of RAW 264.7 cells

A typical procedure for passaging RAW 264.7 cells grown in a 75 cm2 (T-75) flask is described below. The supernatant of confluent cells was discarded, and the cells were washed with 5 mL of PBS before adding 10 mL of supplemented DMEM, and the cells were scraped from the flask's bottom using a cell scraper. The cell suspension was then gently pipetted up and down 5 times using a 10-mL pipette. The cells were counted using a Neubauer chamber, and 10 mL of the medium was transferred into a T-75 flask until 70-80 % confluency (t = ~72 h) was reached for the next cell passaging or assays.

3.8.4 Exposure of biological cells to silica coated upconversion nanoparticles for cytotoxicity assay

For the MTT cytotoxicity assay 6×10^3 HaCaT or 10×10^3 RAW 264.7 cells were seeded per well in a 96-well Corning® plate (replicates: 6 wells/ one particle concentration and 6 wells for blank controls). They were incubated for 24 h at 37 ºC in 5 % CO_2 humidified atmosphere. After the cells became adherent, the medium was removed from each well, and 100 µL of the particles in supplemented DMEM (c =12,5; 25; 50; 100; 150; 200 µg/mL) or pure supplemented DMEM as controls/blank samples were added. The exposed cells and particles were incubated for 24 h at 37 °C in 5 % CO_2. After that, 50 µL of 3-(4,5-dimethylthiazole-2-yl)-2,5-diphenyltetrazolium bromide (MTT; c = 1 mg MTT/mL PBS) were added to each well and the cells were incubated for another 4 h at 37 °C in 5 % CO_2. Afterward, 150 µL of DMSO was added to each well, and the plates were shaken in the dark using an orbital shaker (Mini Shaker Kisker Biotec). Absorbance was recorded at 570 nm using a microtiter plate reader (Synergy HT from BioTeK Instruments Inc).

3.8.5 Exposure of biological cells to silica coated UCNP for confocal laser scanning microscopy measurements

To optically observe the uptake of silica coated UCNP into HaCaT cells, 1×10^6 cells were seeded into a 6-well plate with supplemented RPMI with microscope slides and UC@thin_RBITC_NH_2 or UC@thick _RBITC_NH_2 (c = 100 µg/mL in RPMI) were added to the wells. After 24 h of incubation at 37°C, aliquots were taken out, and the cells were washed with PBS and then fixed with paraformaldehyde. The DNA of the cells was subsequently stained with 4′,6-diamidino-2-phenylindole (DAPI) and the cells were visually characterized.

3.8.6 Exposure of biological cells to silica-coated UCNP for flow cytometry measurements

For flow cytometry measurements, 3×10^4 HaCaT cells or 10×10^4 RAW 264.7 cells were seeded per well in a 12-well plate in duplicates (2 wells for each particle type and concentration and 2 wells for blank samples/controls). The cells were incubated for 24 h at 37 °C in 5 % CO_2 humidified atmosphere. After the cells became adherent, the medium was removed from each experimental well, and 100 µL of particles in supplemented DMEM (c =100 µg/mL) samples were added. Only fresh medium, without particles, was added to the controls/blank wells. The exposed cells and particles were incubated for 24 h at 37 °C in 5 % CO_2. After 30 min., 4 h, or 24 h exposure time, the supernatant was removed, the cells were washed with 1 mL PBS, and the PBS was discarded. Next 0.5 mL 0.25 % Trypsin-EDTA was added to each well, and the cells were incubated for 10 min at 37 ºC in 5 % CO_2. When all cells had detached from the well bottom, 1 ml of supplemented DMEM was added to each well. Finally, the cells were collected for flow cytometry measurements using a flow cytometer.

For the RAW 264.7 cells, the conditions of exposure of the cells to the UCNP were the same as for the HaCaT cells. After 24 h of incubation at 37 °C in 5 % CO_2, the supernatant was removed from each well; the cells were washed once with PBS, and then 1 mL supplemented DMEM was added and finally, the cells were scraped using a cell scraper for flow cytometry measurements with a stopping gate at 10,000 total events.

3.8.7 Sample preparations for ion release experiments

Particles of the samples UC@thin_SiO_2_NH_2, UC@thick_SiO_2_NH_2 and UC@thin were redispersed in 4 mL ultrapure water or supplemented DMEM, so that final particle concentrations of 200 µg/mL of the silica-coated UCNP and the UCNP cores were obtained, left for 24 hr at 37 °C and centrifuged with centrifuge tubes with membrane filters (Amicon Ultracentrifuge, low binding Ultracelmembrane, 3000 Molecular Weight Cut-Off (MWCO)) for 2 hours at 3080 g. Aliquots were then diluted to 10 mL with ultrapure water and aqua regia (water : aqua regia = 4:1 v/v) and measured by ICP OES for determining the concentration of the yttrium, ytterbium and erbium ions.

Aqueous solutions containing 1 and 2 ppm of the to-be-measured lanthanide ions were also centrifuged through the same amicon filter tube mentioned above, diluted to 10 mL with ultrapure water and aqua regia (water : aqua regia = 4:1 v/v) and analyzed by ICP-OES for determining the concentration of yttrium, ytterbium and erbium ions.

4 Results and Discussion

Numerous scientific publications reported that upconversion nanoparticles (UCNP) can be utilized as novel biomarkers for biological imaging applications.[68-69, 161] These types of particles can be excited by low-energy wavelength in the NIR range, and emit wavelengths with higher energy photons in the UV range through sequential photon absorption and energy transfer.[68-69, 162] Some of the advantages that make these particles ideal candidates for biomarkers include their low background or auto-fluorescence when used in biosystems,[163] high penetration depths,[164] and a low degree of cytotoxicity (compared to some quantum dots for example).[165-166]

A typical host structure for UCNP is a hexagonally structured nanocrystal, which has low phonon lattice energy that can ensure a long lifetime of the excited intermediate states and prevent non-radiative relaxation through multiphonon emission, for example fluoride materials.[167] Crystals containing Na^{+}, Ca^{2+} especially Y^{3+} are usually chosen as ions of host lattices due to their similar ion radii to lanthanide dopant ions, that result in lattices with low crystal defects and low lattice mismatch.[70, 80, 168] Moreover, $NaYF_4$ has been reported to deliver the most efficient and highest intensity of upconversion luminescence compared with other host crystals,[169-170] and was therefore used as lattice host in this work. The host crystal is consequently doped with lanthanide ions as absorbers or sensitizers (Yb^{3+} ions) and emitters (Gd^{3+} , Tm^{3+} or Er^{3+} ions). Trivalent lanthanide ions are commonly used because of their ladder-like energy levels and long-lived intermediate states.[10, 69] Since these dopants are separated by a certain distance in the host crystal, UCNP does not suffer from ion concentration-dependent quenching and photobleaching. However, one of the major challenges is to enhance low luminescence intensity and quantum yield that these particles have compared with organic fluorophores and quantum dots, owing to low absorption coefficients of lanthanide ions and surface quenching, especially in small UCNP particles (particle diameter < 50 nm).[68]

Plasmonic metal systems such as metal nanoparticles or metal nanoshell coupled with UCNP can enhance the luminescence of the upconversion emission.[21, 26] The surface plasmon resonance of metal nanoshell coated on UCNP can be tuned over a broad spectral range far into the NIR-range by tuning the UCNP core-shell metal ratio.[104, 171] These nanoarchitectures can be used to increase the luminescence emission of UCNP system only when the noble metal is separated from the UCNP core by a spacer of suitable thickness.[21] The growth of a silica nanoshell onto the UCNP is one of several possibilities of controlling the distance between the UCNP core and the metal shell

as well as protecting the core from surface quenching effects. From the biological perspective, silica coating can increase the hydrophilicity and biocompatibility of the UCNP, since silica itself is hydrophilic and has relatively low cytotoxicity.[39, 89] The advantages of coating with silica are two-fold: firstly, the UCNP core is protected from external factors such as water in the biological environment, which can cause them to aggregate; secondly, silica coating can also reduce possible lanthanide ion leakage, which can cause cell inflammation or toxicity.[42]

The main aim of this thesis was to investigate the changes of upconversion luminescence intensity of structured silica coated UCNP due to their resonant coupling with a plasmonic system; in this case a gold nanoshell coupled to UCNP surface. The UCNP core consisted of $NaYF_4$ doped with 18 % Yb and 2% Er. In chapter 4.1.1, $NaGdF_4$ was used as host lattice since gadolinium can help stimulate the formation of a hexagonal phase structure, [172-173] in line with observations that this can provide a higher luminescence intensity compared to the cubic phase structure.[169] Thus, in a first step, we sought to screen various thermal decomposition synthesis methods to evaluate their ability to produce monodisperse UCNP with high upconversion emission and efficiency. The thermal decomposition method, which involved heating reactants in solvents with high boiling points > 250 ºC in an inert gas atmosphere, was routinely used to produce UCNP with high monodispersity. Variations of the synthesis method mentioned above included the use of precursors such as rare earth trifluoracetates and rare earth oleates or direct heating of rare earth chlorides. The particle size was determined by optical characterization using TEM, STEM or SEM. Measurements of the hydrodynamic diameter of the particles in polar (water, ethanol), as well as non-polar (cyclohexane, hexane) solvents, was done by DLS. The crystal phase of the UCNP core was resolved by X-ray diffraction spectroscopy (XRD). Based on the screening procedure, a standard method to reproducibly produce UCNP cores with similar sizes, lanthanide doping, fluorescence emission, and decay fluorescence lifetime was developed. The spherical core particles produced by the thermal decomposition method (see chapter 4.1.3.3) were designed to be in the size range of 20-30 nm. Further coating with a metal nanoshell could enhance the upconversion emission through coupling of upconversion excitation or emission energy with localized plasmon resonance of the shell, since upconversion emission of UCNP is commonly weak (see paragraph above). The above-mentioned UCNP core size range of 20-30 nm was chosen in this work, since smaller particles can cause higher risks of quenching and bigger particles can have different morphologies such as hexagonal plates (see chapter 4.1.1), which would make the gold coating step more complicated.

Subsequently, silica shell was grown onto the UCNP core (see chapter 4.2.1). The silica shell increased the core size to fit a suitable silica-coated UCNP core-metal shell size ratio for plasmonic enhancement,[21] based on theoretical calculations (see chapter 4.2). Moreover, it also provided a required distance between the core and the metal shell to prevent quenching effects caused by the direct interactions of surface lanthanide ions and metal shells.[174] Surface coating of UCNP with silica was obtained by employing a combination of microemulsion and the Stöber method. There has been no previously reported publications describing the growth of thick silica shell (silica shell thickness (r_{SiO2}) > 20 nm) on small UCNP cores. Hence in this work, a method was developed to gradually grow and increase silica shell thickness on a small UCNP core in a tightly controlled manner. Using a modified microemulsion method developed originally by Arriagada et al.,[84] a thin silica shell (r_{SiO2} = 5 nm) could be synthesized as the first shell, which could be grown further up to 44 nm thickness with further microemulsion steps. A Stöber-like growth process was then implemented to further increase the silica thickness, to the desired final size optimal for the growth of a gold nanoshell for plasmonic enhancement.[83] The upconversion emission and decay fluorescence lifetime of the UCNP core coated with various silica shell thickness were then measured.

Afterward, the coating of a smooth, closed gold shell on silica surface can be achieved by growing a thick gold shell (gold shell thickness (t) > 20 nm), since a thinner gold shell is prone to form an incomplete shell.[25, 175-176] Coating small size nanoparticles with less than 100 nm diameter has been proven to be difficult and resulted in inhomogenous gold coating as shown in several publications.[25, 175, 177] Hence, the UCNP core should be grown to a size > 100 nm before the gold coating procedure. After gold nanoshell coating, upconversion emission and decay emission rate (chapter 4.2.4) due to upconversion excitation or emission energy coupling with gold plasmon resonance were measured. Figure 4.1 depicts the synthesis steps from the UCNP core to the gold coating step.

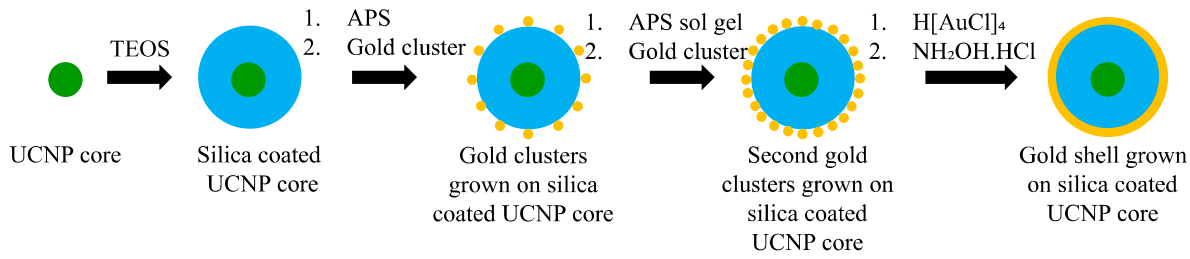

Figure 4.1: General steps of coating UCNP core with gold nanoshell. The synthesized UCNP was coated with a silica shell, followed by the adsorption of gold clusters. The gold shell was finally grown from this gold cluster to form a closed shell. Alternatively, the UCNP core was coated by an RBITC coupled silica shell for FRET measurements. RBITC was coupled with aminopropyltriethoxysilane (APS) and bound into the silica shell along the coating process.

In chapter 4.3 rhodamine B isothiocyanate (RBITC) dye with an absorption energy in the range of upconversion emission energy was coupled into the silica shell coated on UCNP core (chapter 4.3) to investigate a possible non-radiative energy transfer effect initiated by dipole-dipole-coupling between UCNP and dye. The application could be used in bioimaging systems, where the excitation of UCNP using low energy laser in the NIR range could lead to an organic dye excitation delivering optical imaging with a high signal-to-noise ratio. Otherwise, the coupling of UCNP with an organic dye could be utilized as sensor system, such as in pH-, or O_2- or other stimuli-responsive systems. The amount of dye coupled into the silica shell as well as the distance between the dye molecules inside the silica shell and the emitter ions in the UCNP core could influence the rate and intensity of energy transfer. Hence energy transfer efficiency depends on the concentration of the dye coupled in the silica since a high concentration of the coupled dye could cause quenching, and a low concentration could lead to low energy transfer efficiency. Various dye concentrations were coupled inside a 7-nm thick silica shell coated on UCNP and the upconversion emission and decay fluorescence lifetime measurements were done to characterize the dye-influenced energy transfer effect.

The last topic in this thesis is the investigation of the cytotoxicity of silica coated UCNP (chapter 4.4). Various *in vitro* cytotoxicity studies reported that UCNP caused low or no toxicity on cells.[143, 178-179] However, a recent study indicated that $NaYF_4$-nanoparticles doped with Yb^{3+} and Er^{3+} ions were unstable in acidic physiological fluids, e. g. in lysosomes and could cause inflammatory effects.[144] For cytotoxicity evaluation the UCNP were coated with thin silica shell of less than 20

nm thickness to stabilize the particles in cell culture medium. Afterward, an amine ligand with a positively charged surface was coupled onto the surface of the silica shell to enhance cellular uptake into skin cells and macrophage cells.[162] As a reference system, unfunctionalized silica coated UCNP were also exposed to the cells followed by characterization of the uptake. Cell viability was measured and characterized by MTT and flow cytometry assays. RBITC-coupled silica-coated UCNP with and without the amine ligand were observed by confocal fluorescence microscopy after exposure to skin cells to optically observe their uptake. In ion release experiments the question of whether the silica shell could provide sufficient protection to prevent the release of possible toxic ions from UCNP core into biological medium was investigated. For this purpose, the particles were dispersed in cell medium, centrifuged through a centrifuge filter and the amounts of released lanthanide ions in the filtered dispersion was measured with ICP-OES.

4.1 Synthesis and characterization of upconversion nanoparticles

4.1.1 Synthesis and characterization of upconversion nanoparticles from rare earth chlorides

Upconversion nanoparticles as core consisting of a $NaYF_4$ host lattice doped with Gd^{3+}, Yb^{3+}, Er^{3+}-ions (Y : Gd : Yb : Tm = 65:15:18:2 in molar ratios) were synthesized (UC_Gd_1) using the method of Zhang et al.[155] Lanthanide chlorides in the above-mentioned molar ratios, NH_4F and NaOH were mixed in 15:6 v/v of 1-octadecene to oleic acid. The mixture was heated to 300 °C in vacuum for 1.5 h. This method was utilized since this was the most convenient and fastest way to synthesize monodisperse UCNP without the necessity of synthesizing it through precursors. The size distribution of the samples was bimodal since two types of particles were formed (see Figure 4.2): flat plate-like hexagons and spherical particles with average diameters of 106±12 nm and 15±2 nm, which were difficult to separate through centrifugation. Hexagons are commonly formed when the growth in the direction of the [100] lattice plane is significantly faster than in other directions.[155] This could be the result of a low oleate ligand concentration, since oleate ligand tend to attach on the [001] plane,[180] allowing the particles to grow faster in the [100] direction, making the hexagonal-shaped nanoplates to increase in size in this direction. The smaller spherical particles shown in Figure 4.2. were likely α-phase nanocrystals being consumed in the α → β phase transition process (see chapter 2.1.2).[180] Wang et al.[172] reported in Discrete Fourier Transform (DFT) calculations concerning the formation energy of $NaREF_4$ either doped with Y^{3+} or Gd^{3+} ions,

that in the cubic phase $NaGdF_4$ was thermodynamically more stable than $NaYF_4$ under the same reaction conditions, while it is the reverse for the hexagonal phase. This could explain, why there were still small α-phase nanoparticles in the present synthesis after 1.5 h at 300 °C, as the energy barrier of the transition phase from α- to β- transition phase was higher for Gd^{3+} ions in the α-$NaYF_4$ crystals compared to pure $NaYF_4$. The bigger particles (d = 106±12 nm) could not be separated from the smaller particles, since the bigger particles were hexagonal and flat, so that the sedimentation speed could not be precisely calculated.

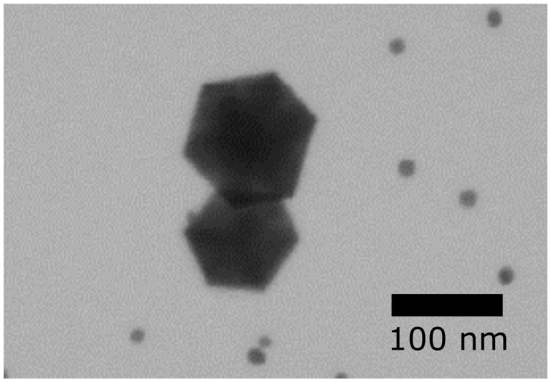

Figure 4.2: STEM image of the $NaYF_4$ cores (Sample: UC_Gd_1) doped with Yb^{3+}, Gd^{3+} and Tm^{3+} ions in a molar ratio of 18:15:2. The average diameter of the hexagons was 106 ± 12 nm and that of the spherical particles 15 ± 2 nm.

Figure 4.3 shows the upconversion spectrum of sample UC_Gd_1 for an emission wavelength range from 400-900 nm after excitation at 980 nm. There are two peaks at 520 nm that could not be assigned to any transitions of Tm^{3+}, but instead to the $^4H_{11/2} \rightarrow ^4 I_{15/2}$ and the $^4S_{3/2} \rightarrow ^4I_{15/2}$ transitions of Er^{3+} ion. Thulium compounds or salts are often contaminated with erbium compounds since these two elements are difficult to separate, owing to the fact that both lanthanides possess similar chemical characteristics. When the sample was excited at 378 nm to measure erbium content in the crystals, there was no clear signal of its presence. Since thulium was doped at a low concentration (i.e., 2 %), the maximum amount of erbium contamination should be lower than 0.01 %.

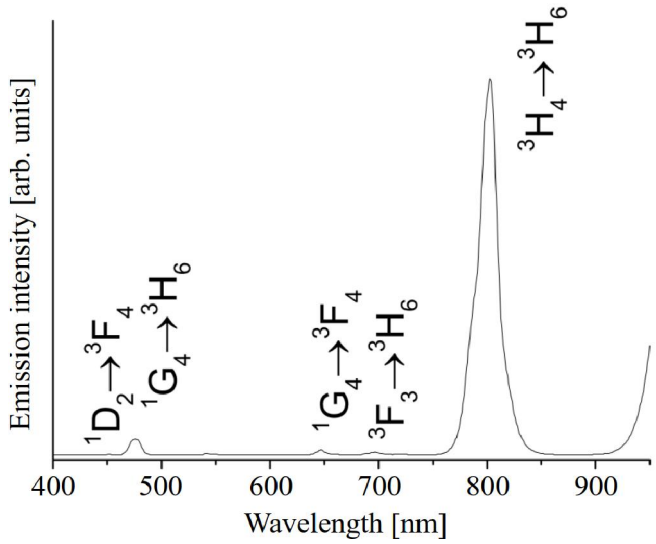

Figure 4.3: Upconversion spectrum of sample UC_Gd_1 in hexane after excitation at 980 nm.

After repeated synthesis and testing for a longer reaction time (120 min), it was concluded that this synthesis method could not be used to produce monodisperse particles. Hence further upconversion luminescence characterization was not carried out.

At a gadolinium concentration of 4 %, particles (sample UC_Gd_2; Figure 4.4) with an average diameter of 37±4 nm and much smaller particles with a size of about 15 nm were formed. The smaller particles could only be partially isolated by centrifugation.

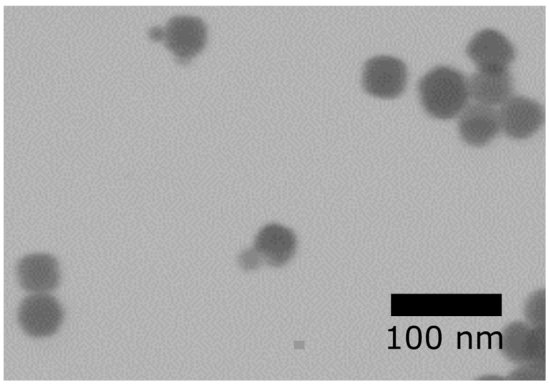

Figure 4.4: STEM image of sample UC_Gd_2. Average STEM-diameter = 37±4 nm.

An upconversion spectrum was measured from the cleaned sample (centrifuged and redispersed in hexane or cyclohexane for three times; see Figure 4.5), after which the typical upconversion emission bands of Tm^{3+} ion were observed. The ratio between the emission of $^3H_4 \rightarrow {}^3H_6$ (800 nm)

and $^3F_2 \rightarrow {}^3H_6$ (700 nm) transition of sample UC_Gd_2 was lower than that of sample UC_Gd_1. The smaller spherical particles in sample UC_Gd_2 have a higher surface-to-volume ratio and consequently higher amount of lanthanide ions on the surface that could be quenched for example by vibrational modes of the oleate ligand, which in turn would promote non-radiative relaxation of the excited photons. The energy states that were usually involved in red emission transitions were much less populated, and the upconversion emission intensity decreased at higher wavelengths.[181]

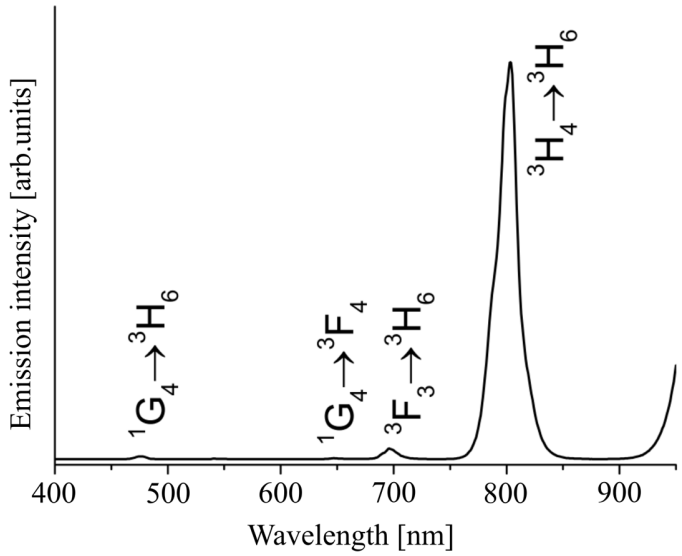

Figure 4.5: Upconversion spectrum of the sample UC_Gd_2 in hexane excitation at 980 nm.

The fluorescence decay time measurements of UC_Gd_1 (black line) and UC_Gd_2 (red line) at 477 nm, 696 nm and 803 nm in hexane are shown in Figure 4.6, and the corresponding lifetime for the different transitions are listed in Table 4-1. The decay curves were fitted by a monoexponential function. From the figures and tables, it can be deduced that the lifetime of the smaller particles is shorter than that of the bigger particles.

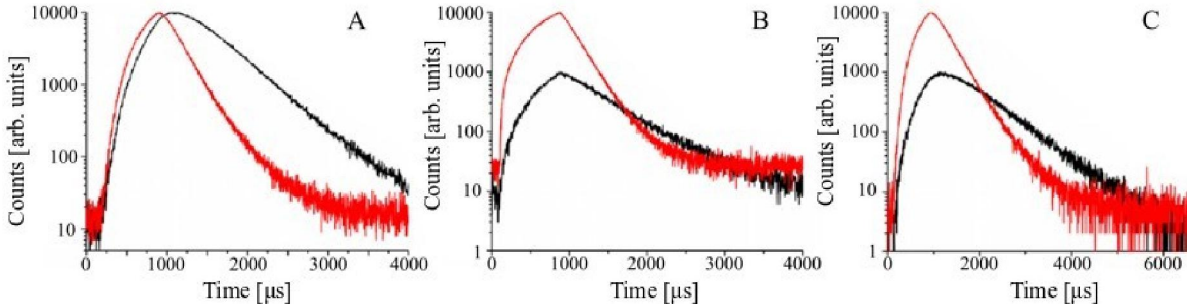

Figure 4.6: Decay of the fluorescence lifetime of samples UC_Gd_1 (black line) and UC_Gd_2 (red line) after 980 nm excitation at A: 477 nm, B: 696 nm, and C: 803 nm in hexane.

Table 4-1: Fluorescence lifetimes of the sample UC_Gd_1 und UC_Gd_2 (in µs)

Sample	**Transition**	**Transition**	**Transition**
	$^1G_4 \rightarrow {}^3H_6$	**$^3F_2 \rightarrow {}^3H_6$**	**$^3H_4 \rightarrow {}^3H_6$**
UC_Gd_1	605±3	562±2	984±5
UC_Gd_2	260±1	217±1	379±1

Smaller particles are more prone to surface related non-radiative recombination, due to the increasing surface-to-volume ratios, which can reduce the decay time because of the self-quenching effect of the emitters that are on the surface of the particles, or due to increasing ion interactions with high energy vibrational modes of C-C or C-H-bonds of the oleate ligands or solvent.[181] The bigger hexagonally shaped particles had fewer surface defects due to the decreased surface-to-volume ratio, which leads to less surface quenching and longer lifetime.[92] Additionally, due to the increased crystallinity of the hexagons, the higher order upconversion emission were promoted in the particles with this morphology, as they possess fewer surface defects.[182]

Syntheses by the same method but without gadolinium or by replacing thulium with erbium also delivered polydisperse and polymorphic nanoparticles. The solvent was also varied by using trioctylamine instead of a mixture of 1-octadecene/oleic acid. Trioctylamine has a higher boiling point (T = 365 °C) than 1-octadecene (T = 315 °C). In this way a higher reaction temperature could be reached and monodisperse particles could be synthesized more easily because ß-phase nanocrystals are easily formed at a higher temperature (T > 300 ºC).[180] Additionally the longer alkane chain of trioctylamine, like oleic acid, can ensure a higher particle dispersibility in a non polar solvent.[183] Based on these considerations, the sample UC_1 was prepared by doping with

2.1±0.1 % Er^{3+}. For a pilot experiment using trioctylamine as solvent, the reaction was kept at 300 °C to imitate the reaction parameter of a synthesis where an 1-octadecene/oleic acid mixture is used as solvent. The XRD diffractogram showed a cubical phase, with spherical particles having a size of 5±1 nm (see Figure 4.8). At 28° is the peak for the [111] reflex, at 32° for the [200] reflex, at 47° for the [220] reflex, at 55° for [311] reflex and at 76° for [331] reflex (ICDD no. 06-0342). No peaks for a hexagonal structure were present, leading to the conclusion that the particles were in the α-phase, an assumption that would be consistent with the very small size of the particles (d < 10 nm) observed.

The fluorescence spectrum (Figure 4.7) after excitation at 378 nm shows the typical transition peaks of erbium, which were: $^2H_{11/2} \rightarrow {}^4I_{15/2}$ at 517 nm, $^4S_{3/2} \rightarrow {}^4I_{15/2}$ at 537 nm, $^4G_{11/2} \rightarrow {}^4I_{11/2}$ at 622 nm, $^2H_{9/2} \rightarrow {}^4I_{11/2}$ at 693 nm, and $^4G_{11/2} \rightarrow {}^4I_{9/2}$ at 723 nm. Upconversion measurements with excitation wavelength at 980 nm were not carried out for this sample, due to limited access to the measurement device at the time. The excitation of a hypersensitive band at 378 nm ($^4I_{15/2} \rightarrow {}^4G_{11/2}$) led to downconversion emission of erbium. The typical erbium emission bands (520 and 540 nm emission bands) in the downconversion spectrum could have been observed in an upconversion process at 800 or 980 nm excitation.[184] A scattering effect of the samples can be observed at the lower wavelength in both fluorescence and the extinction spectrum. In the extinction spectrum, an absorption peak of ytterbium at 930 nm is observed, which is the transition of $^2F_{5/2} \rightarrow {}^2F_{7/2}$ in the cubic phase. The particles were doped with 17±1 % ytterbium according to ICP-OES measurement result. Multiple possible absorption peaks in the range of 910-930 nm and 960-980 nm are a consequence of the Stark effect, explained by the splitting of electronic levels in the ground level ($^7F_{7/2}$) to excited electronic levels of $^7F_{5/2}$.[185] The Stark splitting effect depends on the crystal structure, symmetry sites of the Yb^{3+} ions in the crystal and the resulting crystal field that is experienced by each ion.[186]

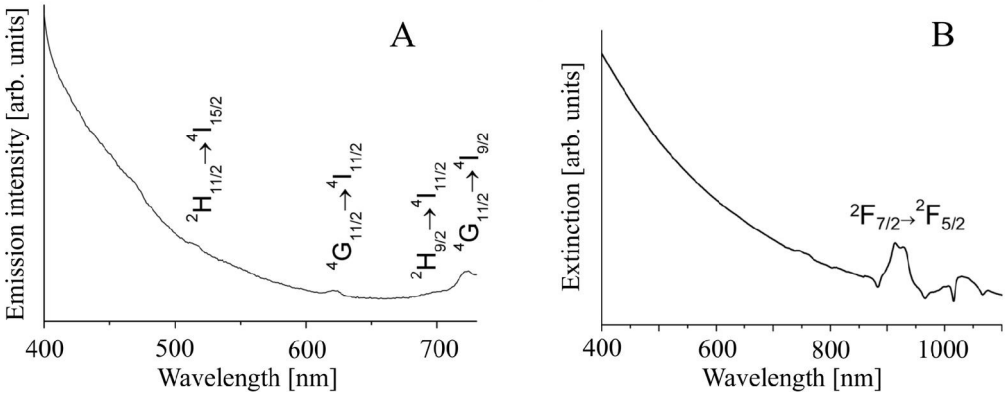

Figure 4.7 A: Fluorescence spectrum of sample UC_1 in hexane after excitation at 378 nm and B: extinction spectrum of sample UC_1 in hexane.

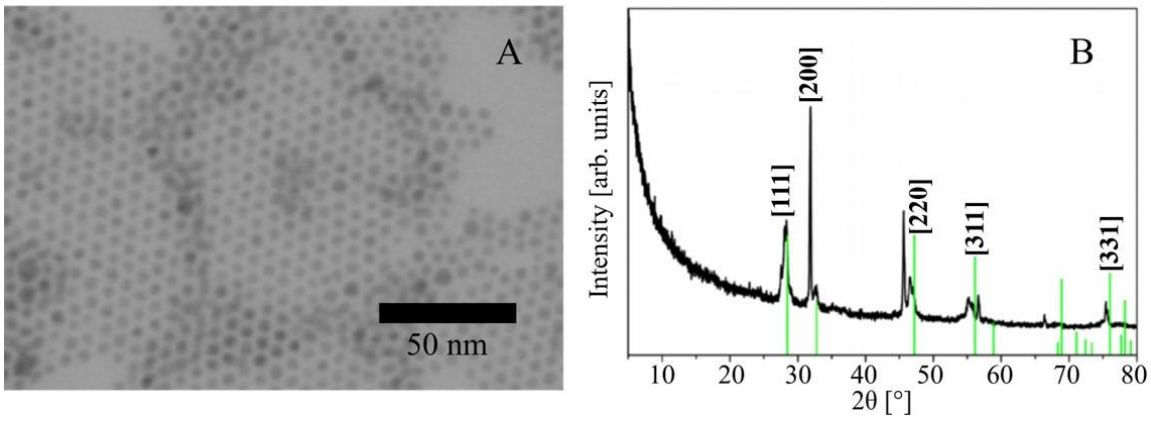

Figure 4.8 A: STEM image (d_{STEM} = 5±1 nm) and B: XRD diffractogram of the sample UC_1 shows predominantly an α-phase structure (ICDD no. 06-0334).

Synthesis using trioctylamine produced only small spherical particles (d = 5±1 nm) which had a cubic crystal phase, due to the low coordinating effect of trioctylamine compared to 1-octadecene. α-phase nanocrystals need to overcome high activation energy to undergo a phase transition into β-phase nanocrystals.[180] With longer reaction times and higher temperature, nanoparticles transist from cubic phase to the thermodynamically more stable hexagonal phase particles, indicating that the reaction is kinetically controlled.[74, 180] As trioctylamine also has coordinating characteristics like oleic acid due to the long alkyl chain, monodisperse particles should also form in this reaction even at a temperature below the boiling point. Though trioctylamine has a higher boiling point than 1-octadecene, the reaction was done under the conditions of the reaction with 1-octadecene, i.e., at

300 °C; consequently, the energy barrier for phase transition was not achieved, hence an α → β-phase transition could not fully occur. The reaction was not done initially at 365 °C in order to prevent the formation of polycrystalline particles.[187] However, particles with a polydisperse size and polymorph shape were already beginning to form at 300 °C. Hence, further experiments with this solvent were waived.

The synthesis of UCNP from rare earth chlorides did not deliver a reproducible result. One assumption to explain this finding is that the chlorides, NaOH and NH_4F absorbed water and humidity over time, which can negatively influence the formation the UCNP cores since an absolute air and water free synthesis environment is required. Air or water can induce side reactions, such as oxidation of oleic acid.[188] For this reason, a synthesis method involving a precursor consisting of lanthanides trifluoroacetates and sodium trifluoroacetates was chosen, as these precursors were less sensitive to oxygen and moisture and did not need NaOH and NH_4F as reactants since the NaF species was readily accessible from the trifluoracetates and sodium trifluoacetates.[73-74]

4.1.2 Synthesis and characterization of upconversion nanoparticles from rare earth trifluoracetates

In this method, a precursor reaction of rare earth chlorides hexahydrates to rare earth hydroxides is performed using ammonia, from which the trifluoracetates are synthesized using trifluoroacetic acid (TFA) (see Scheme 4-1). The trifluoracetate precursor was initially prepared by Boyer et al. from LnF_3 (Ln = lanthanide ions) as educts.[76] However, this method did not initially produce monodisperse particles.

$LnCl_3\ 6H_2O + NH_3 \rightarrow Ln(OH)_3 + 3\ NH_4Cl + 3\ H_2O$

$Ln(OH)_3 + 3\ CF_3COOH \rightarrow (CF_3COO)_3Ln + 3\ H_2O$

$Na_2CO_3 + 2\ CF_3COOH \rightarrow 2\ CF_3COONa + CO_2 + H_2O$

Scheme 4-1: Reaction mechanism the synthesis of trifluoracetate precursors.

Using this method, sodium trifluoroacetate was synthesized from sodium carbonate (Na_2CO_3) using TFA. High yields (90 – 96 %) of rare earth trifluoroacetates can be directly synthesized from lanthanide oxides using TFA. Similarly, sodium trifluoroacetate could be produced with a yield of 95 %. The IR spectra of the trifluoroacetates are shown in Figure 4.9. The strong background signal

was caused by impurities from the synthesis, an observation consistent with the fact that no further purification steps were undertaken.

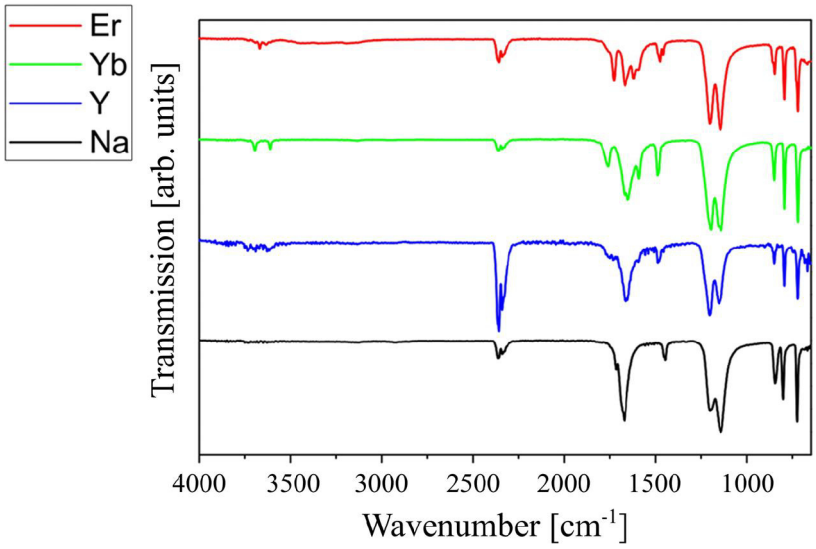

Figure 4.9: IR-spectra of lanthanide trifluoroacetates and sodium trifluoracetate.

The IR spectra of the rare earth trifluoracetates and sodium trifluoroacetate showed similar bands as reported for the IR bands of sodium trifluoracetate in literature.[189] The typical carboxylate asymmetrical vibration peaks were found in the range between 1670±2 cm^{-1} and 1450±3 cm^{-1}.[189] The wavenumber difference (Δν) between the carboxylate symmetrical and asymmetrical vibrations indicates the type of bond between the carboxylate group in the trifluoroacetate molecule and the metal ion. In the spectrum of lanthanide trifluoracetate, Δν was 220 cm^{-1}, indicating that the metal (i.e., sodium or the rare earth)-carboxylate bond type was monovalent/monodentate, i.e., a single covalent bond.[190] In the range from 3500-3700 cm^{-1} were the bands of the rare earth trifluoroacetate. These bands along with the band at 2300±32 cm^{-1} were bands of OH-vibrations that were caused by absorbed water or unreacted trifluoroacetates. The bands at 1400 cm^{-1} were the C-C vibrations of the trifluoroacetates. The valent vibration of C-F-binding was in the range of 1190-1250 cm^{-1}.[191]

The thermal decomposition synthesis of UCNP from lanthanide trifluoroacetates was done at 300 °C. Using this method, various publications reported production of monodisperse particles with a size range between 15-20 nm. The main advantage of this method was especially its simplicity, since the fluoride sources were already available in the trifluoroacetate mixture.[74-75]

Using this method, monodisperse UCNP (sample UC_Gd_4) with a size of 16±1 nm could be synthesized (Figure 4.10.A). The lanthanide ion composition was 18±1 % Yb, 14±1 % Gd and

2±0.1 % Er. The XRD diffractogram shows that the particles had a predominantly hexagonal structure, which are shown by the peaks at 18° for the [100] reflex, at 31° for the [101] reflex, at 44° for the [201] reflex and 54° for the [211] reflex (ICDD no. 28-1192; see Figure 4.10.B). Some peaks belong to the cubic structure of $NaYF_4$, such as the [111] reflex at 28° and the [222] reflex at 58° (ICDD no. 06-0334). In the extinction spectrum, the ytterbium absorption peak at 975 nm corresponded to the transition of $^2F_{7/2} \rightarrow {}^2F_{5/2}$ (see Figure 4.11.A.). To investigate whether erbium was doped in the crystal, a downconversion fluorescence spectrum was recorded. Since suitable methods for the synthesis of monodispersed particles were being screened at this stage, it was practical to initially waive upconversion measurements. In the fluorescence spectrum, erbium peaks after excitation at 378 nm were shown at 378 nm ($^4G_{11/2} \rightarrow {}^4I_{15/2}$), 521 nm ($^2H_{11/2} \rightarrow {}^4I_{15/2}$), and 653 nm ($^4F_{9/2} \rightarrow {}^4I_{15/2}$). The peaks at shorter wavelengths were less observable because of scattering effects (see Figure 4.11.B).

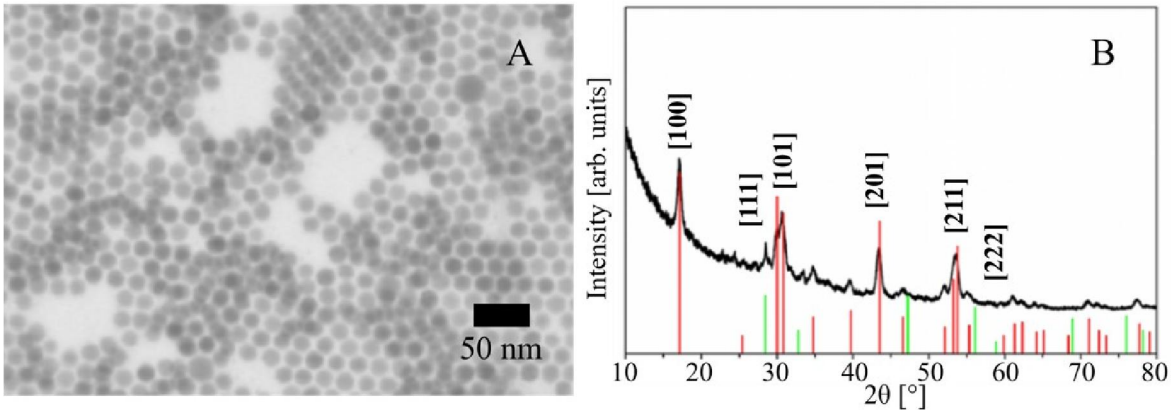

Figure 4.10 A: STEM image (average diameter = 16±1 nm) and B: XRD diffractogram of sample UC_Gd_4 (red lines: hexagonal phase (ICDD no. 28-1192); green lines: cubic phase (ICDD no. 06-0334).

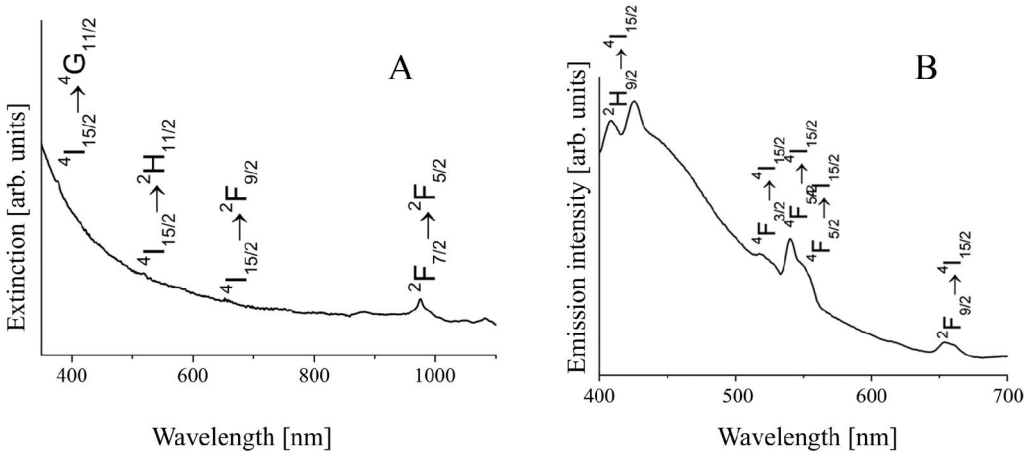

Figure 4.11 A: Extinction spectrum of sample UC_Gd_4 and B: fluorescence emission spectrum of UC_Gd_4 after excitation at 378 nm. Both spectra were taken in hexane.

Although this synthesis method was more promising than the lanthanide chloride method, further syntheses using lanthanide trifluoracetates were not able to produce monodisperse particles. Further variation of reaction parameters, such as the ratio of sodium to lanthanides and variation of the reaction time could not produce a reproducible size or morphology of the particles. There were traces of cubic phase particles such as are shown in the XRD diffractogram of UC_Gd_4 (see Figure 4.10.B).

A similar method using oleylamine (boiling point = 340 °C) was previously experimented.[75] Though the reaction temperature was 330 °C, some α-$NaYF_4$ nanoparticles were still present. This meant that a very high reaction temperature was needed and hence the reaction condition was difficult to control.

Taken together, although the synthesis method using trifluoracetates precursor was promising at first, it was not used further in this work, since the method was not reproducible under initial reaction conditions. Moreover, the fluorinated and oxyfluorinated compounds that were released from this reaction are hazardous to health, so that the search for another alternative less toxic synthesis methods was mandatory.[76]

4.1.3 Synthesis and characterization of upconversion nanoparticles from rare earth oleates

The synthesis of UCNP from lanthanide oleates was based on the thermal decomposition synthesis of iron oxide (Fe_2O_3/Fe_3O_4) nanoparticles from iron oleate, which could yield nanoparticles with a relatively high monodispersity.[82] The synthesis runs according to the following scheme:

Metal chloride + Sodium oleate → Metal oleates complex + NaCl

Metal oleates complex → Metal nanoparticles

Scheme 4-2: Reaction steps of metal nanoparticles' formation from metal oleate complex

Nucleation starts when the first oleate ligand dissociates from the iron oleate complex $Fe(C_{17}H_{33}COO)_3$ at 200-240 °C, while the last two oleate ligands dissociate at 300 °C under the release of CO_2, which occurs when the growth process of the particles begins.[82] Hence the key issue for synthesizing monodisperse particles by this approach is the separation of the nucleation and the growth process phases.

Using this method, the lanthanide oleates were obtained in the form of white waxy solids, that were partly soluble in 1-octadecene/oleic acid at room temperature, but were completely soluble at higher temperatures (T > 50°C). The lanthanide ratios of the UCNP corresponded to the amount of the lanthanide chlorides used at the beginning of lanthanide oleate synthesis. The lanthanide oleates can be directly used for the UCNP synthesis, and the amount of solvent can be adjusted to the amount of precursors synthesized.

4.1.3.1 **Synthesis of rare earth oleates**

Rare earth oleates were synthesized by heating rare earth chlorides hexahydrates with sodium oleate at the intended ratio. Sodium oleate can be prepared by mixing NaOH in water with oleic acid (see Scheme 4-3) or bought commercially. Sodium oleate is an air- and light sensitive product and can decompose during storage, producing sodium bicarbonate upon reaction with carbon dioxide and water vapor from the air.[192] Clean sodium oleate has to be synthesized und used immediately, or a long-stored commercially bought product has to be purified by boiling in ethanol, followed by hot filtration, and precipitation at 4 °C before use.

Commercial sodium oleate was directly used in this work without further purification. For the synthesis of UCNP from oleate precursors made from commercially bought sodium oleate (see Scheme 4-3), no disadvantage such as polydispersity or low luminescence of the UCNP was observed.

$NaOH + C_{17}H_{33}COOH \rightarrow C_{17}H_{33}COO^-Na^+ + H_2O$

Scheme 4-3: Synthesis of sodium oleate from NaOH and oleic acid

Rare earth chlorides were first dissolved in a water/EtOH-mixture and mixed with sodium oleate. The mixture was heated to 70 °C after addition of hexane. Rare earth oleates were formed and dissolved in the hexane layer (see Scheme 4-4). After drying the products could be dissolved in long-chained alkyl solvents such as 1-octadecene, oleic acid, or oleylamine.

$$LnCl_3 \cdot 6\,H_2O + C_{17}H_{33}COO{-}Na^{+} \rightarrow C_{17}H_{33}COO^{-3}\,Ln^{3+} + 3\,NaCl$$

Scheme 4-4: Synthesis of lanthanide oleates from lanthanide chlorides and sodium oleate

The yield of the product in a typical synthesis was 96 %. The IR-spectra (see Figure 4.12) of the lanthanide oleates and yttrium oleate are similar. Asymmetrical and symmetrical carboxylate vibration bands are at 1550 cm^{-1} and 1460 cm^{-1}. From the wavenumber difference ($\Delta\nu$ = 90 cm^{-1}) between the two bands, it could be concluded that the lanthanide ions were bound to the oleate ligand in a coordinative multidentate bond, precisely in a trivalent coordination.[81] At 1600 cm^{-1} is the carbonyl vibration band of the oleic acid residue, while the bands at 1500-1100 cm^{-1} belong to the CH_2-bond vibration. At 3000 cm^{-1} is the stretch vibration band of the CH-bond.

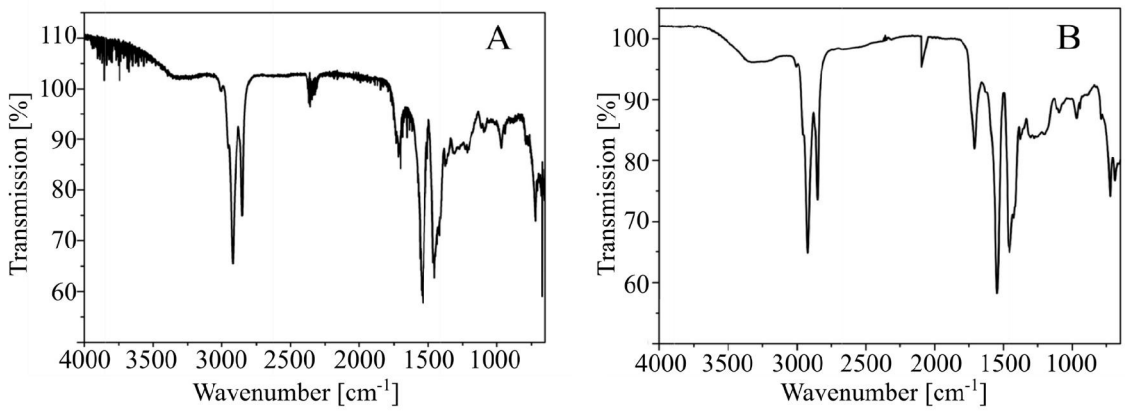

Figure 4.12: IR spectra of A: a mixture of ytterbium and erbium oleates (Yb:Er = 18:2 in molar ratio) and B: yttriumoleate.

4.1.3.2 Synthesis of $NaYF_4$ nanoparticles from rare earth oleates precursors

As a test experiment undoped $NaYF_4$ nanoparticles were made from yttrium oleate. The size measured from STEM images was 25±1 nm (see Figure 4.13.A). The size measured from STEM images was 25±1 nm (see Figure 4.13.A.). The XRD diffractogram shows a purely hexagonal phase, as it could be seen by as the reflexes at 18° for the [100] plane, at 31° for the [101] plane, at

40° for the [111] plane, at 44° for the [201] plane, at 54° for the [211] plane and at 63° for the [200] plane (ICDD no. 28-1192; see Figure 4.13.B). This shows that the method using lanthanide oleates could potentially yield monodisperse hexagonal-phased UCNP.

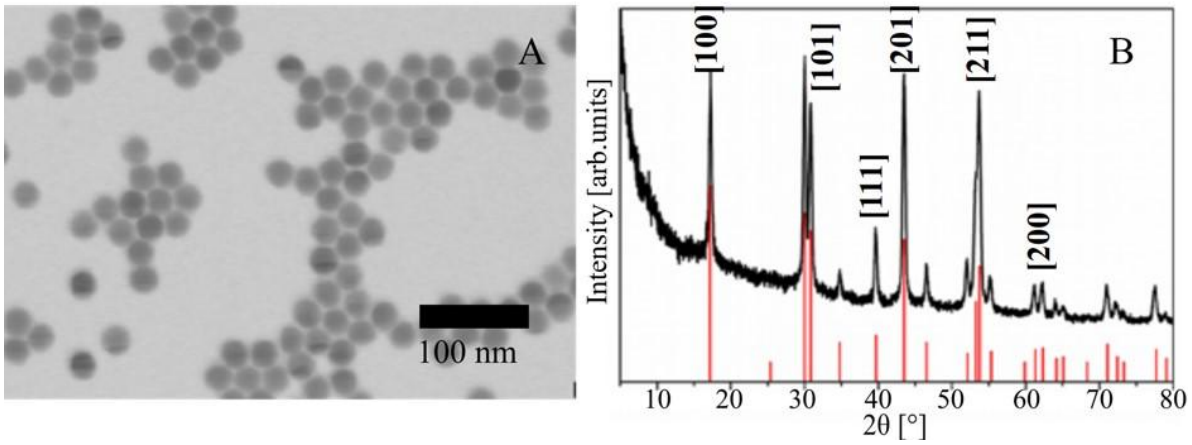

Figure 4.13 A: STEM image of pure $NaYF_4$ nanoparticles with an average diameter (d_{STEM}) of 25 ± 1 nm, B: XRD diffractogram of pure $NaYF_4$ nanoparticles. The red lines are the reflexes of a hexagonal $NaYF_4$ structure according to the literature (ICDD no. 28-1192).

4.1.3.3 **Synthesis of $NaYF_4$: Yb, Er from lanthanide oleates**

For this sample, 18 % Yb and 2 % Er were doped in the $NaYF_4$ core. The average STEM-diameter of the spherical particles (sample UC_Er_1) was 31±2 nm. They were monodisperse and had, similar to $NaYF_4$, a pure hexagonal phase (see Figure 4.14 B). The reflexes correspond to the same reflexes in the XRD diffractogram in Figure 4.15 A.

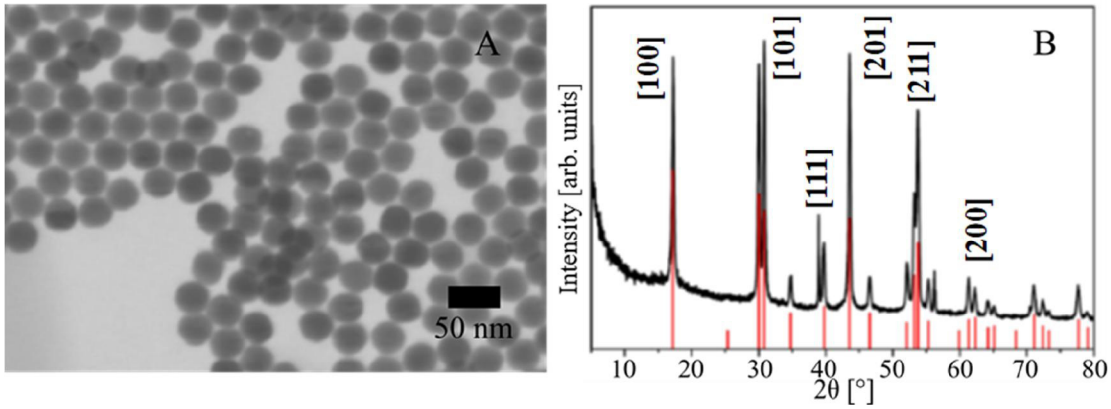

Figure 4.14 A: STEM image of $NaYF_4$: Yb, Er nanoparticles (sample UC_Er_1) with an average diameter (d_{STEM}) of 31±2 nm; B: XRD diffractogram of sample UC_Er_1, red lines: hexagonal phase peaks (ICDD-28-1192).

The extinction spectrum in Figure 4.15.A shows the absorption peak of Yb^{3+} ions at 975 nm ($^2F_{7/2}$ → $^4F_{5/2}$). The absorption peaks of erbium ion were not recognizable due to the high scattering effect of the nanoparticles and the low dopant concentration of erbium. However, in the fluorescence spectrum (Figure 4.15.B) the emissions of erbium are discernible at 520, 540, and 660 nm after excitation at 378 nm.

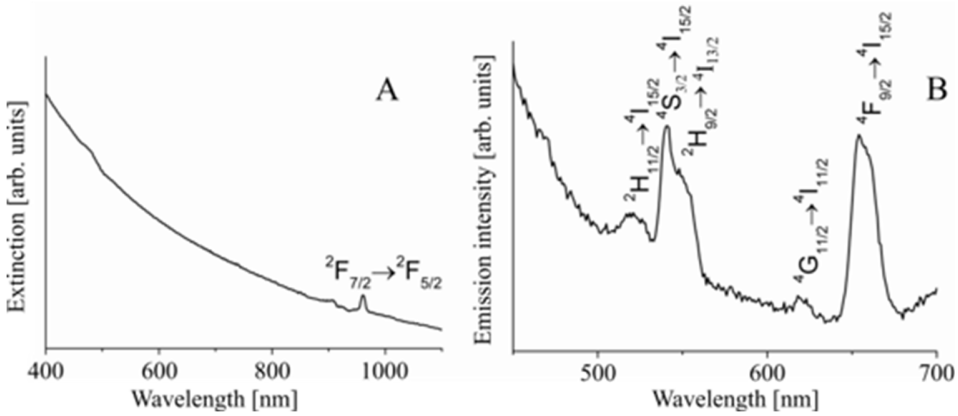

Figure 4.15 A: Extinction spectrum of $NaYF_4$: Yb, Er nanoparticles (sample UC_Er_1) and B: fluorescence spectrum of the same sample after excitation at 378 nm in hexane.

Upconversion measurement was not carried out for this sample, but later erbium-doped samples were prepared by the same approach. The analysis of the nanoparticles prepared with the synthesis method showed that lanthanide oleates are suitable precursors for producing spherical monodisperse doped UCNP cores. A comparison of upconversion fluorescence emission and

$NaYF_4$: Yb, Er nanoparticles with the same core that was coated with an undoped $NaYF_4$ is further discussed in chapter 4.1.4.1.

4.1.3.4 **Synthesis of $NaYF_4$: Yb, Tm from rare earth oleates**

$NaYF_4$ nanoparticles doped with 18 % Yb and 2 % Tm were synthesized. The average STEM-diameter of the spherical particles (samples UC_Tm_1 and UC_Tm_2) was 31±2 nm and 48±4 nm. The z-average of the smaller particles was 145±1 nm (PDI = 0.080±0.010), whereas the bigger particles had a z-average of 67±1 nm (PDI = 0.200±0.050), indicating a higher degree of aggregation of the smaller particles. This aggregation could also be observed from the STEM images (see Figure 4.16). The high z-average was caused more by the insufficient stabilization of the oleate ligands rather than polydispersity. The STEM images show particles that are placed close to each other, indicating probable insufficient stabilization. After synthesis, the smaller particles sedimented faster than would be expected for particles in this size range, as the sedimentation took place within a few hours. The particles had a slightly cubic morphology rather than a spherical one due to thulium doping, which argues for the formation of a cubic morphology and crystal phase.[172]

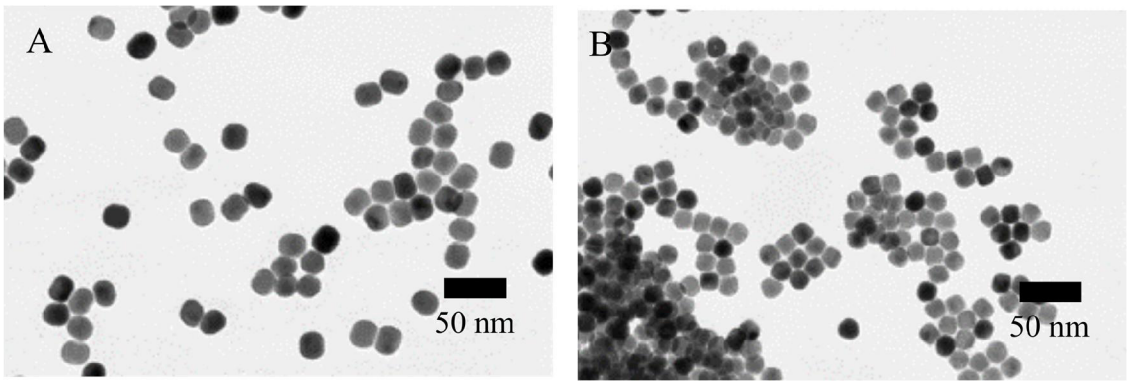

Figure 4.16: STEM images of $NaYF_4$: Yb,Tm nanoparticles with a STEM diameter of A: 48±4 nm (sample UC_Tm_2) and B: 31±2 nm (sample UC_Tm_1).

The cubic phase of the particles is further supported by comparing the XRD diffractograms of both samples (see Figure 4.17). Both spectra show peaks of the cubic phase, where the smaller particles (sample UC_Tm_1) have a higher portion of the cubic crystal phase. ICP-OES measurements showed that sample UC_Tm_2 had an Y: Yb: Tm ratio of [81.0 ±0.4]:[18.0±0.5]:[1.0±0.1], whereas sample UC_Tm_1 has a molar ratio of Y:Yb:Tm = [84.0±0.3]:[15.0±0.1]:[2.0±0.2]. The

differences in the ion concentration of both samples were likely caused by weighing errors of the initial reactants.

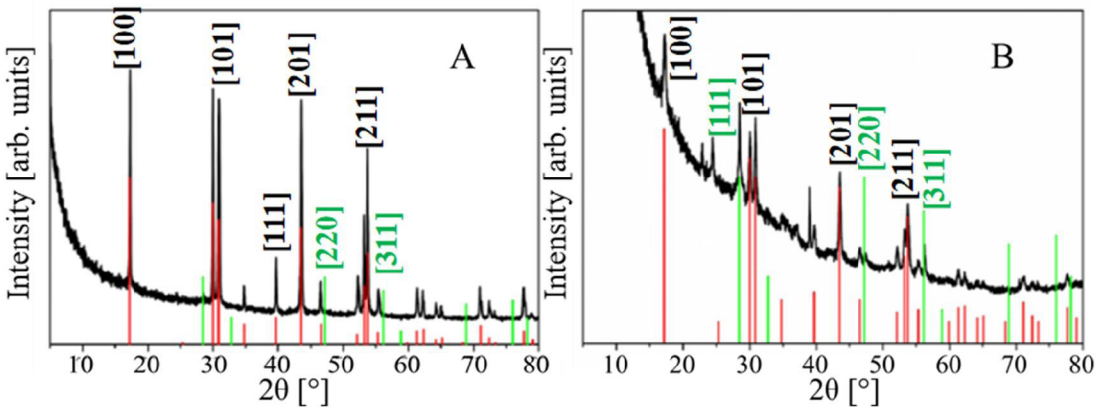

Figure 4.17: XRD diffractogram of $NaYF_4$: Yb,Tm of samples A: UC_Tm_2 (d = 48±4 nm) and B: UC_Tm_1 (d = 31±2 nm). Red lines: hexagonal phase (ICDD no. 28-1192), green lines: cubic phase (ICDD no. 06-0334).

Both samples UC_Tm_1 and UC_Tm_2 have predominantly hexagonal structures with some peaks belonging to the cubic structure, as it can be seen by the hexagonal structure peaks at 18° for the [100] reflex, 31° for the [311] reflex, 40° for the [111] reflex, 44° for the [201] and 54° for the [211] reflex (ICDD no. 28-1192, see Figure 4.18 A and B). Although the bigger particles have a higher percentage of Tm^{3+} ions, the cubic phase peaks, for example at 28° for the [111] reflex, 47° for the [220] reflex and 55° for the [311] reflex (ICDD no. 06-0334), in the XRD diffractogram of the smaller particles (UC_Tm_1) are more pronounced. The formation of larger particles (sample UC_Tm_2) suggests, that the phase transition time occurred faster than UC_Tm_1 during the heating time of 1.5 hours at 300 °C since α-phase particles would first dissolve and reform to build β-phase particles, and the β-phase particles would increase in size by consuming the α-phase particles during the subsequent Ostwald ripening process.[74-75, 172] The smaller amount of Tm^{3+} ions in sample UC_Tm_2 could have shortened the phase transition time, as the formation of the β-phase particles would be more favoured in this case, due to fewer crystal defects than in the particles of sample UC_Tm_1 with a higher Tm^{3+}-ion concentration in the initial mixture. Thus, lowering the energy for crystal phase transition occurred in sample UC_Tm_2.

Additionally, the cooling phase after heating is also important. Palo et al.[193] reported an obvious difference in particle size and morphology in the high-temperature synthesis of $NaYF_4$: Yb, Er between slow (cooling rate = 9±1 °C/minute) and fast cooling (cooling rate = 18±1 °C/minute)

rates to room temperature. A fast cooling rate produced bigger and more polymorph particles compared to a synthesis with a slow cooling rate, with the size of the bigger particles in the "fast-cooling rate" synthesis being twice the size of the particles in the "slow-cooling rate" synthesis. They postulated that at a fast cooling rate, the rare earth $(RE)^{3+}$-ions would occupy predominantly Na/RE-sites, whereas the RE^{3+}-ions would occupy partly the Na^{+}-sites at a slow cooling rate, making the distances between the lanthanides ions shorter, and leading to a consequent decrease in particle size. In this work, the temperature was cooled down slowly to room temperature by simply lowering the heating mantle. The time it took for the reaction temperature to decrease to 25 °C from 300 °C was measured, and the cooling rate was calculated to be 10 K/minute on average.
Extinction and fluorescence spectra of sample UC_Tm_1 were measured. The extinction spectrum shows the typical transition of Yb^{3+} ions in the 960-980 nm range (see Figure 4.18.A). The fluorescence spectrum shows the typical emission peaks of thulium (see Figure 4.18.B). In chapter 4.1.4.2 the emission characteristics of $NaYF_4$: Yb, Tm nanoparticles are compared to the same sample after coating with undoped $NaYF_4$ shell.

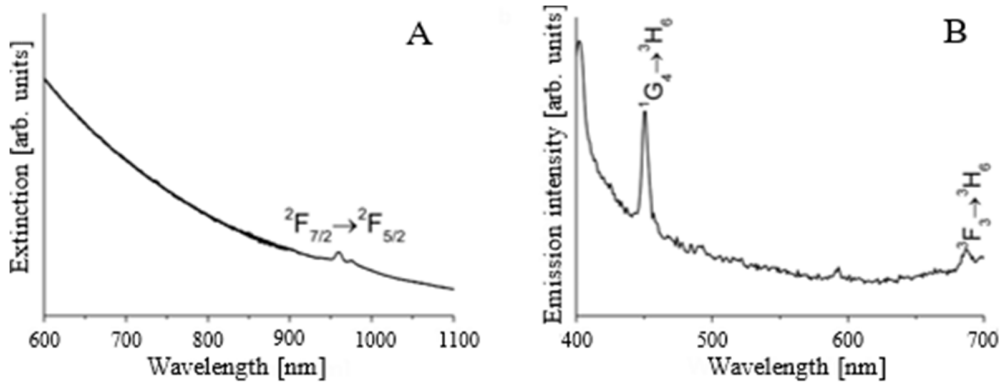

Figure 4.18 A: Extinction spectrum of sample UC_Tm_1 and B: fluorescence spectrum of the same sample after excitation at 360 nm in hexane.

Liu et al.[194] proposed the following mechanism for the synthesis of UCNP from rare earth oleates and NaF: at a sufficiently high temperature (T > 280 °C) F^- ions from NaF compete with alkyl carboxylate ($RCOO^-$) ions from the oleate complex to coordinate with rare earth cations during the nucleation and growth processes to form a $NaYF_4$ precipitate. Due to strong interactions between t 201he rare earth ions and the carboxyl groups in the rare earth oleates, the formation of $NaYF_4$ is initially strongly hindered, hence creating a distinct separation between the nucleation and growth

processes. The carboxylate group attaches strongly to the surface of the nanocrystals and the long non-polar tails ensure the prevention of particle aggregation. Compared to the synthesis using trifluoracetates precursors, particle stabilization was provided only by the oleic acid being used as a solvent. Hence, it was more difficult to synthesize stable, reproducible monodisperse particles in every batch with trifluoracetate precursors.

The synthesis using oleate precursors produced monodisperse particles with high crystallinity, even as oleate oxidation (from oleic acid or of the oleate ligand) is prone to occur more than is the case when trifluoracetates precursors are used. In every synthesis of UCNP core described in this chapter and further chapters in this work, under the same reaction conditions, monodisperse particles with an average size between 20-30 nm were obtained. Even when oxidation of the solvent occurred, due to oxidation, the product remained monodisperse and stable. The upconversion luminescence intensity of these particles did not differ much from that of particles synthesized from experiments, where the oleic acid did not oxidize. Hence, for further UCNP samples, the oleate precursor method was used. $NaYF_4$ nanocrystals doped with 18% Yb and 2% Er were the standard cores used for all following modifications and experiments. Gadolinium was not further used, since the hexagonal phase was readily achievable by the oleate method alone.

4.1.4 Synthesis of UCNP core coated with an undoped $NaYF_4$ shell

Lanthanide ions that are located on the surface of UCNP can suffer emission quenching resulting from their interaction with high energy vibrational energy sources such as organic ligands and solvents due to insufficient protection of the host lattice.[75, 195-196] Surface defects can also enhance non-radiative relaxation processes. Such factors are more prominent in smaller nanoparticles, where the surface-to-volume ratio is higher than in larger particles, thus exposing more lanthanide ions on the surface. By coating UCNP with undoped shells with fewer surface defects due to the absence of doping ions, the surface quenching effect can be reduced.[197]

One of the ways to increase the luminescence intensity of UCNP is to coat the core with a shell that can passivate the surface of the UCNP core and protect it. The shell should not allow any energy transfer from inside the host crystal to the surface, i.e., the shell should have fewer quenching sites than the core surface before coating.[69] Undoped shells with a similar host crystal structure can be used to passivate the UCNP surface to reduce surface defects. Chow et al.[195] reported that upconversion emission increased by a factor of 30 upon coating a 1.5 nm $NaYF_4$ shell on an 8 nm NaYF4:Yb, Er core. Similarly, Mai et al. also reported an up to 30 times increase of

the green-to-red upconversion emission ratio ($f_{g/r}$) after coating a $NaYF_4$: Yb, Er core with an undoped $NaYF_4$ shell.[198]

In this chapter, undoped $NaYF_4$ shells were coated onto $NaYF_4$: Yb, Er or $NaYF_4$: Yb, Tm cores with different thicknesses to enhance their emission intensity. Yttrium oleate was heated in a 1-octadecene/oleic acid-mixture with UCNP cores with various molar ratios of UCNP core to yttrium oleate to vary the shell thickness. The amount of UCNP utilized was only approximated, as the calculated molar ratio of the UCNP core was based on the particles total weight, in which the weight of oleate ligand was included.

4.1.4.1 Undoped $NaYF_4$ shell on $NaYF_4$: Yb, Er core

$NaYF_4$: 18 % Yb, 2 % Er core (UC_Er_2) was coated with undoped $NaYF_4$ shells having different thicknesses. The core had a diameter of 23±2 nm and a predominantly hexagonal crystal phase (see Figure 4.19.A). Figure 4.19.B shows a TEM image of sample UC_Er_2 after coating with a 1 nm thick $NaYF_4$ shell. The size of the coated particles was 25±2 nm (UC_Er_2@1; shell thickness = 1.0±1.0 nm), which corresponds to a particle volume increase of 28±12% compared to the core volume. The molar ratio of rare earth ions (Y, Yb, Er) in the UCNP core: yttrium ion in yttrium oleate utilized in the synthesis was in this case 3:1. A 3 nm shell thickness was reached when the molar ratio utilized in the synthesis was 2:1. The coated particles in this case were 27±2 nm in diameter (UC_Er_2@2; shell thickness = 2.0±1.0 nm), which corresponds to a volume increase of 62±13 %. The percentage of volume increase depends naturally on the original size of the UCNP core; the smaller the core under the same mass of particles, the thinner the shell would be, as more core particles are available. Theoretically at 3:1 molar ratio the shell thickness would be 1.13 nm, whereas at 1:1 molar ratio the shell thickness would be 1.6 nm. Within the accuracy of STEM measurements, the measured shell thickness corresponds well with the calculated thickness, when full conversion of the reactants into $NaYF_4$ shell is assumed.

The growth of shell thickness of 1-2 nm as in case of the samples UC_Er_2@1 and UC_Er_2@2 could not, however, be determined solely from electron microscopy measurements, as the STEM used for the measurements only has a maximum optical resolution of 1.5 nm. With high-resolution TEM (HR-TEM) a resolution of < 0.1 nm is possible, but the real accuracy of the shell thickness, which is calculated by subtraction of the core and core-shell total diameter is limited by the polydispersity of the particles. One way to determine if a closed shell was really grown onto UCNP core is by XRD measurements. Along with the increase of shell thickness, the cubic phase peaks

for example at 28° for [111] reflex and at 47° for [220] reflex (ICDD no. 06-0342) of the nanocrystals decreased, as shown by the XRD diffractograms (see Figure 4.20; for the reflexes of the hexagonal phase see previous XRD diffractograms). This indicates that along with increasing shell thickness, the volume ratio between shell to core increased. Since the shell has mainly a hexagonal structure, the ratio of hexagonal phase peaks to cubic phase peaks increases along with increasing shell thickness. The hexagonal peaks belong to the shell and the core, while the cubic peaks originate only from the core.

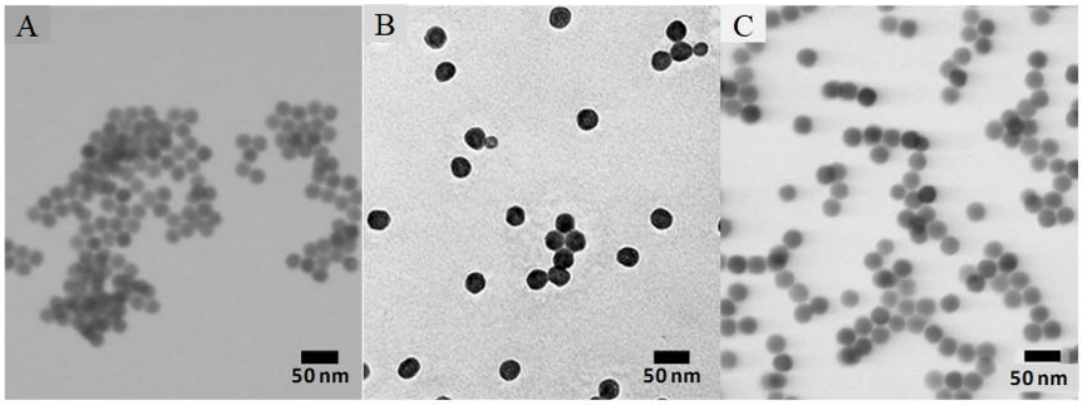

Figure 4.19 A: STEM image of $NaYF_4$: Yb, Er cores (UC_Er_2), B: TEM image of sample UC_Er_2 with 1 nm $NaYF_4$ shell (UC_Er_2@1; average TEM-diameter = 25±1 nm), and C: STEM image of UC_Er_2 with 2 nm $NaYF_4$ shell (UC_Er_2@2; average STEM-diameter = 26±2 nm).

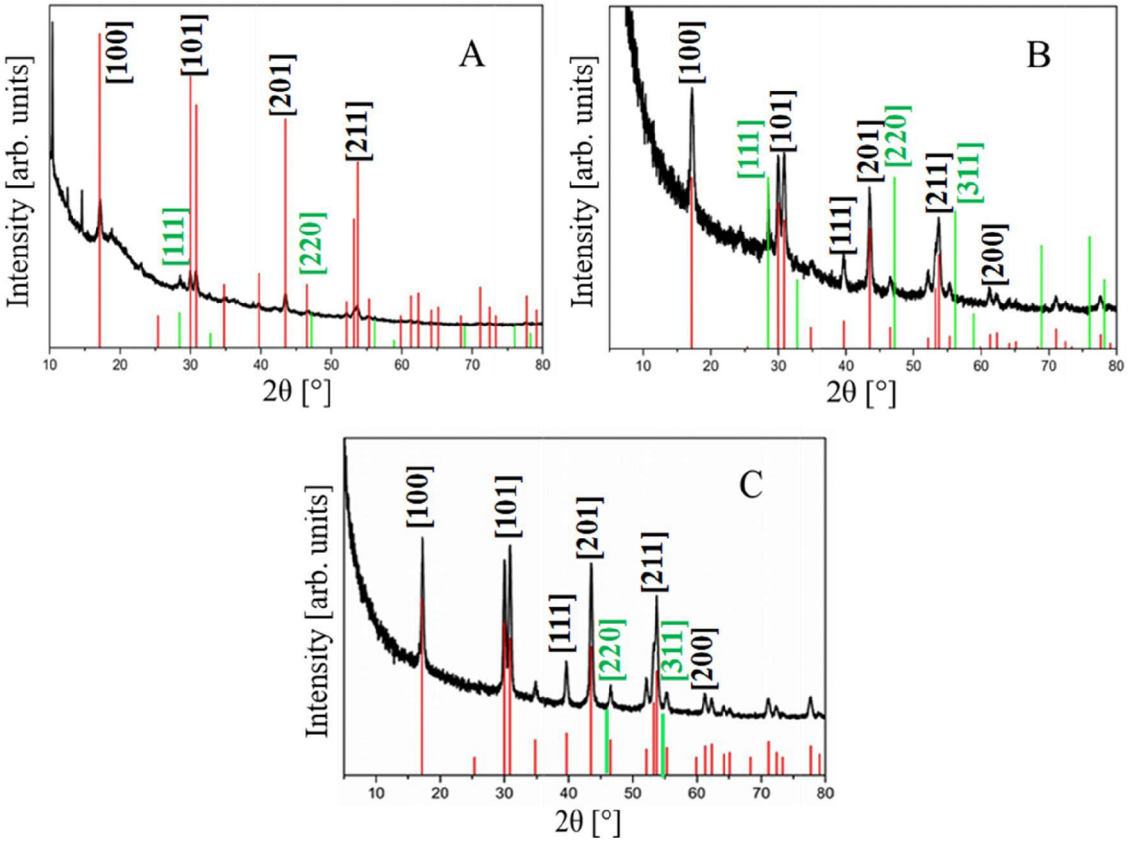

Figure 4.20: XRD diffractograms of A: sample UC_Er_2, B: sample UC_Er_2@1 and C: sample UC_Er_2 @2. Red lines: hexagonal phase (ICDD-28-1192), green lines: cubic phase (ICDD-06-0334).

The extinction spectra of the core and the coated samples were measured and the transition of Yb^{3+} ions at 975 nm ($^2F_{7/2} \rightarrow {}^2F_{5/2}$) was observable in the spectrum of sample UC_Er_2@2. In sample UC_Er_2@1 the same absorption peak could not be observed, likely due to scattering effect and the low concentration of particles measured (see Attachment B). The scattering of the sample UC_Er_2@1 could indicate aggregation of the sample, although TEM images did not show such an effect. The extinction spectrum of sample UC_Er_2 also shows an absorption peak at 960 nm, which belongs to the same transition of ytterbium. This peak was weak in the coated samples.

The emission spectra after 378 nm excitation of the samples were normalized to the amount of erbium for comparison. From ICP-OES measurements the Er^{3+} ions concentrations from the three samples were: 2.2±0.2 % for sample UC_Er_2, 1.8±0.5 % for sample UC_Er_2@1and 1.5±0.5 % for sample UC_Er_2@2. Typical transitions of erbium are present in the fluorescence spectra (see Attachment B). The coated particles show a higher emission than the UCNP core; sample

UC_Er_2@2 has the highest intensity after the baselines were normalized, indicating an effective coating of the $NaYF_4$ shell which reduced surface quenching and increased the fluorescence intensity.

Figure 4.21 shows the upconversion emission spectra of the samples UC_Er_2 and UC_Er_2@2. The spectra were normalized to the ytterbium concentration in each sample. The emission intensity of all peaks is stronger for the coated particles than for the pure UCNP core. The integrated overall emission normalized to the erbium content of the coated UCNP core was 0.45±0.03. In the uncoated core the emission integral was 0.10±0.01, meaning the intensity of the overall upconversion emission increased by a factor of 4.5 after coating. Chow et al.[195] reported an increase of the upconversion emission after coating $NaYF_4$: Yb, Er nanoparticles with ~ 1 nm $NaYF_4$ shell by a factor of 7.4.

As mentioned before, undoped shells can gradually passivate surface defects by a homogeneous shell deposition process and, hence, reduce non-radiative relaxations caused by interactions of surface ions with high energy oscillators such as ligands or solvents.[199] Table 3.2 shows the intensity of the 520 nm ('blue' emission; photon transition: $^2H_{11/2} \rightarrow {}^4I_{15/2}$), 540 nm (green emission; photon transition: $^4S_{3/2} \rightarrow {}^4I_{15/2}$) and 655 nm (red emission; photon transition: $^4I_{9/2} \rightarrow {}^4I_{15/2}$) peaks of both UC_Er_2 and UC_Er_2@2. For each peak, the intensity increased by a factor of 2.3±0.2 for the 540 nm peak and by a factor of 1.9±0.2 for the 654 nm peak in UC_Er_2@2. The ratio of the green to the red emission ($f_{g/r}$) increased from 0.41±0.05 to 0.51±0.05 (see Table 4-2), indicating that surface passivation benefited the green emission more than the red emission. Mai et al.[198] also observed an increase of green emission intensity and $f_{g/r}$ after surface passivation with an undoped shell. The undoped shell decreases the overall non-radiative decay, such as $^2H_{11/2}$,$^4S_{3/2} \rightarrow {}^4F_{9/2}$, which is the transition of the green emission. Hence the radiative green emission transition of $^2H_{11/2}$,$^4S_{3/2} \rightarrow {}^4I_{15/2}$ increased compared to the red emission.

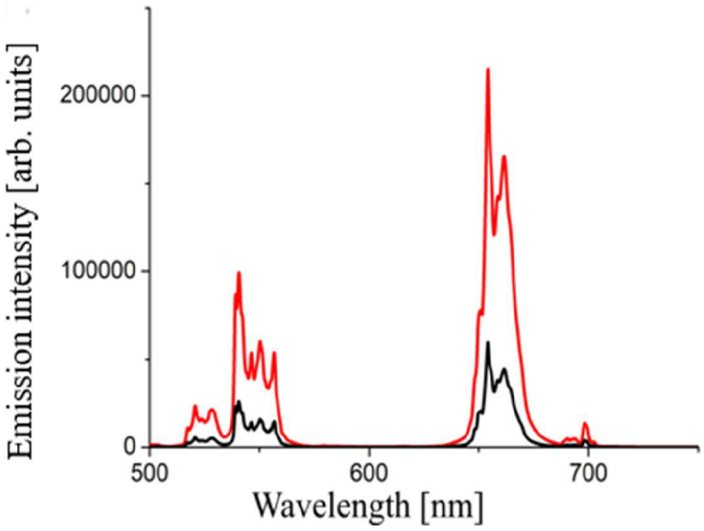

Figure 4.21: Upconversion fluorescence spectrum of $NaYF_4$: Yb, Er nanoparticles (sample UC_Er_2; black-lined spectrum), upconversion spectrum of sample UC_Er_2@2 in hexane after excitation at 980 nm (red-lined spectrum).

Table 4-2: Integrated emission intensities of $NaYF_4$: Yb, Er nanoparticles (UC_Er_2) UC core UC_Er_2@2

Sample	**Blue emission (520 nm)**	**Green emission (540 nm)**	**Red emission (655 nm)**	**$f_{g/r}$**
UC_Er_2	62800±5800	213000±13000	515000±32000	0.41±0.05
UC_Er_2@2	262000±23000	500000±50000	990000±10000	0.51±0.06

4.1.4.2 Undoped $NaYF_4$ shell on $NaYF_4$: Yb, Tm

$NaYF_4$: Yb, Tm nanoparticles (sample UC_Tm_1; d_{TEM} = 31±2 nm; z-average = 67±1 nm, PDI = 0.200±0.050) were coated with undoped $NaYF_4$ shells having two different thicknesses. The core had a Tm^{3+} ion concentration of 1.3±0.1 % and a Yb^{3+} ion concentration of 17.0±0.3 %. From a molar ratio of rare earth ions in the UCNP core : yttrium in yttrium oleate of 2:1 (theoretical shell thickness = 2.3 nm) particles with a total diameter of 41±2 nm were synthesized, while from a molar ratio of 3:1 (theoretical shell thickness = 1.6 nm) particles with a diameter of 34±2 nm were obtained. At molar ratio of 3:1 in, the resulting shell thickness was 2±1 nm (sample UC_Tm_1@2; see Figure 4.22) which corresponded to a volume increase of 32±5 % after coating, while at rare earth ions in the UCNP core : yttrium in yttrium oleate molar ratio of 1:2 the shell thickness was 5±2 nm (sample UC_Tm_1@5) which corresponded to a volume increase of 131±5 %. The 5 nm

shell thickness exceeded the calculated shell thickness value, suggesting a probable weighing error for the core mass prior to synthesis.

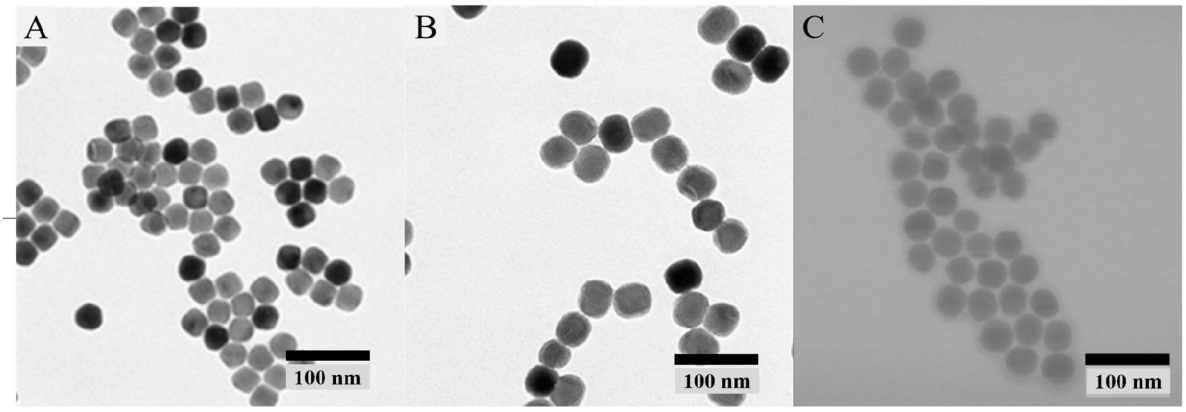

Figure 4.22: TEM images of A: $NaYF_4$: Yb,Tm-UCNP cores (sample UC_Tm_2) and of NaYF4:Yb,Tm-UCNP cores (sample UC_Tm_1) with B: 5 nm $NaYF_4$ shell (UC_Tm_1@5) and C: STEM image of 2 nm $NaYF_4$ shell (UC_Tm_1@2).

XRD diffractograms were taken from all three samples. The crystal phase of the core was a mixture of hexagonal and cubic phase (see Figure 4.23.A). With increasing shell thickness, the cubic phase peaks intensity decreased, and the hexagonal phase became the main phase of the coated particles, as shown in the XRD diffractogram of UC_Tm_1@1 and UC_Tm_1@5 (see Figure 4.23.B and C). This indicates that the coating was successful and suggests that the UCNP core was entirely coated by a 5 nm $NaYF_4$ shell, since along the decrease core-to-shell volume ratio, the hexagonal structure peaks of the shell and the core started to dominate over the cubic phase peaks of the particles. The XRD diffractogram of sample UC_Tm_1@1 still shows some cubic phase peaks, but less than the sample UC_Tm_1 core, indicating a thin shell was formed.

Abel et al. [200] demonstrated that $NaYF_4$@$NaGdF_4$ nanoparticles have a core-shell structure by using X-ray photoelectron spectroscopy (XPS) measurements. Along with increasing photoelectron kinetic energy, the intensity ratio of the Y^{3+} 3d /Gd^{3+} 4d electron shell increases, indicating that a core-shell structure was indeed present instead of the formation of a $Na(Y/Gd)F_4$ alloy. The undoped shell was hexagonal, as there were fewer surface defects that are usually shown by uncoated particles.

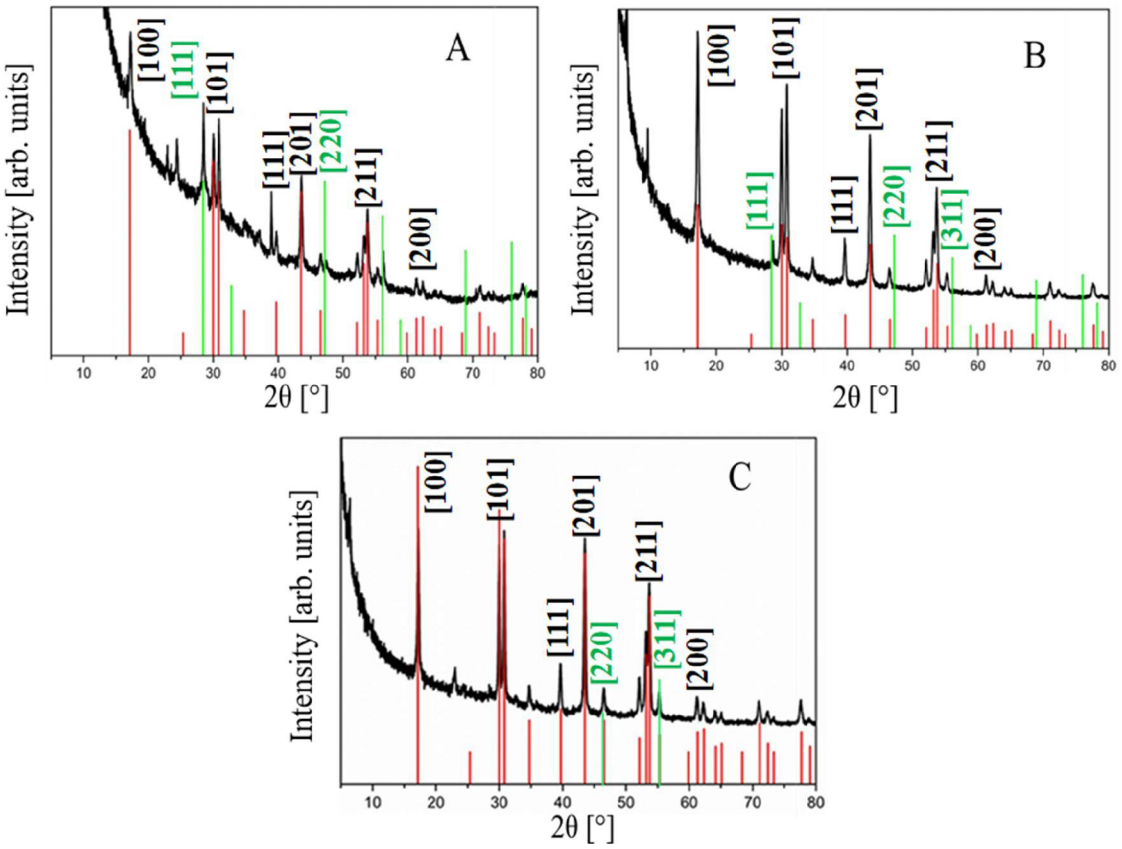

Figure 4.23: XRD diffractograms of A: $NaYF_4$: Yb,Tm-UCNP core (UC_Tm_1) with B: 1 nm $NaYF_4$ shell (UC_Tm_1@1) and C: 5 nm $NaYF_4$ shell (UC_Tm_1@5); red lines = hexagonal phase, green lines = cubic phase. Red lines: hexagonal phase (ICDD-28-1192), green lines: cubic phase (ICDD-06-0334).

The extinction spectra of the UCNP core and the UC core with 1 nm shell (sample UC_Tm_1@1) and 5 nm $NaYF_4$ shell (sample UC_Tm_1@5) show an absorption peak at 960 nm, which belongs to the $^2F_{7/2} \rightarrow {}^2F_{5/2}$ transition of Yb^{3+} ions. The extinction spectra of the samples, however, cannot be directly compared with each other due to scattering effect of sample UC_Tm_1@1 and sample UC_Tm_1@5 (see Attachment C), which were likely caused by slight aggregation of the particles. Upconversion fluorescence spectra of UC_Tm_1, UC_Tm_1@1, and UC_Tm_1@5 (see Figure 4.24) were measured and the integrated emission of each emission peak is listed in Table 4-3. The emission peak at 360 nm corresponds to the transition of $^1D_2 \rightarrow {}^3H_6$, the 450 nm emission peak tothe $^1D_2 \rightarrow {}^3F_4$ transition, and lastly the 803 nm peak to the $^3H_4 \rightarrow {}^3H_6$ transition. The intensity of the upconversion emission peaks corresponds to the downconversion fluorescence spectra from 360 nm excitation (see Figure 4.24), where sample UC_Tm_1@5 shows the highest emission intensity followed by the UCNP core, while the lowest intensity belongs to the emissions of

UC_Tm_1@1. UC_Tm_1@5 shows an emission enhancement of a factor 1.4 at 360 nm, 1.6 at 450 nm, and 1.1 at 803 nm emission.

The enhancement was however minimal compared to the results obtained from the sample UC_Er_2@2. Typically, the distance of interaction between lanthanide ions and surface oscillators lies in the range of 3 nm.[201] A shell thicker than 3 nm would not necessarily lead to further enhancement of the upconversion luminescence, as now the shell has become too thick, and thus hindering the excitation light to the sensitizer ion, or the emission light of the emitter ions to be detected. Although the emission of sample UC_Tm_1@1 was weak compared to the other two samples, the blue-to-red emission ratio increased compared to the UC_Tm_1 core (see Figure 4.24). However, a direct comparison of the emission intensities between UC_Tm_1@2 and UC_Tm_1 could not be observed, due to scattering effects that were already indicated by the extinction spectrum of the coated sample.

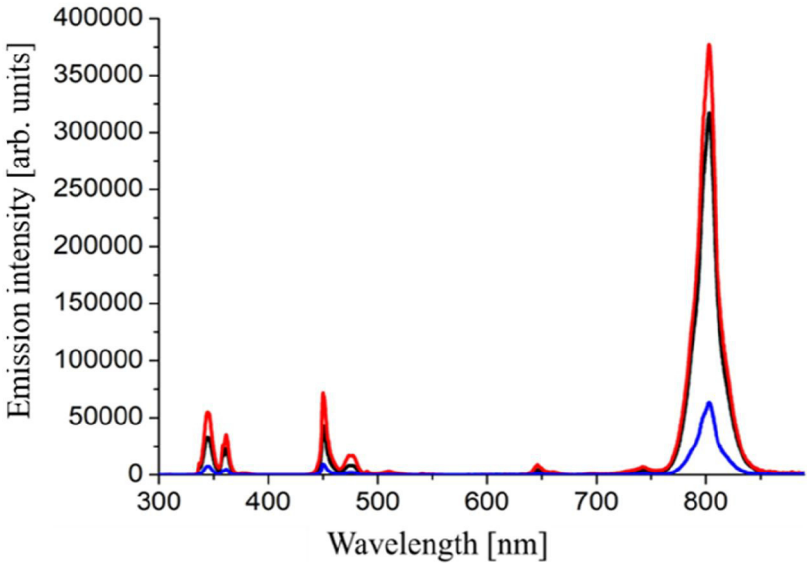

Figure 4.24: Upconversion fluorescence spectra of $NaYF_4$: Yb,Tm-UCNP cores (black lines; sample UC_Tm_1); blue lines: UC_Tm_1@2; red lines: UC_Tm_1@5 in hexane after excitation at 960 nm.

Table 4-3: Integrated emission intensities of $NaYF_4$: Yb, Tm (UC_Tm_1) UCNP core and UCNP core with 1 and 5 nm $NaYF_4$ shell.

Sample	**UV emission (360 nm)**	**Blue emission (450 nm)**	**Red emission (803 nm)**	**$f_{b/r}$**
UC_Tm_1	190000±10000	340000±21000	2500000±160000	0.14±0.02
UC_Tm_1@5	70000±17000	140000±36000	760000±19000	0.19±0.05
UC_Tm_1@1	10000±3000	21000±5000	130000±32000	0.16±0.08

It was shown that coating with an undoped $NaYF_4$ shell could improve the luminescence of UCNP cores. With a shell thickness as thin as 1 nm, the XRD diffractogram of UCNP doped with either Er^{3+} or Tm^{3+} ions indicated an increasing presence of hexagonal phase compared to XRD diffractogram of UCNP without an undoped shell. The thin shell could sufficiently cover the UCNP surface and reduce the quenching effect and non-radiative relaxation process. The shell thickness could be well controlled by adding a controlled amount of yttrium oleate relative to the quantity of UCNP core. Taken together, it can be concluded that the more suitable shell thickness for optimal emission enhancement was 2±1 nm, where a green and red emission enhancement factor of 2.34±0.12 and 1.92±0.10 times for erbium-doped particles were observed. The green and red

emission of the erbium-doped samples and the blue and red emission of the thulium-doped samples (except for UC_Tm_1@2) increased for all coated samples. The $f_{g/r}$ of UC_Tm_1@5 was higher than UC_Tm_1@1 due to better passivation of the core surface which decreases the non-radiative decay, especially the $^2H_{11/2}$, $^4S_{3/2}$ → $^4F_{9/2}$ transitions.[198, 202]

4.2 Characterization of the influence of plasmonic metal clusters and metal shell on upconversion emission

In this chapter, UCNP consisting of $NaYF_4$ nanocrystals doped with Yb^{3+} and Er^{3+} ions were coated consecutively with silica shells and gold nanoshells to investigate plasmon-enhanced upconversion emission. Theoretical calculations were done beforehand to calculate which UCNP core-gold nanoshell-size ratio was suitable for optimal emission enhancement. Thick silica shells were coated onto UCNP core through modified microemulsion and the Stöber method to grow the particles to a certain size before coating them with gold nanoshell of a certain thickness for optimal plasmon enhancement based on the calculated core-shell size (see Figure 4.25).

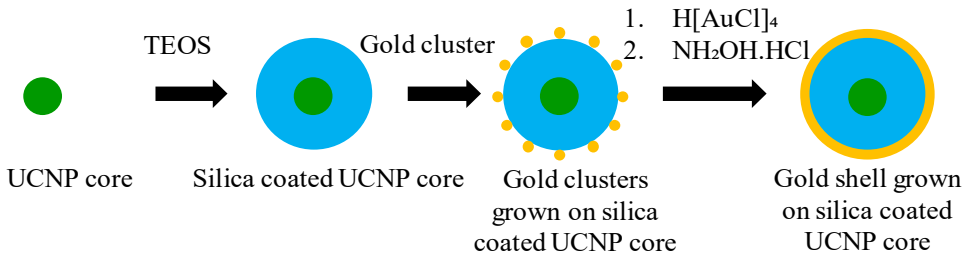

Figure 4.25: General scheme of growing gold shell on silica coated UCNP according to Graf et al.[159] The UCNP core is first coated with a silica shell through a microemulsion-based method and thicker shells are further grown by a modified Stöber method. Gold clusters are then grown onto the silica surface and finally closed gold nanoshell can be grown by reducing $H[AuCl]_4$ with $NH_4OH.HCl$.

Gold nanoclusters were coupled onto surface functionalized silica coated UCNP and gold nanoshells were grown subsequently on these clusters to investigate how plasmonic metal shells can modify upconversion emission characteristics and emission intensity due to changes of local electric field, surface plasmon-coupled emission, or excitation or emission light absorption by the metal shell.[203] Plasmon-enhanced upconversion emission can be achieved through enhancement of the incident excitation flux or the radiative decay rate of the upconversion emission, which depends on the overlap of the surface plasmon resonance energy with the upconversion excitation or emission energy.[27, 38, 203] On the contrary emission quenching can be induced by an increase of the non-radiative decay rate by means of absorbing the emission light from the emitting ions or absorption of the excitation light by the metal shell which leads to thermal quenching.[27, 38, 203]

The gold nanoclusters on silica surface act mainly as seeds, on which closed gold nanoshells could be grown by reducing $HAuCl_4$ with $NH_2OH{\cdot}HCl$ (see Figure 4.26). Small gold clusters with a size of 2-3 nm were synthesized by reduction of aqueous $HAuCl_4$ with NaOH and THPC (see chapter 3.7.1 for synthesis procedure). The coupling of the gold nanoclusters onto the silica surface was done by functionalizing the silica shell coated onto the UCNP surface with amine ligands such as aminopropytriethoxysilane (APS) and subsequently attaching gold clusters to these ligands to create gold-cluster-decorated silica surface. The population density of these gold clusters could be increased by functionalizing the already coupled gold clusters with APS, followed by coupling of further gold clusters onto these APS-functionalized gold clusters. It was presumed that by varying the concentrations of the gold clusters coupled onto the silica surface, one can also influence the homogeneity or smoothness of the gold shell. Thus, the aim of varying the concentrations of these gold nanoclusters on the silica surface coated on the UCNP was originally to evaluate the effect of variable amounts of gold clusters on the homogeneity of the gold shell. The concept of coupling of gold cluster with high deposition density can alternatively be used as a method to model a very thin gold shell (gold shell thickness (t) < 5 nm) and investigate the resulting plasmon-enhanced upconversion emission effect. However, it has to be taken into account that the plasmon resonance of a layer of independently coupled gold clusters differs strongly from the plasmon resonance of a closed gold shell. The general scheme of growing gold nanoclusters onto silica coated upconversion nanoparticles is shown in the following Figure 4.26:

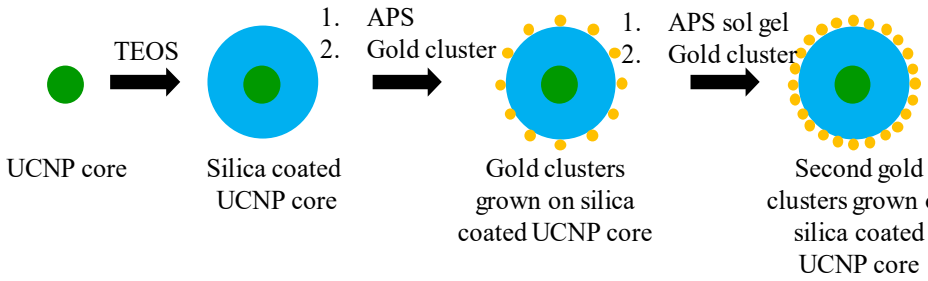

Figure 4.26: Scheme for gold cluster deposition onto the silica-coated UCNP surface for the investigation of the influence of the degree of gold clusters' coverage on the growth of the gold shell. The UCNP core are coated with silica through the reverse microemulsion method and subsequently a modified Stöber method with TEOS as silica source. The silica-coated UCNP are then functionalized with APS before the first deposition of the gold clusters. After functionalization of the gold clusters with an APS sol gel solution, the deposition of a second gold cluster is performed to achieve a higher population of gold clusters on the silica coated UCNP.

Theoretical calculations to determine the optimal size and structure of the UCNP core, silica shell thickness, and gold shell thickness were done for an external excitation at 980 nm. Based on these calculations, the UCNP cores were coated with silica shells with an appropriate thickness followed by coating the particles with closed gold shell using the method of Graf et al.[159]

The calculations and simulations of the optimal geometrical parameters of UCNP core-silica spacer-metal shell, which could deliver the strongest emission enhancements, were done by Meng from the Nanophotonics theory group at the ICFO (Institut de Ciències Fotòniques, Barcelona, Spain). The simulations were based on the Mie theory combined with predictive theory of rate equations (refer to thesis of Meng[204]). The field enhancement from an external (laser) excitation source and the average emission enhancement of point dipoles distributed inside a 20 nm $NaYF_4$: Yb, Er coated with a silica shell acting as a spacer between the UCNP core and a plasmonic metal shell consisting of gold was calculated. Figure 4.27 shows a schematic presentation of the structure of the particle dispersed in water used as a model for the theoretical calculations. The UCNP core diameter is 20 nm, the refractive index of silica is 1.46, and that of $NaYF_4$ is 1.475.[205-206] The refractive index of water as solvent is set at 1.33. Three different size parameters were varied in these calculations: r_1 is the radius of the whole particle (i.e., silica coated UCNP with a gold shell), r_0 is the radius of the UCNP coated with silica (UCNP@SiO_2), and t is the gold shell thickness, which was obtained from the subtraction of r_0 from r_1.

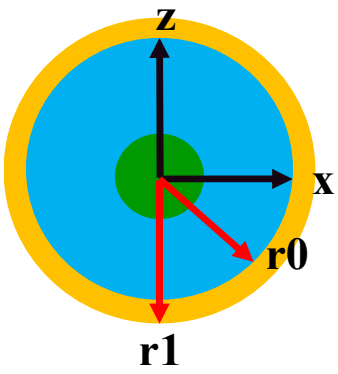

Figure 4.27: Particle model structure for theoretical calculations of the plasmonic field and emission enhancement of gold-coated silica coated UCNP. In this model t is the gold shell thickness, which resulted from subtraction of r_1 (total particle diameter) and r_0 (diameter of silica coated UCNP). The average diameter of the UCNP is 20 nm (particle density = 1.475 g/cm^3), while the pump excitation light is 980 nm. The surface enhancement energy product is depicted in the xz-plane.

Two contributions to the total plasmonic emission enhancement are considered: the first is the field enhancement due to external excitation, i.e., excitation enhancement, while the second contribution is emission enhancement of point dipoles in a core-shell structure.

p is the fraction of the erbium ions in the UCNP core that is excited by the pump laser at a definite time. The change of p within a specific period of excitation can be described with the following equation (4.1) consisting of two terms:

$$\frac{dp}{dt} = [I_0 \cdot FE \cdot \sigma \cdot (1 - p)] - [LDOS \cdot g_0 \cdot p] \qquad (4.1)$$

Where LDOS (local density of states) is commonly defined as density of available states for an emitter to decay or local density of electric field vacuum fluctuations.[207] Here LDOS is defined more accurately as the total decay rate divided by decay rate in free space.[204], g_0 is the intrinsic decay rate of the UCNP core without coating, I_0 is the pump laser intensity, σ is the coefficient proportional to the cross-section of excitation in each ion in the UCNP core, and FE is the field enhancement factor at the pump laser frequency on the position of the UCNP. The first term of the equation contains all factors (I_0, FE, σ and 1-p) important in the excitation process and in the second term are all factors (LDOS, g_0, and p) considered for the emission process.

Under continuous wave (CW) excitation: dp/dt = 0, as there is always the same amount of erbium ions excited at a definite period, so the above equation can be written as (4.2):

$$p = \frac{1}{1 + \frac{LDOS \cdot g_0}{I_0 \cdot FE \cdot \sigma}} \tag{4.2}$$

The emission probability $I_{emission}$ is a product of $LDOS_{rad}$, which is the contribution of radiative emission to the decay rate and p and can be described in the following equation (4.3):

$$I_{emission} \propto \frac{\gamma}{\frac{1}{LDOS} + \frac{g_0}{I_0 \cdot FE \cdot \sigma}} \tag{4.3}$$

Where γ (yield) = $LDOS_{rad}/LDOS$.

There are two restricting conditions following equation (4.3). One is the excitation at pump saturation, i.e., maximum excitation intensity, which leads to the following condition (see equation (4.4)):

$$I_0 \gg \left[\frac{g_0 \cdot LDOS}{FE \cdot \sigma}\right], \text{then} \tag{4.4}$$

$$I_{emission} \propto LDOS_{rad}$$

The other would be excitation at the dimmed pump, which leads to the following condition (see equation (4.5)) :

$$I_0 \ll \left[\frac{g_0 \cdot LDOS}{FE \cdot \sigma}\right] \tag{4.5}$$

$I_{emission}$ can then be rewritten as (4.6):

$$I_{emission} \propto \frac{I_0 \cdot \sigma \cdot \gamma \cdot FE}{g_0} \tag{4.6}$$

where

$$\sigma = \frac{I_0 \cdot \sigma}{g_0} = \text{constant}$$

Then $I_{emission}$ is proportional to the product of γ and FE.

In general, $I_{emission}$ can also be described by the following equation:

$$I_{emission} = \frac{\gamma}{\frac{1}{LDOS} + \frac{1}{FE} \cdot \frac{I_s}{I_0}} \quad (4.7)$$

Where I_s (saturation intensity) is g_0/σ. Calculations based on equation (4.6) under consideration of the particle model (see Figure 4.27) yield contour plots of the product of field enhancement and yield as a function of the shell thickness t and the radius r_0. The product of the field enhancement and the yield is limited to the excitation at dimmed pump intensity, at the limiting case of the excitation at pump saturation the yield is proportional to $LDOS_{rad}$.

The pumping light wavelength considered in these calculations is 980 nm. With increasing r_1 and t values, there are different resonant modes that can be induced, these are (with increasing r_1 and t): dipole mode, quadrupole mode, hexapole mode and cavity mode (see resonance mode excitation in chapter 2.2). The area of the local average field enhancement of each resonance mode is roughly shown in Figure 4.28 below, where the red area describes maximum enhancement, yellow describes middle-strong enhancement, light blue describes weak enhancement and dark blue represents suppressed enhancement or quenching.

From the rough sketch in Figure 4.28, one can see that along with the increase of r_1 and t values, higher order resonance modes are excited. Each resonance mode relates to a certain range of r_1 value with a limited range of gold shell thickness, especially in the multipole modes. Meanwhile the enhancement in the cavity mode is possible for certain range of r_1, where the gold shell thickness can be varied up to $t < 70$ nm, as can be seen in Figure 4.29 and Figure 4.30, and would still result in strong field enhancement. The maximum possible enhancement in the dipole and quadrupole mode is higher than the hexapole and cavity mode.

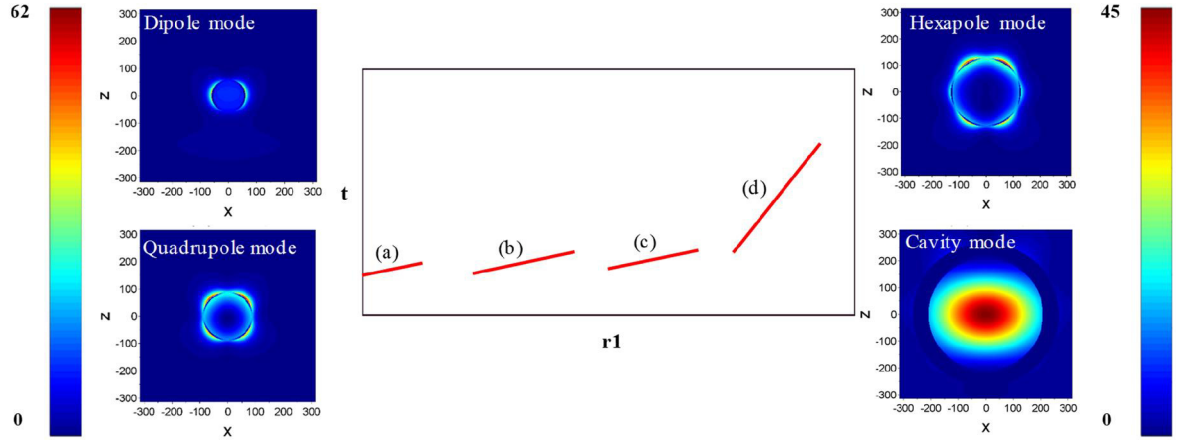

Figure 4.28: Local average field enhancement of each resonance mode: (a) dipole mode, (b) quadrupole mode, (c) hexapole mode and (d) cavity mode. The smaller figures on the left and right side depict the enhancement areas of each resonance modes after 980 nm excitation on xz-plane in the whole dielectric core. T is the gold shell thickness and r_1 is the total radius of particle. The color bar on the left side depicts the enhancement scale of in the dipole and quadrupole mode, whereas the color bar on the right side depicts the enhancement in the hexapole mode and cavity mode. The red area describes maximum enhancement, the yellow area middle-strong enhancement, and the light blue area weak enhancement, while the dark blue area represents suppressed enhancement or quenching.

Figure 4.29 shows a contour plot of the field intensity enhancement after excitation at 980 nm (upper plot) and the product of the field enhancement (FE) and the yield ($LDOS_{rad}/LDOS$) which is the total enhancement of the emission in case of a low excitation density, i. e. a strongly dimmed pump laser (bottom plot; see equation (4.5)). The bar on the right side of each plot represents the enhancement factor depicted by the colours in the plots. As an example, the dark blue colour in the bottom plot (FE × yield) represents suppressed enhancement or quenching, whereas the red colour represents the highest enhancement with a maximum enhancement factor of 110. Based on the contour plots high emission enhancement after 980 nm excitation can be achieved, when the core size is in the range of $r_0 < 60$ nm and $t < 10$ nm for dipole mode enhancement, or 240 nm $< r_0 <$ 260 nm with 20 nm $< t <$ 60 nm for enhancement in the cavity mode. The FE × yield region of 80 nm $< r_0 <$240 nm delivers only minimal enhancement in any resonance mode.

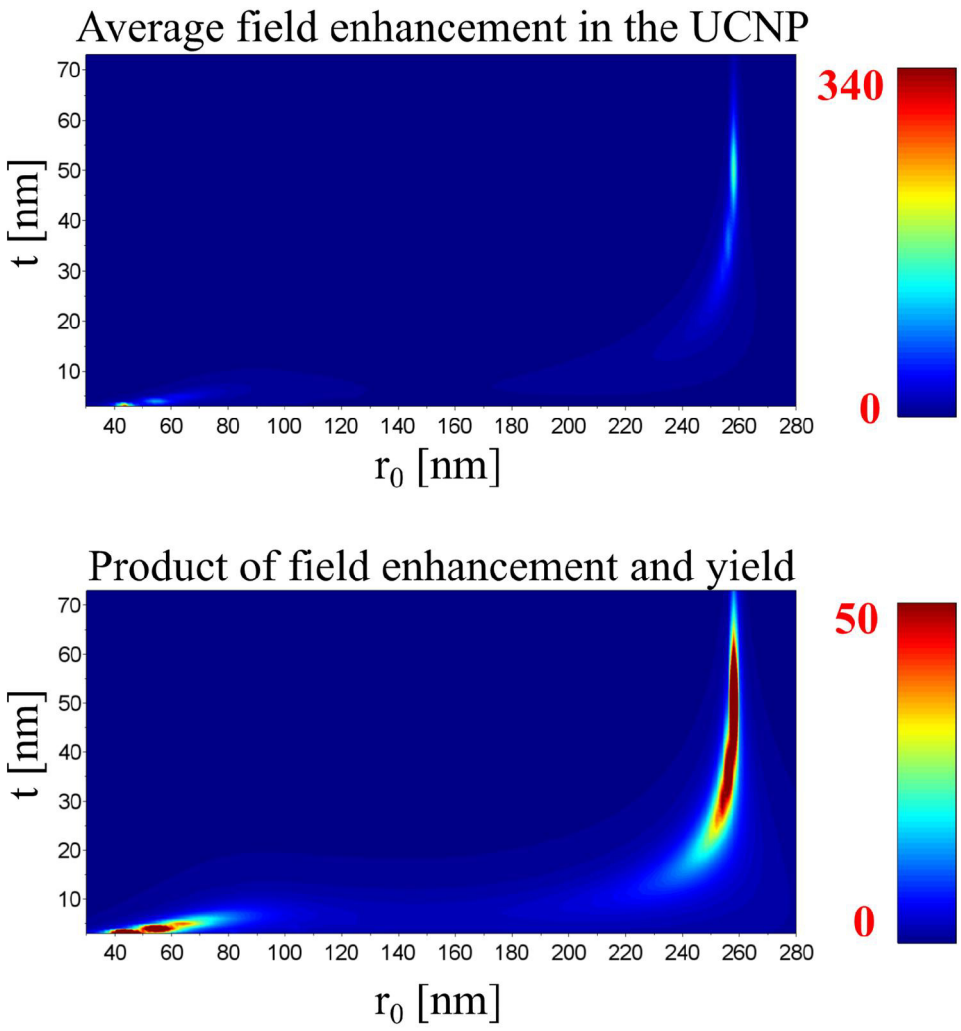

Figure 4.29: Top contour plot: average field enhancement in the UCNP and bottom contour plot: product of yield enhancement (FE) and yield at 980 nm excitation. The right color bars represent the enhancement factor of the depicted colours in the plots.

Figure 4.30 shows the LDOS (top plots), $LDOS_{rad}$ (middle plots) and yield enhancements from $LDOS_{rad}$/LDOS of UCNP (bottom plot) at 540 and 654 nm emission. As was mentioned before, when the UCNP are excited by a maximum pump intensity, i.e., pump saturation, then the $I_{emission}$ enhancement is proportional to $LDOS_{rad}$, as the emission intensity becomes linear with the pump power.[208] This means a maximum emission intensity enhancement (up to 7 times enhancement) at pump saturation could be achieved if the (silica coated) UCNP for example have an $r_0 < 40$ nm and t = 10-30 nm for 540 nm emission according to the $LDOS_{rad}$ plot, whereas for 654 nm emission the maximum enhancement at pump saturation excitation would be achieved if the structural

parameters are $r_0 < 40$ nm and $t \sim 10$ nm (see Figure 4.30.B and E). The $LDOS_{rad}$ enhancement at the 654 nm emission could achieve a maximum factor of 75, whereas at the 540 nm emission the maximum enhancement factor is only 7. The LDOS enhancement at the 654 nm emission could achieve a maximum factor of 140, while for the 540 nm emission a maximum enhancement factor of only 20 could be reached. Hence, although significant enhancement for the green 540 nm emission could be reached for a wider range of size parameters of the core-shell particles ratio than in case of the red emission, the maximum possible red emission enhancement factor is much higher. The maximum yield (see Figure 4.30.C and F) for the 654 nm emission covers a wider area: up to $t < 35$ nm at $r_0 > 40$ nm, whereas for the 540 nm emission the maximum yield is achieved when $t < 20$ nm.

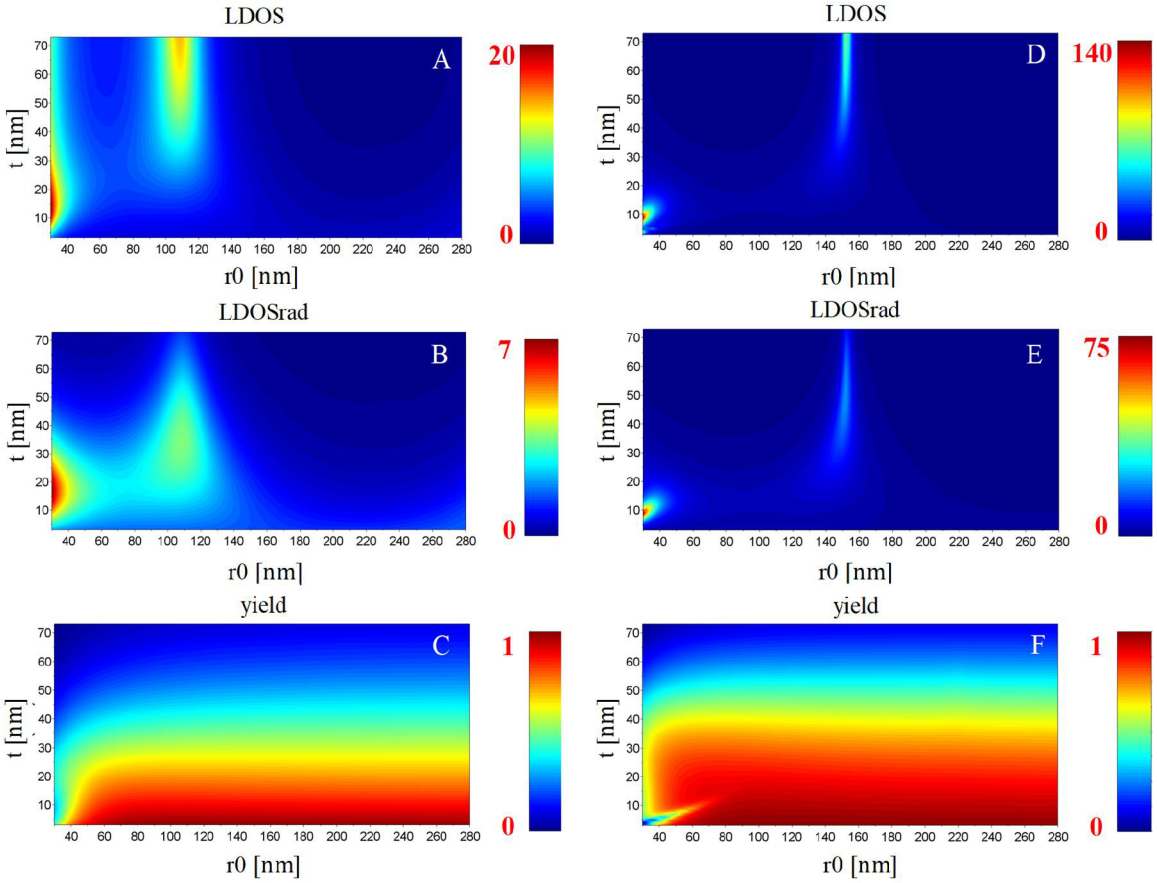

Figure 4.30 Top plots A: and D: LDOS, middle plots B and E: $LDOS_{rad}$ and bottom plots C and F: yield = LDOSrad/LDOS at 540 nm (left row) and 654 nm (right row) emissions. The color bars on the right side of each contour plots represent the enhancement factor or yield of the depicted colors in the plots.

Figure 4.31 shows plots FE x product yield at the 540 nm and the 654 nm emission after excitation at 980 nm with a dimmed pump. Enhancement is possible in the dipole mode and in the cavity mode for both emissions. The regions of significant enhancement are at $r_0 < 80$ nm and $t < 10$ nm for the dipole mode and at $r_0 = 240$-260 nm and $t = 10$-60 nm for the cavity mode enhancement. The emission enhancement is stronger at the 654 nm emission than at 540 nm emission, e.g. for $r_0 = 252$ nm, $t = 35$ nm (the structure is marked by an arrow in Figure 4.32). The emission enhancement factor at the 540 nm emission is 11, whereas at the 654 nm emission the enhancement factor for the same particle size structure is 15. Since the preparation of UCNP coated with thick silica of $240 < r_0 < 260$ nm thickness with a thick gold shell ($t = 20$-60 nm) is experimentally more feasible than the synthesis of much smaller cores with thin gold shell, this work will focus more on the synthesis of core-shell structure for the cavity mode enhancements of the particles.

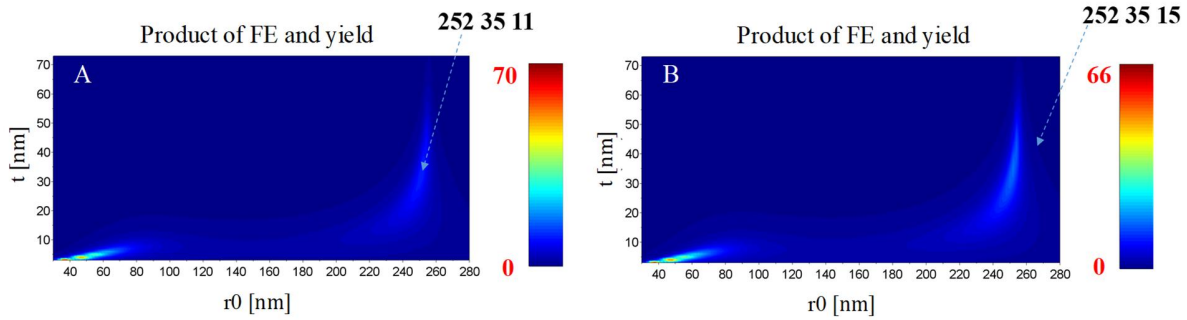

Figure 4.31 Product of FE × yield (enhancement factor) at A: 540 nm and B: 654 nm emission after 980 nm excitation. The arrows point to an example structure of $r_0 = 252$ nm, $t = 25$ nm which delivers an enhancement factor of 11 for the 540 nm emission and 15 for the 654 nm emission. The color bars on the right side of each contour plots represent the FE × yield enhancement factor of the depicted colours in the plots quantitatively.

4.2.1 Coating of upconversion nanoparticles with silica nanoshells

Coating of nanoparticles with silica nanoshell has become one of the most versatile ways to protect the surface of nanoparticles. Silica shells are also suitable as an anchor for biofunctionalization with for example DNA, bioligands or polymers.[51] Silica has many advantages: it is chemically inert, has low bio- and cytotoxicity and is transparent. By coating with a silica shells UCNP can be used safely in various bioapplications such as in bioimaging, photodynamic therapy, radiotherapy, and NIR medicine.[209-210]

In this work, coating UCNP with silica of different thicknesses served several purposes; the first one was to provide a suitable distance between the UCNP core and the gold shell with certain

thickness for plasmon-enhanced upconversion emission enhancement. This required a thick silica shell on small-sized UCNP (d = 20 nm) synthesized from a combination of the stepwise microemulsion and a modified Stöber method. The purpose of thick silica coating is to expand the size of silica coated UCNP to 240-260 nm radius for cavity mode enhancement. Alternatively, thin silica shell can be coated onto 20-nm sized UCNP core to reach a maximum radius of 80 nm for dipole mode enhancement.

Furthermore, thin silica shells synthesized by the microemulsion coating method were coupled with the dye RBITC for luminescence energy transfer or Förster resonance energy transfer measurements (FRET; see chapter 4.3). A major precondition was that the silica shell coupled with the dye should not be too thick. Ideally the donor-acceptor (UCNP-dye) distance should not be larger than the Förster's distance. Typically, the distance between the dye and the emitting Er^{3+} ions should be less than or at least in the range of the Förster distance, which is mostly between the 1.0-5.5 nm range.[107, 211] Hence only a one step-silica coating was employed to synthesize thin shell less than 10 nm.

Conversion of the initially hydrophobic UCNP core into hydrophilic systems through thin silica coating enables their applications in biological systems and for cytotoxicity investigations (see chapter 4.4). Depending on the silica shell thickness, the release of toxic fluoride or lanthanide ions into the cells' environment from the UCNP can be prevented.[212]

Nanoparticles with a host lattice consisting of oleate functionalized $NaYF_4$ with 18 % Yb^{3+} and 2 % Er^{3+} ions in different batches were coated with silica shells with an adjustable thickness between 7±1 nm and 150±10 nm through a combination method comprising of a stepwise coating process in a reverse microemulsion for thin shell silica coating, followed by a Stöber-like method to further grow the particles to diameters in the range of hundreds of nanometer. The lanthanide ion dopant concentrations were determined by ICP-OES. The size of the silica-coated UCNP, their hydrodynamic diameter, and their surface charge was measured by STEM imaging, DLS, and zeta-potential measurements, respectively. The UC-emissions were measured using a 980 nm laser diode with a power excitation density of 2 W/cm^2.

Coating of UCNP with silica served the main purpose of increasing the size of the UCNP-contained nanoparticles to a suitable size for growing gold nanoshells for a plasmon-enhanced upconversion emission. Based on theoretical calculations introduced at the beginning of chapter 4.2, an emission enhancement of the green and red emissions in the limiting case of a dimmed pump excitation is either possible in the dipole mode or in the cavity mode. Enhancement of the green and red

emission is expected for 20-nm sized UCNP with either very thin silica shells for dipole mode enhancement or with thicker silica shells and thick gold shells enhancement in the cavity mode (for the exact values of suitable UCNP core-silica shell size (r_0) and gold shell thickness (t) refer to chapter 4.2). In this chapter and the following ones the main focus is in coating UCNP core with thick silica shells and subsequently gold shell with a thickness $t < 60$ nm, since the method for coating thick gold shell on large particles ($d > 200$ nm) is already well-established. As was mentioned before (see the introduction to chapter 4.2), the coating of the core will focus initially more on synthesizing thick silica shells to reach an average size of silica-coated UCNP of at least 120 nm for later coating with gold shells with $t < 10$ nm for dipole mode enhancement. However, based on earlier experiments, it was challenging to grow closed gold nanoshells thinner than 20-25 nm. Additionally, core particles smaller than 100 nm are also more difficult to coat compared to bigger particles. Therefore, the cores could alternatively be coated with thicker silica shells to reach a total diameter of the silica-coated UCNP of 460-520 nm for later gold coating with 10-60 nm thickness for cavity mode enhancements under dimmed pump excitation.

Ideally, the silica coating method applied on any hydrophobic nanoparticles should produce silica coated nanoparticles that are monodisperse and free of core-less silica particles. Until recently most publications reported the reverse microemulsion method as the only method used to coat hydrophobic nanoparticles, for example, oleate coated iron-oxide particles or quantum dots particles could be coated with silica shells up to certain thickness (mostly below 40 nm).[90, 213-215] Even then core-less silica particles could still emerge as side products. One way to control the thickness of silica shell while maintaining high monodispersity is the employment of stepwise-coating of silica. Although this technique is known and well-established for the Stöber-like growth processes, which are done in a hydrophilic environment for hydrophilic or water-dispersible nanoparticles, such stepwise-growth approaches are almost not known for the reverse microemulsion method, at least for growing silica shell thicker than 40 nm.[216] Mostly in a reverse (water-in-oil) microemulsion synthesis, the addition of TEOS as the silica precursor is done in one step.[92, 215-217] In the next chapter a stepwise reverse microemulsion method to coat thick silica shells on hydrophobic particles was developed. Afterward silica shell synthesized from microemulsion method could be further grown by employing a modified Stöber method.

4.2.1.1 **Growing thin silica shells with reverse microemulsion**

Oleate-functionalized UCNP with a $NaYF_4$ host structure were doped with 18% Yb and 2% Er by the thermal decomposition method with lanthanide oleate precursors as reactants (see chapter 3.5.3 for the synthesis procedure).[156] The particles were dispersed and stored in cyclohexane. Spherical UCNP cores with average diameters of 24±1 nm and 24±2 nm (sample UC_Er_3 and UC_Er_4 correspondingly) are shown in Figure 4.33.A and Figure 4.37.A.

Thin silica shells were then grown onto the UCNP cores through a reverse microemulsion method. The reverse microemulsion method is a simple method for coating silica on (mostly) hydrophobic particles, where the silica growth occurs in the water phase inside micelles formed by surfactant molecules with a hydrophilic head and hydrophobic long-chained carbon tail. The medium of the continuous phase is a non-polar solvent such as hexane or cyclohexane. In the reverse microemulsion synthesis, the numbers of micelles and the UCNP cores should match to prevent the formation of core-free silica particles or particles with multiple cores.[90] The size and number of the aqueous domains are determined by the ratio of ammonia to Igepal CO-520 (R-value).[85, 90, 217-218] The higher an R-value is, the bigger is the micelle size, and the number of micelles would be lower. Furthermore, under low ammonia water concentration, the aqueous domain in the micelles will remain small to control the hydrolysis rate of TEOS. A slow TEOS hydrolysis rate will promote thin silica first shell without any risk of secondary nucleation, since monomer formation from TEOS is controlled. For UCNP with 24 nm diameter with a particle concentration of 3 g/L, an ammonia water-to-surfactant weight ratio of 1:9.5 or a molar ratio of 1:2.7 and an ammonia water concentration of 1.7±0.5 wt% in cyclohexane lead to the nearly non-existant core-free particles (< 1%).

A general mechanism scheme for the growth of the first silica layer on the UCNP in a reverse microemulsion process is shown in Figure 4.32. Ding et al.[90] and Zhang et al.[219] coated oleate-functionalized paramagnetic iron oxide nanoparticles with a single step reverse microemulsion method, and both observed that the ligand exchange between the oleate ligands on the UCNP and the surfactant Igepal CO-520 occurs upon addition of the oleate-functionalized nanoparticles to the Igepal-cyclohexane-system.[90, 219] As the condition of their microemulsion synthesis regarding the oleate functionalized core and the type of surfactant was similar to the one in this work, it can be assume that the same ligand exchange process also occurs between oleate-functionalized UCNP and Igepal.

The R-value for silica growth on UCNP core with a size of 24 nm was estimated, since the R-value determines the size and number of micelles in the microemulsion. Ding et al.[90] employed an R-value of 1:2.7 for their 12.2 nm iron oxide particles, while Katagiri et al.[213] employed an R-value of 1:6.1 to coat 10 nm iron oxide particles. The particle number concentration per volume of cyclohexane was 9×10^{17} in this present work, $2.3\text{-}3.6 \times 10^{17}$ and 5.5×10^{17} in the works of Ding et al. and Katagiri et al. respectively, i.e. 3-4 times and 1.6 times lower than in this work. Hence, the R-value was chosen to be much smaller to get higher surfactant concentration and subsequently larger micelles to accommodate the larger volume and higher amounts of UCNP particles. Therefore, for the first shell silica growth a higher amount of surfactant and consequently a lower R-value of 1:9.5 was used. With this significantly lower ratio of surfactant to particle surface (1.6 mol/m² in the present case, 9.5 mol/m² and 5.2 mol/m² in the cases of Ding et al. and Katagiri et al. respectively) no silica particles with multiple UCNP cores were formed, which meant that the number of micelles was not lower than the number of particles.

For further shell growth, it was possible to slightly lower the Igepal concentration in cyclohexane (from 16 wt% for the first to 14 wt% for the further shell growth) and increase the ammonia concentration (from 1.7 wt% for the first and to 3.3 wt% for further shell growth), which increased the R-value from 1:9.5 to 1:4.3. In this way, the number of micelles was kept constant while their size was increased to adapt them to the growing size of silica-coated UCNP while maintaining the micelle number to match the number of UCNP cores. The adjustment of the R-value could keep the small aqueous domain small to prevent the formation of core-less silica particles as side-products while still enabling a complete hydrolysis of TEOS to produce maximum growth of the silica layer in a single step. If the number of UCNP cores and micelles does not match, either due to insufficient R-value (high surfactant concentration) or an overly high R-value (high water concentration), the formation of core-less silica would be certain.

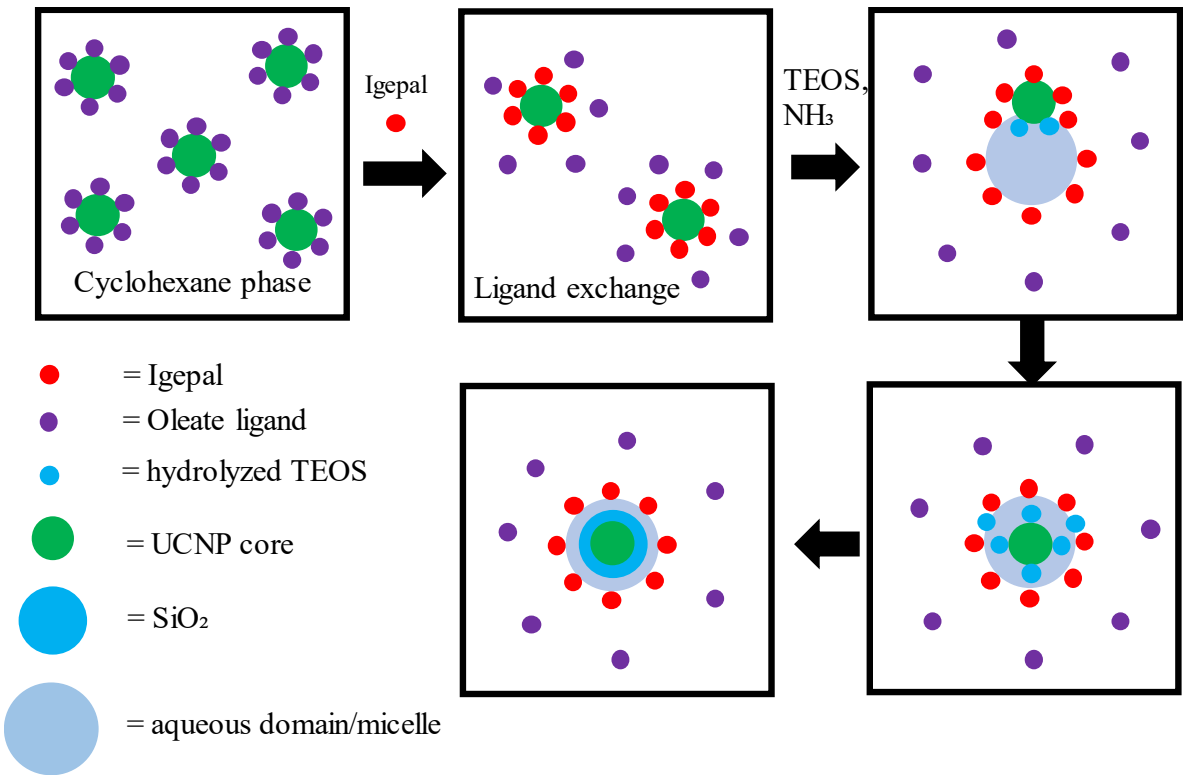

Figure 4.32: General scheme of the reverse microemulsion synthesis for the first coating of thin silica shells on oleate-functionalized UCNP core. A ligand exchange occurs upon addition of the surfactant Igepal CO-520 in the UCNP dispersion. After addition of TEOS and ammonia water hydrolysis of TEOS at the interface between the oil (cyclohexane) and the water phase follows. Then a second ligand exchange between hydrolyzed TEOS (silica monomers) and Igepal takes place, which transfers the UCNP into the micelles, where further condensation reaction of the silica monomer occurs, leading to the formation of the final silica shell.

As a preliminary experiment, a thin silica layer was grown onto the UC_Er_3 particles via a reverse microemulsion process in cyclohexane with Igepal CO-520 as surfactant and ammonia as a catalyst. After coating, the size grew to 42±2 nm (sample UC_Er_3@SiO_2_42), the silica shell thickness (r_{SiO2}) was 9±1 nm. The z-average of the cores was 48±2 nm (PDI = 0.300±0.100), and that of the silica-coated ones was 89±2 nm (PDI = 0.150±0.050). The high z-average and PDI of the sample indicated either aggregation or particles that were grown together after silica coating. The STEM image in Figure 4.33.B shows that some particles were indeed grown together.

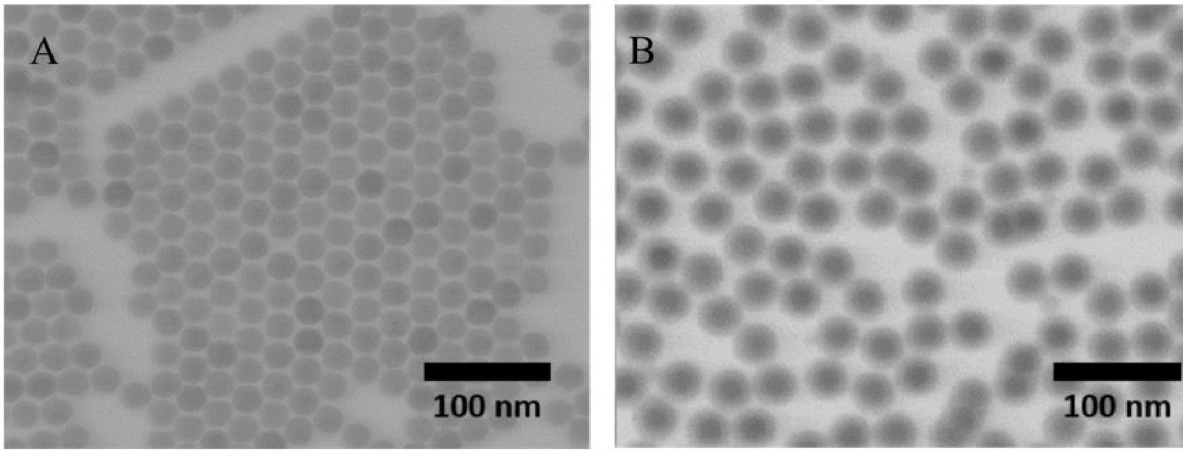

Figure 4.33: STEM images of A: $NaYF_4$: Yb, Er cores 112(UC_Er_3; d = 24±1 nm) and B: $NaYF_4$: Yb, Er cores after coating with silica (UC_Er_3 @SiO2_42, r SiO_2 = 9±1 nm).

The optimal condition for the growth of silica shell on hydrophobic nanoparticles and possible formation of core-less silica particles can be explained qualitatively according to the La Mer theory.[90] Based on the La Mer theory about the formation of monodisperse colloidal particles, the process of nanoparticle formation usually involves three stages. In the first phase, the concentration of the monomer precursor (in this case hydrolyzed TEOS) increases along with the hydrolysis to a certain concentration where heterogeneous nucleation starts (after the monomers reach a certain concentration (C_{hetero})). In phase II the monomer concentration ($C_{monomer}$) further increases until it surpasses the critical concentration (C_{homo}), where many nuclei are spontaneously created at once, and the monomers are further hydrolyzed to form silica shells on UCNP core or core-free silica particles. In the third stage, the formed silica shell or new nuclei are further grown to thicker shell or larger core-free particles. Hence to prevent the formation of core-free silica, the monomer concentration should be kept between C_{homo} and C_{hetero} (see Figure 4.34). According to Ding et al. the LaMer theory can also be applied for explaining silica coating on oleate-functionalized iron oxide nanoparticles at least for the growth of the first shell.[90, 220]

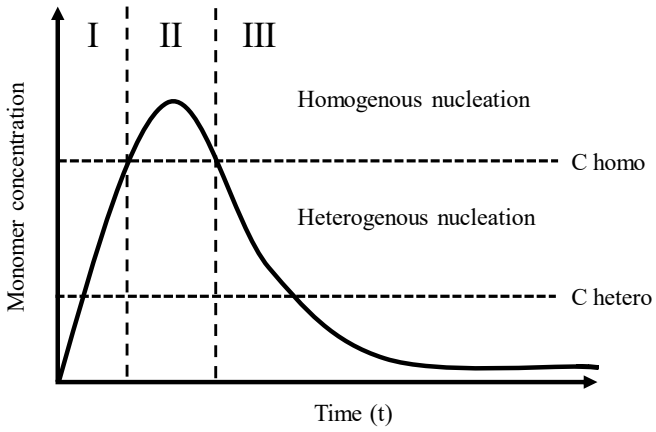

Figure 4.34: Different stages of particle formation according to a La Mer like theory: UCNP and silica particles co-exist when the monomer concentration ($C_{monomer}$) > C $_{homo}$; UCNP@SiO2 exist when C_{hetero}<C<C_{homo}. Phase I is the monomer growth stage, phase II is the nucleation stage and phase III is the particle growth stage.[90]

A direct Stöber coating after the growth of the first shell led to particles growing together as well as to the formation of core-less silica particles as side product (see Attachment D). As an example, a UCNP core consisting of $NaYF_4$: Yb, Er was coated by an initial first silica shell by the reverse microemulsion method. The thickness of the first shell was 11±1 nm. The silica-coated UCNP from the first step microemulsion method was cleaned through centrifugation, redispersed in ethanol, followed by the addition of TEOS and ammonia in a Stöber-like growth process.

The zeta potential of the particles after the first thin silica coating by reverse microemulsion was only around -20 mV, which indicates the low colloidal stability of these particles. Low colloidal stability was also reported for nanoparticles coated with silica in a reverse microemulsion in several publications.[89, 221-223] This could be related to the presence of excess Igepal as a surfactant on the nanoparticle surface.[89, 212] As explained before upon hydrolysis of TEOS, a second ligand exchange between hydrolyzed TEOS and Igepal occurs. Once the particles were taken out of the microemulsion, the possibility of them to aggregate was higher as they were now separated from the stabilizing surfactant. Extensive cleaning of the particles after growth of the first silica shell by repeated centrifugation and redispersion in ethanol did not significantly alter the zeta potential, which also indicated that the surfactant could not be completely removed. Removal of more surfactant molecules could also increase necking effect between the silica surface, which would increase aggregation.[89] Low colloidal stability was also confirmed by the high z-average of the particles (sample: UC_Er_4@SiO_2_38; see Table 4-4), which would explain why a direct Stöber

coating after the first microemulsion shell resulted in secondary nucleation and particles that grew together.

For the second and further silica shell growth, the reverse microemulsion approach was employed, until the particles had sufficient colloidal stability for the next large growth step of the silica shell using the Stöber method. The following method was developed from a concept of Ding et al. for coating silica on iron oxide NP.[90] According to the authors, a low R-value produces thin silica shells without side-products, as the aqueous domain will remain small, and a low ammonia concentration leads to a slow hydrolysis rate and thus thin silica shell without secondary nucleation (see Figure 4.35 Path A).[85] Moreover, by rapidly increasing the amount of ammonia water concentration, for a constant surfactant concentration (corresponding to increasing R-value), the aqueous domain and the hydrolysis rate increase, leading to thicker silica shells and the formation of new micelles, causing the formation of core-less silica particles (see Figure 4.35 Path B).[90]

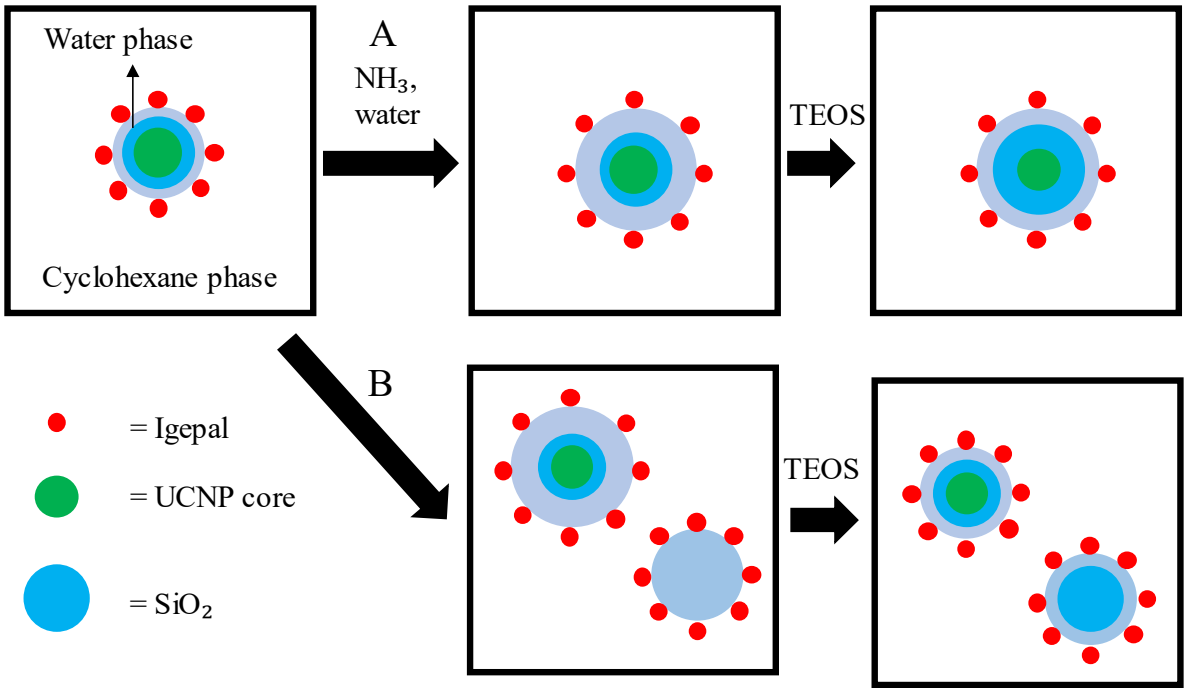

Figure 4.35: Scheme of the reverse microemulsion synthesis for growing thicker silica shells after the first silica coating on UCNP. Path A describes the controlled growth of the silica shell, while path B depicts the formation of core-free silica particles due to an increased TEOS hydrolysis rate and an increasing ammonia water-to-surfactant (R) ratio caused by ammonia water addition during further silica shell growth steps.

An example was a silica coating on UC_Er_4, where the R-value for a four-step reverse microemulsion synthesis was 1:2.2 instead of 1:4.3 after the first silica layer which led to the formation of many core-less silica particles. The size of the silica-coated UCNP was 107±6 nm, and the core-less particles had an average diameter of 60±15 nm (see Figure 4.36).

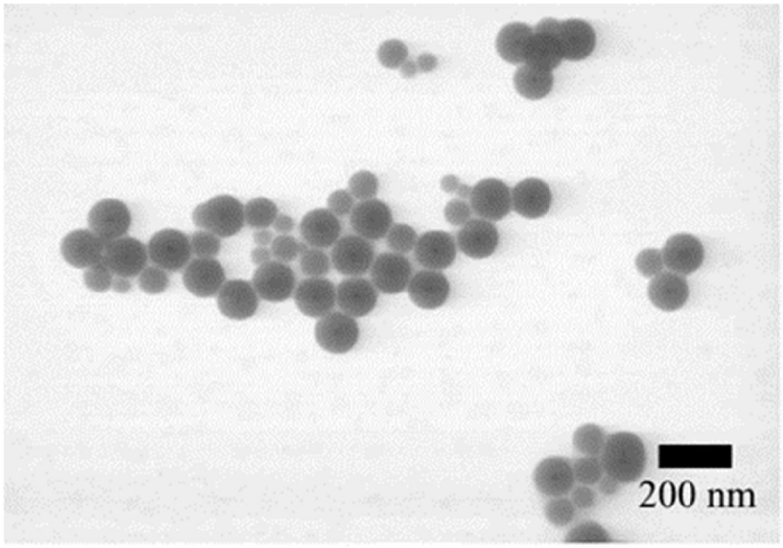

Figure 4.36: STEM image of UCNP (core: UC_Er_4, d = 24±2 nm) which were coated in a four-step silica shell process in a reverse microemulsion process with an R-value or 1:2.2, which led to formation of core-free silica particles due to a too high ammonia water concentration, which accelerated the hydrolysis rate of TEOS.

For the calculation of the TEOS amount needed for the silica growth, equation (4.8) was utilized. In the stepwise synthesis of the silica shell where the microemulsion process was not broken between each growth step, the amount of TEOS needed to be added for the next step was equal to the total volume of TEOS needed for the intended total shell thickness in the last coating step minus the amount of TEOS already given in the previous step(s). As an example, the TEOS amount (V_{TEOS}) needed for the second silica shell (t_1+t_2) was calculated such that the whole TEOS amount needed for this shell thickness was subtracted by the amount of TEOS already utilized in the growth of the first shell (t_1).

$$V_{TEOS} = \left(\frac{\left(\frac{d_{UCNP}}{2} + t_1 + t_2 \right)^3 - \left(\frac{d_{UCNP}}{2} + t_1 \right)^3}{\left(\frac{d_{UCNP}}{2} \right)^3} \right) \cdot \frac{\rho_{SiO_2}}{\rho_{UCNP}} \cdot m_{UCNP} \cdot \frac{M_{TEOS}}{M_{SiO_2} \cdot \rho_{TEOS}} \tag{4.8}$$

where t_1 is the thickness of the first silica shell, ρ_{SiO2} is the density of colloidal silica (2 g/cm³), ρ_{UCNP} is the density of the UCNP cores (4.21 g/cm³), M_{TEOS} is the molar mass of TEOS (208.32 g/mol), M_{SiO2} is the molar mass of SiO_2 (60.08 g/mol) and ρ_{TEOS} is the density of TEOS (0.94 g/cm³). The added volume of ammonia was set to be the same as the added volume of TEOS in each step. The added volume of cyclohexane was calculated in each growth step so that the ammonia concentration in cyclohexane was 3.3±0.1 wt%. Lastly, the concentration of Igepal was kept constant at 14±1 wt% in cyclohexane throughout all growth steps, resulting in an R-value for the further shell growth of 1:4.3 in weight ratio or 1:6.0 in molar ratio. The R-value was increased to 1:4.3 in the second and further shell coating from 1:9.5 in the first shell coating to keep the water domain large enough for increasing the size of the particles while maintaining a constant number of micelles relative to the number of particles. The Igepal concentration was kept constant to keep the aqeous domain in the micelle size large enough to contain the growing particles while preventing the formation of new micelles. High Igepal concentration, however, can lead to the formation of new micelles and eventually formation of core-free silica particles.

Ding et al. used a slightly lower concentration of ammonia water (1 wt% compared to 1.7±0.5 wt% in this work) and a lower surfactant concentration (5.6 wt% compared to 14 wt% in this work) for the growth of the a single shell, which corresponded to an R-value of 1:5.5 for 12.2 nm diameter iron oxide core particles.[90] By using this condition, they were able to vary the added amount of TEOS between 75-600 µL so that they could adjust the thickness of the silica shell, whereby the TEOS was added stepwise in fractions to prevent unwanted silica nucleation. However, they could not grow the shell to more than 15 nm thickness, and only described a one-step reverse microemulsion synthesis without additional surfactant and ammonia addition for further silica growth. Katagiri et al. also used lower concentrations of ammonia water and surfactant of 0.83 wt% and 5.1 wt% respectively for 10 nm iron oxide particles (R = 1:6.1 in weight ratio).[213] The Igepal concentration was much lower than the one presented in this work, which was probably why a silica shell thickness exceeding 50 nm could not be achieved, as the surfactant could only form small micelles with smaller water domains. In general, the R-value can be adapted and adjusted for a wide range of particle sizes; a lower R-value should be employed for smaller particles, than would be for larger particles of a similar or same concentration.

Upconversion core (UC_Er_4; $NaYF_4$ doped with Yb and Er) with a size of 24±1 nm was coated with silica nanoshells through a stepwise reverse microemulsion synthesis. The Y:Yb:Er molar ratio was [78.6±1.0]:[19.4±0.3]:[2.00±0.04]. The silica shell thickness grew from 7 to 44 nm (see

Figure 4.37) through a four-step reverse microemulsion process using an R-value of 1:9.5 for the first silica shell growth and 1:4.3 for the consecutive silica shell growth steps. The sample names after each coating step are UC_Er_4@SiO_2_38 for the first shell, UC_Er_4@SiO_2_60 for the second shell, UC_Er_4@SiO_2_ 94 for the third shell, and UC_Er_4@SiO_2_112 for the fourth shell coating. The last fifth shell (UC_Er_4@SiO_2_ 321) was grown through a modified Stöber method since the zeta potential of the fourth shell sample (-45±1 mV) showed sufficient colloidal stability for Stöber growth (for the further silica shell growth with Stöber method see chapter 4.2.1.2).

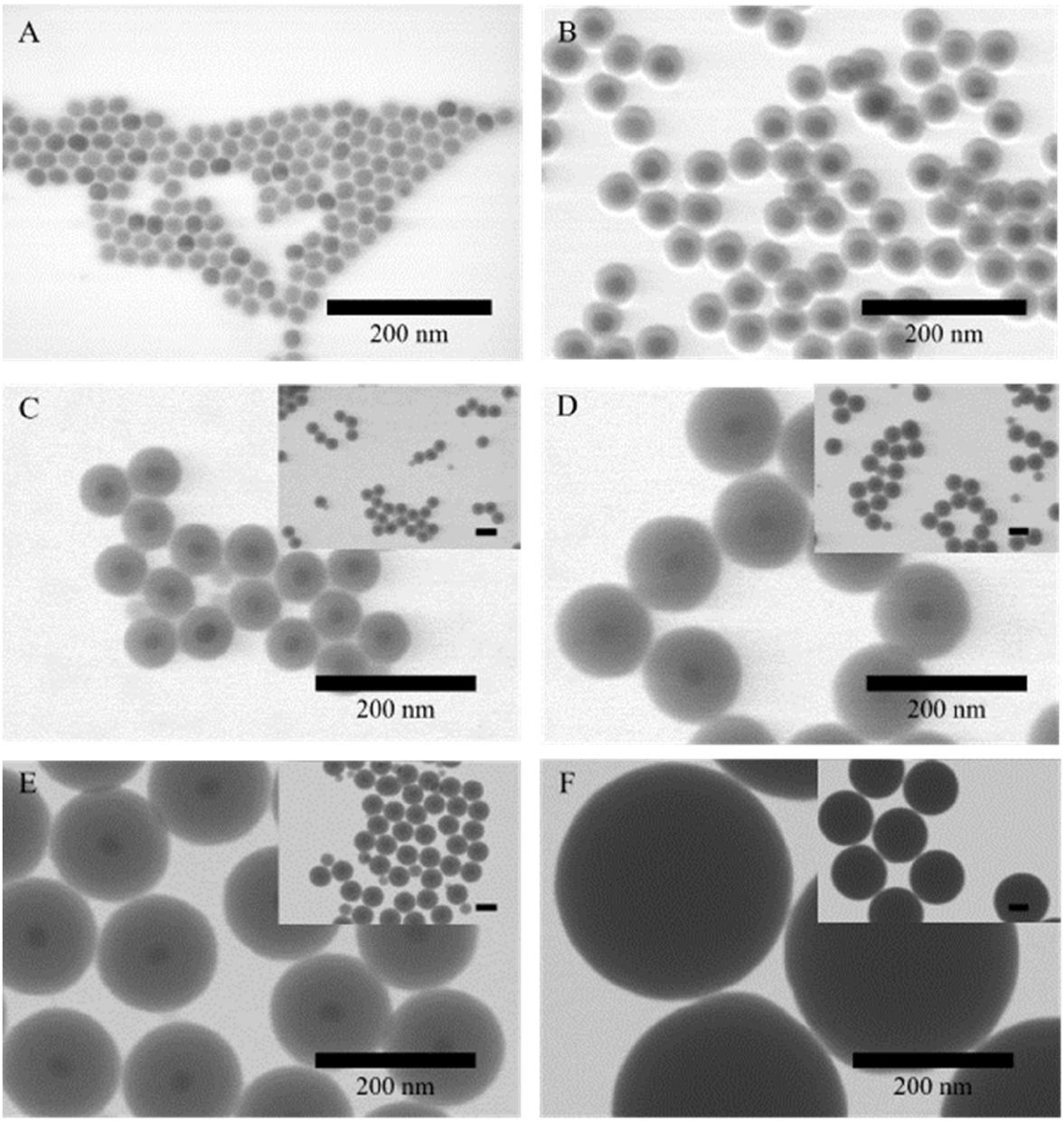

Figure 4.37: STEM images of A: $NaYF_4$: Yb, Er core (UC_Er_4; d = 24±1 nm) and B: the same core after coating with the first thin silica shell (UC_Er_4@SiO_2_38, r SiO_2 = 7±1 nm). Image C: shows the same UCNP core after the second silica coating step (UC_Er_4@SiO_2_60, r SiO_2 = 18±2 nm), D: after the third silica coating (UC_Er_4@SiO_2_94, r SiO_2 = 35±2 nm);), E: after the fourth shell silica coating (UC_Er_4@SiO_2_112, r SiO_2 = 44±2 nm), and F: after the fifth silica growth step (UC_Er_4@SiO_2_321, r SiO_2 = 149±8 nm). The first to the fourth silica shell were grown with the reverse microemulsion method, whereas the fifth shell was grown using a modified Stöber growth. The scale bar in the insets of Figure C-F represents 100 nm.

The results of characterizations of the particles by STEM, DLS, and electrophoretic light scattering are listed in Table 4-4, where the size, silica shell thickness, z-average, PDI, and zeta potential of each silica coated samples are given. The hydrodynamic diameter of the core was measured in cyclohexane, while the silica-coated samples were measured in ethanol and their zeta potentials were measured in ultrapure water.

Table 4-4: Characterization of UCNP with silica shells obtained via an inverse microemulsion method

Sample	**Shell**	**d**	**r SiO_2**	**z-average**	**PDI**	**Zeta potential (ultrapure water)**
		[nm]	[nm]	[nm]		[mV]
UC_Er_4	core	24±2	0	44±2	0.360±0.020	n.d
UC_Er_4@SiO_2_38	1st	38±2	7±2	89±2	0.090±0.020	-
UC_Er_4@SiO_2_60	2nd	59±3	18±4	98±2	0.110±0.030	-32±1
UC_Er_4@SiO_2_94	3rd	93±4	35±4	116±2	0.013±0.005	-41±1
UC_Er_4@SiO_2_112	4th	112±4	44±4	137±2	0.040±0.010	-45±1
UC_Er_4@SiO_2_321 (Stöber)	5th	321±16	149±16	376±9	0.095±0.020	-37±1

The calculated shell thicknesses for the amount of TEOS used were similar to the diameter of the synthesized particles (see Table 3-4 and Table 3-5), which proved that TEOS was entirely hydrolysed in each coating step. Slightly larger shell sizes compared to theoretically calculated shell thicknesses could be caused by the oleate ligands on the UCNP core, that was also weighed

with the particles used for the synthesis. The oleate ligands that were detached from the UCNP surface during the ligand exchange process in the reverse microemulsion corresponded to approximately 5-10 % of the total weight of the total mass of particles in a similar particle diameter range.[224]

The z-average values of UC_Er_4@SiO_2_38 and UC_Er_4@SiO_2_60 were 57 % and 45 % higher than the measured STEM-diameter, indicating partial aggregation, which was also confirmed by the relatively high PDI values. Low colloidal stability could be the cause of this aggregation, since the zeta potential value of the second shell sample was only -32±1 mV, indicating that the surfactant was still bound to the silica surface as mentioned earlier. Other publications also observed low colloidal stability on thin silica coated nanoparticles.[89, 221-223] After the growth of the third and fourth shell, the colloidal stability improved, as was confirmed by the z-average, PDI, and zeta potential values. The z-average values of UC_Er_4@SiO_2_94 and UC_Er_4@SiO_2_112 were 20 % and 18 % higher than the measured STEM diameter, whereas the zeta potential values were -41±1 mV and -45±1 mV respectively, values which are typical values for Stöber particles,[54] indicating high colloidal stability.

Figure 4.38 shows XRD diffractograms of the oleate-coated UCNP core UC_Er_4 and the core after the coating of two (UC_Er_4@SiO_2_38), three (UC_Er_4@SiO_2_60), four (UC_Er_4@SiO_2_112) and five (UC_Er_4@SiO_2_321) silica shell layers. The cores have predominantly hexagonal crystal structures. Minor peaks at 47° for [220] reflex and 55° for [311] reflex indicate a small fraction of cubic phase (ICDD no. 06-0342). The spectra of the silica-coated UCNP show mainly hexagonal peaks with decreasing intensity and increasing silica shell thickness. Accordingly, the broad signal of the amorphous silica at 20°-25° becomes more dominant with increasing silica shell thickness. These data indicate that the crystal structure of the particles was not changed by the growth conditions in the entire shell formation process.

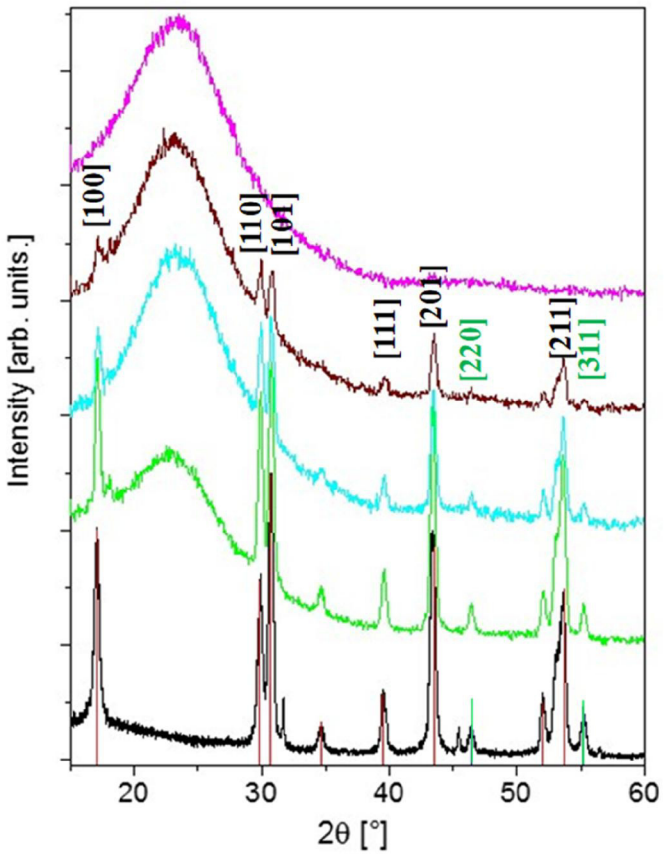

Figure 4.38: XRD diffractograms of oleate-coated UC_Er_4 UCNP core (black line), the same core with first silica shell coating UC_Er_4@SiO_2_38 (green line), third silica coating UC_Er_4@SiO_2_60 (cyan line), fourth shell silica coating (UC_Er_4@SiO_2_112, (brown line) and fifth silica coating UC_Er_4@SiO_2_321 (pink line). Red bars indicate the hexagonal phase and green bars indicate the cubic phase.

4.2.1.2 **Growth of silica shells through Stöber method**

A modified Stöber growth process could be carried out after the growth of the fourth silica shell by the reverse microemulsion method, once the particles reached sufficient colloidal stability. Continuous addition of TEOS to the ethanolic dispersion (c = 14.4 wt%) of the silica-coated particles was done to grow several hundred nanometers of silica shell in one step.[225] The fifth shell was called UC_Er_4@SiO_2_321, the total diameter was 321±16 nm, i. e. the silica shell thickness was 149±16 nm (see Figure 4.37.B and Table 4-4) and the particle volume could be grown over 23 times larger in one step, which was not possible by the above described reverse microemulsion method.

The modified Stöber growth could also be applied to other UCNP cores to grow thick silica shell. Figure 4.39 shows UCNP core with a size of 20±2 nm was coated with silica shells first through a six-step microemulsion method. The silica shell was 43±1 nm after the last step. This shell could be further grown by a modified Stöber method to grow a total thickness of 95±4 nm.

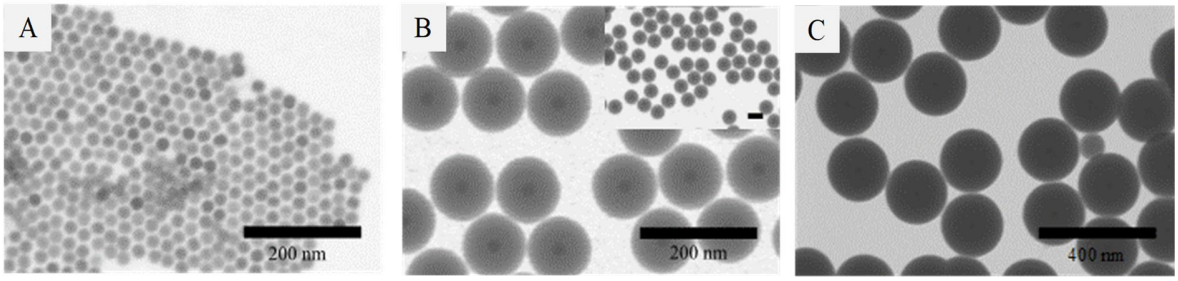

Figure 4.39: STEM images of A: oleate-stabilized UCNP cores (d = 20 ±2 nm), B: which was coated by an optimized six-step reverse microemulsion method (r SiO_2 = 43±1 nm). C: the final seventh layer was grown by a modified Stöber process (r SiO_2 = 95±4 nm).

4.2.1.3 **Upconversion fluorescence characterization of silica-coated samples**

The upconversion fluorescence spectra of the samples UC_Er_4@SiO_2_38, UC_Er_4@SiO_2_112 and UC_Er_4@SiO_2_321 are shown in Figure 4.40 (power excitation density = 8 W/cm^2). All spectra were normalized to the red emission (655 nm) to visually compare the shape and the $f_{g/r}$ of the spectra of the three samples. From the sample with the thickest silica shell to the thinnest silica shell the $f_{g/r}$ ratios are 2.7±0.5, 0.80±0.20 and 0.55±0.10. With increasing silica thickness the samples also scattered more intensely, and the overall emission was weakened.

The green emissions at 520 and 540 nm (transitions from $^2H_{11/2} \rightarrow {}^4I_{15/2}$ and $^4S_{3/2} \rightarrow {}^4I_{15/2}$, respectively) are reduced compared to those of the oleate functionalized particles. This effect can be explained by the presence of the OH-group in ethanol that quenches the green emission more intensely than the CH_2-group in cyclohexane. The OH-group in ethanol has a vibrational frequency energy of 3320 cm^{-1}, which matches the transition energy gap from $^4S_{3/2} \rightarrow {}^4F_{9/2}$, which is a non-radiative relaxation transition before consecutive red emission of $^4F_{9/2} \rightarrow {}^4I_{15/2}$ transition in Er^{3+} ions. Similar vibrational frequencies of the solvent and the transition in the UCNP can facilitate or increase non-radiative relaxation of the excited photons, resulting in a quenching effect. In this case, the OH-group vibrational frequency of ethanol could facilitate increased non-radiative relaxation of $^4S_{3/2} \rightarrow {}^4F_{9/2}$, reducing green emission intensity. The hydrocarbon group of

cyclohexane has a vibrational frequency that is lower than the $^4S_{3/2} \rightarrow {}^4F_{9/2}$ and the $^4I_{11/2} \rightarrow {}^4I_{13/2}$ transition (ν C-H = 2850-3000 cm^{-1})[226] and thus is not in the range of the green upconversion emission of the UCNP.[227] The red emission, however, is not influenced as much by the solvent, hence a decrease of the green emission compared to the red emission is observed when UCNP are transferred from cyclohexane to ethanol.

When comparing the green emission between the silica-coated samples, one can observe an increase of the green emission in UC_Er_4@SiO_2_321 compared to UC_Er_4@SiO_2_38 and UC_Er_4@SiO_2_112. With increasing thickness of the silica shell, the UCNP core is better protected from the diffusion of ethanol into the silica shell, so that the quenching of the OH-group is less effective than in thinner-shelled UCNP.

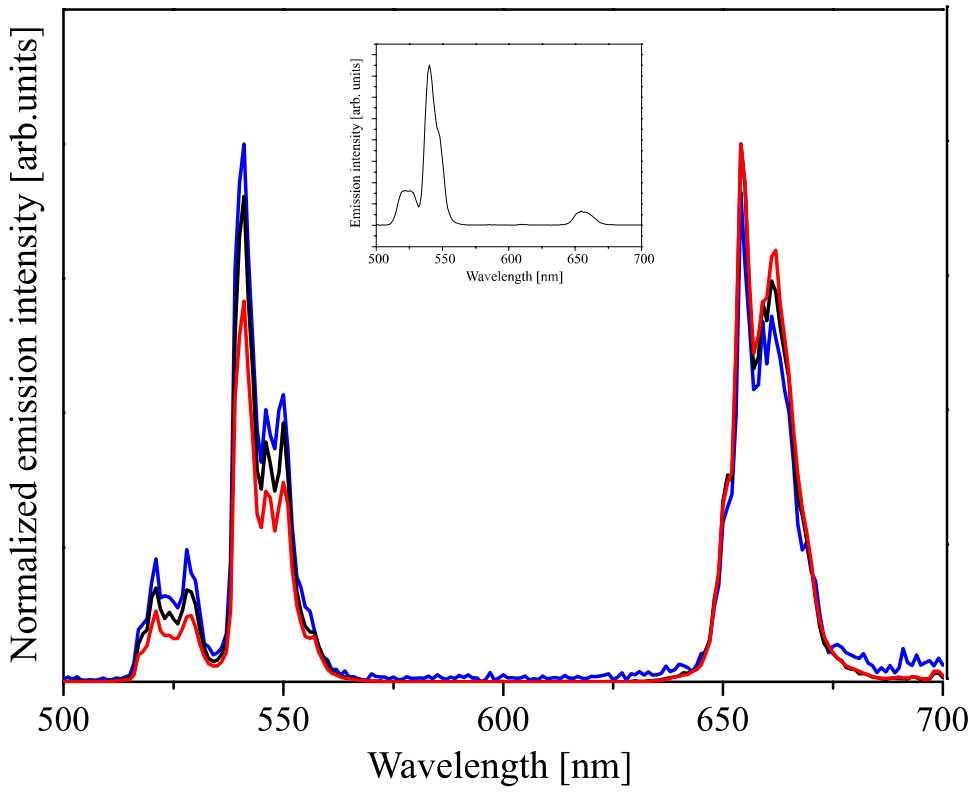

Figure 4.40: Upconversion fluorescence spectra of UC_Er_4@SiO_2_38 (black line), UC_Er_4@SiO_2_112 (red line) and UC_Er_4@SiO_2_321 (blue line) after excitation at 980 nm in ethanol normalized at red emission. In the inset is UC-spectrum of the core UC_Er_4 in cyclohexane after 980 nm excitation, power excitation density was 2 W/cm^2.

It was possible to do a stepwise growth of silica shells on UCNP using a modified reverse microemulsion approach. The maximum surfactant concentration did not exceed 14 wt%, while the NH_3 concentration was kept at 3.3±0.1 wt% for 24 nm-sized core particles to keep the hydrolysis rate of TEOS low, the aqueous domain small, and thus allowing for creating thin silica shells without secondary nucleation. Through a stepwise reverse microemulsion method, silica shells could be grown up to a thickness > 40 nm with a four-step silica coating. A low R-value of 1:4.3 in weight ratio prevented new formation of core-free silica particles in further steps of the silica shell growth. The Igepal concentration was kept constant to keep the micelles large enough to contain the growing particles and to allow optimum TEOS hydrolysis rate, while preventing the formation of new micelles. The R-value can be adapted and adjusted for a wide range of particle sizes; for smaller particles under a similar number concentration of particles, a lower R-value should be employed than for larger particles.

Along with the increase of shell thickness, the colloids were more stabilized, as was proven by their increasing zeta potential. Once the particles were stable, i.e., the zeta potential > -40 mV, a modified Stöber method could be applied to further grow the particles to hundreds of nanometer diameter in one step.

4.2.2 Coupling of small gold nanoclusters on silica coated UCNP for further growth into gold nanoshell

Prior to growing gold nanoshell (see chapter 4.2.3) on silica coated UCNP, the silica surface was functionalized with APS before subsequent coupling with small gold nanoclusters. The challenge in the preparation of the gold nanoshell is to prepare a closed homogenous shell with certain thickness in a controlled manner. After the adsorption of gold clusters onto the silica surfaces with a certain degree of coverage, a homogenously closed gold nanoshell can be synthesized. Normally, the deposition of gold clusters is done in one step; however, the homogeneity of the thickness of the later-obtained gold shell is limited. Gold shells with a thickness of less than 25 nm on core particles bigger than 200 nm in diameter are often inhomogeneous,[159] while synthesis of thin gold shells on smaller particles (d < 200 nm) also often delivers incomplete shells.[30-31, 175, 228] Homogenously closed gold nanoshell can be achieved by increasing the degree of coverage of gold clusters on the core surface by performing a two-step gold cluster deposition method,[160] since there are more gold clusters available, from which the gold shells can grow and coalesce.[160]

Silica coated UCNP in the size range of with r_0 = 40-60 nm (as in the case of UC_Er_4@SiO_2_112) can be coated with a thin gold shell with a maximum thickness of 30 nm to deliver a moderate upconversion emission enhancement after saturated pump excitation (see calculated contour plot in Figure 4.30). Homogenously closed gold shell with a defined thickness is essential for the measurement, since a slight deviation in the gold shell thickness will strongly affect overall upconversion enhancement due to the thickness-dependent nature of surface plasmon resonance. Furthermore fractal, incomplete gold shells or assemblies of gold clusters on silica surface deliver completely different plasmon resonance energy than a complete gold shell.

In this chapter, one and two-steps of gold cluster deposition on silica coated UCNP were carried out (see Figure 4.26 for the general scheme of gold cluster's deposition on silica surface). It is significant that the gold clusters have a size of 2±1 nm, since bigger clusters generally produce rough structured gold shells. In a typical synthesis, silica coated UCNP were first functionalized with APS to provide the silica surface with a positive charge. Negatively charged gold clusters are subsequently coupled onto this ligand.

As an example, gold clusters are grown on UC_Er_4@SiO_2_112 (r_0 = 56±2 nm) following the above-described method (the gold-cluster functionalized sample is UC_112@Au; see Figure 4.42.C). The gold clusters were synthesized via a reduction reaction of an aqueous solution of $HAuCl_4$ with THPC and NaOH.[229] Imaging via SEM and STEM reveals that the gold nanoclusters were evenly distributed on the nanoparticle surface, i.e., they did not build large clusters during deposition. Halas et al.[230] observed a coverage degree of ≤ 30 % of 2-3 nm gold nanoparticles on APS functionalized silica particles. Presumably, the degree of coverage of the gold clusters in this work was similar. However the exact size was difficult to determine in STEM or SEM images, since the maximum resolution of the measuring device was only approximately 1.0 nm at 15 kV acceleration voltage.[231]

To couple the second batch of gold nanoclusters, the gold clusters from the first deposition were functionalized with hydrolyzed APS from a sol-gel solution, and the sythesis proceeded through a hydrolysis and condensation reaction as shown in Figure 4.41.

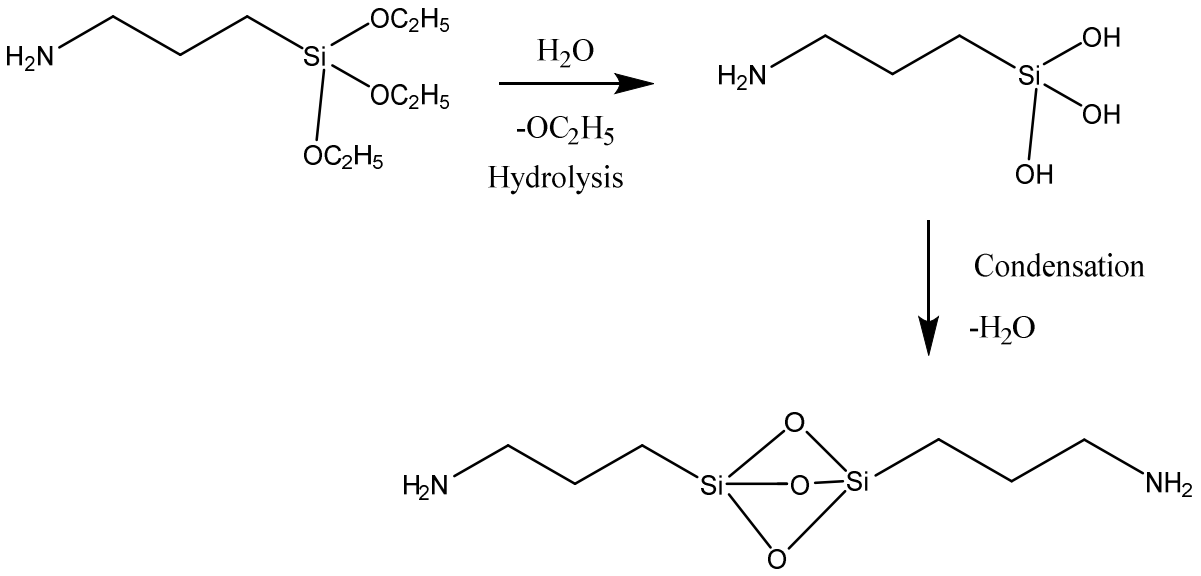

Figure 4.41: Hydrolysis and condensation reaction of APS in sol-gel solution. The modified APS has two positively charged amine ligands at the end to be coupled on the gold clusters.

The modified APS has two amine ligands on each end of the molecule, so that one end can be coupled to the gold cluster from the first deposition while the other end can be coupled to a gold cluster in the second deposition. Gold cluster dispersion for the second gold cluster deposition was added to UC_112@Au, which was mixed with the APS sol-gel solution. The sample with the second gold cluster deposition is called UC_112@Au@Au. The gold nanoclusters also had an average diameter of 2±1 nm (see Figure 4.42), however, the exact size was difficult to determine in STEM or SEM images, since the maximum resolution of the used device was only approximately 1.0 nm in vacuum at an accelerating voltage of 15 kV,[231] while with HRTEM an approximate resolution < 0.1 nm can be reached.

Figure 4.42 shows STEM images of sample UC_Er_4@SiO_2_112 and the particles after two steps of gold cluster deposition. The sample UC_112@Au@Au has a higher coverage degree of clusters. Zhang et al. [160] reported an increase of the degree of coverage from 30 % to 60 %. However, no further increase in coverage after the second deposition was observed. ICP-OES measurements were used to determine the amount of gold in each sample. UC_112@Au@Au had a gold concentration of 0.20±0.02 mg Au/mg Si or 0.030±0.003 mmol Au/mmol SiO_2 and UC_112@Au had a gold concentration of 0.07±0.01 mg Au/mg Si or 0.010±0.001 mmol Au/mmol SiO_2. That means there was an increase of 185±21 % of the total amount of gold cluster after the second deposition. Based on the measurement results, it was calculated that [2.42±0.10] × 10^{-13} mmol SiO_2

were in one particle of UC_Er_4@SiO_2_112, thus there were [2.6±0.1] × 10^{-11} mmol Au/particle of silica coated UCNP (590±70 gold clusters particle per silica coated UCNP) in UC_112@Au and [0.9±0.4] × 10^{-11} mmol Au/particle of silica coated UCNP (1800±200 in UC_112@Au@Au) in UC_112@Au@Au, assuming the gold cluster size was 2 nm. The mentioned values of gold clusters per particle are listed in Table 4-5.

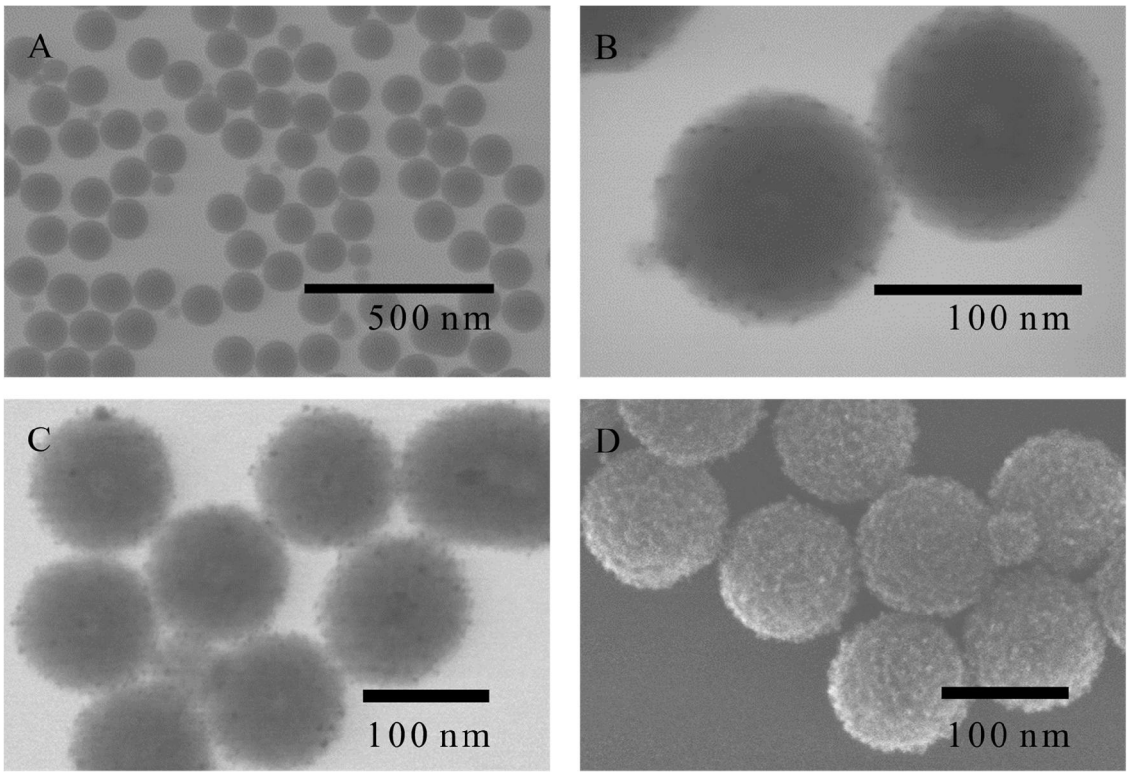

Figure 4.42: STEM images of A: sample UC_Er_4@SiO_2_112, silica coated UCNP cores (d UCNP = 24±1 nm; r SiO_2 = 44±2 nm); B: sample UC_112@Au, sample UC_112 after the first gold cluster deposition; C: sample UC_112@Au@Au after the second gold cluster deposition; and D: SEM image of sample UC_112@Au@Au showing dense gold cluster deposition.

Table 4-5: Amount of gold cluster coupled on UC_Er_4@SiO2_112 after first (UC_112@Au) and second (UC_112@Au@Au) gold cluster deposition

Sample	**mg Au / mg Si**	**mmol Au/mmol SiO_2 in UC_Er_4@SiO_2_112**	**mmol Au per particles of UC_Er_4@SiO_2_112**	**Number of Au clusters per particles of UC_Er_4@SiO_2_112**
UC_112@Au	0.07±0.01	0.010±0.001	$2.4±0.3*10^{-15}$	585±73
UC_112@Au@Au	0.20±0.02	0.030±0.003	$7.3±0.8*10^{-15}$	1800±197

Another way to qualitatively determine the gold concentration was to measure the extinction spectra of the samples. The extinction spectra of the core and the two samples with gold clusters show a strong background effect due to scattering, as expected for silica particles in general or particles with silica coating in this size range (see Figure 4.43). Gold clusters with a size between 1-2 nm generally do not have any surface plasmon resonance, which typically lies at around 520 nm for bigger gold nanoparticles.[230] However, in this case, the particles coated with nanoclusters have a broad plasmon resonance band at ~520±10 nm, which indicates some clustering of the small gold nanoparticles or particles that are located very close and interact with each other.[29] The small peak at 860 nm was due to a change in detector of the spectrometer during the measurements.

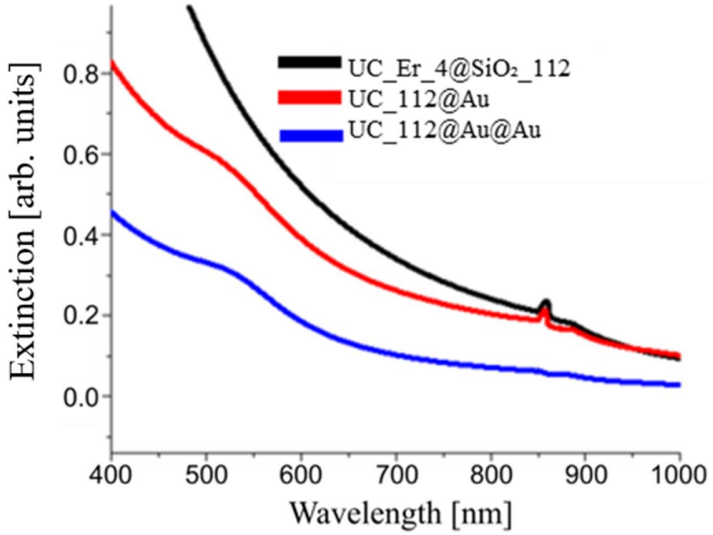

Figure 4.43: Extinction spectra of UC_Er_4@SiO2_112 (black line), UC_112@Au (red line) and UC_112@Au@Au (blue line) measured in EtOH, the gold clustered samples were measured in water.

Taken together, the two-step deposition of gold nanoclusters could deliver a high degree of coverage for the silica-coated UCNP, which increased the gold nanoclusters coverage to around 66 % after the second deposition. The extinction spectra suggest clustering effects of the closely packed gold nanoclusters of the samples on silica coated UCNP.

4.2.3 Synthesis and extinction spectra measurements of gold nanoshell on silica coated UCNP

4.2.3.1 Growth of gold nanoshell on silica coated UCNP

Gold nanoshells were grown after gold nanoclusters were coupled onto the silica-coated UCNP through reduction of previously prepared H[AuCl4] aqueous solution with hydroxylamine hydrochloride into elementary gold, whereby the newly reduced gold grew on the previously coupled gold clusters (see reaction in Scheme 4-5; for synthesis steps see Figure 4.1). The $[AuOH_4]^-$-solution was prepared from chloroauric acid through a reaction with K_2CO_3 in an aqueous solution. Both reactions (synthesis and reduction of $[AuOH_4]^-$) are depicted in the following scheme:

$$[AuCl_4]^- + 4\ OH^- \rightarrow [AuOH_4]^- + 4\ Cl^-$$

$$6\ NH_2OH{*}HCl + 4\ H[AuCl_4] \rightarrow 3\ N_2O + 3\ H_2O + 4\ Au + 22\ HCl$$

Scheme 4-5: Reaction mechanism of gold shell growth from reduction of $[AuOH_4]^-$ by hydroxylamine.

Silica-coated UCNP with a total diameter of at least 100 nm were coated with gold shell, since growing homogenous thin gold nanoshell with a thickness < 25-30 nm onto smaller particles and a diameter less than 100-200 nm is generally complicated.[30-31, 175, 228] The method of controlling the gold shell thickness with homogenous coating is well-established for bigger particles.[159, 229, 232-233] Efforts to coat thin gold shells on silica coated UCNP in this work did not lead to satisfactory results. Thin gold shells reported in other publications were often inhomogeneous and not completely closed.[30-31, 175, 228] However some publications could observe improvement or changes in upconversion emission after coating with plasmonic metal shell. Fujii et al.[30] for example synthesized 70 nm UCNP coated with 15 nm silica shell and consecutively with a 20 nm gold shell. They measured an increase of the red emission intensity and a decrease of the green emission after the formation of the gold shell. Furthermore, both emissions experienced an increase in quantum

efficiency. The enhancement factor of the quantum efficiency of the red emission was twice that of green emission. Green et al.[175] compared single-particle upconversion spectra of 25 nm silica-coated UCNP with and without a 12-nm shell. They observed an overall three times emission intensity enhancement, besides a decrease of $f_{g/r}$, compared to silica coated UCNP without a gold shell. These publications suggest that with proper selection of the ratio of UCNP core, spacer and gold shell thickness, upconversion emission enhancement due to plasmon coupling is possible.

The first successful experiment for coating closed gold shell was done on UC_Er_4@SiO_2_112 as a test system. The gold shell thickness (t) was 30±6 nm. Medium-to-strong enhancement is expected at the 540-nm emission after saturated pump excitation (LDOSrad) when a gold shell with a thickness of 30 nm is grown onto the particles. On the contrary, emission quenching at 540 nm and 654 nm emission is expected in case of dimmed pump excitation (see contour plots in Figure 4.30 and Figure 4.31). The exact calculated enhancement values under saturation pump excitation and dimmed pump excitation in water and air as a medium are presented in chapter 4.2.4. Additionally, gold shells with two different thicknesses of 48±20 and 68±10 nm were grown on UC_Er_4@SiO_2_321. The values of for FE × yield and $LDOS_{rad}$ were calculated for these core-shell architectures (see calculated values for FE × yield and LDOSrad in chapter 4.2.4.1). Based on the plots in Figure 4.30 and Figure 4.31, it was initially concluded that these samples could only deliver a weak enhancement of the red emission when the shell thickness t = 30-70 nm in the case of saturated pump excitation.

Various experiments for coating smaller silica coated UCNP particles (d < 100 nm) with thin gold shells were not successful, even after coupling of two layers of gold clusters (see chapter 4.2.2). In an experiment of growing gold shells on UC_Er_4@SiO_2_112, the particles were coated with a double layer of gold clusters based on the method of Zhang et al.[160] Almost all particles were covered with gold clusters with a size of 2±1 nm. However, the clusters were not attached to all particles homogenously. Based on optical observations through STEM images some particles were coated with more gold clusters than the others (see Figure 4.44.A). Thin gold shells with a calculated thickness of 5 nm assuming full conversion were grown. This thickness was chosen, since the resulting particle structure would fulfill the conditions for a medium-to-strong enhancement by a factor of 30 under saturated pump excitation (see Figure 4.30) and a medium-to-strong enhancement after dimmed pump excitation of 980 nm excitation at 540 and 654 nm emission (see Figure 4.31.A and B). However, the utilized amount of $[Au(OH)_4]$-solution did not yield gold shells of the same thickness on all particles. Some particles had a closed gold shell of

16±3 nm thickness (see Figure 4.44.C), whereas there were also unclosed gold shells in the same sample, where the gold clusters grew into bigger clusters (see Figure 4.44.B). Particles with non-continuous gold shells have a significantly different extinction spectrum than those with a continuous shell and hence would deliver different plasmon enhancement effects for UC-emission.[159] Since several further experimental attempts to coat small UCNP with continuous thin gold shells through a two-layer deposition of gold cluster did not deliver consistent and successful results, the alternative procedure of coating with thicker gold shells through the deposition of one-layer cluster will be the main focus of the next chapters.

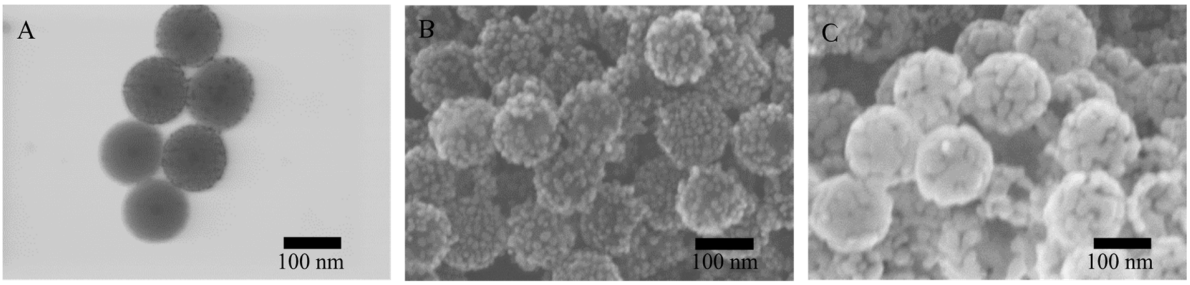

Figure 4.44 A: STEM image of a double layer of gold clusters on UC_Er_4@SiO_2_112 (r SiO_2 = 44 ± 2 nm) followed by; B and C: SEM images of attempts to grow a gold shell with an intended thickness of 5 nm. Figure C shows more closed gold shell with t = 16 ± 3 nm, while Figure C shows particles with gold clusters with an increased size but not closed gold shell.

Upconversion and decay rate measurements of two samples of silica coated UCNP core already with gold shell (core: UC_Er_4@SiO_2_112 and UC_Er_4@SiO_2_321) in chapter 4.2.4 are discussed. The sample UC_Er_4@SiO_2_112 was coated with 30±6 nm gold shell, for which dipole mode enhancement at 540 nm emission under saturated pump excitation is possible. On the other hand, UC_Er_4@SiO_2_321 was coated with 48±20 nm gold shell, for which cavity mode enhancement under saturated pump excitation at 540 nm and 654 nm emission is possible.

Figure 4.45 shows STEM images of sample UC_Er_4@SiO_2_112 (Figure 4.45.A) and the same particles after the growth of a gold nanoshell (sample UC_112@Au_shell, Figure 4.45.B and C) shown. As can be seen from the pictures, the gold shells were not completely closed on some particles, and some smaller gold particles could not be removed by sedimentation. The smaller gold particles were uncoupled gold clusters that grew into bigger particles during the reduction of $H[AuCl_4]^-$ with $NH_4OH.HCl$. Although the gold cluster-coated particles were already cleaned several times, not all small gold clusters could be removed completely. The separation of the gold

shell particles from the gold clusters through centrifugation could induce aggregation of the particles according to earlier experiments, due to decrease of interparticle distances and a consequent increase of interparticle interactions during centrifugation, leading to destabilization of the particles. To prevent aggregation, particles were centrifuged at a centrifugation speed of 31 g, which was the lowest possible speed for the utilized centrifuge (see chapter 3.1). In this way, one could decrease the risk of particle aggregation, which occurred several times during the cleaning of the particles. However, even at this speed not all gold clusters could be completely removed, and aggregation partly occurred. Based on this observation, the particle sedimentation process was done at ambient temperature by letting the particles sediment with the help of gravitational force in the dark for a few days. This way, aggregation could be prevented, and most gold clusters could be removed, although not completely.

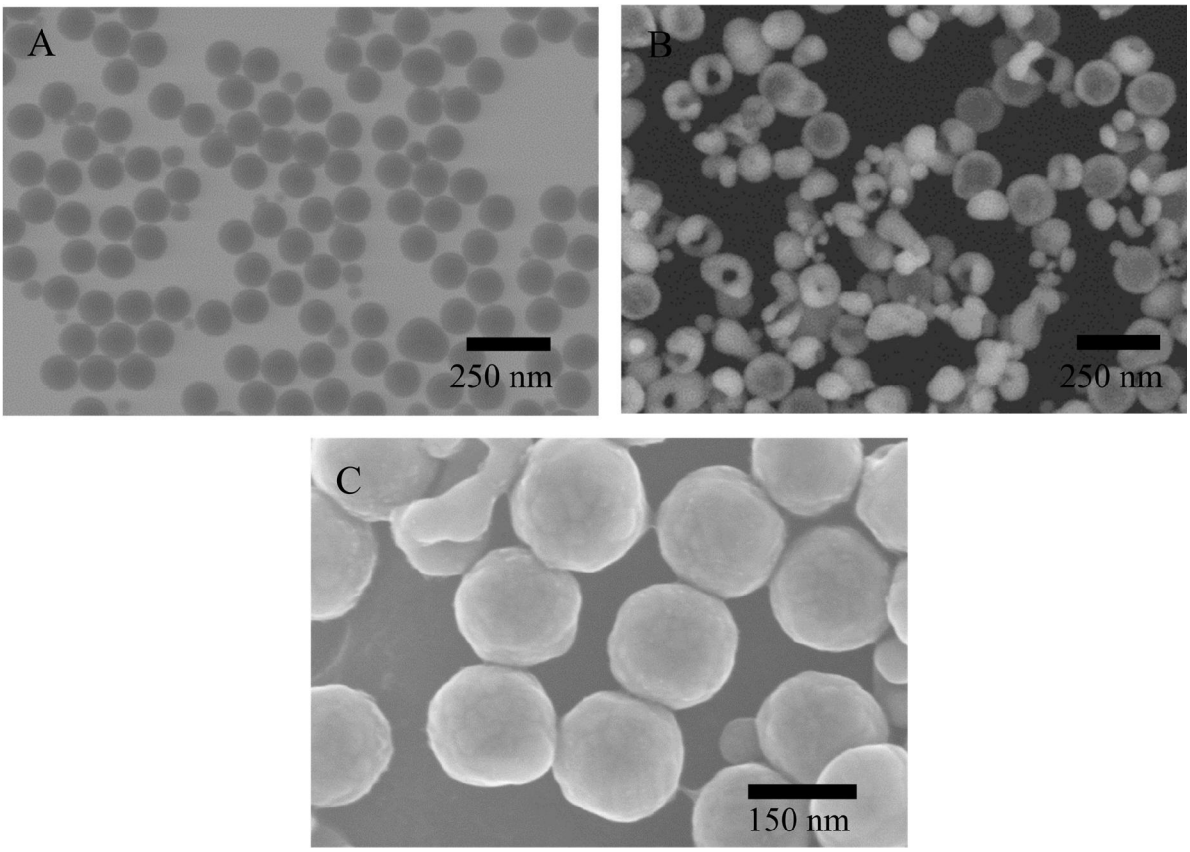

Figure 4.45 A: STEM image of sample UC_Er_4@SiO_2_112, silica coated UCNP (d_{total}= 112 ± 4 nm); B and C: SEM images of sample UC_112@Au_shell, gold coated UCNP with a silica shell (thickness of the Au shell (t = 30±6 nm).

Figure 4.46 shows the STEM image of sample UC_Er_4@SiO_2_321, which was coated with a 68±10 nm thick gold shell (Figure 4.46.B; UC_321@Au_shell_B) and a less homogenous gold shell with a thickness of 48±20 nm (Figure 4.46 C; UC_321@Au_shell_A). The gold shell of the first-mentioned sample could be grown more homogenously on the silica surface compared to sample UC_112@Au_shell, as it was commonly easier to grow a smooth gold shell on bigger particles with radius > 200 nm. The high polydispersity of the gold shell thickness, especially for UC_321@Au_shell_A (size variation = 42 %) was likely due to the calculations of the shell thickness, in which the total diameter (r_0+t = 417±37 nm; relative error = 9 %) was substracted by the silica-coated UCNP (r_0+t = 321±16 nm; relative error = 5 %), which caused high propagation of error. There were also some smaller gold particles (d = 87±20 nm) present that were formed during the growth of the gold shell. These gold particles were difficult to separate from the gold-coated UCNP since they have similar sedimentation speeds due to their higher density (19 g/cm^3 for gold particles and 11.2±1.0 g/cm^3 for gold-coated UCNP@SiO_2) than the gold coated UCNP. The sedimentation speed of gold coated UC_321@Au_shell_A was [1.2±0.2] × 10^{-7} m/s whereas the gold particles had a sedimentation speed of [8.6±3.8] × 10^{-9} m/s, i.e., about 14±7 times slower than that of the gold-coated UCNP. UC_321@Au_shell_A had a nearly smooth gold shell, although it was not completely closed. Similar to the case of UC_321@Au_shell_B, small core-free gold particles were observed alongside the bigger gold coated UCNP. The size of these gold particles was also in the range of 87±20 nm. The sedimentation velocity of the gold-coated UCNP would be [1.62±0.05] × 10^{-7} m/s.

Hence, it was still a challenge to separate both pure gold particles and silica-coated UCNP-shell gold particles, as can be observed from the STEM picture.

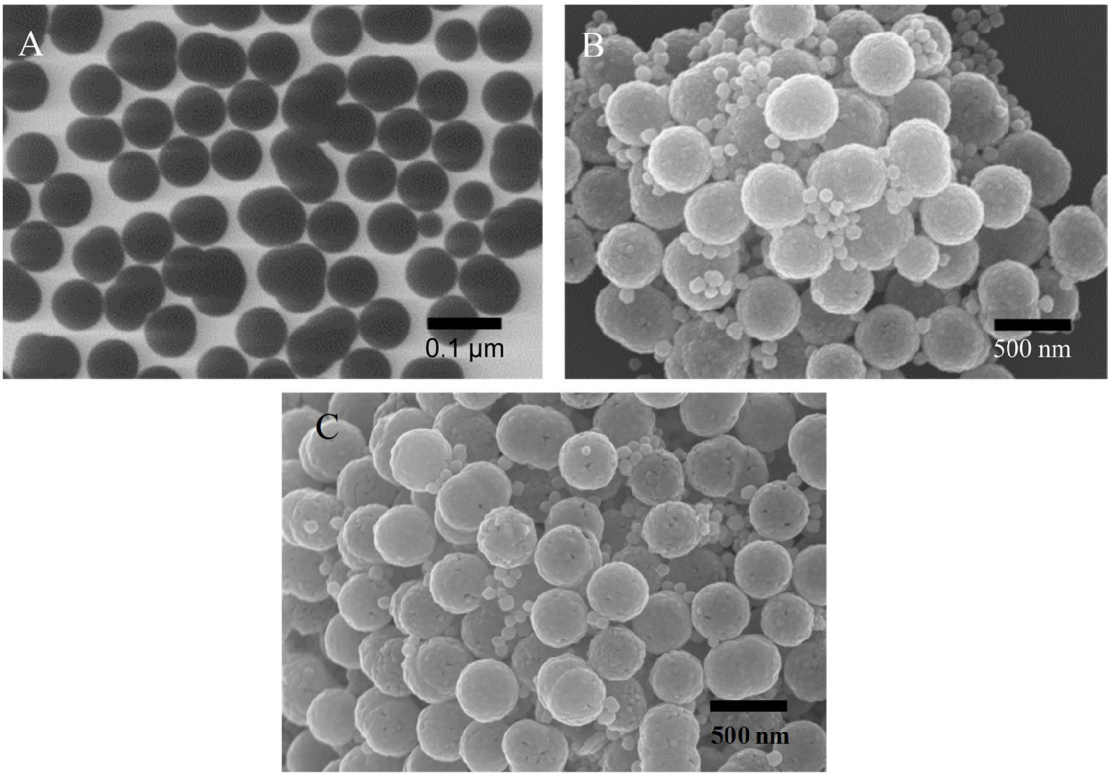

Figure 4.46 A: STEM image of sample UC_Er_4@SiO_2_321 (d core = 24±2 nm; r SiO_2 = 149±8 nm), B: SEM image of sample UC_Er_4@SiO_2 with a gold shell: sample UC_321@Au_shell_B (t = 68±10 nm) and C: sample UC_321@Au_shell_A (t = 48±5 nm).

4.2.3.2 Comparison between the calculated and measured extinction spectra of gold shelled silica coated UCNP

The calculated extinction spectra of both samples: UC_112@Au_shell and UC_321@Au_shell A are compared with the measured extinction spectra to investigate the real gold shell, since it can deviate from the thickness measured from SEM pictures.

The plasmon resonance of gold nanoshells coated on a dielectric core such as silica can be tuned into the infrared range through variation of the gold shell thickness, much further than that of the corresponding solid metal particles.[104, 171] The plasmon resonance frequency can be controlled by adjusting the dielectric core-metal shell size ratio of the particles, resulting in characteristic extinction spectrum for each core-shell size ratio.[104, 171] The precise size of silica-gold core-shell can be determined by comparing the experimentally obtained extinction spectrum with a theoretically modelled spectrum. The exact size determination is significant, since the measured

size of the dielectric core might be smaller than the true size, due to shrinking effect caused by the damage from the electron beam and high vacuum atmosphere in SEM.[161] However, the gold-coated particles do not shrink under electron microscope measurements. As a result, the calculated final gold shell thickness might be misleading.[159, 171, 234] For this purpose, the core-shell input size for calculating the theoretical extinction spectrum is adjusted until it matches the measured spectrum. Interfering effects such as inhomogeneous or unclosed gold shell, polydispersity, aggregated particles, and core-less gold particles should also be considered in calculating the extinction spectrum.

Extinction spectrum of sample UC_112@Au_shell in water was measured and compared with the calculated spectrum. The calculations were done with the program "sphere.f." from Moroz[98] based on the theory of the absorption and scattering of spheres by Bohren and Huffman,[235] and developed from the light scattering theory of Mie.[236] In the calculations, the refractive index of the surrounding medium, which is water, is 1.33. The refractive index (1.45) and density of silica (2 g/cm^3) was used as the input value for the core.[159] The total size of the silica-coated UCNP with and without the gold coating were used as input values for the total size of the particles and the core size, respectively. These input sizes were then adjusted in the calculations to fit the experimentally measured spectra. The size of the core influences the position of the resonance modes peaks (dipole, quadrupole, or higher order modes), whereas the gold shell thickness under the same core size influences the shape of the extinction spectrum.[104, 171] Polydispersity usually causes line broadening and aggregation, which causes increased interparticle interactions, could lead to "tailing" in the higher wavelength range and an additional peak in the extinction spectrum.[171]

After several adjustments of the above-mentioned parameters, the input value for the total diameter of the sample in water was 172 nm, and that of the silica-coated UCNP core diameter was 112 nm, which corresponded exactly to the size obtained from SEM measurements. A shrinking of 5-15 % of the silica particle size resulting from TEM measurements was observed in earlier studies,[159, 234] but the shrinkage should be lower in SEM measurement, due to the lower accelerating electron beam energy of SEM (30 kV is used in SEM, while TEM generally utilized an accelerating voltage of 80-400 kV. The deviation of the measured extinction spectrum to the calculated one in terms of the spectrum shape likely resulted from the existence of core-less gold particles (see Figure 4.47.B and C), causing a broadening of the extinction peak and almost no distinction between the quadrupole peak at 540 nm and broad dipolar plasmon peak. The polydispersity of the particles

could also cause a deviation between the measured and the calculated extinction spectrum in the higher wavelength range. However, the shoulder of the quadrupole peak at 500 nm is observable in the measured spectrum. In Figure 4.47 the octupole mode could not be observed, since the octupole contribution usually is more distinctive for particles with thicker gold shells and bigger cores (d > 200 nm)[159].

The calculated extinction spectrum in water shows a peak at 540±2 nm, which corresponds to the quadrupole plasmon resonance of the gold shell,[237] while a broad dipolar plasmonic band from 720±3 nm to the infrared range is shown. The peak broadenings to the visible range are typical for the growth of closed gold shells with increasing gold shell thickness. Penninkhof et al. calculated the dipole (1430 nm), quadrupole (820 nm) and octupole (680 nm) contributions to the extinction spectrum of silica-gold core-shell particles with a core diameter of 156 nm and a total diameter of 181 nm with the same program "sphere.f".[105] With increasing shell thickness the resonance peaks shifted to higher wavelength (red-shift).[30, 237] In the spectrum of UC_112@Au_shell the calculated peaks are at 500±5 nm for the dipole, 540±2 nm for the quadrupole, and 720±3 nm for the octupole mode plasmon resonance. The scattering contribution to the extinction efficiency was higher than the absorption contribution consistent with what was expected for measurements of gold shell particles in the dispersion. Additionally, for such large particles, the scattering effects dominate over the absorption.[105]

Next, the extinction spectra on a glass substrate of the same sample with the same size input parameters as for the extinction spectrum in water was measured and calculated. This step was necessary, since the samples will be measured on a glass substrate after spin-coating for single-particle upconversion emission and decay rate measurements. The measured extinction spectrum on a glass substrate (dielectric constant of air of 1 was used as the background medium) is shown in Figure 4.47 B. The measured spectrum shows broad extinction bands in the range between 500 nm to 800 nm which was likely due to clustering of the particles on the glass substrate or existence of unclosed gold nanoshell. Clustering was caused by the tendency of particles to aggregate once they were dried, due to sterical stabilization loss caused by decrease of surface charge repulsion and increasing van der Waals force.[159] Clustering leads to wider extinction curves, making the scattering of objects in the dispersion are more polydisperse due to the formation of aggregates, whereas the present calculations do not consider polydispersity.[105] Particles with incompletely closed gold nanoshells also have different extinction spectra and broader peaks which shift into the infrared direction, [159,160,237]and differ in this aspect from particles with homogenously closed shells.

The calculated absorption band with air as medium shows a quadrupole resonance peak at 540±3 nm. The maximum extinction peak from the dipole resonance was at 650±2 nm, and the scattering spectrum dominates over the absorption spectrum. Although the measured extinction peak was in a similar range as the calculated extinction peak, the measured peak was too weak to be compared with the calculated spectrum due to particle aggregation on the substrate.

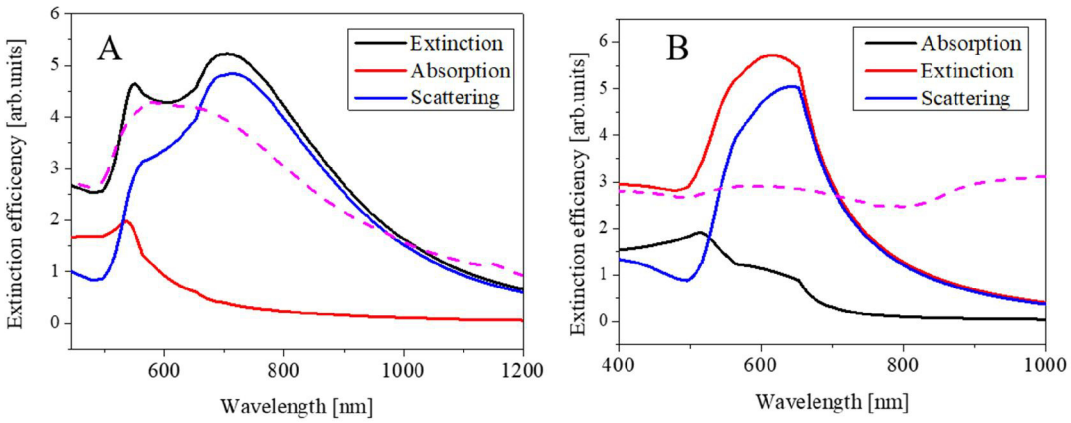

Figure 4.47 A: Measured extinction spectrum and calculated extinction, absorption, and scattering spectra of sample UC_112@Au_shell in water (r core = 56 nm and r total =86 nm) and B: Measured extinction spectrum and calculated extinction, absorption and scattering spectra of sample of UC_112@Au_shell on a glass substrate (r core = 56 nm and r total = 86 nm). The dashed magenta lines are the measured extinction spectra.

Corresponding extinction spectrum measurements and calculations of the extinction, absorption, and scattering spectra were also carried out for sample UC_321@Au_shell_A with air and water as medium. The best agreement between the measured and calculated extinction spectrum with water as background was obtained for a core radius of 161 nm and a total radius of 209 nm, which are exactly the sizes obtained from the SEM measurement (see Figure 4.48). The calculated spectrum shows a broad dipolar resonance peak, which is typical for a thick gold shell.[202] Due to core-less smaller gold particles, the measured extinction spectrum deviated from the calculated extinction spectrum and showed a single narrower dipole resonance peak at 580±5 nm, whereas the calculated spectrum showed a broader peak in this wavelength range. The gold coating of the sample was not homogenous, as indicated in SEM by small visible silica surface areas, which were not fully covered by gold (see Figure 4.46.C). This can lead to different extinction spectrum than that of the fully-coated particles. In the measured spectrum there is a peak at 940±2 nm, which could be caused by possible aggregation of the particles.

As in the case of sample UC_112@Au_shell, the calculated scattering spectrum dominates over the absorption spectrum, and the quadrupole plasmonic mode in the absorption spectrum was almost non-visible due to the dominance of the broader and more intense dipole resonance peak.[105,237] The octupole mode was not observable in the measured and calculated extinction spectrum.

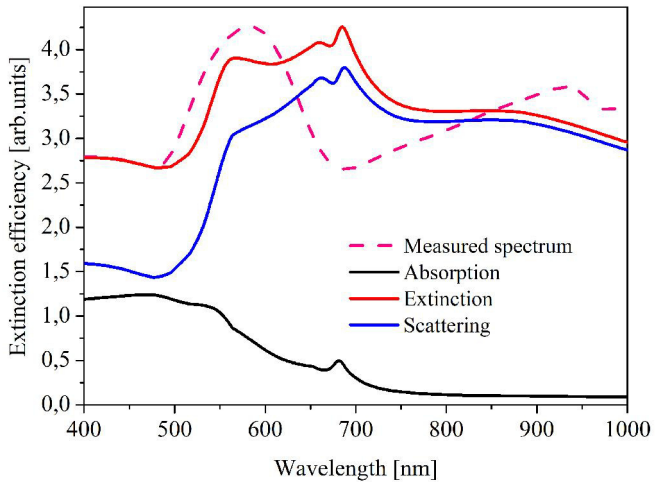

Figure 4.48 A: Calculated extinction, absorption, and scattering spectra and measured extinction spectrum (dotted magenta line) of sample UC_321@Au_shell_A in water. The input core radius was 161 nm and total radius was 209 nm.

It was not possible to present a measured extinction spectrum on a glass substrate for UC_321@Au_shell_A due to high clustering, hence a calculated extinction spectrum was waived for this case.

4.2.4 Characterization of plasmon influenced upconversion emission by gold nanoshell on silica coated UCNP

4.2.4.1 Upconversion and decay rate measurements of gold shelled silica coated UCNP in solution and on a glass substrate

The upconversion luminescence of the gold-coated samples UC_112@Au_shell and UC_321@Au_shell_A were measured in dispersion and on a glass substrate after spin coating. The expected values of the field enhancement (FE), FE × yield which is the enhancement factor after

dimmed pump excitation, LDOS, $LDOS_{rad}$ for saturated pump excitation of the 540 nm and 654 nm emission based on theoretical calculations for each sample are listed in Table 4-6.

For comparison, these parameters were also calculated and listed in the same table for particles which were experimentally studied by Green et al.[175] These calculations are described in detail in chapter 4.2. Green et al. synthesized $NaYF_4$: Yb, Er nanoparticles with 25 nm diameter coated with a 12 nm thick amine-functionalized silica shell and a 12 nm thick gold shells.[238] In single particle measurements, they could observe a three times overall upconversion enhancement of the emission after excitation at 980 nm at a power density (P) of 4×10^4 W/cm^2 as well as shorter rise and decay times of the green and red emission. Figure 4.49 shows the contour plots of LDOS, $LDOS_{rad}$, and the yield of silica coated core and the corresponding gold shell thickness. The size structure of each samples and that reported by Green et al. listed in Table 4-6 are marked in these plots.

Table 4-6: Enhancement of the upconversion luminescence at 540 and 654 nm emission of the gold-coated samples after 980 nm excitation according to theoretical calculations introduced in chapter 4.2

Sample	**r_0 [nm]**	**t [nm]**	**FE**	**Emission at 540 nm [arb. unit]**				**Emission at 654 nm [arb. unit]**			
				LDOS	**$LDOS_{rad}$**	**yield**	**FE × yield****	**LDOS**	**$LDOS_{rad}$**	**yield**	**FE× yield****
Medium: water							$\times 10^{-3}$				$\times 10^{-3}$
UC_112@Au_shell	56±2	30±6	0.14	4.28	2.11	0.49	69.0	1.93	1.49	0.77	107.8
UC_321@Au_shell_A	160.5±8.0	48±5	0.028	0.67	5.49	8.19	229.3	5.49	2.7	0.49	13.7
UC_321@Au_shell_B	160.5±8.0	68±10	0.005	0.53	0.07	0.13	0.6	4.37	0.86	0.20	1.0
Comparison with NP of Green et al.[238]	24.5±3.0	12±7	0.13	51.93	9.62	0.19	24.7	31.58	11.12	0.35	45.5
Medium: air (on glass substrate)											
UC_112@Au_shell	56±2	30±6	0.035	5.44	2.52	0.46	16.1	1.71	1.03	0.60	21.0
UC_321@Au_shell_A	160.5±8.0	48±5	0.033	0.66	0.19	0.29	9.6	5.03	2.3	0.46	15.2
UC_321@Au_shell_B	160.5±8.0	68±10	0.006	0.53	0.064	0.12	7.0	4.24	0.74	0.17	1.0
Comparison with NP of Green et al.	24.5±3.0	12±7	0.036	102.22	8.94	0.09	3.2	9.79	0.87	0.09	3.2

*FE = field enhancement

** at dimmed pump excitation

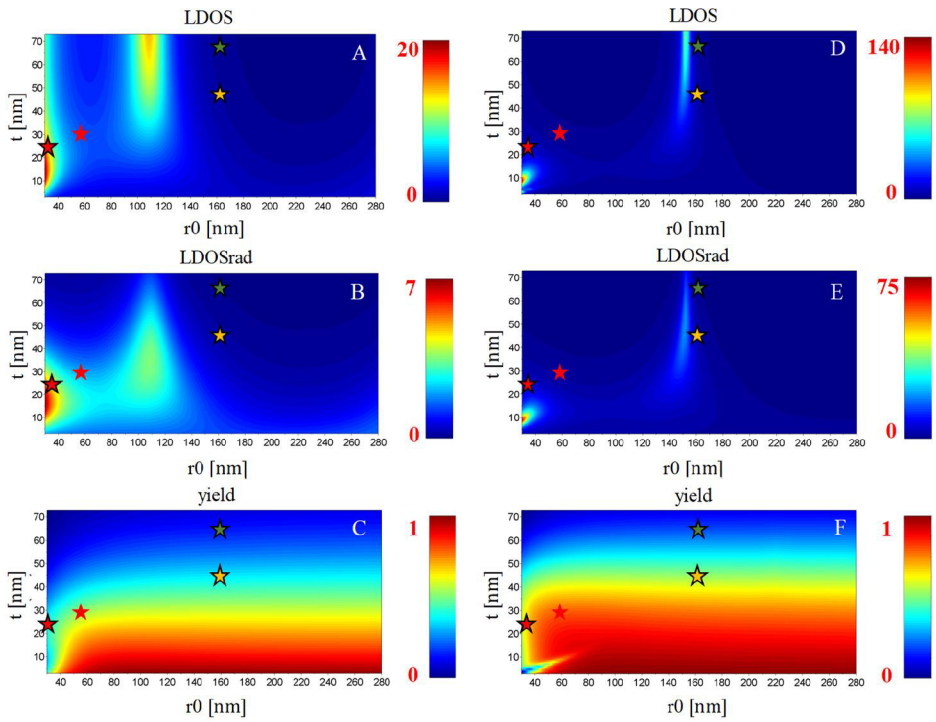

Figure 4.49: Top plots A and D: LDOS, middle plots B and E: $LDOS_{rad}$ and bottom plot C and F: yield $=LDOS_{rad}/LDOS$ of the 540 nm (left row) and 654 nm (right row) emissions. The structure of UC_112@Au_shell ($t = 30\pm6$ nm and $r_0 = 56\pm2$ nm) is marked by red stars, UC_321@Au_shell_A ($t = 48\pm5$ nm and $r_0 = 160.5\pm8.0$ nm) by yellow stars, UC_321@Au_shell_B ($t = 68\pm10$ nm and $r_0 = 160.5\pm8.0$ nm) by green stars and particles from Green et al. ($t = 12\pm7$ nm and $r_0 = 24.5\pm3.0$ nm) are marked by black framed red stars within each plot. The color bars on the right side of each contour plots represent the enhancement factor or yield of the depicted colors in the plots quantitatively.

Table 4-6 shows the calculated values of FE × yield of the gold-coated samples in two different media: water as solvent for the measurement in a dispersion and air as medium for the measurement on a glass substrate. As a reminder: in the limiting case of the dimmed pump excitation, the enhancement factor is proportional to the product of FE × yield, while in the limiting case of pump saturation excitation the enhancement factor is $LDOS_{rad}$. All values of FE × yield were multiplied by a factor of 10^{-3}, meaning there was only suppressed emission or quenching under dimmed pump excitation. At saturated pump excitation, an enhancement for the samples UC_321@Au_shell_A and UC_112@Au_shell is expected. Enhancement factors of 5.49 or 2.11 at 540 nm emission for the sample UC_321@Au_shell_A and UC_112@Au_shell respectively in water and under 980 nm excitation are expected. In air as medium, the corresponding values for these samples are 0.19 and 2.52. At 654 nm emission in water, the emission would be enhanced by a factor of 2.7 and 1.49 for the respective samples, while the enhancement factor would be 2.3 and 1.03 in air.

Sample UC_321@Au_shell_B has the weakest values for FE × yield and $LDOS_{rad}$ in measurement on a glass substrate, probably due to the large thickness of the gold shell which could hinder the excitation light from entering the sample as well as the exiting upconversion emission light. Overall the FE × yield values are low, even for the particles with the size parameters reported in the publication of Green et al.[175] It was reported in this publication that an overall emission enhancement by a factor three was observable at an excitation power density of 4×10^4 W/cm^2, which can be considered as saturated pump excitation. In the theoretical calculations, the enhancement factor of the green emission after saturated pump excitation was 8.92, and that of the red emission was 0.87, corresponding to a partial compression of the red emission.

Based on the calculated values, sample UC_112@Au_shell and UC_321@Au_shell_A were chosen as the most promising samples to be used for further upconversion emission measurements.

A test system for upconversion emission measurements on glass substrates and in dispersion with ethanol or water as solvent was established. The chosen samples were UC_Er_4@SiO_2_112 and UC_112@Au_shell, since the latter sample was the first system that was successfully coated by a closed gold shell. The upconversion spectra of the samples were measured in dispersion and on a glass substrate with spectrofluorometer FLS 980 (see chapter 3.2.6).

Figure 4.50 shows the upconversion spectra of UC_Er_4@SiO_2_112 and UC_Er_4@SiO_2_321 in dispersion and on a glass-substrate normalized to the emission at 654 nm. Both measurements

were important to determine which set-up was appropriate for further upconversion measurements. The $f_{g/r}$ of the sample UC_Er_4@SiO_2_112 in ethanol was 1.874±0.020 and decreased to 0.616±0.005 in the measurements on a glass substrate. The red emission decreased by 68±7 % upon measurements in ethanol compared to the one on a glass substrate. The $f_{g/r}$ of the sample UC_Er_4@SiO_2_321 in ethanol was 0.78±0.08 and 0.58±0.06 on a glass substrate. The intensity of the green emission in ethanol was 22±2 % higher than on the glass substrate. Upconversion measurements of UC_112@Au_shell and UC_321@Au_shell_A in water delivered low signals and high scattering. Hence, for the next upconversion experiments, measurement on a glass substrate was the main focus.

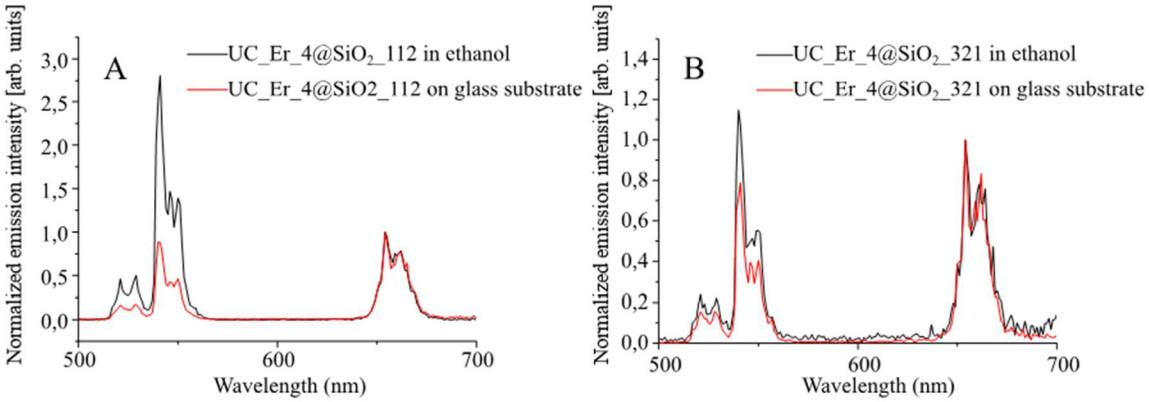

Figure 4.50: Upconversion fluorescence measurements of A: UC_Er_4@SiO2_112 in ethanol (black line) and on a glass substrate (red line) and B: UC_Er_4@SiO2_321 in ethanol (black line) and on a glass substrate (red line). Excitation wavelength was 980 nm and excitation power density was 75 W/cm².

Figure 4.51 shows the fluorescence spectra of UC_Er_4@SiO_2_112 (black line) and UC_112@Au_shell on a glass substrate (red line) shown. There is a red-shift of the emissions of the sample with the gold shell, which was likely caused by the set-up of the measurement devices, though the exact cause was not known. These shifts were not observed in single particle measurements on a glass substrate. The emissions of UC_112@Au_shell decreased compared to UC_Er_4@SiO_2_112; the green emission decreased by 56±6 %, while the red emission decreased by 51±5 %. The $f_{g/r}$ of UC_Er_4@SiO_2_112 ($f_{g/r}$ = 0.61±0.06) was slightly higher than that of UC_112@Au_shell ($f_{g/r}$ = 0.55±0.06), where the quenching of the green emission of the latter sample was higher compared to the red emission. Theoretical calculations on glass substrate indicate suppressed emission on both green and red emissions at dimmed pump excitation, as confirmed by the measured upconversion fluorescence spectra. The calculated absorption spectrum (see Figure 4.48.B) also predicted absorption peaks at 515-560 nm,

indicating the absorption of upconversion green emission energy by the gold shell, which could be the cause for the stronger weakening of the green emission than that of the red emission.

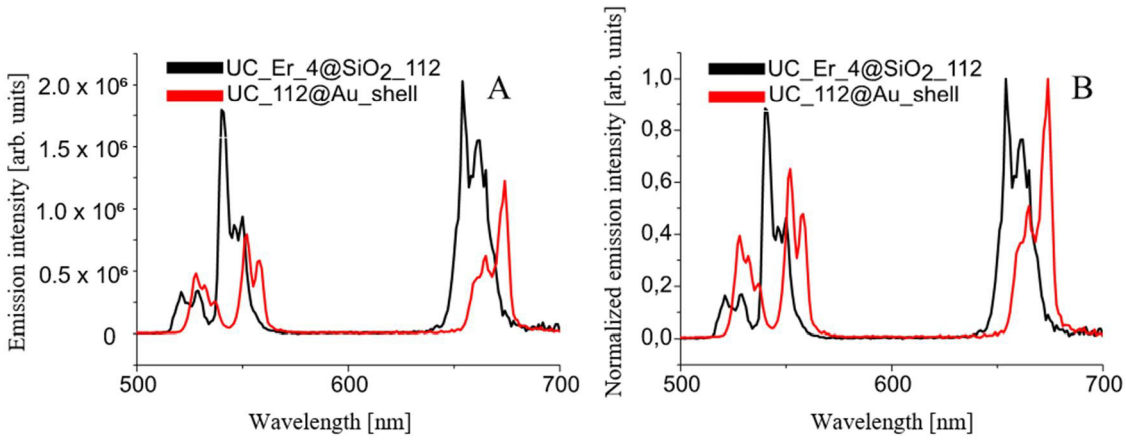

Figure 4.51 A: Upconversion fluorescence spectra of UC_Er_4@SiO₂_112 (black line) and UC_112@Au_shell on a glass substrate (red line) and B: the same spectra normalized to the red emission. The excitation wavelength was 980 nm, the excitation power density was 20 W/cm² for UC_Er_4@SiO₂_112 and 75 W/cm² for UC_112@Au_shell.

The excitation power density was almost 4 times higher for the upconversion measurement of UC_112@Au_shell than the one used for the measurement of silica-coated UCNP, since more energy was needed to excite the Yb^{3+}-ions which are now, in addition to the silica shell, shielded from external excitation light by the gold shell. However, this should not heavily influence the red and green emission intensity and $f_{g/r}$-ratio of UC_112@Au_shell. Below P = 100 W/cm^2 similar population dynamics of each excited state on UCNP would occur, which would minimally influence the value of $f_{g/r}$ of the UC-emissions.[239] According to the calculations, the values for FE × yield should be 0.016 for the green emission and 0.021 for the red emission, indicating suppressed emissions of 1.6 % and 2.1 % respectively. In the measurements, one can only see quenching of both emissions.

Figure 4.52 shows the decay curves of the upconversion emissions of the samples UC_Er_4@SiO_2_112 and UC_112@Au_shell at 545 nm and 655 nm emission. The rise times and consecutive decay times of both the green and red emission were shortened after coating with a gold shell, indicating an increase of radiative relaxation after coating with the gold shell. The same effect was also observed by Green et al. for 25 nm $NaYF_4$: Yb, Er particles coated with 12 nm silica shell and 12 nm gold nanoshell.[175] The particles investigated by Green et al., like UC_112@Au_shell, would experience dipole mode enhancement at saturated pump excitation (P = 4 × 10^4 W/cm^2) according to calculations. Theoretical calculations predicted $LDOS_{rad}$ enhancement of 8.94 and 0.87 at 540 nm and 654 nm, respectively. In the literature a

five- and two-times emission enhancement at 540 and 654 nm emission on a quartz substrate were observed, which corresponded to the general stronger enhancement of the green emission compared to the red emission predicted in calculations.

The FE × yield values of the green and the red emission were 0.161 and 0.021 in sample UC_112@Au_shell, respectively, as predicted, indicating suppressed emissions. The decrease of the overall emission intensities was likely caused by enhanced non-radiative relaxation due to scattering of gold on the glass substrate and reabsorption of the emission energies by the gold shell. [22, 203] The decrease of the green emission at P = 75 W/cm^2 was 75±8 %, while the decrease for the red emission was 66±7 % after coating with a gold shell.

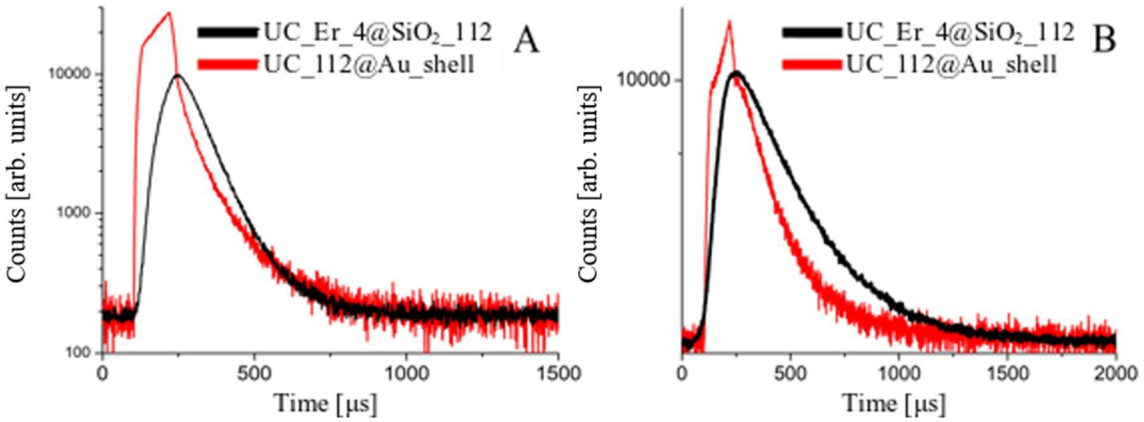

Figure 4.52 A: Decay of the upconversion fluorescence of the samples UC_Er_4@SiO$_2$_112(black line) and UC_112@Au (red line) at 540 nm emission; B: decay of the upconversion fluorescence of the samples UC_Er_4@SiO$_2$_112 (black line) and UC_112@Au (red line) at 655 nm. All four measurements were carried out with particles on a glass substrate; the excitation wavelength was 980 nm.

Scattering effects were observed in the upconversion spectra of the UC_Er_4@SiO$_2$_321 and UC_321@Au_shell_A on a glass substrate and in dispersion due to the clustering of the particles, and hence no reliable spectra could be depicted.

Conclusively, upconversion fluorescence measurement on a glass substrate with FLS 980 ensemble delivered shifted emission peaks and low signals for the gold-shelled sample. Hence, single particle measurements with a confocal setup on the gold shelled samples will be discussed in the next chapters.

4.2.4.2 Upconversion and decay rate measurements of gold-coated UCNP on single particle measurements set up

Dimmed pump excitation delivered suppression of enhancement for UC_112@Au_shell on a glass substrate as calculated and measured in the previous chapter. In dispersion, the same sample and sample UC_321@Au_shell_A showed weak emission signals and high scattering as well as shifting of emission peaks, which was probably due to the measurement set up. On glass substrate the UC_321@Au_shell_A sample could not be measured properly due to clustering of the gold shell on the substrate. Because of these reasons, a general upconversion emission enhancement of the particles could not be properly observed. Hence, single particle measurements on a glass substrate with subsequent averaging of the decay rates and emission of the single particles were carried out. Single particle measurements were necessary, as this approach allows for the elimination of the aggregation effects of the closely located gold shell from different particles after spin coating, which would cause different electric field distributions and hence, different plasmon-influenced upconversion emission characteristics in common measurements compared to the cumulated emission measurements of single particles.[176] The sensitivity of the upconversion luminescence to different architectures of gold shell-silica core systems and the surface plasmon resonance can be more accurately observed in single particle measurements.[203] For this purpose, UC_112@Au_shell and UC_321@Au_shell_A are spin coated on a glass substrate and the UC-luminescence were observed through a confocal microscope at 980 nm excitation (see experiments set up in chapter 3.2.7).

4.2.4.2.1 Upconversion and decay rate measurements of gold-coated UC_Er_4@SiO_2_112 with a single particle measurement set up

The $LDOS_{rad}$ enhancement contour plot (see Figure 4.49) was chosen as reference of the emission intensity enhancement in single particle measurements, as a high excitation power density (1.6 MW/cm^2) was employed. Based on the calculated contour plot of sample UC_112@Au_shell (t = 30 nm, r_0 = 44 nm) in Figure 4.49, an enhancement factor of 2.52 would be expected at the 540 nm emission, and a factor of 1.03 at the 655 nm emission.

Figure 4.53 shows the upconversion spectra of UC_Er_4@SiO_2_112 and UC_112@Au_shell in single particle measurements. The green emission intensity of UC_112@Au_shell was 38±4 % lower than that of UC_Er_4@SiO_2_112, whereas the red emission intensity was 56±6 % lower than that of the non-gold shelled sample. The $f_{g/r}$ was increased after gold shell growth. The $f_{g/r}$ of sample of UC_Er_4@SiO_2_112 was 0.49±0.05 and the value increased by 41±4 %

to 0.68±0.07 for sample UC_112@Au_shell, indicating a higher weakening of the red emission for the gold shelled samples in single particle measurements compared to the green emission. Theoretically, the $LDOS_{rad}$ enhancement of the green emission after gold coating would be higher than that of the red emission. However, both emissions experienced quenching of different degrees. Quenching can be induced by an increase of non-radiative energy transfer of the UCNP emission to the gold shell or by absorption of the upconversion emission energy by the gold shell, which promotes an increase of non-radiative relaxation of the excited photons in the excited states ($^4S_{3/2}$ or $^4F_{9/2}$) to the ground states of the Er^{3+} ions. Presumably, in the case of UC_112@Au_shell, the non-radiative rate dominated over the radiative rate relaxation in each emission, however, since the green emission theoretically has a higher $LDOS_{rad}$ value, making the quenching effect weaker compared to that of the red emission.

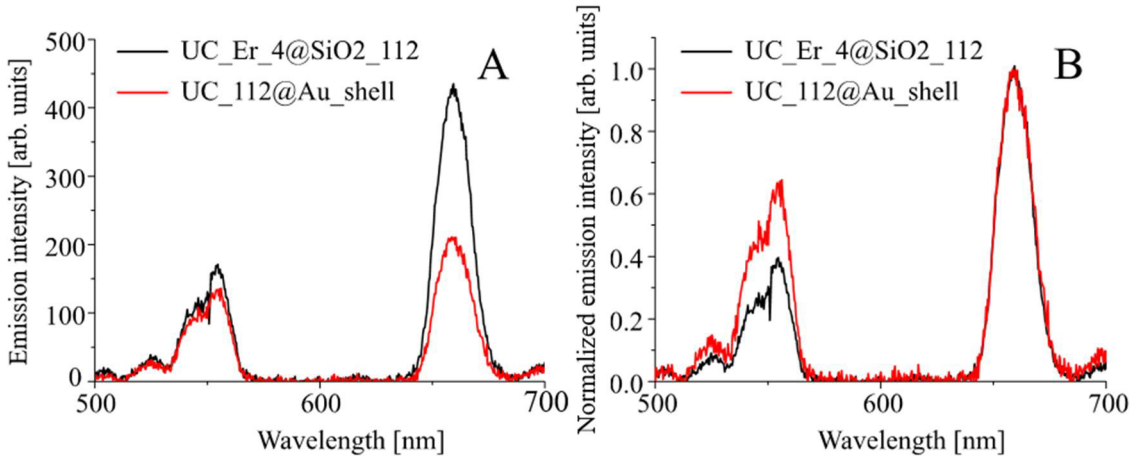

Figure 4.53 A: Upconversion emission spectra of UC_Er_4@SiO_2_112 (black line) and UC_112@Au_shell (red line) from single particle measurements after excitation at 980 nm at 50 seconds light exposure time. Figure B is the red emission-normalized spectra with the same excitation parameters. The excitation power density was 1.6 MW/cm^2.

The decay time of the green and red emission of the samples UC_Er_4@SiO_2_112 and UC_112@Au_shell were measured after 8000 (8k) pulses and 16000 (16k) consecutive pulses, which represents lower and higher power density, respectively, with both power densities still in the range of saturated pump excitation (P = 1.6 MW/cm^2; see the introduction to chapter 4.2 about theoretical calculations of core-shell size ratio for plasmon enhancement). Each pulse (laser puls rate = 80 × 10^3 MHz, pulse to pulse time = 12.5±0.5 ns) led to average excitation time of 100 and 200 µs, respectively. The decay rate value of sample UC_Er_4@SiO_2_112 was based on mean values of 5 particles, whereas the decay rate value of UC_112@Au_shell was

based on mean values of 12 particles. Representative images of single particles of UC_112@Au_shell in the confocal setup are shown in Figure 4.54.

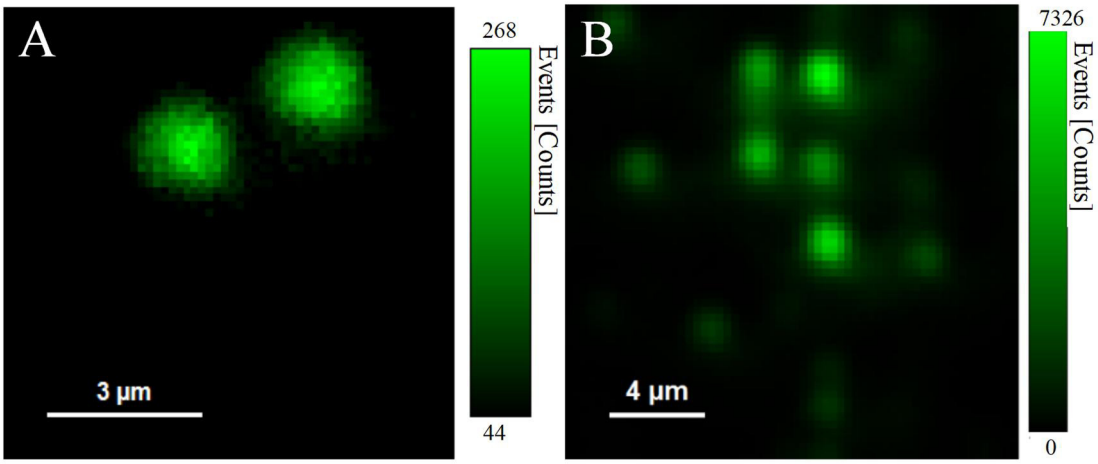

Figure 4.54: Detection of single particles in the confocal measurements. A is the confocal fluorescence image of two particles in sample UC_Er_4@SiO_2_112, and B is the confocal fluorescence image of particles in sample UC_112@Au_shell on a glass substrate, measured on air after sputtering the particles on a glass substrate through spin coating. The excitation wavelength was 980 nm, the excitation power density 1.6 MW/cm^2.

Figure 4.55 shows a chart bar of averaged decay times of UC_Er_4@SiO_2_112 and UC_112@Au_shell at higher (after 16k laser pulses) and at lower power density (after 8k laser pulses) at pump saturated excitation. The decay rate at all emission wavelengths in the single particle measurements decreased (i.e., longer decay time results) after coating with a gold shell. The decay time of the green emission of UC_112@Au_shell increased by 60±7 % for lower power density and by 50±1 % for higher power density compared to UC_Er_4@SiO_2_112, whereas the decay time of the red emission of UC_112@Au_shell increased by 79±11 % for lower power density and by 70±8 % for higher power density compared to UC_Er_4@SiO_2_112. The decay time of the green emission of both samples was slightly higher at higher power density than at lower power density, whereas the decay time of the red emission was higher for lower power density.

The increase of decay time was accompanied by emission quenching, which indicates an increase of the non-radiative decay rate for both emissions, either due to absorption of upconversion emission energy by the gold shell or by a non-radiative energy transfer of the emission to the gold shell.[203, 240]

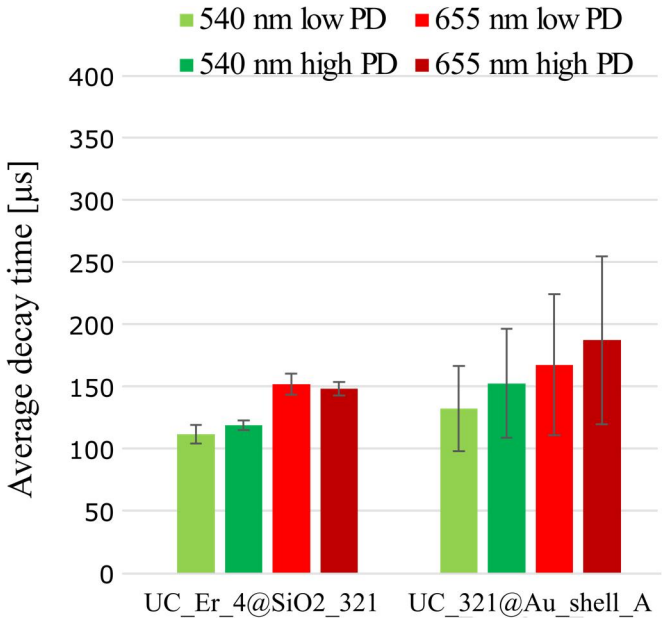

Figure 4.55: Average decay rates of green (540 nm; green bars) and red (655 nm; red bars) emission of UC_Er_4@SiO_2_112, UC_112@Au_shell after 980 nm excitation in single particle confocal measurements after low (8k laser pulsed length) and high (16k laser pulsed length) power density (PD). Both are considered pump saturated excitation.

Presumably the $LDOS_{rad}$ enhancement (2.52 at the green emission and 1.03 at red emission), was weaker due to the emission energy absorption by the plasmonic metal shell as shown in the calculated absorption spectrum, where an absorption peak of 515-560 nm and weaker absorption peak at 645±2 nm are shown, which each resonates to the green and red emission energy, respectively.

Furthermore, absorption of excitation light by metal plasmons could promote the thermal quenching effect, which is insignificant at lower excitation power density, but becomes significant at the high excitation power density that was utilized in the single particle measurements.[203] For both utilized power densities (8k and 16k pulses), thermal quenching may have occurred as both power densities were high. Accordingly, an increase of the decay time at higher excitation power density (16k pulses), which is one of the signs of quenching, of the green emission was higher than at lower pulses.

By correlating the longer decay time and the luminescence quenching of sample UC_112@Au_shell compared to sample UC_Er_4@SiO_2_112, one can assume that luminescence quenching was caused by an increase of the non-radiative relaxation in the Er^{3+}-excited state's transition due to absorption or energy transfer of Er^{3+}-emission to the gold shell, which prolonged the emission lifetime and induced quenching. The increase of the non-radiative rate dominates over the rise of the radiative rate due to surface plasmon-coupled

emission, which in theoretical calculations should have resulted in a slight enhancement of the emissions.

4.2.4.2.2 Upconversion and decay rate measurements of gold-coated UC_Er_4@SiO_2_321 with a single particle measurement set up

As in the case of UC_112@Au_shell, the enhancement of UC_321@Au_shell_A is considered as being proportional to the $LDOS_{rad}$ value due to saturated pump excitation in the confocal measurements (see Figure 4.49). According to the contour plots of LDOS and $LDOS_{rad}$ at 655 nm emission, the core-shell structure of UC_321@Au_shell_A could yield a slight enhancement in the LDOSrad at 654 nm emission. Theoretical calculations predict an enhancement factor of 0.19 at 540 nm emission, and 2.3 at 654 nm emission, which are consistent with suppressed enhancement and slight enhancement, respectively.

Figure 4.56 shows upconversion spectra of the samples UC_Er_4@SiO_2_321 and UC_321@Au_shell_A from single particle measurements. The emission intensities after gold shell coating decreased: the green emission intensity of sample UC_321@Au_shell_A was 43±4 % lower than that of UC_Er_4@SiO_2_321, whereas the red emission intensity decreased by 67±7 %. The $f_{g/r}$ of both systems were increased due to gold shell growth. The $f_{g/r}$ of UC_Er_4@SiO_2_321 was 0.40±0.05 and the value increased by 83±8 % to 0.73±0.07 in UC_321@Au_shell_A, indicating a stronger weakening of the red emission in UC_321@Au_shell_A compared to the green emission. Although the $LDOS_{rad}$ value in the calculations for the red emission is theoretically higher than for the green emission, the degree of weakening of the red emission was higher than for the green emission, indicating a higher increase of non-radiative decay for the red emission compared to the green emission. The calculated extinction spectrum of UC_321@Au_shell_A showed a strong extinction peak at 550±10 nm (see Figure 4.48.B), which indicates a plasmon frequency that resonates with the green emission, thus preventing the higher quenching of the green emission intensity compared to the red emission.

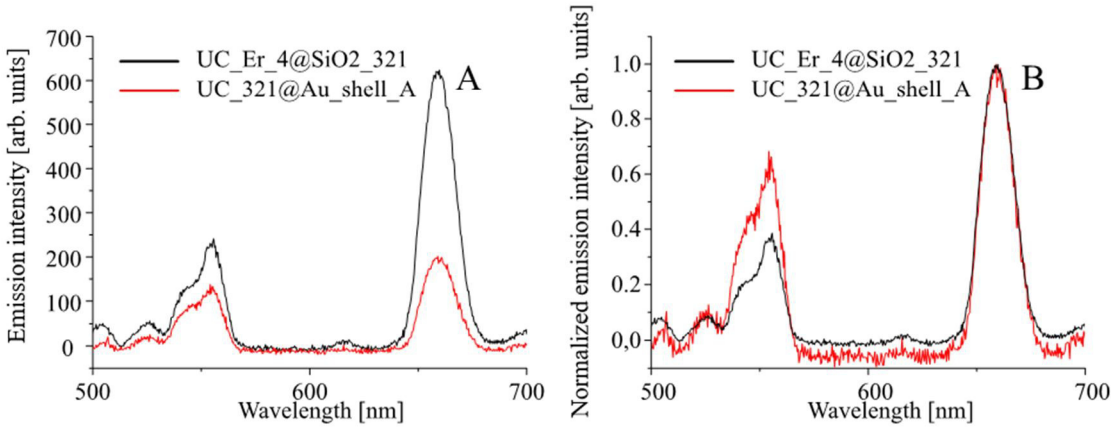

Figure 4.56: Upconversion emission spectra of UC_Er_4@SiO_2_321 (black line) and UC_321@Au_shell_A (red line) from single particle measurements after excitation at 980 nm at 40 % of the average power density and 50 seconds light exposure time. Figure B is the red emission normalized spectra with the same excitation parameters. The average excitation power density was 1.6 × 10^6 W/cm^2.

The average decay rate of UC_Er_4@SiO_2_321 was calculated based on measurements of 7 particles, whereas the decay rate of UC_321@Au_shell_A was based on an analysis of 6 different particles (see Figure 4.57 for confocal fluorescence image of the particles).

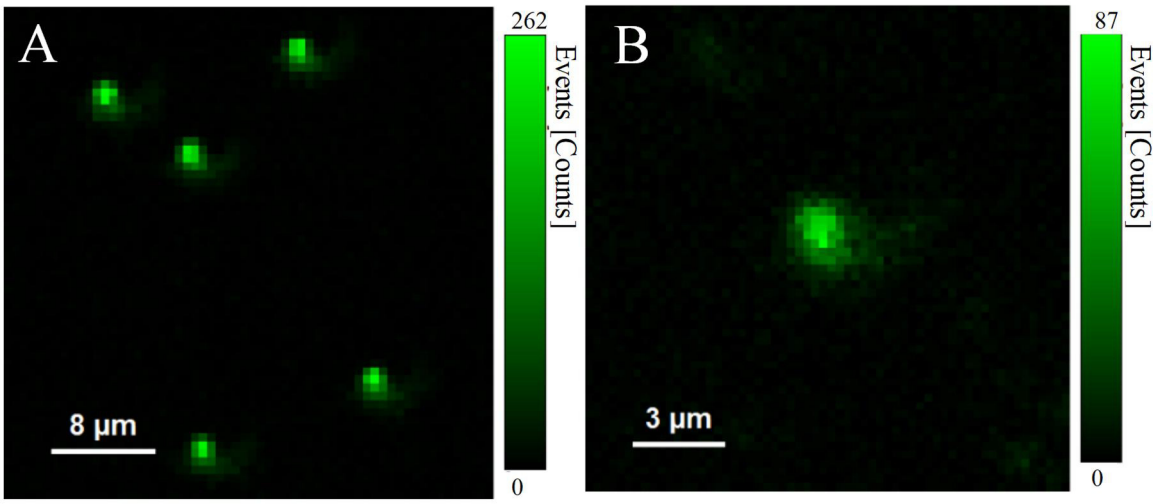

Figure 4.57: Detection of single particles in the confocal measurements. In Figure A is the confocal fluorescence image of five particles in sample UC_Er_4@SiO_2_321, and on Figure B is the confocal fluorescence image of one particle in sample UC_321@Au_shell_A on a glass substrate, measured on air after sputtering the particles on a glass substrate through spin coating. The excitation wavelength was 980 nm and the average excitation power density 1.6 × 10^6 W/cm^2.

Figure 4.58 shows bar charts of the average decay time of UC_Er_4@SiO_2_321 and UC_321@Au_shell_A at 540 and 655 nm emission after pump saturated pump excitation at higher (16 k) and lower (8k) power density (see chapter 4.2.4.2.1) for measurement parameters), respectively. The decay time of the green emission in sample UC_321@Au_shell increased by 17±5 % for the lower power density and by 29±8 % for the higher power density compared to UC_Er_4@SiO_2_321. The decay time of the red emission of UC_321@Au_shell increased by 10±3 % for lower power density and by 27±10 % for higher power density. Emission quenching, which is accompanied by an increase of decay time or luminescence lifetime, is usually caused by an increase of the non-radiative energy transfer from Er^{3+} ions to metal plasmon particles or emission energy absorption by the metal plasmon system, causing an increase of non-radiative rate.[203, 240]

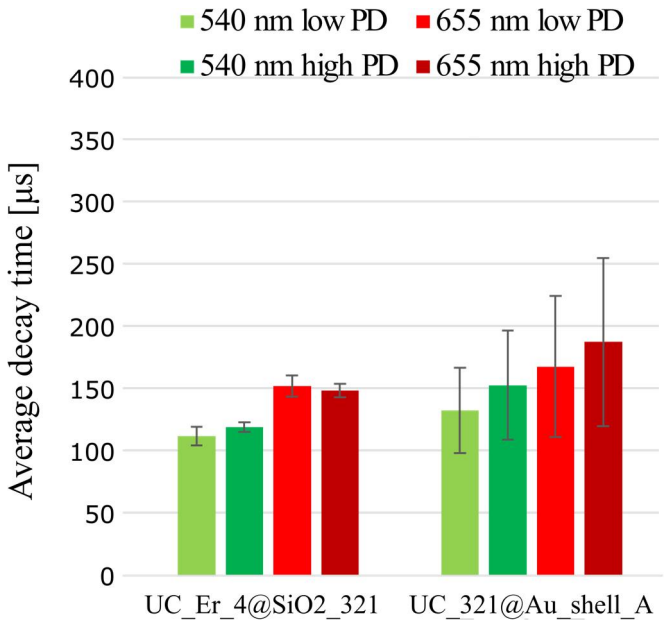

Figure 4.58: Average decay rates of the green (540 nm; green bars) and red (655 nm; red bars) emission of the samples UC_Er_4@SiO_2_321 and UC_321@Au_shell_A after measurements at low (8k laser pulsed length) and high (16k laser pulsed length) power density (PD). Both are considered pump saturated excitation. The excitation wavelength was 980 nm.

The increase of both, the decay time of the green and red emission is not as intense as in the UC_Er_4@SiO_2_112 system. As in the case of sample UC_112@Au_shell, a thermal quenching effect, indicated by an increase of lifetime at different excitation energies, should also be considered as a quenching factor for high excitation power densities in the single particle measurements. In the case of UC_321@Au_shell_A a cavity mode enhancement in the red emission is expected. A very thick gold shell could, however, cause stronger cavity

confinement, where the thick shell obstructs the excitation photons from reaching the UCNP and also preventing the emitted photons from being detected.[31]

4.3 Investigation of the luminescence resonance energy transfer effect at the interactions between UCNP and rhodamine B isothiocyanate

UCNP can be used in biosensors or bioimaging applications due to their distinct and narrow emission bands,[111] low toxicity, minimum photodamage,[241] high sensitivity, and high penetration depth.[241] The main advantage of using NIR light excitation, contrary to commonly used UV-VIS light excitation in the downconversion fluorescence of most fluorophores, is the prevention of auto-fluorescence in the surrounding biological systems.[45, 241] Despite many possible applications for *in vivo* bioimaging applications, multimodal bioimaging agents, drug or gene delivery agents (see extensive reviews by Wolfbeis et al.[242] or Duang et al.[243]), UCNP alone is not suitable for biological applications, due to their low quantum yield, which is a magnitude lower than for commonly used chromophores in biological applications under similar excitation power.[45] Liu et al.[244], for example, observed that the *in vivo* detection limit of UCNP was one magnitude lower than for quantum dots. Moreover, UCNP is not sensitive for the detection of O_2-, pH- or metal ions in a biological environment. To circumvent this problem, the emission of UCNP can be tuned to certain wavelengths by coupling to various chromophores or dyes for sensor applications. Through excitation in the NIR-range and the consecutive energy transfer to the coupled dyes or chromophores that have absorption wavelengths in the range of upconversion emission, one can excite the dyes for metal detection, or as O_2- or pH-dependent sensor.

For the investigation of a possible FRET effect from upconversion fluorescence emission to a nearby dye, rhodamine B isothiocyanate (RBITC) was coupled in the silica shells coated on UCNP as core. RBITC was chosen, as its excitation energy is in the range of green upconversion emission of $NaYF_4$: Yb, Er nanoparticles (see Figure 4.59). The amount of RBITC in the silica shells was varied to evaluate the influence of coupled-dye quantity to the FRET emission intensity. The value of FRET efficiency (E_{FRET}), which is the part of the excited photon energy of the donor (i.e., Er^{3+}-ions) that is transferred non-radiatively to the acceptor (i.e., dye), is proportional to the inverse of the sixth power of the distance between the donor and the acceptor. This distance dependency is often characterized by the Förster radius (R_0), which is a donor-acceptor distance where 50 % transfer efficiency is reached (see chapter 2.3).

The Er^{3+} ions act as donors for RBITC absorption and are spread homogenously inside and on the surface of the UCNP. The RBITC dye molecules are also spread homogenously inside and

on the surface of the silica shell. This means that the distance of each donor-acceptor varies. The emission of each acceptor resulting from FRET-excitation can vary in its intensity, depending on the location of Er^{3+} ions in the UCNP and the type of dye inside the silica shell. E_{FRET} also depends on the size of the UCNP, since more Er^{3+} ions are located in the inner part of the UCNP with increasing UCNP size. Thus, the distance between these inner ions and the dye increases possibly further than the Förster radius, leading to a decrease of E_{FRET}.[47] A scheme of the dye coupled system is depicted in Figure 4.60, and the energy transfer mechanism of the FRET transfer is shown in Figure 2.8.

In Figure 4.59, an overlap between the RBITC absorption, the RBITC fluorescence emission spectrum after excitation at 540 nm, and the upconversion emission spectrum of $NaYF_4$: Yb, Er nanocrystals after excitation at 980 nm is shown. The green emission of the UCNP at 540 nm can be transferred to a neighboring RBITC molecule, which has an absorption wavelength in the range of the upconversion fluorescence emission. At an excitation of 980 nm, within a suitable distance between UCNP and dye, excitation of the UCNP would result in FRET emission in the range between 560-580 nm.

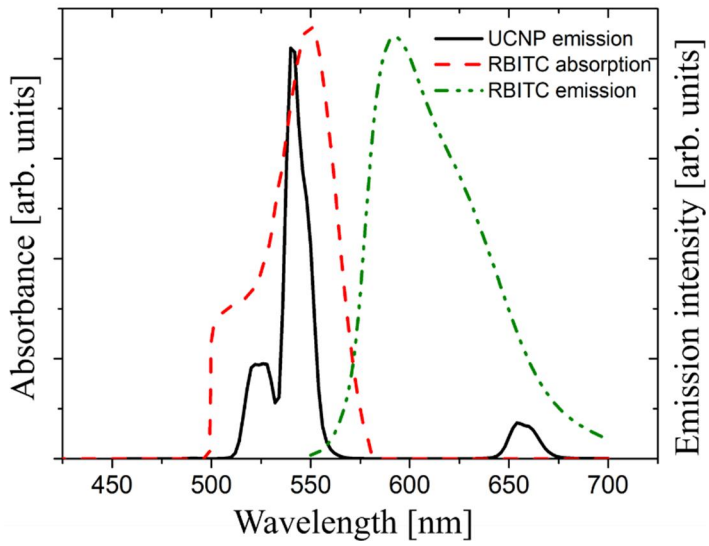

Figure 4.59: Spectral overlap of RBITC absorption, RBITC fluorescence emission after excitation at 540 nm, and UC emission of a typical $NaYF_4$: Yb, Er nanoparticles after excitation at 980 nm in cyclohexane.

As in previous chapters, the UCNP consisted of $NaYF_4$: 18 % Yb, 2% Er cores which are coated by a dye-doped silica shell. The dye is covalently bound on and into the silica shell. The synthesis of the coupling product of RBITC-APS, which was covalently bound into the silica shell is described in Figure 4.60. and described in chapter 3.6.3 following protocols from the literatures.[158, 245] The UCNP core size of 24 nm could provide a high FRET efficiency with the rhodamine dye.[47] Smaller particles (d < 15 nm) have bigger surface-to-volume ratios which

could lead to surface quenching, due to interactions of surface Er^{3+} ions with high vibrational energy of ligands or solvents, leading to the non-radiative energy loss of the excited photons.[246] Bigger particles (d > 30 nm) have a lower surface-to-volume ratio, which means there are fewer surface Er^{3+} ions which contribute to high-efficiency FRET, since the surface Er^{3+}-ions are the nearest ones to the bound dyes in the silica shell, and can consequently provide the highest E_{FRET}. Hence, UCNP with a diameter between the two size limits (15 and 30 nm) were chosen as core for the FRET experiments.

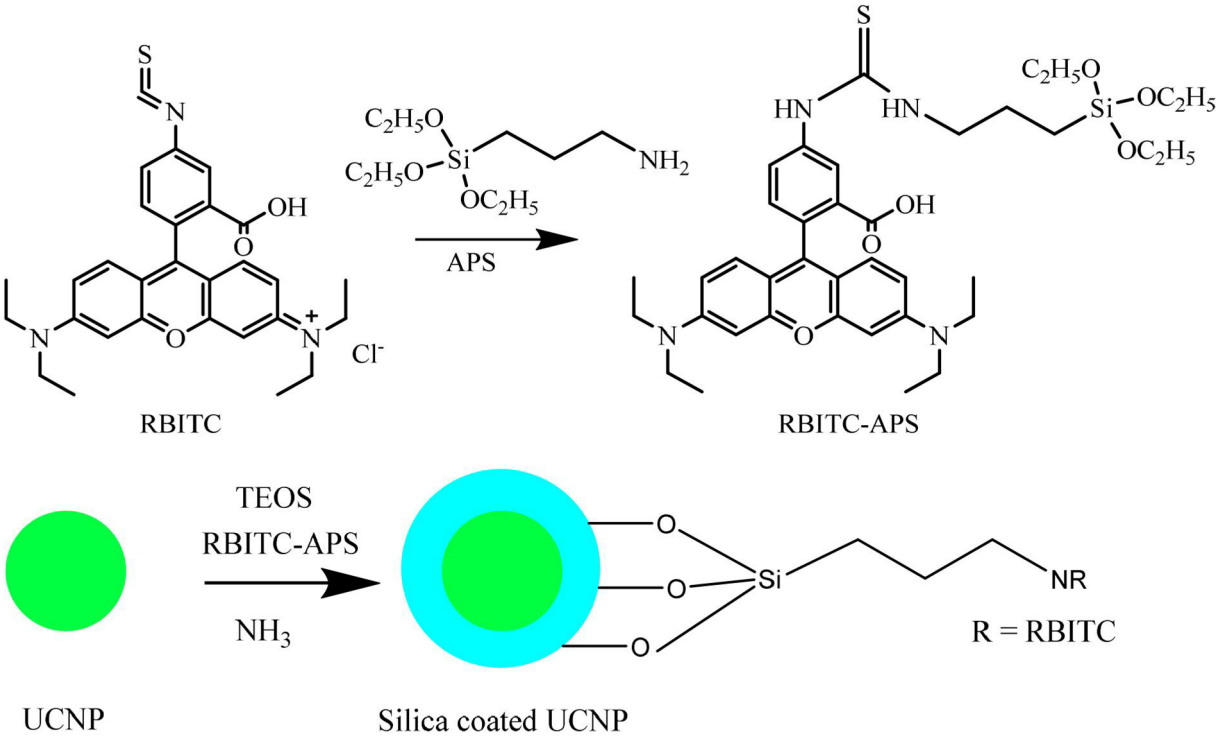

Figure 4.60: Reaction equation of coupling of RBITC with APS (top image); and general scheme of coupling of RBITC-APS into the silica shell (bottom image).

RBITC-APS was added to a reverse microemulsion dispersion consisting of UCNP cores, the surfactant Igepal CO-520, and TEOS in cyclohexane. The formation of the silica shell, except for the dye coupling, is similar to the silica shell formation described in chapter 4.2.1.1. After silanization activation with ammonia, the dye was coupled covalently inside and onto the silica shell (see Figure 4.61).[247-248] The amine group in the APS was coupled to the dye on one side and the siloxane group was coupled to the hydrolyzed TEOS and underwent a polycondensation reaction until the formation of the silica shell. The nanoparticles were purified by repeated sedimentation and redispersion until the supernatant was free of fluorescent dye. After this procedure leaching of the dye was not observed at any given time, thus supporting the assumption that the dye covalently bound into the silica shell.

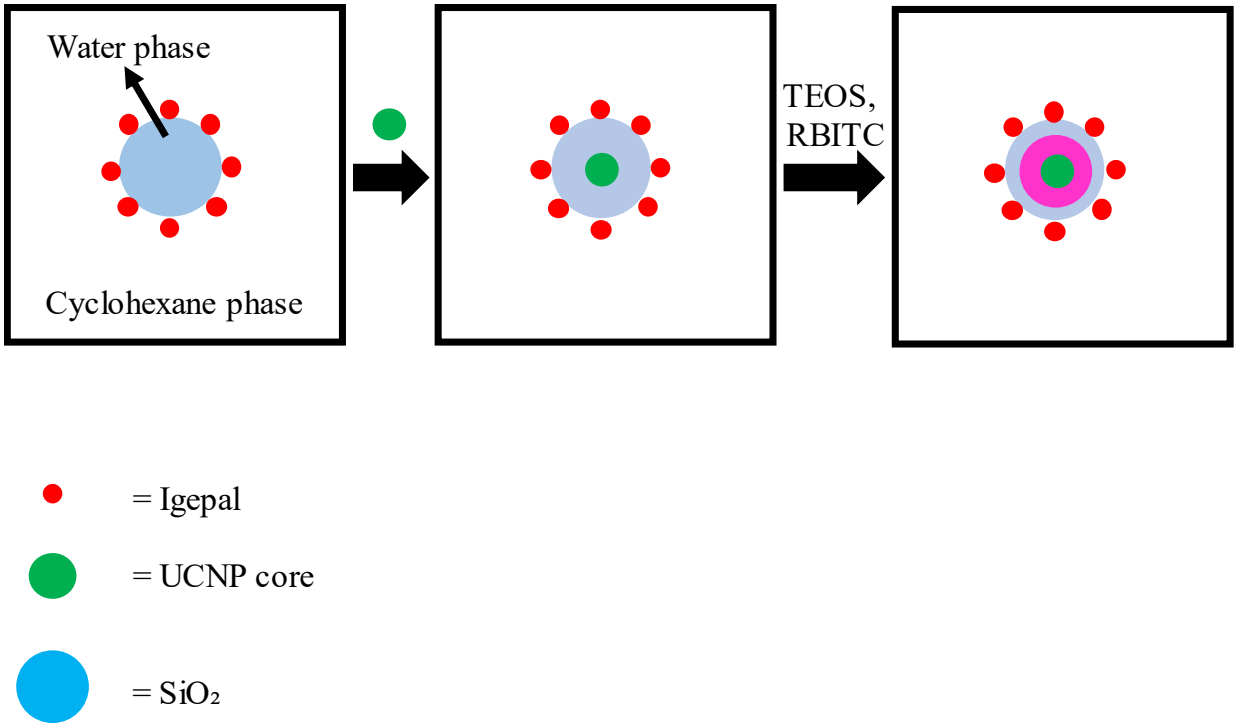

Figure 4.61: Studied dyed/UCNP systems. Direct growth of an RBITC-doped shell on a UCNP core. Red spheres: Igepal CO-520 as surfactant, green sphere: UCNP core, pink sphere: silica shell coupled with RBITC-APS and blue: undoped silica shell. The UCNP core was added to a micelle containing an aqueous phase formed by Igepal CO-520 as surfactant. TEOS and RBITC-APS were added consecutively and finally the growth of the silica shell is initiated upon addition of ammonia water.

A thin silica shell of < 5nm with an optimal loading of dye would be favorable for the FRET effect as the Förster distance for RBITC and Er^{3+}-ions in $NaYF_4$: Yb, Er is 2.5-5 nm.[47] Ideally, the silica shell thickness should be below the above-mentioned Förster radius. Based on past experiments, the thinnest silica shell coupled with dye, that could be synthesized with minimal particle aggregation was of 5±1 nm. Thus, this particular thickness was aimed for during the FRET experiments.

The UCNP core UC_Er_4 (see chapter 4.2.1.1) was coated with a silica shell containing covalently bound RBITC-APS. The amounts of TEOS, RBITC-APS as well as the calculated RBITC per particles are listed in Table 3-8. The amounts of TEOS and UCNP core were the same for all samples, and only the RBITC-APS amount was varied (see Table 4-8). There were in total 5 samples, which were named based on increasing dye concentration per particle or per volume of silica as: UC_Er_4@RBITC_1, UC_Er_4@RBITC_2, UC_Er_4@RBITC_3, UC_Er_4@RBITC_4, and UC_Er_4@RBITC_5

The particles were dissolved in 0.43 M NaOH (EtOH: NaOH = 1:1 v/v) to determine the amount of dye coupled into the silica shell, and the released dye was measured by UV-VIS-absorption

spectroscopy. Additionally, the extinction coefficient of RBITC was determined to calculate dye amount or concentration (equation (2.32)). For this purpose, the absorption spectrum of RBITC in various concentrations after dissolution in EtOH/ 0.43 M NaOH (1:1 v/v) mixture were measured. The maximum absorption peak was at 547 nm. The integrated value of each spectrum was calculated, the values depicted on a calibration curve (see Attachment E) and the extinction coefficient value (ε) was calculated. The extinction coefficient of RBITC at the maximum absorption wavelength (λ_{max}) of 547 nm was 91.9±2.3 1/mM·cm. The absorption spectrum of RBITC in silica coated sample after it was dissolved in the mixture mentioned above was measured, and the dye concentration (mmol/L) was determined.

The maximum absorption peak of RBITC-APS in silica coated samples in ethanol was at 549±1 nm. Red-shifting was commonly observed after incorporation of RBITC into silica shell, but should not influence the value of the general integrated emission.[245] The calculation for the determination of the concentration of the amount of dye per silica volume and the absorption spectra of the samples are shown in Attachment F.

In five different batches, UC_Er_4 was coated with silica shell with a similar shell thickness and variable amounts of RBITC-APS (see Table 3-7). As a reference sample, a silica shell without dye was grown onto sample UC_ Er_4 (UC_Er_4@Ref). Figure 4.62 shows the STEM images of RBITC doped silica coated UCNP and Table 4-7 lists the diameter and z-average of the samples.

The average diameter of the samples was 38±1 nm, and the average silica shell thickness of the five samples was 7±1 nm, which was still in the calculated range of the thickness of 5±1 nm. The incorporation of both APS and the APS-dye coupling product can lead to an increase of the calculated silica thickness due to an increase of the porosity of the silica shell. RBITC has a diagonal size of ~ 1 nm which requires a significant expansion of the pores in the silica network.[249] APS could also cause an increase of the porosity of the silica network.[250]

The samples UC_Er_4@RBITC_3, UC_Er_4@RBITC_4 and UC_Er_4@RBITC_5 had 33 %, 42 %, and 33 % higher z-averages than their STEM-diameter, respectively. Upon addition of APS, the initial particle charge decreased due to the positively charged amine group of the APS that decreased the surface charge of the silica consisting predominantly of negatively charged silanol groups.[250-251] This could lead to a decrease in overall surface charge and stability.

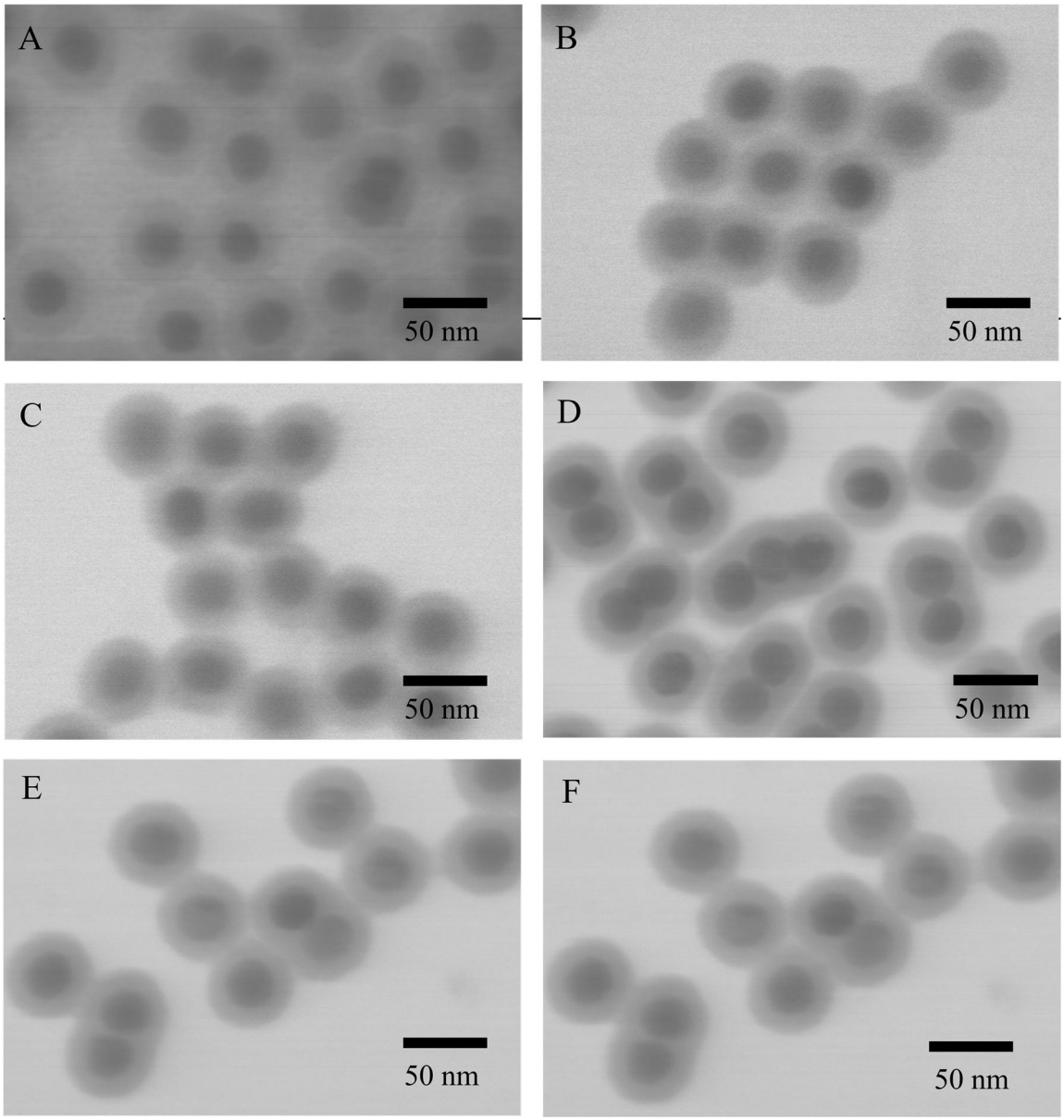

Figure 4.62: STEM images of A: UC_Er_4@RBITC_1; B: UC_Er_4@RBITC_2; C: UC_Er_4@RBITC_3; D: UC_Er_4@RBITC_4; E: UC_Er_4@RBITC_5; and F: UC_Er_4@Ref. The core was UC_Er_4 and the average SiO_2 thickness was 7±1 nm.

Table 4-7: Average measured STEM-diameter, silica shell thickness, z-average, and PDI of RBITC-APS coupled silica coated UC_Er_4

Sample	**d_{STEM} [nm]**	**r_{SiO2} [nm]**	**z-average [nm]**	**PDI**
UC_Er_4@ RBITC_1	38±2	7±1	48±1	0.145±0.030
UC_Er_4@ RBITC_2	38±2	7±1	42±1	0.190±0.010
UC_Er_4@ RBITC_3	38±2	7±1	54±1	0.120±0.010
UC_Er_4@ RBITC_4	36±2	6±1	48±1	0.110±0.014
UC_Er_4@ RBITC_5	39±2	8±2	52±1	0.109±0.020
UC_Er_4@ Ref	38±2	7±1	89±1	0.093±0.013

In Table 4-8 the absorption intensities, measured amounts of dye, and dye concentration per litre SiO_2 that were coupled into the silica shell are listed. The measured quantity of the coupled dye (in mmol dye /L SiO_2) increased in the following order: UC_Er_4@RBITC_1 < UC_Er_4@RBITC_2 < UC_Er_4@RBITC_3 < UC_Er_4@RBITC_4 < UC_Er_4@RBITC_5, consistent with the expected order of RBITC content used in the synthesis. The percentual coupling efficiency increased from UC_Er_4@RBITC_1 to UC_Er_4@RBITC_3, before decreasing again in sample UC_Er_4@RBITC_4 and UC_Er_4@RBITC_5, indicating that a maximum dye loading capacity for a 7±1 nm silica shell on a 24 nm UCNP core was reached in sample UC_Er_4@RBITC_3. The labeling efficiencies in this work was higher than the labeling efficiencies reported by Imhof et al. [245, 251] and slightly lower than those reported by van Blaaderen et al.[250] The highest efficiency was found in UC_Er_4@RBITC_3 (dye coupling efficiency = 35±8 %), and the lowest was in UC_Er_4@RBITC_5 (dye coupling efficiency = 27±8 %). The average dye coupling efficiency was 31±8 %. The numbers of dye molecules per UCNP core increased with the increasing amount of utilized dye, except in the case of UC_Er_4@RBITC_4, since this sample had a slightly thinner shell than the others.

Gunawardana et al. reported a 95% labeling efficiency for rhodamine dye covalently loaded in a 7 nm silica shell on 16 nm silica particles.[252] Imhof et al. however reported a coupling efficiency of < 10 % for fluorescein isothiocyanate (FITC) coupled with APS into 200-300 nm

diameter silica particles,[251] whereas van Blaaderen reported a 37 % APS coupling efficiency (without dye) in silica and 49 % coupling efficiency for RBITC-APS in 91 nm silica particles, where the dye concentration was 26 mmol/L particles, corresponding to 66000 dye molecules/particle.[245, 250] Imhof et al. reported that the use of NH_3 could compete with NH_2-group in APS in the coupling reaction, causing low labeling efficiency. Liang et al.,[253] however, reported a high labeling efficiency for FITC and tetramethylrhodamine isothiocyanate (TRITC) covalently coupled to APS functionalized silica through a separated hydrolysis and condensation process. The labeling efficiencies were 98 % for FITC and 76 % for TRITC. In this work, the labeling efficiency was higher than that reported in the work of Imhof et al. since ammonia was added after the addition of the dye coupling product and TEOS, causing a higher coupling rate between the dye-APS and TEOS before hydrolysis could occur. However, FITC can be coupled with higher efficiency in the silica shell than RBITC, due to steric hindrance of the larger RBITC.[254]

The low dye coupling efficiency was likely due to competitive condensation between APS and TEOS.[253] Since the hydrolysis and condensation rate of APS is slower than that for TEOS,[250] there was a high amount of unhydrolyzed dye-coupled APS left in the solution upon completion of the TEOS polycondensation.[253]

Table 4-8: Measured and calculated RBITC concentrations coupled in the silica-coated UCNP samples, distance between the dye molecules in the silica shell, number of dye molecules per UCNP core, ratio of erbium ions to dye molecules and ratio of surface erbium ions to dye molecules

Sample	**Absorption**	**Measured amount of RBITC/L SiO_2**	**Calculated amount of RBITC/L SiO_2**	**Labeling efficiency**	**Dye distance**	**Numbers of dye molecules per UCNP core**
	arb. unit	**mmol/L SiO_2**	**mmol/L SiO_2**	**%**	**nm**	
UC_Er_4@RBITC_1	0.0429±0.0004	0.71±0.02	2.4±0.1	29±7	8±1	31±1
UC_Er_4@RBITC_2	0.0702±0.0007	1.16±0.03	3.7±0.2	32±8	8±1	47 ±3
UC_Er_4@RBITC_3	0.1017±0.0010	1.68±0.04	4.9±0.3	35±8	7±1	63±4
UC_Er_4@RBITC_4	0.1101±0.0011	1.93±0.06	6.2±0.3	32±8	7±1	63±3
UC_Er_4@RBITC_5	0.1238±0.0012	1.99±0.06	7.4±0.4	27±8	6±1	105±6

Figure 4.63 A shows absorption spectra of samples with the highest amounts of coupled dye molecules, i.e., UC_Er_4@RBITC_3, 4, 5 and absorption spectra of the reference sample UC_Er_4@Ref. All UV-VIS-NIR absorption spectra of the dye-doped samples show the typical RBITC absorption with a maximum at 540 nm while the reference sample does not show any absorption peak. Figure 4.63.B shows upconversion fluorescence spectra of the dye-doped silica coated UC_Er_4 samples (power excitation density = 2 W/cm^2), normalized to the emission at 655 nm and Figure 4.64 shows a diagram depicting the $f_{g/r}$ value as a function of the amount of dye in mmol/L SiO_2. The characterization of the upconversion fluorescence emission indicated an energy transfer causing slight dye emission in the 580 nm range. However, without decay time measurements, it is not yet certain if the energy transfer is radiative or non-radiative. Figure 4.63.C shows an enlarged view of the RBITC emission range from Figure 4.63.B. The intensity of the dye emission corresponds to the amount of coupled dye as listed in Table 4-8, where the highest dye emission intensity corresponds to UC_Er_4@RBITC_5 and the intensity decreases with decreasing of coupled dye amount, with the lowest intensity corresponding to sample UC_Er_4@RBITC_1.

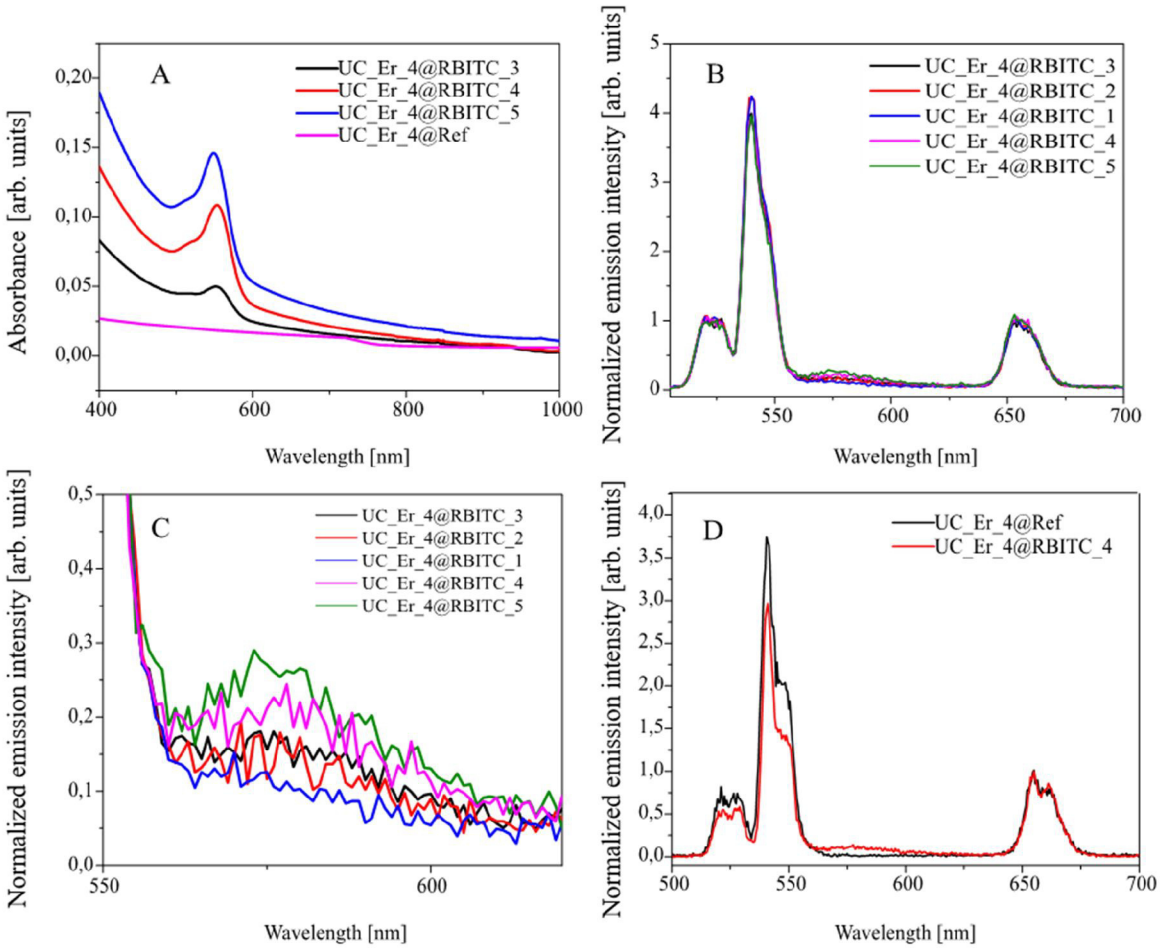

Figure 4.63 A: Extinction spectra of UC_Er_4@RBITC_3, 4, 5 and UC_Er_4@Ref as reference sample without RBITC, B: upconversion fluorescence spectra of the UC_Er_4 dye-doped samples (excitation wavelength = 980 nm, excitation power density = 2 W/cm^2) normalized to red emission; C: enlarged view of the RBITC dye emission around 585 nm and D: upconversion fluorescence spectra of UC_Er_4@Ref (black line) and UC_Er_4@RBITC_4 (red line)in ethanol after excitation at 980 nm normalized at the red emission.

The $f_{g/r}$ values of all samples were similar and decreased only slightly with an increasing amount of coupled dye, indicating that the weakening of the green emission of the UCNP correlated to an increasing dye emission intensity. However, due to the weak dye emission intensity of all samples, the decreasing intensity of the green emission was also minimal. The weakness of the dye emission intensity could be due to self-quenching effects. The dye quenching effect directly influences the weakening of the green emission, where the dye molecules already quench each other before the

energy transfer from an emitted photon of UCNP occurs. The green emission would decrease significantly if the dye molecules are well separated, and no self-quenching takes place.

Figure 4.63.D shows upconversion emission spectra for UC_Er_4@RBITC_4 ($f_{g/r}$ = 1.96±0.20) and UC_Er_4@Ref normalized to the 655 nm emission. The $f_{g/r}$ ratio of sample UC_Er_4@Ref was 2.67±0.30 in ethanol and 2.77±0.30 for UC_Er_4@RBITC_4, which confirmed the decrease of $f_{g/r}$ of dye-doped samples compared to the reference sample, accompanied by 580 nm dye emission. The last figure was measured at the BAM with another instrument setup so that they could not be directly combined with spectra in Figure 4.63.B.

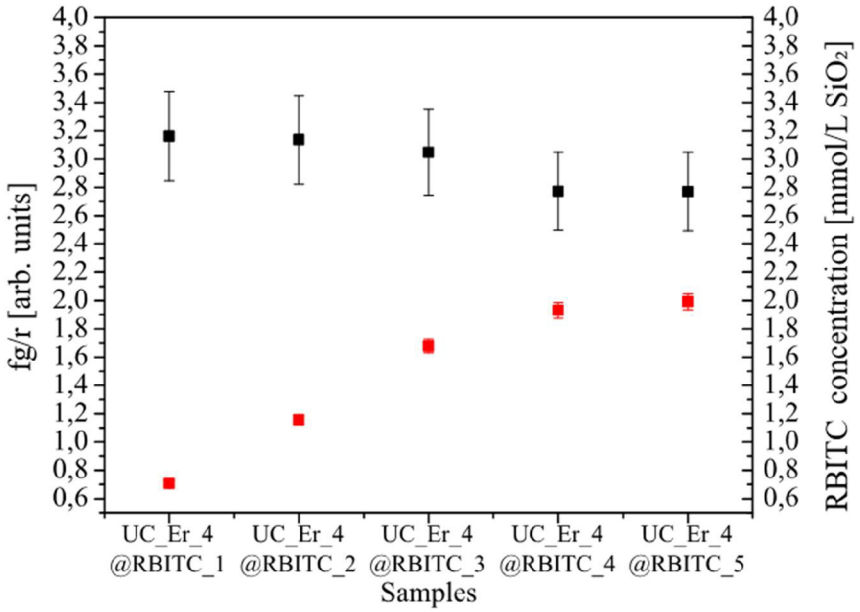

Figure 4.64: Green-to-red emission ratio of dye-coupled samples (black squares) and amount of dye coupled in mmol/L SiO_2 for each sample (red squares).

Table 4-9: List of integrated 540 nm (green), 580 nm(dye) and 655 nm (red) emission (normalized to the emission at 656 nm wavelength), as well as $f_{g/r}$ (ratio of green to red emission) and dye concentration (mmol dye/L SiO_2) of dye-doped silica, coated UC_Er_4 samples

Integrated intensity [arb. unit]	**Emission at 540 nm**	**Emission at 655 nm**	**Emission at 580 nm (dye)**	**$f_{g/r}$**	**Measured amount of RBITC/L SiO_2**
Sample					**mmol/L SiO_2**
UC_Er_4@ RBITC_1	52.69±0.50	16.67±0.17	3.68±0.40	3.16±0.30	0.71±0.02
UC_Er_4@ RBITC_2	53.20±0.50	16.97±0.17	5.09±0.50	3.14±0.30	1.16±0.03
UC_Er_4@ RBITC_3	49.73±0.50	16.32±0.16	5.92±0.60	3.05±0.30	1.68±0.04
UC_Er_4@ RBITC_4	48.65±0.50	17.55±0.17	7.20±0.70	2.77±0.30	1.93±0.06
UC_Er_4@ RBITC_5	48.85±0.50	17.64±0.17	8.85±0.80	2.77±0.30	1.99±0.06

The $f_{g/r}$ of the dye coupled samples were in general reduced compared to UC_Er_4@Ref along with the increase of the coupled dye amount, owing to either increased energy transfer (radiative, in the form of reabsorption; or non-radiative in the form of FRET) of the green upconversion emission to the dye. Both effects will be investigated through lifetime measurements of the green emission. If a decrease of the lifetime of the UCNP donor is accompanied by an increase of the acceptor lifetime, it can be concluded that FRET emission has occurred (see chapter 2.3).

Imhof et al.[251] reported a self-quenching effect for a FITC dye concentration of 2.7 mmol/L SiO_2. The dye concentrations of all samples in the present study were similar or above this value, which could promote the self-quenching effect.

The distances between each dye molecules could be approximated by the following equation:[251]

$$R = c^{-\frac{1}{3}} \qquad (4.9)$$

Where R is the distance between dye molecules, and c is the number of molecules per unit volume. The interdye distances of the samples were in the range of 6-9 nm (see Table 4-8). An increased self-quenching effect is hence expected especially for the sample the UC_Er_4@RBITC_5 since this sample has the highest dye concentration, owing to close placement of the dye molecules .[251, 255-256] RBITC is also known to build dimers and trimers in ethanol, especially at a concentration above 5 mM, which could also be coupled into silica in these forms.[49] In this work, the RBITC-APS was coupled at a concentration of 4-12 mM, which would promote the formation of dimers

or trimers. Formation of dimers can be observed in the extinction spectra, where the ratio between the emission peak at 549 nm and the shoulder at around 510 nm changes with the increase of dye concentration in the silica shell (see Attachment F).[257] The formation of dimers was also confirmed by a slight red-shift and peak broadening of the down conversion emission of the dye-doped samples in ethanol (see Figure 4.65).[257]

The dye-coupled silica-coated UCNP samples and RBITC solution under various concentrations were excited at 540 nm, and the emission shifts were observed. The solution with RBITC had an emission peak at 570±2 nm in the 0.01-0.04 mM concentrations, while at 0.08-0.1 mM the emission shifted to 574±2 nm, indicating a self-quenching effect. The UCNP samples show a further emission red-shift. Especially the samples UC_Er_4@SiO_2_4 and UC_Er_4@SiO_2_5 show stronger shifts at 575±2 nm, indicating stronger fluorescence quenching (see Figure 4.65). Dye molecules embedded in silica matrices often build aggregates due to restricted movements in the matrix and limited diffusion, which lead to red-shift of the absorption peak.[245] As the dye concentration increased inside a small silica volume, for example, inside a thin shell, the formation of aggregates becomes more likely,[49, 256] and could lead to a red-shift of the emission peak.

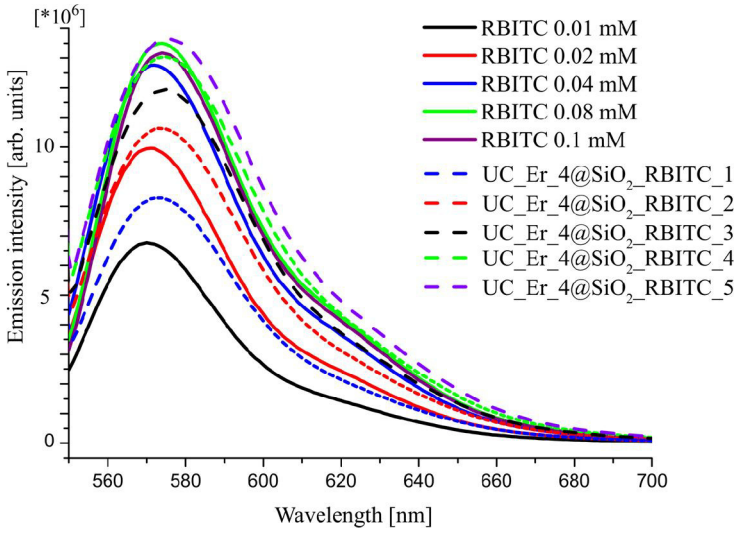

Figure 4.65: Downconversion fluorescence emission of RBITC solution in ethanol under various concentrations and dye coupled silica coated UCNP samples also in ethanol.

Table 4-10 shows the lifetime decay measurement values at 540 nm and 654 nm emission for the samples UC_Er_4@Ref (black line) and UC_Er_4@RBITC_4 (red line) in Figure 4.63.D. The measurements reveal that there was no significant difference between the decay rate of the

reference sample and the dye-doped sample. The slight decrease of the decay rate of the dye-coupled sample was within error margins. The decay time increased for UC_Er_4@RBITC_4 at the green emission slightly by 1,4 µs. This leads to the conclusion that photon reabsorption is the reason for the dye emission at 580 nm, as reabsorption and reemission could prolong the decay lifetime. Reabsorption is especially prominent at high concentrations of fluorophores or dye.[258] Presumably, the longer red emission lifetime was due to an energy back transfer from RBITC to the $^4F_{9/2}$ excited states of the Er^{3+}-ions, which led to an extension of the lifetime of the photons in the mentioned state.[112]

Figure 4.66 shows the decay curves for UC_Er_4@RBITC_3, UC_Er_4@RBITC_4 and UC_Er_4@RBITC_5 at 540 nm and 580 nm emission. The 585-nm (dye) emission lifetime of the three samples was similar (see Table 4-11) as well as the lifetime of all samples at the green upconversion emission, indicating there were no dye concentration-dependent changes of the emission intensity.

Table 4-10: Fluorescence lifetime values for UC_Er_4@Ref and UC_Er_4@RBITC_4 in ethanol at 540 and 655 nm emission after excitation at 980 nm

Sample	**τ at 540 nm emission[µs]**	**τ at 654 nm emission[µs]**
UC_Er_4@Ref	73.6±0.7	161.0±1.6
UC_Er_4@RBITC_4	75.0±0.8	211.0±2.0

However, all three samples have a longer 540 nm emission decay lifetime than the reference sample, which has a lifetime at 540 nm of 65.7±0.7 µs, indicating that photon reabsorption predominantly caused the emission of the dye. The decay lifetime of the dye in the microsecond range was caused by radiative energy transfer from the donor green emission. Pure RBITC in ethanol only has a decay rate in the ns range (see Attachment G); which is 2.0±0.7 ns in ethanol at the 10^{-3} M concentration range according to Kristofferson et al.,[259] while the luminescence lifetime of rhodamine doped silica nanoparticles with a size of 20-50 nm is in the range of 2-3 ns,[260] indicating that radiative energy transfer due to reabsorption (instead of FRET) is the process that occurs. Yan et al. [261] also reported a decay lifetime in the microsecond range for TRITC after interactions with $NaYF_4$: Yb^{3+}, Er^{3+} nanorods, which confirmed radiative energy transfer of upconversion emission to TRITC.

Table 4-11: Lifetimes of UC_Er_4 samples at 540 and 585 nm emission after 980 nm excitation. The power density was 75 W/cm²

Samples	τ at 540 nm emission [µs]	τ at 585 nm emission [µs]
UC_Er_4@ Ref (without dye)	65.7±0.7	-
UC_Er_4@ RBITC_3	79.2±0.8	76.4±0.8
UC_Er_4@ RBITC_4	77.3±0.8	72.9±0.7
UC_Er_4@ RBITC_5	78.7±0.8	75.4±0.8

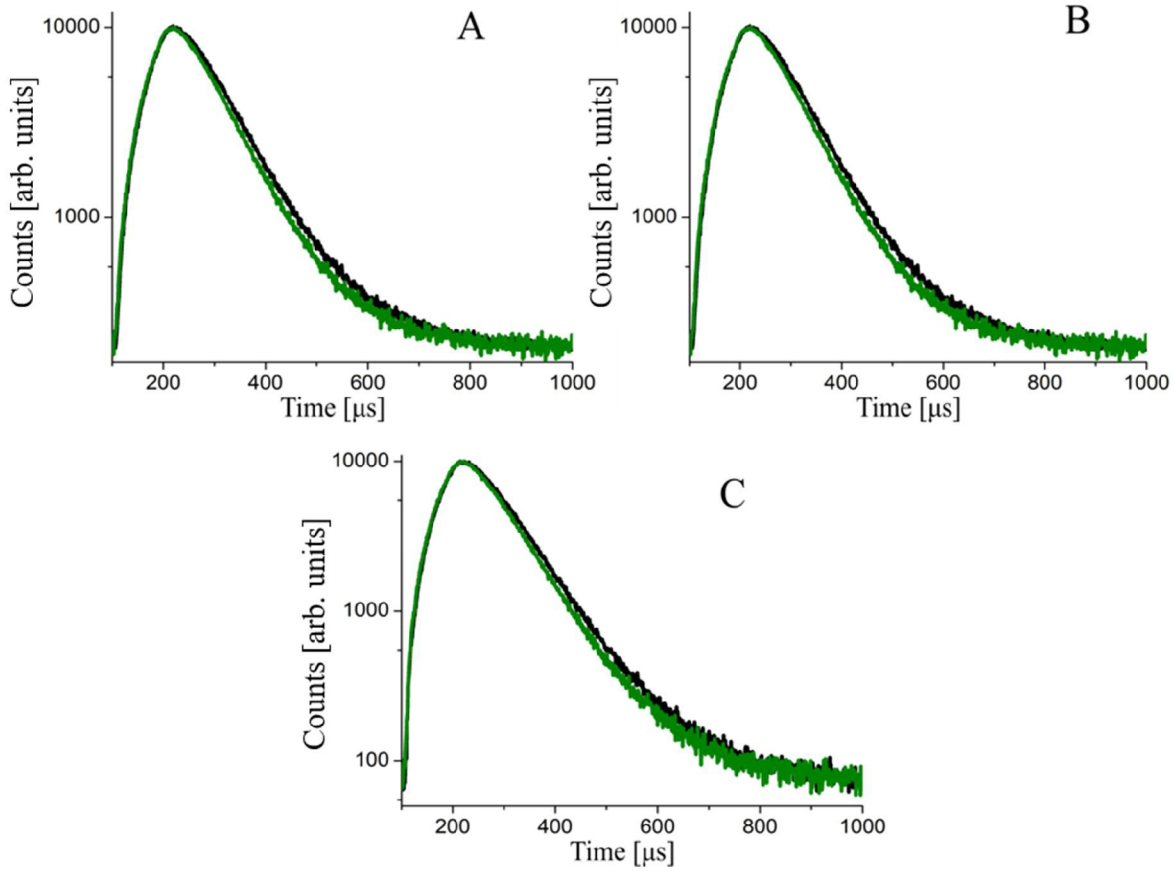

Figure 4.66: Decay curves at 540 nm (black line) and 585 nm (green line) emission of A: UC_Er_4@RBITC_3; B: UC_Er_4@RBITC_4 and; C: UC_Er_4@RBITC_5 in ethanol after 980 nm excitation.

Unlike in a general FRET system, where organic chromophores or quantum dots act as donors, in UCNP every lanthanide ion (erbium ion) acts as its own energy center, so that the energy transfers (radiative or non-radiative) are a sum of interactions between each dopant (erbium) ion and dye molecules.[211, 262] FRET only occurs predominantly between lanthanide ions on or close to the

UCNP surface as donors and acceptor, while the erbium ions in the core center transfer their energy through reabsorption processes.[107, 263] It is possible that in this case, the erbium ions on the surface transferred their energy through FRET process to the rhodamine dye, as the FRET efficiency is the highest for dye located within a radius smaller than the Förster radius, while the reabsorption occurred between the erbium ions in the in the inner UCNP core and the dye molecules in the silica. The reabsorption effect was stronger as there were more near-center erbium ions than surface erbium ions. However, erbium ions that were located near the surface could also transfer their emission energy via FRET to nearby dye molecules (see Figure 4.67).

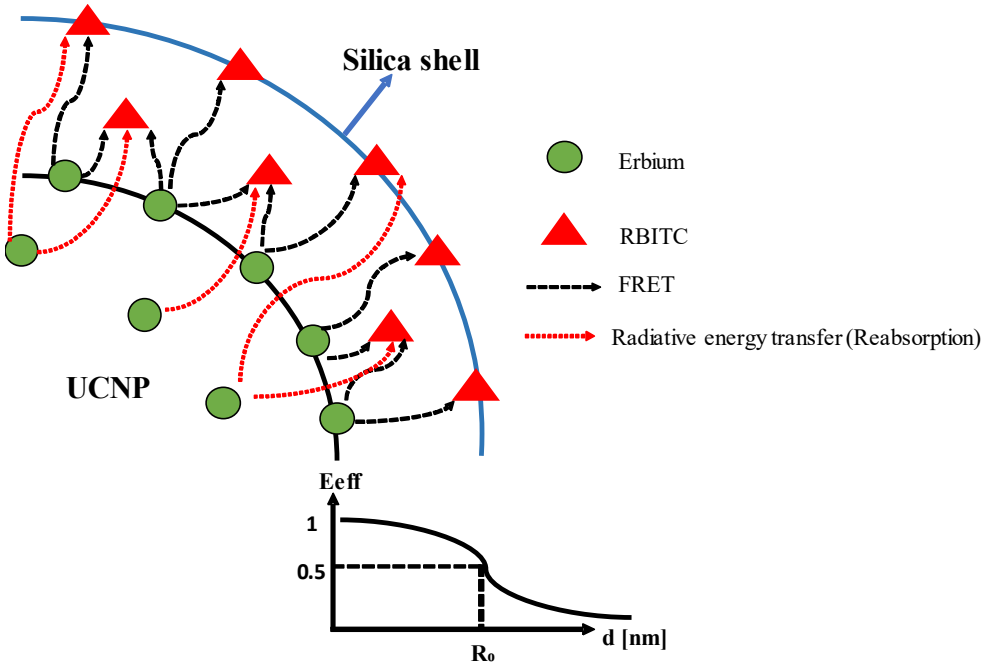

Figure 4.67: Scheme of energy transfer processes between erbium ions in UCNP as donor and dye RBITC as acceptor on the periphery between UCNP and silica shell. The surface erbium ions transfer their emission energies through FRET, while most inner erbium ions transfer their energies through reabsorption. The highest possible energy transfer efficiency between the donor (Er^{3+}) and acceptor (dye) is 1 and decreases to 0.5 when the distance between the donor and acceptor is the Förster radius (R_0) of 5 nm.[47, 48] With increasing distance between the donor, the Eeff decreases even further.

The ICP-OES measurement yield an erbium concentration of 2.45±0.01 mmol/L UCNP dispersion in UC_Er_4 (d = 24±1 nm; c dispersion = 25 g/L), which corresponds to [3.59±0.01] × 10^3 number of erbium ion in each UCNP. Muhr et al.[47] observed a high E_{FRET} of 50-60 % between 20-25 nm diameter $NaYF_4$: Yb, Er UCNP and Rose Bengal or sulforhodamine B dye coupled directly on the UCNP surface. The ratio of dye molecules to erbium ions was 1:23 for 21 nm diameter particles

and 1:29 for 26 nm diameter particles. These two sizes were compared with the results in the present study as they represented the most similar particle size used in this work. However, in this present work, there were more dye molecules than donor ions; the ratio of erbium ions to dye molecules in UC_Er_4@RBITC_1 was 1:[115±4] and in UC_Er_4@RBITC_5 was 1:[34±2], which could explain the self-quenching of dye molecules.

Since the emission of surface erbium ions is the main part that influences the FRET effect, the number of the surface erbium ions have to be determined and compared to reported publications. For this purpose, the number of erbium ions in one particle was divided by the volume of one UCNP (volume of 1 UCNP = [7.24±0.30] × 10^3 nm^3) to calculate the erbium occupancy density, which was approximately 1.0±0.1 erbium ions for every 2 nm^3 core volume. One can then estimate the number of surface ions by calculating the volume of one 24-nm diameter UCNP sphere and subtracting it by a sphere volume with a diameter of 23 nm, assuming every single erbium ion occupied a surface space with a size of 2 × 1 × 1 nm (which represent the width, length, and depth area respectively) and multiplying this volume difference with erbium occupancy density. As a result, there were approximately 434±28 surface erbium ions on each particle and the ratio of dye to erbium ions was 1:[14±1] for UC_Er_4@SiO_2_1 and 1:[4.0±0.3] for UC_Er_4@SiO_2_5, while Muhr et al. had a ratio of 1:0.79 for 26 nm diameter UCNP and 1:0.78 for 21 nm particles, arguing for an insufficient number of surface rhodamine molecules for FRET in this work.

The dye molecules used in this work were randomly distributed across the silica shell, hence the distance and the sum of energy transfer for each dye from the surface erbium ions were also variable, whereas the dye molecules in the work of Muhr et al. were all coupled directly on the UCNP surface. The dye that was located nearer to the erbium ions experienced a stronger FRET effect compared to the dye molecules located further away from the ions. Most probably the more distant dye molecules experienced energy transfer through reabsorption.

The other possible cause for the difficulties for proving a FRET effect in the system even though of Er^{3+} ions of an acceptor were within the Förster distance (5-6 nm according to Mattson et al.[48], 2.5-5 nm between Er^{3+}-ions and rhodamine according to Muhr et al.[47]) could be that the dye was spread inside and on the surface of the silica shell, due to the APS-siloxane bond. However, for a FRET effect to occur both transition dipole orientations of the donor and acceptor should be parallel to each other.[264] In the synthesized systems the dye tend to be located randomly with a certain rotational orientation inside the silica matrix.[251] Hence, absorption transition dipole moments of the dye molecules were most likely not parallel to the dipole of the upconversion emission, and

this could lead to depolarization of the energy transfer and hence lower the energy transfer efficiency.

Additionally, UCNP usually suffer from low quantum yield as the erbium ions on the surface interact with organic/inorganic molecules, in this case, the Si-O-Si and OH-bond of the silica shells, causing non-radiative relaxations. Although silica should be an inert shell, it could nevertheless limit the energy transfer to a certain degree, due to the scattering effect of the silica matrix.[265] This effect is stronger on smaller nanoparticles compared to their bulk counterparts, as the surface-to-volume ratio increases and hence more erbium ions are found on the surface.[266]

Deng et al.[211] could improve the efficiency and intensity through a resonant energy migration process in a $NaGdF_4$ lattice doped with Yb^{3+} and Tm^{3+} by confining the excitation energy on the particle's surface. The acceptor was a fluorescein isothiocyanate (FITC) conjugated to a thin silica layer. The energy migration succeeded through the transition $Tm^{3+} \rightarrow Gd^{3+} \rightarrow Tm^{3+}$ before the energy transfer to the dye. With this process, the authors managed to keep the FRET efficiency high even though the donor-acceptor was larger than the Förster distance. The requirement for the occurrence of such a resonance energy migration process is an energy matching between the lattice ion and the emitter, in this case, Gd^{3+} and Tm^{3+} ions. Another way to increase the FRET efficiency is the separation of the activator and sensitizer in a core-shell system, as Yb^{3+} ions are more sensitive to surface quenchers than Er^{3+} ions, for example. Zhang et al.[267] managed to improve FRET efficiency by six times under this optimized condition.

Conclusively, a FRET effect could not be observed in all silica coated samples due to reabsorption effect and self-quenching of the dye molecules. Although most dye molecules in the silica shell were within the Förster radius to the surface erbium ions, which could non-radiatively transfer their emission energy, stronger reabsorption effects which dominated the energy transfer process occurred.

4.4 Characterization of cytotoxicity of silica coated upconversion nanoparticles on HaCaT cells and RAW 264.7 macrophage cells

Despite their possibility to be used in biodetection and medicinal applications,[43-44] the toxicity of UCNP on biological cells have not been fully explored. In various *in vitro* cytotoxicity studies, UCNP have been shown to have low or no toxicity effects on cells.[142, 268] However, a recent study indicates that $NaYF_4$ nanoparticles doped with Yb and Er are unstable in acidic physiological fluids e. g. in lysosomes and cause inflammatory effects in the cells.[53] UCNP may also have some degree of *in vitro* toxicity, as the lanthanide ions can be released to the surroundings and could cause inflammation.[53] These are unwanted effects during the use of UCNP in bioimaging and or other biomedical agents. Silica shells can be grown onto the UCNP as a protective coating that prevents the release of the ions and increases their biocompatibility. Also, silica can turn the hydrophobic UCNP into hydrophilic structures that serve as an anchor to couple various ligand, drugs, and macromolecules.[51] In this chapter, the cytotoxicity of UCNP cores coated with silica shells of different thicknesses and two different surface charges were investigated on human keratinocyte HaCaT cells and murine macrophage cells RAW 264.7. Silica shells can be grown onto the UCNP as a protective coating that prevents the release of the ions and increases their biocompatibility.
Upconversion cores consisting of $NaYF_4$ doped with 18% Yb and 2% Er were synthesized. Then silica shells with microporous structures and various thicknesses were coated onto the UCNP to increase the hydrophilicity of the particles, making them available for biological experiments. Two silica thicknesses were coated onto UCNP to investigate a possible relation between the degree of cytotoxicity on particle size and silica shell thickness. The particles were subsequently functionalized with N-(6-Aminohexyl)aminopropyltrimethoxysilane (AHAPS) that provided a positive charge on the nanoparticle surface to increase uptake rate into the cells. The particles were characterized by STEM, DLS, electrophoretic light scattering and ICP-OES. Before the cell experiments with HaCaT cells (an immortal keratinocyte cell line from adult human skin) and RAW 264.7 (macrophages derived from a tumor caused by Abelson murine leukemia virus), their stability in the cell culture medium was investigated through DLS and zeta potential measurements. Experiments to quantify the amount of possible released lanthanide ions in the cell culture medium were also performed to relate possible ion dissolution with their degree of cytotoxicity. UCNP uptake potential was evaluated by flow cytometry through the measurement of light side scattering which is proportional to changes in cell granularity or internal complexity. Silica-coated samples

coupled with RBITC-APS were exposed to HaCaT cells, and particle uptake was optically observed by confocal fluorescence microscopy.

4.4.1 Sample preparations for cytotoxicity experiments on HaCaT and RAW 264.7 cells

The upconversion cores prepared for the experiments were $NaYF_4$: Yb, Er (sample UC_Er_6; see Figure 4.68.A; d_{STEM} = of 33±2 nm) nanocrystals. The hydrodynamic diameter (d_{ave}) was 47±1 nm (PDI = 0.383±0.051). ICP-OES measurement yielded a percentual molar ratio of Y: Yb: Er = [74±1]:[25±1]:[2±0.5]. The XRD diffractogram shows a predominantly hexagonal crystal structure for example at 18°, 29°, 44° and 54° (ICDD no. 28-1192), with two minor peaks from the α-phase at 47° for [220] reflex and 55° for [311] reflex (ICDD no. 06-0334; see Figure 4.68.B).

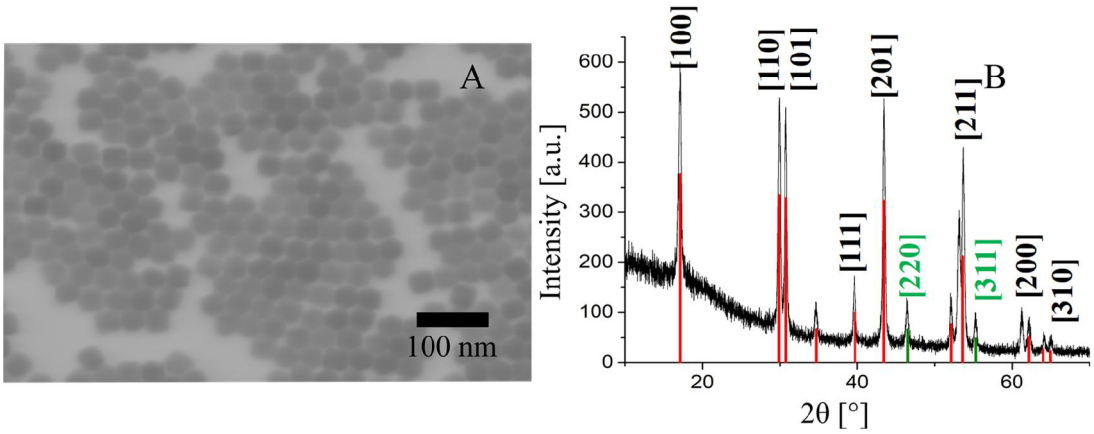

Figure 4.68 A: STEM image of UC_Er_6 (average diameter = 33±2 nm); B: XRD diffractogram of UC_Er_6. (red lines: hexagonal phase peaks (ICDD no. 28-1192); green lines: cubic phase peaks (ICDD no. 06-0334).

The core was coated with two different silica thicknesses: 7±1 nm for the thin-shelled silica and 21±2 nm for thick shelled silica, since thicker silica shell should protect the UCNP core more efficiently than a thinner silica shell by preventing possible leaking of ions from the core. Additionally, samples with the same two different shell thicknesses were surface-functionalized with AHAPS (see Figure 4.69, samples are called UC@thin_NH_2, and UC@thick_NH_2 for thin and thick silica shelled UCNP functionalized with AHAPS, respectively), so that in the end there were four silica coated samples with and without AHAPS (simply called UC@thin and UC@thick in case of the unfunctionalized samples). AHAPS was chosen as a surface ligand, due to its ability to provide the particles with a positive surface charge, since it is known that positively charged silica particles could be taken up more efficiently than negatively charged particles through the

negatively charged cell membrane. This process was supported by the fact that the hydrodynamic diameter of the AHAPS-functionalized particles would be small enough for an endocytic uptake.[54] APS was not chosen as amine ligand due to the increased aggregation of APS functionalized particles in cell culture medium.[54]

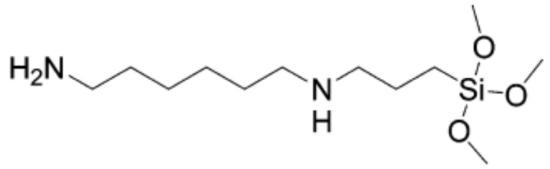

Figure 4.69: N-(6-aminohexyl)-aminopropyltrimethoxysilane (AHAPS).

In addition, particles were prepared where RBITC-APS was coupled into the silica shell to study their uptake under fluorescence microscopy measurements. Samples with two different thicknesses were prepared: 9±2 nm for the thin-shelled samples and 22±2 nm for the thick-shelled samples (UC@thin_RBITC_NH_2 and UC@thick_RBITC_NH_2 for the thin and thick shelled dye-coupled silica coated UCNP, respectively). The silica shells of the dye-doped samples were thicker than those of the samples without dye, as the APS and the dye increased the porosity of the silica shell, and subsequently the silica shell thickness (see chapter 4.3). As a reference sample, pure silica nanoparticles with a size of 50 nm were also coupled with RBITC and functionalized with AHAPS (sample SiO_2 @RBITC_NH_2).

STEM images for each sample are shown in Figure 4.70.

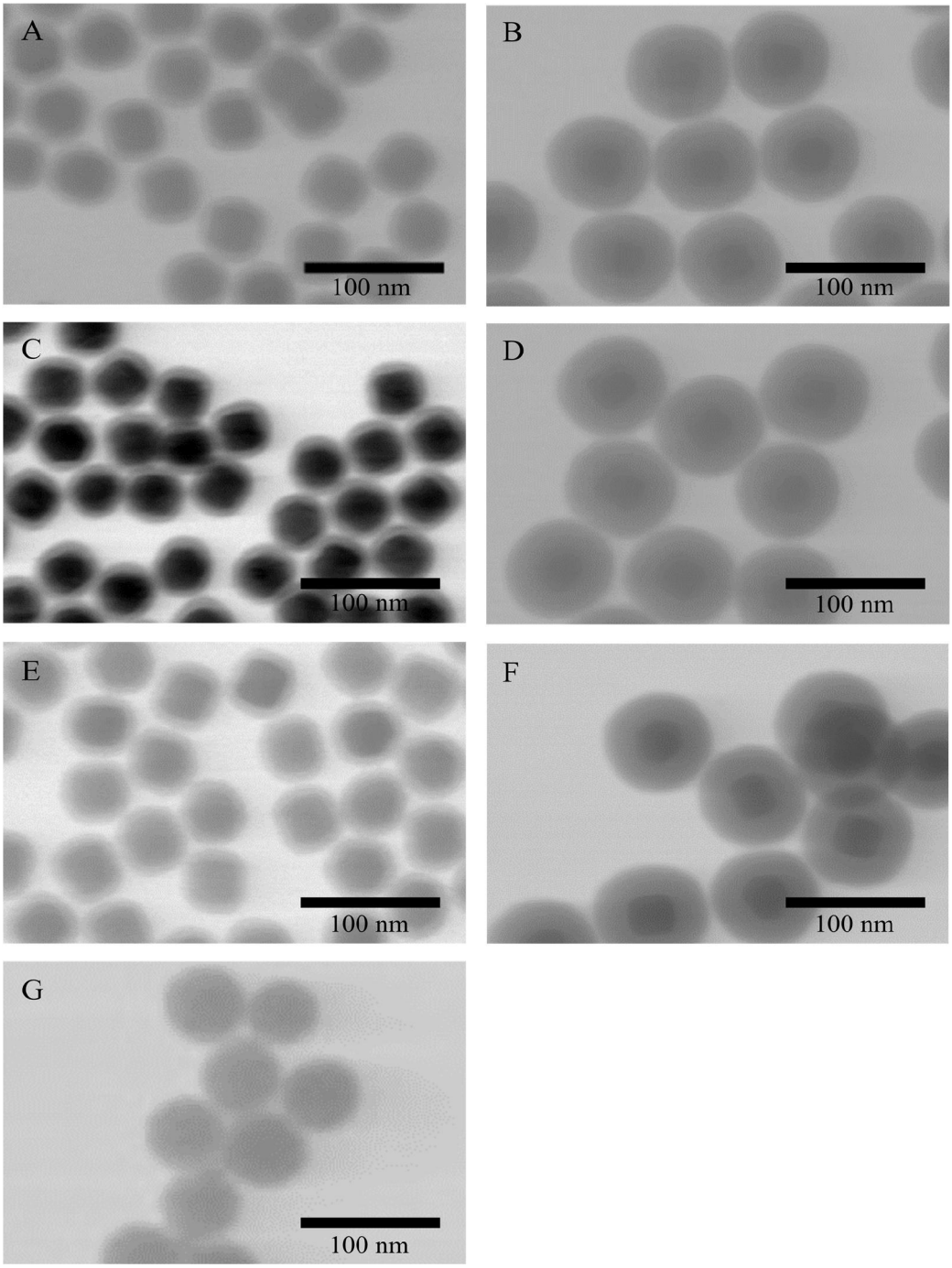

Figure 4.70: STEM images of A: UC@thin_NH_2 (r_{SiO2} = 8±2 nm); B: UC@thick_NH_2 (r_{SiO2} = 21±2 nm); C: UC@thin (r_{SiO2} = 7±2 nm); D: UC@thick (r_{SiO2} = 21±3 nm); E: UC@thin_RBITC_NH_2 (r_{SiO2} = 9±2 nm); F: UC@thick_RBITC_NH_2 (r_{SiO2} = 22±2 nm); G: functionalized SiO_2-nanoparticles SiO_2@RBITC_NH_2 (average STEM-diameter = 52±3 nm). The core was UC_Er_6 ($NaYF_4$: 18 % Yb, 2 % Er).

The samples are listed in Table 4-12 below, alongside their STEM average diameters and corresponding silica shell thicknesses:

Table 4-12: STEM diameter and silica shell thickness of silica coated UC_Er_6 and sample SiO_2@RBITC_NH_2.

Samples without Rhodamine	**d_{STEM} [nm]**	**r_{SiO2} [nm]**
UC@thin_NH_2	48±2	8±2
UC@thick_NH_2	75±2	21±2
UC@thin	47±2	7±2
UC@thick	75±3	21±3
Samples with Rhodamine		
UC@thin_RBITC_NH_2	50±2	9±2
UC@thick_RBITC_NH_2	76±3	22±2
SiO_2@RBITC_NH_2	52±3	-

The dispersion behavior and changes of the surface charge of the samples in various media were closely studied by conducting DLS- and electrophoretic light scattering (zeta potential/ZP) measurements in different media (ethanol, water, and Dulbecco's Modified Eagle Medium (DMEM) supplemented with 10 % fetal bovine serum (FBS), 1 % glutamine, 1 % fungizone and 1% penicillin). Table 4-13 shows a summary of the DLS and ZP results.

Table 4-13: Hydrodynamic diameter, polydispersity index, and zeta potential in EtOH, water, and supplemented DMEM of silica coated UCNP without AHAPS (UC@thin, UC@thick), silica coated UCNP functionalized with AHAPS (UC@thin_NH_2, UC@thick_NH_2), dye-doped silica coated UCNP functionalized with AHAPS (UC@thin_RBITC-NH_2, UC@thick_RBITC-NH_2), and SiO_2@RBITC_NH_2

Samples	**EtOH**		**Water**		**Supplemented DMEM**		**Ethanol**	**Water**	**Supplemented DMEM**	
	Z-ave [nm]	**ZP [mV]**	**Z-ave [nm]**	**ZP [mV]**	**Z-ave [nm] after 30 min**	**Z-ave [nm] after 24 h**	**PDI**	**PDI**	**PDI after 30 min**	**PDI after 24 h**
UC@thin_NH_2	105±1	34±1	128±5	26±2	336±14	67±2	0.099±0.005	0.118±0.004	0.720±0.045	0.587±0.012
UC@thick_NH_2	145±1	37±2	295±2	29±1	220±2	205±6	0.177±0.015	0.258±0.028	0.460±0.010	0.549±0.026
UC@thin_RBITC_NH_2	127±1	30±2	138±2	26±1	97±8	48±1	0.117±0.014	0.172±0.028	0.575±0.098	*
UC@thick_RBITC_NH_2	118±1	27±2	139±2	19±1	144±2	152±4	0.065±0.009	0.161±0.023	0.367±0.049	0.573±0.028
UC@thin	80±2	-24±1	104±1	-31±2	93 ±1	32±1	0.112±0.004	0.203±0.006	0.460±0.004	0.322±0.004
UC@thick	98±2	-21±1	142±1	-29±1	125±3	**	0.037±0.006	0.098±0.014	0.159±0.011	**
SiO_2@RBITC_NH_2	98±1	-16±1	103±2	-10±1	208±5	30±1	0.100±0.010	0.100±0.010	*	0.941±0.009

* These samples aggregated, so there was no useful PDI value that could be obtained.

**No measurement due to insufficient sample amount.

The zeta potential turned from negative to positive after AHAPS-functionalization, due to the positive surface charge of the amine group in the AHAPS -ligand. The zeta potential of the AHAPS functionalized samples decreased after a transfer from ethanol to water, as reported in several publications.[54, 142] Asenath-Smith et al.[269] reported that the amine group in amino-silane ligands bound to silica can interact with the silanol group on the silica surface, forming a cyclic intermediate, which further breaks the bond of the Si-O-group to the silica and consequently leads to the breakage of the amine-ligand. This would naturally destabilize the particles, as the zeta potential decreases due to the loss of positive surface charge along with the loss of the amine group and subsequently induce aggregation. Since AHAPS have longer alkyl chains than APS, the formation of cyclic intermediates is sterically more unfavorable with AHAPS. Therefore the aggregation will remain comparatively low. UCNP functionalized with AHAPS seemed to maintain a stable positive zeta potential in water, indicating sufficient stabilization. The z-average increased however to 30 %-45 % for the samples UC@thin and UC@thick, indicating insufficient stabilization in water, although the z-averages of these samples were still lower than those of the other AHAPS-functionalized samples. The zeta potential of SiO_2@RBITC_NH_2 was already quite low in water, due to probable destabilization from amine coupled RBITC in the silica shell. The z-average of the samples 30 minutes after redispersion in DMEM were expectedly lower than in water, except for the samples UC@thin_NH_2, UC@thick_RBITC_NH_2, and SiO_2@RBITC_NH_2. The lower z-average of these samples may indicate increased stabilization by a protein corona.[270-273] The z-average of UC@thin_NH_2 and SiO_2@RBITC_NH_2 increased after redispersion in cell culture medium, indicating increased destabilization. However, a low z-average in DMEM is not necessarily a consequence of increased stabilization of the particles in DMEM. On the contrary large aggregates could be formed due to increased destabilization followed by sedimentation. Various proteins with different sizes in the cell culture medium, especially in samples UC@thin_RBITC_NH_2, UC@thin_RBITC_NH_2 and UC@thin_RBITC_NH_2 could be measured instead, since the PDI values for these samples in DMEM were large. This finding can be explained by the composition of the cell culture medium, most importantly the fetal calf serum (FCS) contained therein.[54, 142] Fetal calf serum (FCS) that was diluted up to 10% in DMEM in the present study can influence the measured hydrodynamic diameter for nanoparticle dispersion. FCS consists mostly of bovine serum albumin that has a wide size distribution and high polydispersity index (PDI) when measured with DLS.[54] Zhang et al.[142] suggested that the serum albumin can also be adsorbed on the particles' surface. Izak-Nau et al.[271] investigated the aggregation of silica

nanoparticles that occurred after redispersion in buffer solution and physiological medium. They reported that various proteins in medium containing FCS were adsorbed onto the surface of bare SiO_2 and amine functionalized SiO_2 nanoparticles and formed a protein corona with a new surface charge, depending on the type of proteins that build the corona. The adsorbed protein corona consisting of the proteins present in FCS, could increase or reduce the stability of the particles and consequently their hydrodynamic diameter.[270-273] The z-average of the supplemented DMEM used in this study without particles was 13±1 nm (PDI = 0.380±0.003), which indicates that the protein molecules in the medium can contribute to the measured particle hydrodynamic diameter, for example, by forming the above-mentioned protein corona but as well as single small molecules. The samples showed indeed an increased PDI value in DMEM compared to the PDI in ethanol or water.

Increased aggregation could be observed after 24 h of redispersion in DMEM, since the PDI values increased in most samples. The causes are mainly the following two factors: first was the adsoption of protein corona as explained previously. Second was the lowering of the repulsive force between the samples in the cell culture medium due to high ionic strength caused by salt contained in DMEM (ionic strength in DMEM (I) = 168 mmol/L). [54, 274] The increased aggregation could be observed after 30 minutes redispersion in DMEM.

UC@thin_RBITC_NH_2 and SiO_2@RBITC_NH_2 showed a significant increase of aggregation after dispersion in DMEM after 24 h, indicated by a PDI of 1. UC@thin_RBITC_NH_2 showed peak intensities at 300±50 nm, 30±10 nm and at 7±1 nm in the intensity distribution obtained by a non-negative least squares (NNLS) fit of the DLS data. SiO_2@RBITC_NH_2 also showed three different intensity peaks at a similar range as in the previously mentioned sample. This indicates extremely variable sizes of objects measured, which could be caused by the protein corona or other macromolecules in the cell culture medium. .A smaller z-average value in DMEM after 24 h could have several reasons: It might indicate increased stabilization of the particles due to the proteins on their surface and, hence, less aggregation so that their average hydrodynamic diameter decreases but it might also mean that a part of the protein corona was partially detached after a few hours, so that the average diameter is more determined by the free protein molecules. The former would go along with a decrease in PDI the latter with an increase. Since the data for the PDI are rather indifferent in the present measurement. Reliable DLS measurements at this time were hence not possible.

The non-functionalized samples, which have a negative surface charge, due to surface silanol groups, were generally more stable in the cell culture medium. Graf et al.[54] showed that non-functionalized silica particles were more stable in cell culture medium with fetal calf serum (FCS). Izak-Nau et al.[271] also reported that the aggregation level of NH_2-functionalized particles in FCS supplemented DMEM was higher than that of non-functionalized silica particles. Kurtz-Chalot et al.[275] observed increased internalization of silica nanoparticles functionalized with a carboxyl group and amine group ligands for negatively and positively charged particles, respectively, into macrophage cells compared to the same functionalized particles with PEG as ligand, despite the increased size and PDI in DMEM of the former particles.[275] Although the particles in this work showed increased aggregation in DMEM, the particles can still interact with the cell membrane, as proven by different degree of the cytotoxicity of the samples in HaCaT and RAW 264.7 macrophage cells, where the cytotoxicity of most samples was dose-dependent (see 4.4.3 and 4.4.6). Indeed, adsorption of the particles on the cell membrane were visualized by confocal microscopy after 24 h exposure and are shown in chapter 4.4.4.

4.4.2 Ion release experiments

For the investigation of released lanthanide ions, UC@thin _NH_2 and UC@thick _NH_2, as representative samples for thin and thin-shelled samples and UC@thick as representative sample for unfunctionalized particles were redispersed in water or supplemented DMEM to reach a silica coated UCNP and UCNP core concentration of 200 µg/mL, left for 24 h and centrifuged with centrifuge tubes with a filter unit (pore size: 3000 NWCO) to separate the UCNP from possibly released ions. A concentration of 200 µg/mL was chosen since this was the highest concentration used in the cytotoxicity experiments, and hence the released ions would be representative for the maximum ions released which should correlate to the cytotoxicity results. The filtrates were measured by ICP-OES regarding their content of yttrium, ytterbium, and erbium ions. Additionally, a certain amount from each lanthanide chloride was dissolved in cell culture or water to reach a lanthanide ion concentrations of 1±0.1 ppm and 2±0.1 ppm. The solutions were then centrifuged and measured with ICP-OES to determine which percentual amount of the ions was filtered through the centrifuge filter.

Table 4-14 shows the amounts of filtered ions detected by ICP-OES after 24 h of redispersion in water and supplemented DMEM. Table 4-15 shows the amounts of detected filtered ions from an initial ion concentration of 1±0.1 ppm and 2±0.1 ppm after dissolution in water.

Table 4-14: Released values of lanthanide ions from silica coated UCNP obtained from ICP-OES measurements after dispersion in water and supplemented DMEM.

Sample	**Water**						**Supplemented DMEM**	
	c = 200 µg/mL silica coated UCNP			**c = 200 µg/mL UCNP core**			**c = 200 µg/mL silica coated UCNP**	**c = 200 µg/mL UCNP core**
	Y	**Yb**	**Er**	**Y**	**Yb**	**Er**	**Er**	**Er**
	10^{-4} mmol/L	**10^{-5} mmol/L**	**10^{-5} mmol/L**	**10^{-4} mmol/L**	**10^{-5} mmol/L**	**10^{-5} mmol/L**	**10^{-5} mmol/L**	**10^{-5} mmol/L**
UC@thin_NH_2	[6.29±0.22]	[4.62±0.62]	[3.36±1.89]	[6.76±0.04]	[4.33±0.61]	[3.44±1.59]	[1.87±0.80]	[1.76±1.52]
UC@thick_NH_2	[1.10±0.03]	[0.58±0.30]	[3.59±1.59]	[2.31±0.11]	[4.62±0.55]	[2.17±0.43]	[3.58±1.90]	[1.97±1.40]
UC@thick	[20.00±0.3]	[3.36±1.12]	[5.98±0.24]	[20.00±0.23]	[3.8±1.06]	[6.72 ±0.85]	[3.14±1.83]	[2.02±0.91]

Table 4-15: Filtered lanthanide ions value from the corresponding chlorides obtained from ICP-OES measurements. The error range lies at 10 % for all samples.

Initial ions concentration	**Water**						**Supplemented DMEM**	
	Y		**Yb**		Er		**Er**	
ppm	**mmol/L**	**% ions filtered**	**mmol/L**	**% ions filtered**	**mmol/L**	**% ions filtered**	**mmol/L**	**% ions filtered**
1	[4.30±0.05] × 10^{-3}	38±3	[1.00±0.01] × 10^{-3}	17±2	[3.32±0.05] × 10^{-4}	6.0±0.6	0.002±0.001	34±3
2	[1.00±0.01] × 10^{-2}	45±4	[2.40 ±0.01] × 10^{-3}	21±2	[7.48 ±0.05] × 10^{-4}	6.4±0.6	0.003±0.002	25±3

In all measurements, there were no yttrium or ytterbium ions detected in the filtered dispersion in cell culture medium, although the recovery rate of the ions in water was the lowest for erbium (6.0±0.6 % for 2 ppm and 6.4±0.6% for 1 ppm) followed by ytterbium and yttrium. In supplemented DMEM, only erbium ions could be detected (34±3 and 25±3 % for 1 and 2 ppm initial concentration respectively), indicating probable stronger binding of the ions with macromolecules (protein or amino acids) in DMEM, which hindered the ions from being filtered through the membrane. Lanthanide ions are known to bind with phosphate in phosphate buffered saline (PBS) and form stable lanthanide phosphates.[276] As DMEM contains Na_2HPO_4,[277] it can be assumed that the lanthanide ions were also bound to these mentioned compounds. Dukhno et al.[278] reported faster ion release from UCNP in water than in PBS, which could explain why a higher amount of lanthanide ions was detectable in water. However, the bond strength of each ion depends on the type of protein corona formed and should be further investigated, as there seems to be a difference in coupling affinity for different lanthanide ions in supplemented DMEM, that caused them to be filtered to different degrees.

The sample UC@thin _NH_2 showed the highest amount of lanthanide ions released after 24 h of redispersion and centrifugation in water, followed by UC@thick (see Table 4-14). UC@thick showed a higher degree of released lanthanide ions compared to the functionalized samples, due to a lower degree of particle aggregation in water (see DLS results in chapter 4.4.1). Measurements of erbium in water with both concentrations delivered similar values for both thinly and thickly coated functionalized samples, as well as high error, since the recovery rate for this particular ion is low. In supplemented DMEM the values showed a slight dependency of the released ions relative to the silica shell thickness, where the concentration of the released yttrium and ytterbium ions from thinly coated UCNP were higher than for thickly coated UCNP, depending on the silica shell thickness. The real amount of the released ions were higher, as some released ions could also be trapped in the centrifuge filter, as shown by the ion recovery rate measurements results in Table 4-15. The real amount of released ions of yttrium, for example, could be 55-62 % higher than the values measured by ICP-OES.

The pore size is often described by filtered molecules that have known molecular weight, labeled as molecular weight cut off (MWCO), with typical values between 1-300 kDa.[279] Alternatively, centrifuge filters with larger pores (> 3kDa) could be used for a higher recovery rate of the lanthanide ions, as centrifuge filters of up to 100 kDa have been proven to separate smaller nanoparticles better than the mentioned filter size better in simple solutions.[280] Colloidal silica can be separated in ultracentrifugation with a pore size between 0.01-0.1 µm, under the condition that the silica particle size is below the pore size of the utilized filter. The selection

of the filter size is important to hinder the remaining particles or other macromolecules to pass through the filters, causing inaccuracy of recovery rate of released ions. However, Johnsen et al. [281] reported that the molecular size selectivity of the centrifugation filters of Amicon Ultracentrifuge filters with MWCO betweenof 10-100 kDa was minimal for proteins, as all pore sizes in this range had similar performance and are sufficient enough to separate drug and nanoparticles in simple aqueous solutions, but less advisable for filtration in biological samples. In this work no yttrium or ytterbium ion could be detected after redispersion in cell culture medium. Hence, it is recommended to use larger pore size membranes for centrifugation in a biological medium, i.e., microfiltration should be used for future experiments.

Thick silica coated UCNP functionalized with an amine group protected the UCNP better from possible ion leaking compared to functionalized thin silica-coated UCNP, UC@thick_SiO_2 showed a higher degree of released ions than amine-functionalized particles with the same silica shell thickness.

4.4.3 Quantification of the cytotoxicity of silica coated UCNP on HaCaT cells with MTT assays

Human keratinocytes from the HaCaT cell line were used for the particle cytotoxicity experiments. The cells were cultured in supplemented DMEM at 37 °C in a humidified atmosphere composed of 95 % air and 5 % CO2 and subsequently exposed to the UCNP for 24 h in the conditions described above. Cell viability was determined by the colourimetric MTT assay, measuring the intracellular reduction of tetrazolium salts into purple formazan by viable cells (see Figure 2.17). The same procedure was applied to the RAW 264.7 macrophage cell line. The number of cells cultured in a well for the MTT assay was 10000 cells/well.

The percentage of cell growth inhibition was calculated by the following equation:

$$\%\ \text{of inhibition} = \frac{\text{Absorption at 570 nm from sample}}{\text{Absorption at 570 nm from negative control}} \cdot 100\% \qquad (4.10)$$

Figure 4.71 shows bar charts of cytotoxicity on the HaCaT cells.

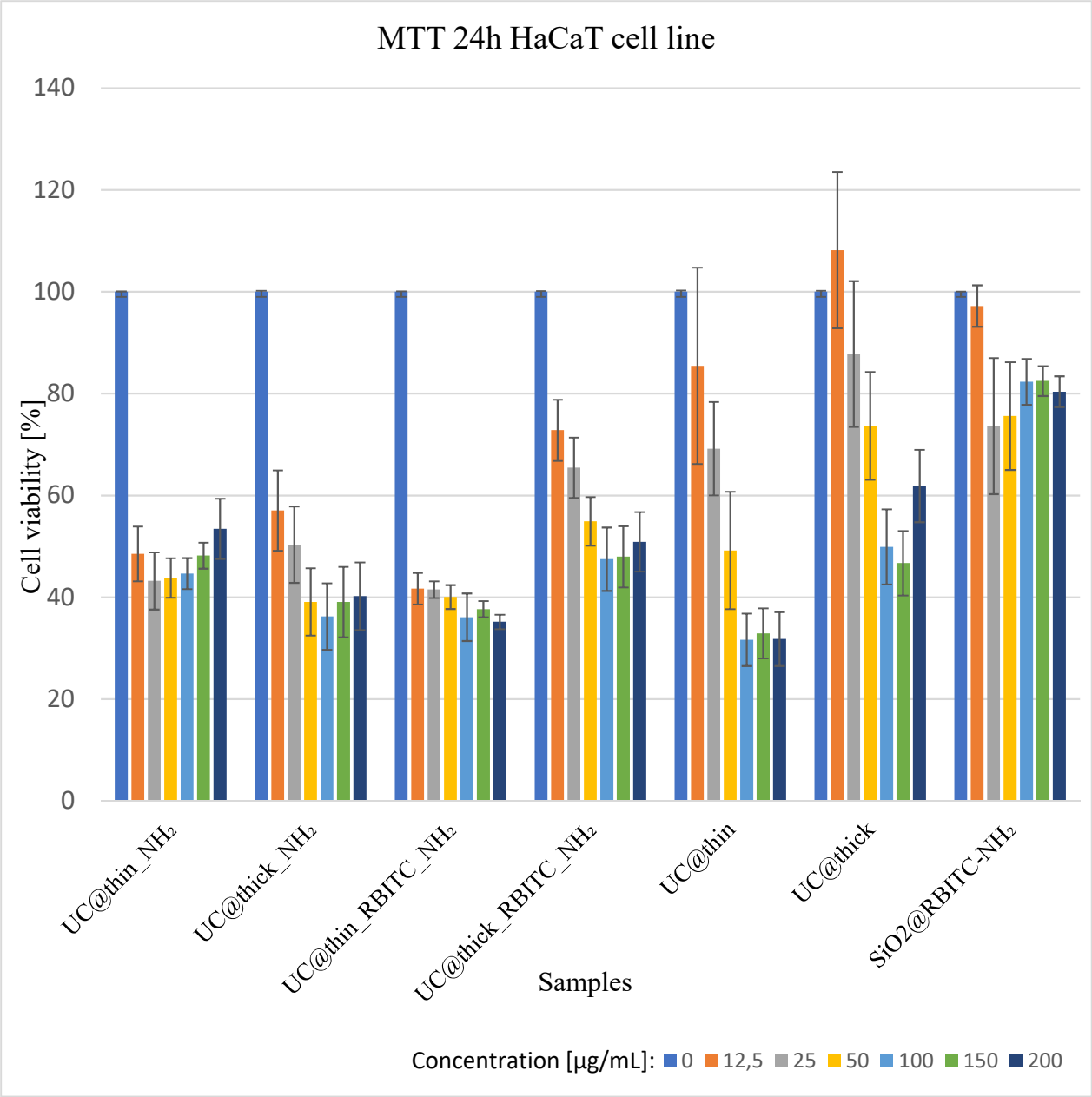

Figure 4.71: MTT assay results of silica coated UC_Er_6 and SiO_2 nanoparticles on HaCaT cells.

The samples with AHAPS ligand showed higher cytotoxicity for the HaCaT cell line than the non-functionalized particles. At the lowest concentration (c = 12.5 µg/mL) of UC @thin_NH_2, the cell viability was 48±2 % and 53±6 % at the highest concentration (c = 200 µg/mL). Sample UC@thin_RBITC_NH_2 reduced the cell viability to 41±3 % at the lowest concentration and to 35±1 % at the highest concentration. There is no significantly lower cytotoxicity of UC@thick_NH_2 compared to UC@thin_NH_2 or UC@thin_RBITC_NH_2. The cytotoxicity of UC@thick_NH_2, UC@thin_NH_2 and UC@thin_RBITC_NH_2 was on a similar level. All these samples showed almost no concentration-dependent cytotoxicity. In the case of UC@thick_RBITC_NH_2, there was in general indeed higher cell viability and concentration-

dependent cytotoxicity. Possible causes of this observation are lower cell proliferation in cells that were exposed to this sample, and lower uptake of the particles, since this sample had a lower zeta potential in water and ethanol compared to UC@thin_NH_2 and UC@thin_RBITC_NH_2, which is consistent with lower interaction with the negatively charged cell membrane. Positively functionalized particles interact more with the negatively charged cell membranes and will increase the probability of uptake into cells,[54, 282-284] which in turn will increase cell toxicity. Sonawane et al.[285] observed that toxicity of amine functionalized nanoparticles was caused by increased pumping of chloride ions in the cells to balance the sudden increase in acidity, causing osmotic swelling and damage to the lysosome.

Samples UC@thin and UC@thick showed more concentration-dependent cytotoxicity compared to the unfunctionalized particles. They were less cytotoxic than their amine-functionalized counterparts at lower concentrations (12.5 and 25 µg/mL). This indicates either a lower uptake of the samples into the cells or a less active metabolism of the HaCaT cells in the presence of the unfunctionalized particles. However, UC@thin caused high cell mortality at 200 µg/mL particle concentrations, with the cell viability being only 31±1 %. The non-functionalized samples showed minimal degrees of aggregation upon dispersion in cell culture medium, which led to the conclusion that the cytotoxicity was caused by non-specific particle adsorption through electrostatic interactions, since silica particles could penetrate into the cell without having a positive surface charge.[140, 267, 286-287] The degree of non-specific adsorption through electrostatic interactions was caused by interactions between the negatively charged surface with specific binding sites of the cell membranes, followed by particle internalization.[287] The uptake, however, was less strong than for the functionalized samples, as the non-functionalized samples showed a lower cytotoxicity rate.

UC@thick caused the lowest cytotoxicity, i.e., the highest cell viability compared to the other samples. The cell viability after exposure was 108±15 % at the highest concentration and 61±7 % at the lowest concentration. Cell viability higher than the control was possible due to high cell proliferation and minimal variability in the number of cells seeded per well. However, the difference to the control was still within the error margin. The lower toxicity of the thickly coated UCNP could be related to a lower aggregation rate of the sample, since the z-average value in DMEM after 30 minutes did not indicate any signs of increased aggregation. Additionally, it can be assumed there was indeed size- or silica thickness dependent cytotoxicity in case of the non-functionalized samples, where UC@thin was more cytotoxic than UC@thick. Smaller sized particles are commonly more cytotoxic to cells, due to their increased surface-to-volume ratio and consequent increase in interactions with cell membranes.[288-289] The thin silica

shell might also lead to an increased degree of ion release into the cell culture medium. Based on the results of the ion release experiments, the thinly coated UCNP could also be expected to release more lanthanide ions into the environment, causing a higher rate of cell mortality. UC@thick had low cytotoxicity despite having a higher degree of ion release compared to functionalized UCNP with the same shell thickness. However, since UC@thick had a negative surface charge, it was less adsorbed on the cell membrane than the functionalized particles, besides having less aggregation degree in DMEM. Consequently, the particles did not have higher cell toxicity.

Sample SiO_2@RBITC_NH_2 exhibited a high cell compatibility (cell viability = 97±4 % at c = 12.5 µg/mL and 80±2 % at c = 200 µg/mL) compared to several publications: Mu et al.[290] tested 14 nm size silica-NP on HaCaT cells at a particle concentration of 100 µg/mL, and after 24 h the cell viability was at 35 %; whereas Liang et al.[286] reported the cytotoxicity of 50 nm SiO_2 NP on HaCaT cells. At c = 200 µg/mL particle concentration the cell viability was 37±2 %. Based on this reported literature, the pure silica particles in the current work were small enough to enter the HaCaT cells and be internalized in the cytoplasm, phagosomes, and autophagosomes. However, SiO_2@RBITC_NH_2 did not cause a high rate of cell mortality due to a strong aggregation effect in DMEM, causing low particle uptake through the cell membrane through endocytosis.

4.4.4 Confocal laser scanning microscopy measurements on HaCaT cells

Optical observation of particle uptake into the HaCaT cells was done by using a confocal laser scanning microscope. The HaCaT cells (1×10^6 cells) were seeded into a 6-well plate with supplemented RPMI on microscope slides. UC@thin_RBITC_NH_2 and UC@thick_RBITC_NH_2 (c = 100 µg/mL in RPMI) were added to the wells. Supplemented RPMI was used as this was the only available medium at the time of the confocal measurements. However, RPMI and DMEM are commonly used media for growing adherent cells (cells that are grown as monolayers on an artificial substrate) such as HaCaT cells. The DNA of the cells were stained with 4′,6-diamidino-2-phenylindole (DAPI) after 24 h and visually characterized by a confocal laser scanning microscope (CLSM).

Figure 4.72 and Figure 4.73 show the CLSM images of the HaCaT cells after 24 h of exposure to UC@thin_RBITC_NH_2 and UC@thick_RBITC_NH_2. The positively functionalized particles were adsorbed onto the negatively charged cell membrane, as indicated by the yellow circles. Aggregates are shown by yellow arrows. In both cases, aggregates, as well as single particles, are adsorbed onto the cell surface. UC@thick_RBITC_NH_2 seem to form more

aggregates on the cell surface compared to the corresponding thin silica coated particles. However, based on the MTT assay the cytotoxicity of the thinly-coated samples was higher, indicating that the cytotoxicity was caused by single particle uptake and not by aggregates.

The green arrows show the particles that were adsorbed onto the cell membrane. Additionally, particle uptake is shown in enlarged areas marked by green squares. The particles that were taken up are located inside 'black spots' that presumably are the endocytic vesicles formed after endocytosis.[55, 140] HaCaT cells prefer to endocytose larger aggregates of up to a size of 200 nm than smaller aggregates or particles, which can explain why more aggregates of UC@thick_RBITC_NH_2 were internalized compared to UC@thin_RBITC_NH_2.[55] The uptake was probably facilitated by the formation of the protein corona on the particle surface, due to the presence of FCS in the cell culture medium. [270-273]

UC@thin_RBITC-NH_2 appear to be more cytotoxic than their UC@thick_RBITC-NH_2 despite their lower uptake into HaCaT cells, which indicates that the cytotoxicity might have been partly caused by cell membrane damage due to a higher degree of adsorption of smaller particles. Otherwise, higher levels of release of lanthanide ions from thin silica coated particles could also cause higher damage to the cell membrane (see chapter 4.4.2).

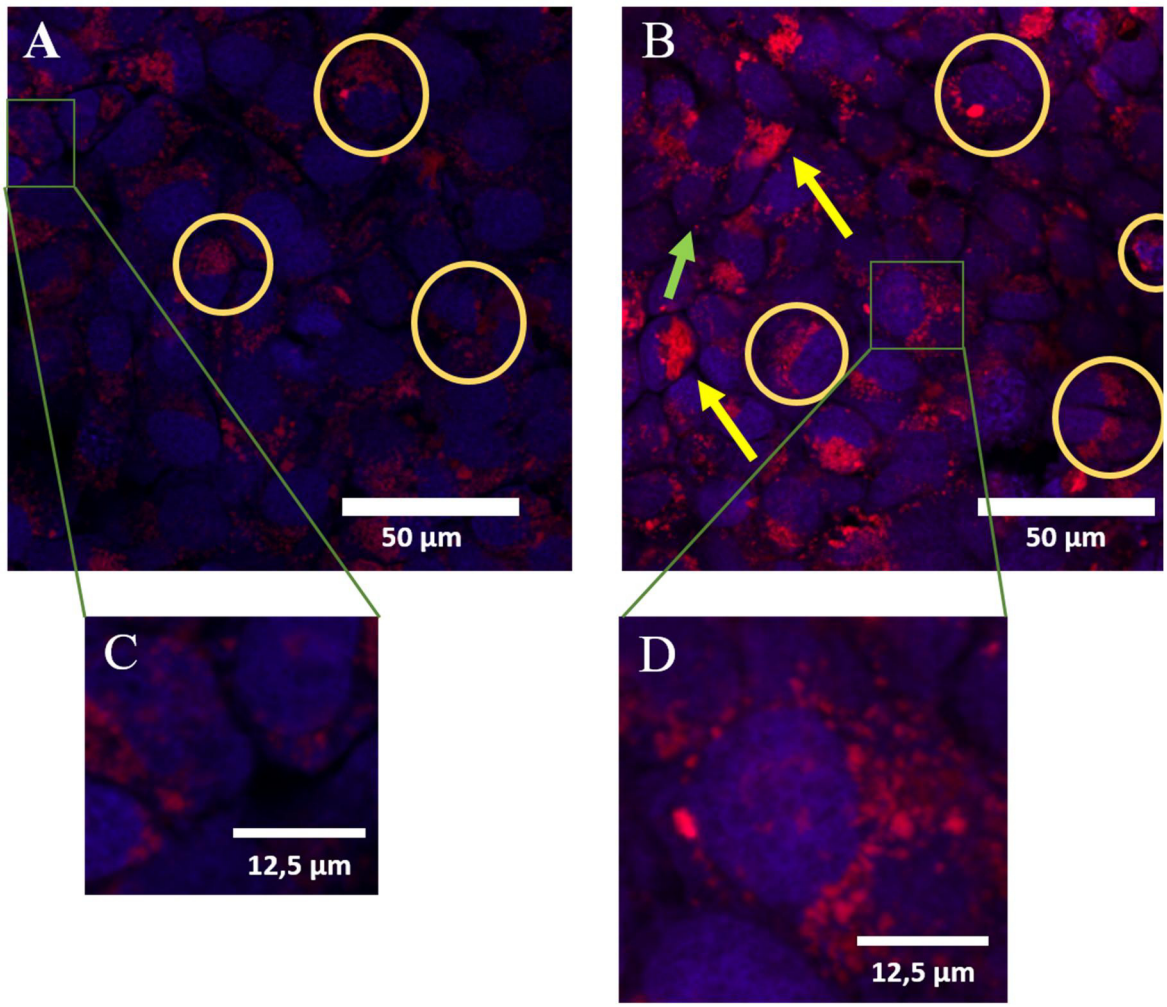

Figure 4.72 A and B: CLSM images of UC@thin_RBITC_NH_2 exposed to HaCaT cells after 24 h. The green arrow indicates the particles that were taken up into the cells; yellow arrows show aggregates of particles. The images C and D are enlarged views of the particle uptake in the areas marked by the green squares.

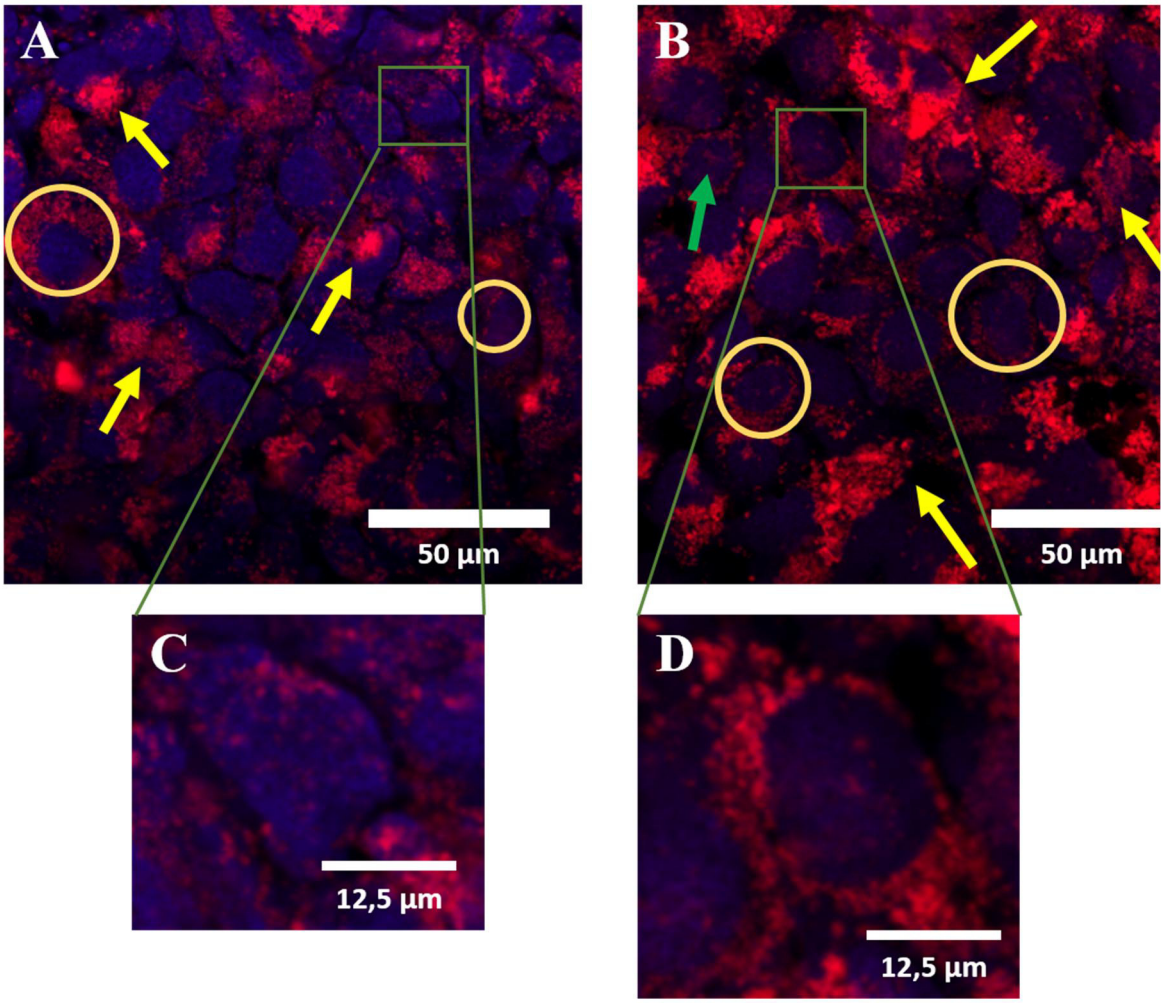

Figure 4.73 A and B: CLSM images of sample UC@thick_RBITC_NH_2 exposed to HaCaT cells for 24 h. The green arrow marks the particles that were taken up in the cells; yellow arrows indicate aggregates of particles. The images C and D are enlarged views of the particle uptake in the areas marked by the green squares.

4.4.5 Flow cytometry measurements of HaCaT cells

Flow cytometry can provide qualitative and quantitative information about internalized particles in cells or those adsorbed onto cellular membranes, relying on the facts that cells that have internalized external molecules have a different granularity and size compared to normal cells before uptake.[291] For the flow cytometry measurements 1 mL of supplemented DMEM medium as control or 100 µg/mL of nanoparticle samples in supplemented DMEM medium was added in duplicates to RAW 264.7 cells or HaCaT cells in 12-well plates and incubated at three different conditions: for 4 hours at a temperature of 4 ºC in the fridge (4h@4 °C), 4 hours at 37 ºC (4h@37 °C) and 24 hours at 37 °C (24h@37 °C) in 5 % CO_2 atmosphere in an incubator. At a temperature of 4 °C, all metabolic activities of cells would be minimal, hence the non-specific adsorption (passive uptake) or initial endocytosis process of the particles with

the cells can be observed.[292] At 37 °C, i.e., at physiological temperature, the metabolic activities of the cells would at the maximum, hence allowing the observation of the active uptake of the particles into the cells. Flow cytometry measurements of UC@thin_RBITC_NH_2 in the HaCaT cells could not be carried out due to an insufficient amount of sample.

After the incubation the medium was removed, the cells were washed with PBS and measured with a cytometer. Two possible measurement parameters can be used: forward scattering (FS), which gives information of the sample size and side scatter (SS) analysis provides information on the granularity or inner density of the cells.[293] Both measurements depend on the fact that an active or undisturbed cell scatters differently than an unhealthy or non-viable cell. [294-295] The granularity and volume of cells depend on the viability of the cells, which can be influenced by the amount of uptaken or adsorbed particles.[291] As an example, the SS intensity increases in the case of apoptotic cells, due to a decrease of cell size and increase of cell inner density.[294] FS results would show a peak intensity decrease in an FS-counts-histogram in case of a decrease in cell viability after particle adsorption or uptake.[291, 293] SS peak intensity would increase when the cell granularity increases after particle uptake or adsorption.[291]

Positively functionalized silica coated UCNP should have higher uptake in the cells, since they can interact better with the negatively charged cell membranes of the cells compared to non-functionalized particles.[54, 282-284] This effect can be observed from the cell viability results in the cytotoxicity experiments from the previous chapter 4.4.3.

In the flow cytometry measurements, the FS and SS measurements should deliver a peak shift and change of intensity after exposure to particles: the FS peak intensity should decrease when the cell viability decreases with increasing particle uptake, owing to the increase in cell volume which in turn increases scattering. On the other hand, SS intensity should increase as cell viability decreases, owing to the increase in cell granularity. The shift of peak and changes in intensity on FS and SS measurement should be observable, since the cell viability of the HaCaT cells decreased to approximately 50 % in almost all samples (except UC@thick) after exposure to 100 µg/mL of silica-coated UCNP. Since FS measurements are mostly used to distinguish cell types based on their different sizes, and SS is predominantly used to measure changes in inner cell density, this chapter will focus more on SS measurements results.

The influence of various silica shell thicknesses on the cell granularity after uptake was further characterized in the SS histograms. The y-axis represents the cell number counts, and the x-axis represents signal intensity. Figure 4.74 shows an example of SS histograms overlap for HaCaT cells after exposure for 4 h at 4 °C(A), 4 h (B) and 24 h (C) at 37 ºC with control (blue-coloured peak), UC@thin_NH_2 (red-coloured peak) and UC@thick_NH_2 (green-coloured peak). The

histograms also only represent a qualitative value of the SSC value, since each histogram only represents one replicate (there were in total two replicates or duplicates of each sample in each condition) and not the overall SS mean value. After incubation for 4 h at 4°C, the SS histograms of cells exposed to UC@thick_NH_2 and UC@thin_NH_2 show a change in peak intensity compared to the control, where the peak change in UC@thick_NH_2 was more prominent than for UC@thin_NH_2. The same effect was also observed after 4 h at 37 °C. This indicates that UC@thick_NH_2 influenced the cell granularity more than the thinly-coated UCNP, which probably was caused by a higher uptake or adsorption of thickly-coated UCNP sample. After 24 h at 37°C, the SS histogram of UC@thick_NH_2 shows a similar intensity as in the other two incubation conditions and the SS intensity was lower than in the cells exposed to UC@thin_NH_2. It was challenging to compare the intensities of the UCNP samples to the control under the last condition, as the control showed lower intensities to the exposed samples, indicating a change of cell granularity (viability) after 24 h due to unknown factors.

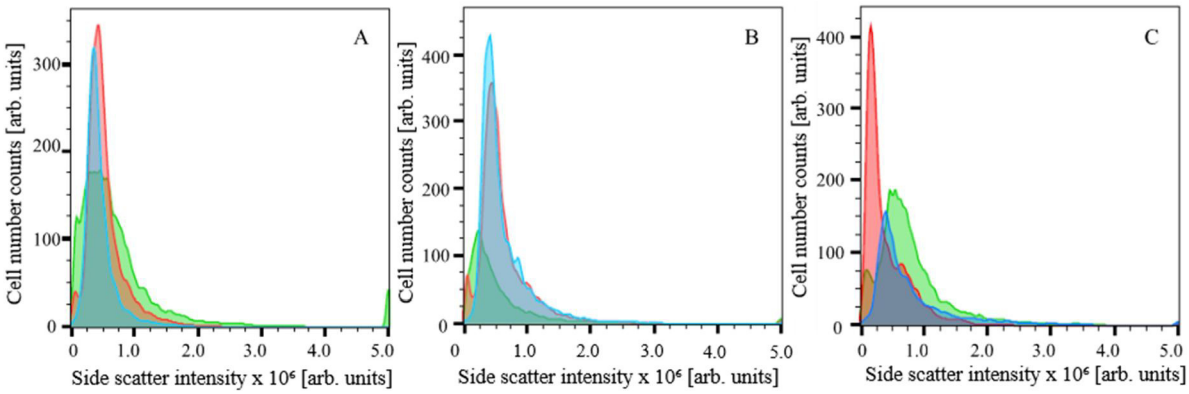

Figure 4.74: SSC (side scatter) histograms of controls (blue-colored peak), UC@thin_NH_2 (red-colored peak) and UC@thick _NH_2 (green-colored peak) after A: 4 h at 4 °C, B:4 h and C: 24 h at 37 °C of incubation with HaCaT cells at 37°C.

Figure 4.75 shows a summary of the SS mean values from duplicates of each samples at the three incubation conditions. The unit of SS mean value is an arbitrary unit. The samples show similar cell granularity, after 4 h at 4 °C, where a low metabolic activity occurred due to low temperature, indicating that under this condition low degree uptake takes place. Only UC@thin and UC@thick show SS mean values that are lower than the control, indicating higher cell proliferation or cell division in these samples. After 4 h at 37 °C the cells exposed to the particles also show similar cell granularity or SS mean value compared to the control, indicating low uptake.

After 24 h incubation at 37 °C, the SS mean value for the thickly-coated UCNP increased compared to the thinly-coated UCNP, indicating higher cell granularities after uptake of thickly-coated UCNP. Samples exposed to UC@thin_NH_2 had an SS mean value of [598±130] × 10^3, whereas samples exposed to UC@thick_NH_2 had an SS mean value of [857±8] × 10^3, which meant a 43±23 % higher SS mean value for UC@thick_NH_2 than for UC@thin_NH_2.

UC@thick_NH_2 had similar cytotoxicity on HaCaT cells as UC@thin_NH_2 at a particle concentration of 100 µg/mL according to MTT assay result. From the SS measurement, one can assume that UC@thick_NH_2 was uptaken by HaCaT cells to a higher degree compared to UC@thin_NH_2, based on the higher degree of change in the peak intensity compared to the control. The higher degree of uptake was likely due to lower z-average value, i.e. higher stability of UC@thick_NH_2. The z-average of UC@thin_NH_2 was 336±14 nm, whereas UC@thick_NH_2 had a z-average of 220±4 nm, which is a suitable size for endocytosis, and consistent with the higher uptake and cellular granularity observed for the latter sample.[55]

After 24 h the SS mean value for UC@thin_NH_2 was [598±130] × 10^3, and that of UC@thin was [765±116] × 10^3, which means the cells exposed to the latter sample had higher cell granularity. The cytotoxicity of UC@thin was higher at c = 100 µg/mL than for UC@thin_NH_2, causing the cell viability of the sample exposed to the unfunctionalized particles to be lower than for UC@thin_NH_2. After 24 h the SS mean value for UC@thick_NH_2 was [857±8] × 10^3 and that of UC@thick was [822±10] × 10^3, while the control was [881±15] × 10^3. UC@thick had decrease of SS mean value of 7±2 % compared to the control while UC@thick_NH_2 had a 3±2 % decrease, which indicates that the cells exposed to the latter sample were not influenced in terms of cell granularity.

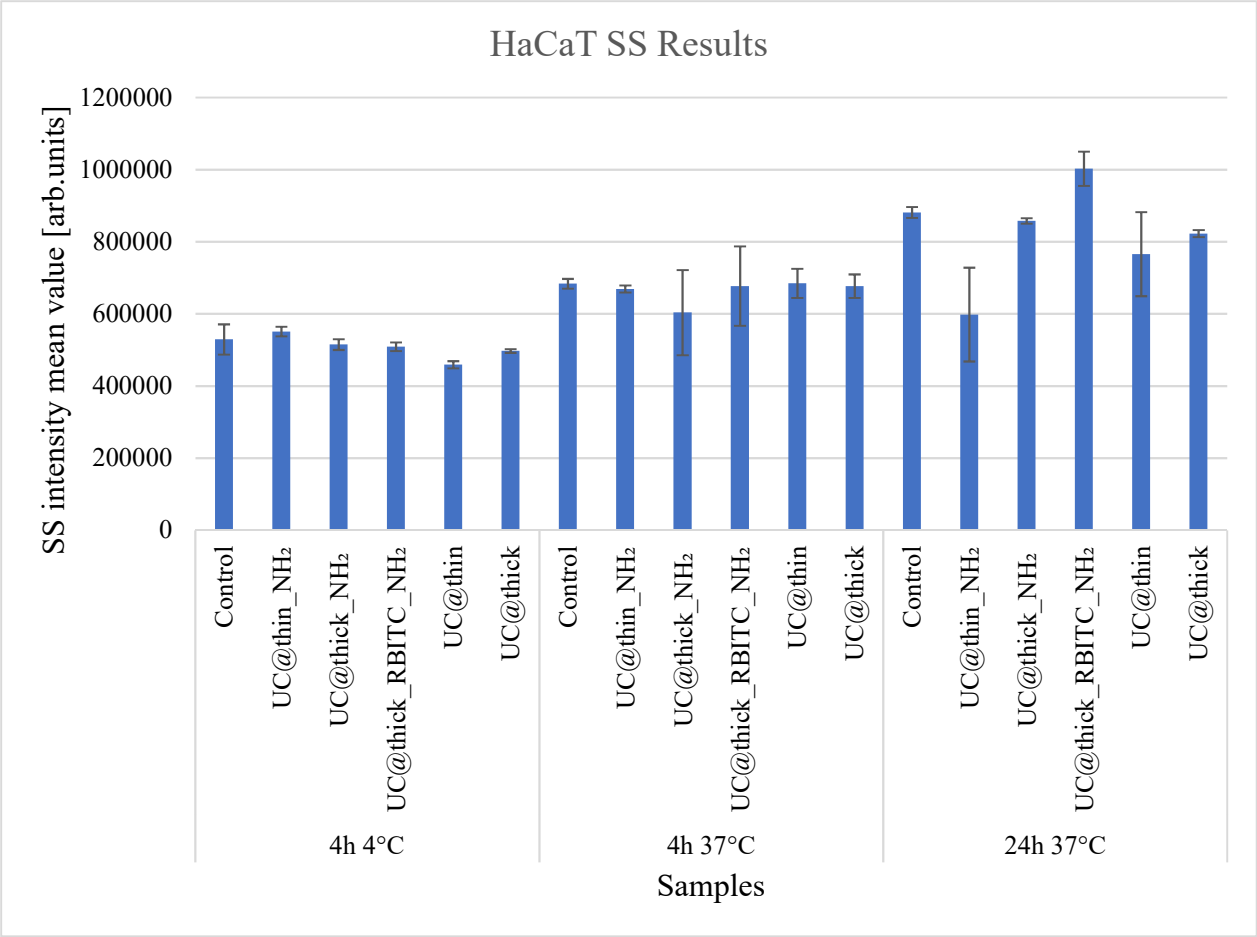

Figure 4.75: Summary of SS flow cytometry measurements on exposed HaCaT cells at three conditions: 4 h @ 4 ºC, 4 h @ 37 ºC and 24 h @ 37 ºC.

In conclusion, the cytotoxicity of the amine functionalized thick and thin silica coated UCNP is similar for HaCaT cells. UC@thick_RBITC_NH_2 was less cytotoxic than the other functionalized UCNP, despite higher SS intensity after 24 h. However, more tests have to be done to prove the consistency of the results.

The degree of particles' cytotoxicity based on the MTT assay results can be directly correlated to the SS intensity or changes thereof compared to the control. As an example, the cells exposed to UC@thin_NH_2 and UC@thick_NH_2. The cells exposed to UC@thick_NH_2 later had a higher degree of cytotoxicity at 100 µg/mL and caused bigger changes of the SS mean value compared to the UC@thin_NH_2, suggesting bigger changes of the cell granularity of the former compared to the later. The general cytotoxicity across all concentrations, however, is similar for both samples. UC@thin_NH_2, despite its smaller size than UC@thick_NH_2 which should lead to a higher change in cell granularity, formed bigger aggregates in DMEM, as can be seen from the z-average values of the particles in DMEM after 24 h redispersion in DMEM, causing less internalization and therefore less toxicity according to the MTT assay.

The non-functionalized particles generally caused a lower degree of cytotoxicity compared to the amine-functionalized particles, due to a higher uptake of the positively functionalized particles resulting from a higher degree of initial interactions with the negatively charged membranes. [238-240]

Indeed, the samples with non-functionalized particles caused fewer changes (increase) in the SS peak intensity compared to the amine functionalized particles.

The degree of lanthanide ions released from the particles, as shown by the ICP-OES measurement results, was as expected higher in case of the thinly-coated UCNP, suggesting that the cytotoxicity could also be partly caused by the released ions. Although lanthanide ions are mainly non-toxic compared to other non-dietary elements, they can readily form insoluble colloids of carbonate, phosphate or hydroxide at around neutral pH.[295] Several *in vitro* studies also suggested that rare earth ions could change metabolic pathways and physiological processes.[296-297] Fluoride ions and sodium ions could also be released to a higher degree in the thinly-coated UCNP, which would cause higher cytotoxicity compared to thickly-coated sample. Fluoride ions and NaF-compounds are known to cause cell apoptosis in *in vitro* or *in vivo* experiments. [298]

4.4.6 Quantification of the cytotoxicity of silica coated UCNP on RAW 264.7 cells with MTT assays

Figure 4.76 shows the MTT *assay* results for the RAW 264.7 cells. Compared to the HaCaT cells, the silica-coated UCNP have lower cytotoxicity in the RAW 264.7 cells, and a silica shell thickness and concentration-dependent cytotoxicity of the particles is observed in these cells. The cytotoxicity of UC@thin_NH_2 in RAW cells was higher than that of UC@thick_NH_2. At the highest particle concentration (c = 200 µg/mL) the cell viability after exposure to UC@thin_NH_2 was about 51±5 %, whereas in the sample UC@thick_NH_2 cell viability was 75±6 %. At the lowest concentration (c = 12.5 µg/mL) the cell viability was 110±12 % for UC@thin_NH_2 and 95±14 % for UC@thick_NH_2. UC@thin_RBITC_NH_2 caused a slightly higher cytotoxicity than UC@thin_NH_2 especially at lower concentrations of 12.5 and 25 µg/mL. At these concentrations, the cytotoxicity of the former sample was about 74±1 %. In general, UC@thick_NH_2 was the least cytotoxic particle for all samples. At the highest concentrations (c = 150 and 200 µg/mL) of UC@thick_NH_2, no significant difference in the cell viability was observed between the two concentrations. The cytotoxicity of pure silica without a UCNP core (sample SiO_2@RBITC_NH_2) was also measured. The cell viability at the

lowest concentration was 83±5 %, and 68±4 % at the highest concentration, arguing for moderate cytotoxicity.

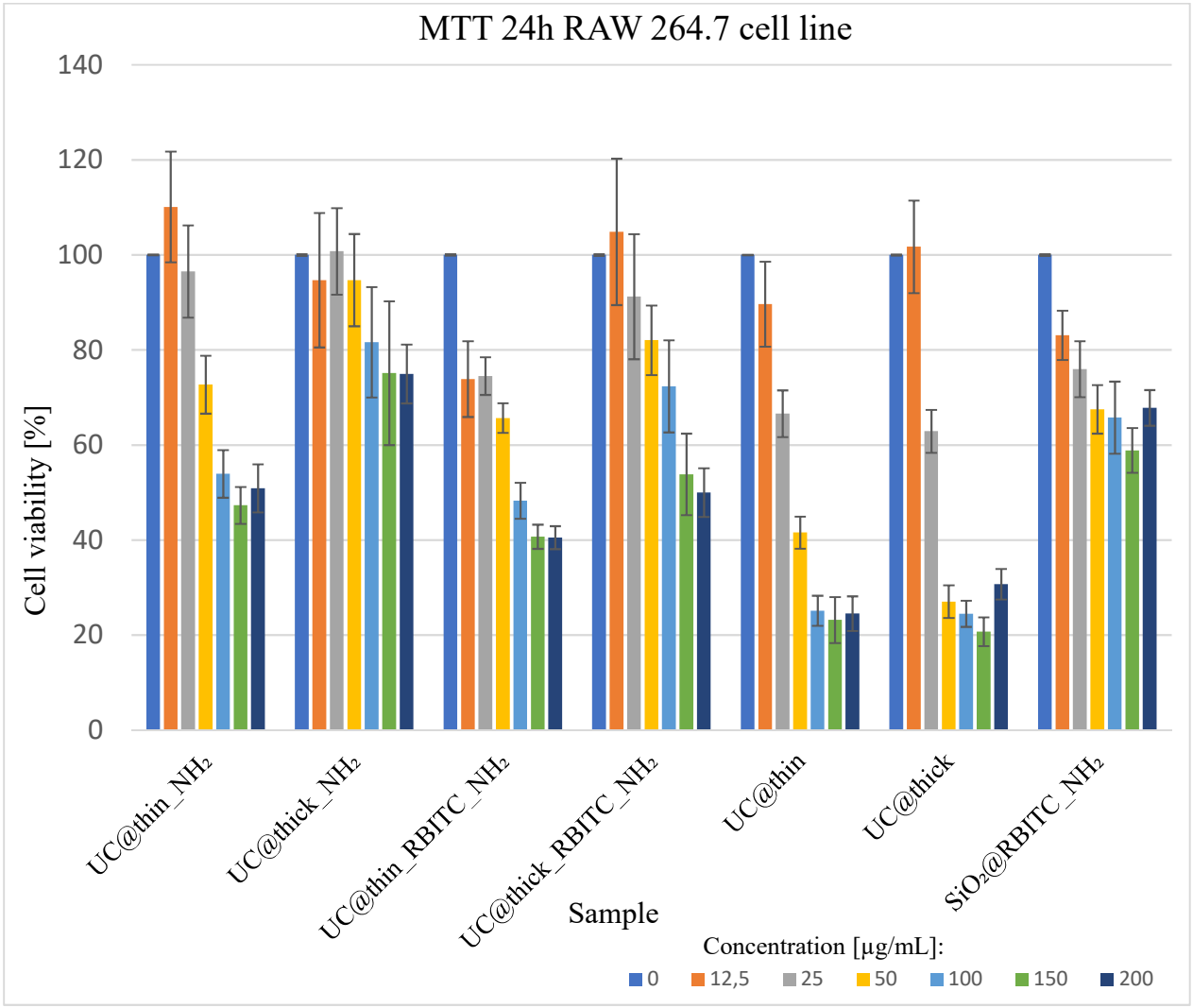

Figure 4.76: MTT assay results of silica coated UC_Er_6 and SiO_2 nanoparticles in RAW 264.7 cells.

The unfunctionalized samples were more cytotoxic compared to the amine-functionalized particles. UC@thin had a higher degree of cytotoxicity than UC@thick, which were contrasting results compared to the experiments with HaCaT cells. In HaCaT cells there was no silica thickness dependent cytotoxicity of the non-functionalized and amine functionalized particles, whereas in RAW 264.7 cells exposed to unfunctionalized UCNP, the cell viability decreased with increasing concentration. The cell viability was already below 70 % at concentrations higher than 25 µg/ml. The cytotoxicity of UC@thin and UC@thick was relatively low only at c = 25 µg/mL. Nabeshi et al.[299] investigated the cytotoxicity of non-modified, amine functionalized, and carboxyl functionalized 70 nm SiO_2 NP in RAW 264.7 cells. They observed that unmodified SiO_2 nanoparticles had the highest cytotoxicity due to higher degree of uptake into the cells, whereas the amine-functionalized particles were only adsorbed onto the cell

membrane. Similar results were also obtained by Kurtz-Chalot et al.[275] where highly positively charged SiO_2 nanoparticles were more adsorbed than taken up compared to the corresponding non-modified particles. Xia et al.[284] observed cell type-dependent cytotoxicity for RAW 264.7, epithelial (BEAS-2B) cells, human microvascular endothelial (HMEC), hepatoma (HEPA-1), and pheochromocytoma (PC-12) cells after exposure to amine-functionalized polystyrene nanoparticles (NH_2-PS). They observed that lysosomal permeabilization and mitochondrial damage happened in RAW cells but not in other cell types. The particles were cytotoxic to RAW 264.7 and BEAS-2B cells but not to other cells. The nanoparticles perturbed the proton pump activity in RAW 264.7 cells, causing osmotic swelling and finally ruptured of the lysosomes. Sohaebuddin et al.[300] reported severe cytotoxicity after exposure of 30 nm SiO_2 nanoparticles to RAW 264.7 cells (100 % cell mortality after 24 h exposure at c = 100 µg/mL). According to these literature results, the RAW 264.7 cells internalize the negatively charged particles better than the positively functionalized ones, causing the former particles to have higher cytotoxicity on RAW 264.7 cells, as could also be observed in this work. The silica shell thickness seems to influence the degree of cytotoxicity of the functionalized samples in the macrophage cells, but not that of the unfunctionalized particles, as both the thick and thin coated unfunctionalized silica samples caused similar cytotoxicity degree to the cells.

The results depicted in Figure 4.76 suggest that the samples with thin silica shells are more cytotoxic than those with thick silica shells. This could be the result of the higher amount of lanthanide ions released from thinly-coated UCNP. It is also assumed that other ions could be released at a higher degree from the thin-shelled UCNP compared to the thick-shelled UCNP, for example, fluoride (F^-)-ions and Na^+-ions in the ratio of Na:Y:F = 1:1:4. Depending on the concentration of fluoride ions and NaF can cause cell apoptosis.[298] Further investigation on the amount of released fluoride and sodium ions should be done in further experiments.

Generally, the samples with unfunctionalized silica shells caused higher cytotoxicity, compared to the functionalized samples. The amine functionalization played a bigger role in decreasing cell viability than the particle size or silica shell thickness.

4.4.7 Flow cytometry measurements of murine macrophage RAW 264.7 cells

The SS measurements results of macrophage cells RAW 264.7 after exposure to silica-coated UCNP are discussed in this chapter. Since the controls for samples with functionalized particles and non-functionalized particles (UC@thin and UC@thick) at 37 °C did not come from the same cell proliferation batch due to technical reasons, the comparison of changes of SS peak

intensity can only be made qualitatively between the functionalized and unfunctionalized samples.

Figure 4.77 shows SS histograms of RAW 264.7 cells after exposure for 4 h at 4°C, 4 h at 37°C, and 24 h at 37 ºC to UC@thin_NH_2 (blue framed peak) and UC@thick_NH_2 (red framed peak), the controls are marked with a yellow framed peak. The peak intensities after 4 h and 24 h at 37 °C exposure show obvious differences between the controls and the samples, where the intensities of the samples were lower compared to the control. After 4 h of exposure at 4 °C, the peak intensity of the control was less intensive than that of the samples, indicating increased cell granularities of the exposed cells even at low temperature. The SS mean value (see Figure 4.78) for UC@thin_NH_2 after 4 h at 4 °C was [390±5] × 10^3, and that of UC@thick_NH_2 was [427±1] × 10^3, while the control was [344±63] × 10^3. The absolute increase of the SS mean value of the thick-shelled UCNP was 13±21 % and 24±23 % for the thinly-coated UCNP compared to the control, which indicates a higher increase of cell granularity in the sample with thickly-coated UCNP, although the value was still within the error margin of the control. The SS mean value for UC@thin_NH_2 after 4 h at 37 °C was [247±14] × 10^3, and that of UC@thick_NH_2 was [279±90] × 10^3, the control was [219±11] × 10^3. The absolute increase of SS mean value of the thick-shelled UCNP was 27±6 %, and that of the thinly-coated sample was 13±6 % compared to the control, which indicates a higher increase of cell granularity in the sample with thickly-coated UCNP.

After 24 h the SS mean value for UC@thin_NH_2 was [251±8] × 10^3, and that of UC@thick_NH_2 was [323 ±17] × 10^3, while the control was [212±6] × 10^3. The percentage increase of the SS mean value for UC@thin_NH_2 was 18±5 % and 52±9 for UC@thick_NH_2, indicating a higher increase of cell granularity for UC@thick_NH_2 compared to the samples with the thin-shelled particles. The MTT cytotoxicity assay showed higher cytotoxicity for UC@thin_NH_2 compared to UC@thick_NH_2, which means the stronger increase of cell granularity due to exposure to thickly-coated particles did not directly lead to higher cytotoxicity. Samples exposed to UC@thin_NH_2 did not show a cytotoxicity-related increase of cell granularity.

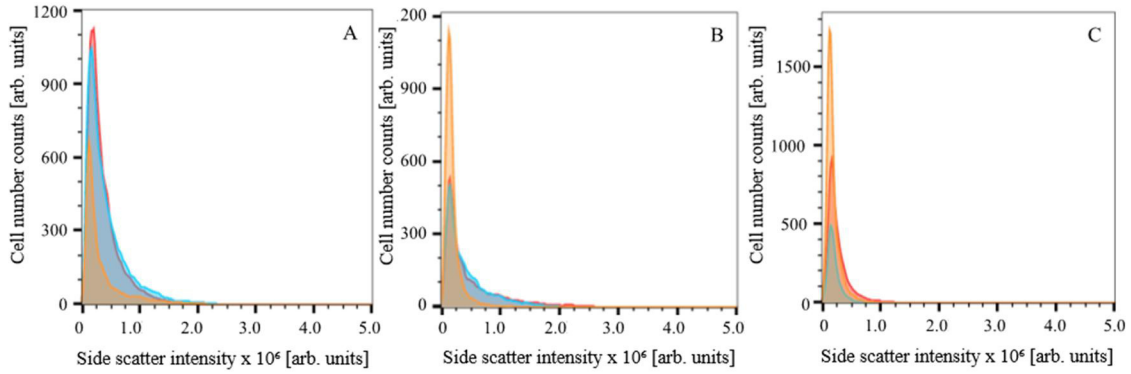

Figure 4.77: SSC histograms of RAW 264.7 cells after particle exposure for A: 4 h at 4 °C; B: 4 h at37 °C, and C: 24h at 37 °C. UC@thin_NH_2 is marked by a blue framed peak, UC@thick_NH_2 is marked by red framed peak and the control is marked by a yellow framed peak.

Figure 4.78 shows a bar chart of the SS mean values for RAW 264.7 cells. The flow cytometry measurements of UC@thin and UC@thick after 4 h and 24 h at 37 °C were done at another time than the rest of the samples. Hence, they had their own negative (control) samples. Mostly, the UCNP samples with thicker shells had higher SS mean value than those with thin shells, indicating higher changes of cell granularity after exposure to the nanoparticles. However, this did not directly lead to higher cytotoxicity, since the thinly-coated samples had a higher degree of cytotoxicity in the MTT test than the thickly-coated particles. The cytotoxicity of the thinly-coated samples must have been caused by other effects that did not result in higher increase of cell granularity, such as the higher release of ions, as indicated in the previous chapter of ion release experiments.

At 4 h at 37 °C, the samples with unfunctionalized silica coated UCNP have similar SS mean values independent of the shell thickness, indicating the similar degree of particle uptake or adsorption, where UC@thin caused a slightly higher increase of cell granularity after 4 h and 24 h at 37 °C than UC@thick. In the cytotoxicity tests, both samples have a similar degree of cytotoxicity at c = 100 µg/mL.

As can be seen in Figure 4.78, the SS mean values of the controls for all incubation conditions were quite variable, so it was difficult to draw general conclusions. Still, the relative increase of the SS mean value of each sample compared to the controls at each condition can be qualitatively analyzed.

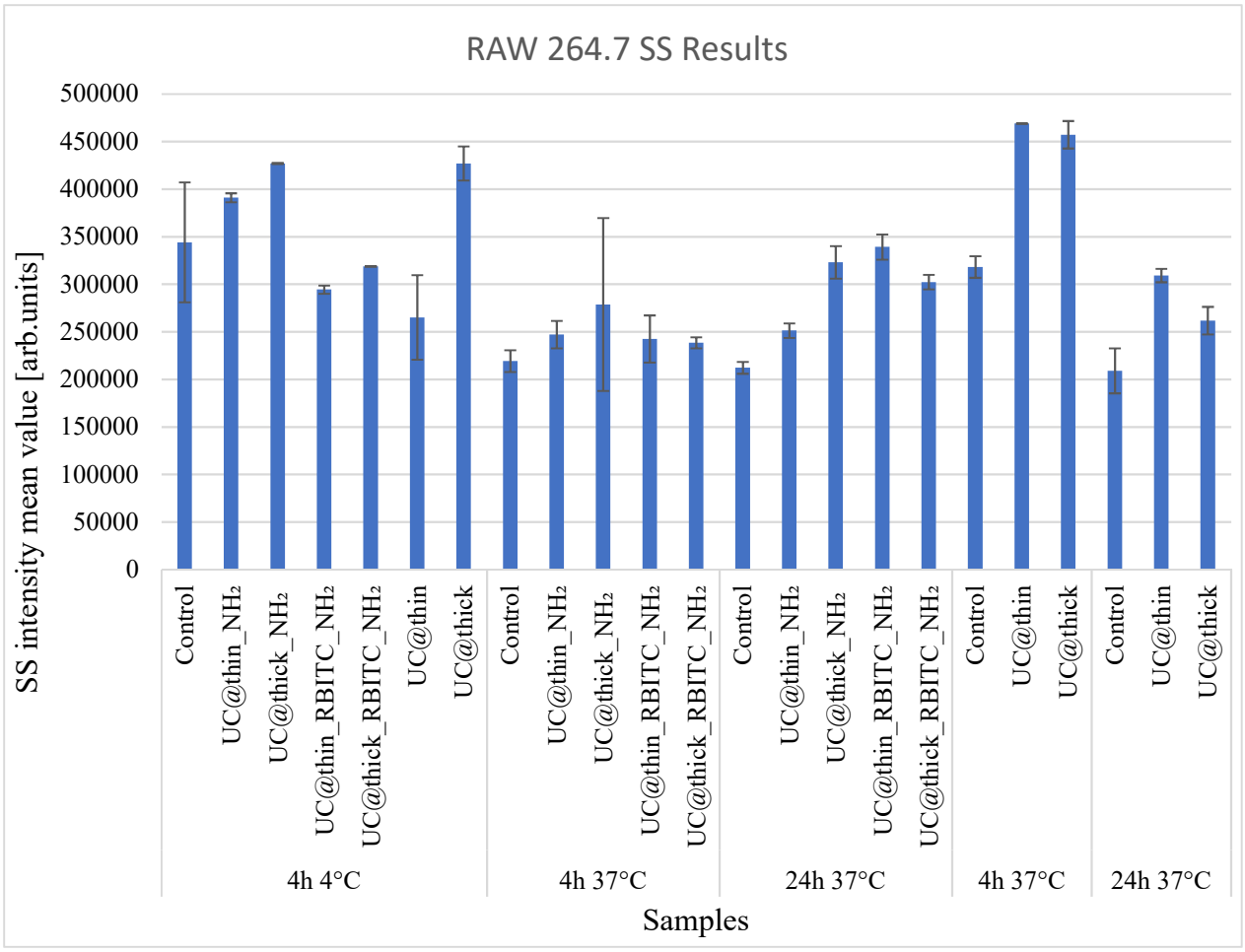

Figure 4.78: Summary of mean SSC flow cytometry measurements on all samples in RAW 264.7 cells at three conditions: 4 h @ 4 ºC, 4 h @ 37 ºC, and 24 h @ 37 ºC.

By correlating the results of the cell viability from the MTT assay with the flow cytometry measurements of the macrophage RAW 264.7 cells, it could be surmised that there is reduction of cell viability and an increase of the cell granularity dependent on the silica shell thickness. Thinly- coated functionalized particles caused lower cell viability than thicker shelled particles. However thickly-coated particles caused stronger changes in cell granularity than the thinly-coated particles. The higher change in cell granularity could mean that a higher degree of adsorption or uptake occurred, which did not necessarily lead directly to higher cytotoxicity.[301] The cytotoxicity of the functionalized samples with the thinly-coated particles was likely due to a higher degree of ion release to the environment. Except after exposure for 4 h at 4 °C, both UC@thin and UC@thick caused similar changes in cell granularity. As in the MTT cytotoxicity test, both samples caused a similar change in cell viability.

The thickness of the silica shell did not heavily influence the extent of cytotoxicity in HaCaT cells. Except for UC@thin_RBITC_NH_2, which due to increased aggregation did cause slightly higher cytotoxicity compared to UC@thick_RBITC_NH_2. In the macrophage cells, the

thickness of the silica shell played a significant role in the degree of cytotoxicity, at least for the functionalized particles, where the thinly-coated particles were more cytotoxic due to a higher degree of ion release.

Generally, the amine-functionalized particles caused higher cytotoxicity to HaCaT cells than to RAW 264.7 cells, whereas the unfunctionalized samples caused higher cytotoxicity to RAW 264.7 cells than to HaCaT cells. The samples with thin silica shells were more cytotoxic to macrophage RAW 264.7 cells than the samples with thick silica shells. The number of released ions from the UCNP core depending on the silica shell thickness could be detected in pure water, whereas in the cell culture medium the released ions were either very small or not detectable. The amount of the released ions depended on the initial concentration of the contained ions and the type of ions. Lower degrees of doping of ions in UCNP or lower ion concentration in solution caused a lower degree of filtered ions than was the case at higher initial ion concentration. Overall, samples with thicker silica shells have lower cytotoxicity than the ones with thinner silica shells. Generally, the HaCaT cells showed more sensitivity to the samples compared to the macrophage cells.

In flow cytometry measurements the cells exposed to samples with thicker silica shells caused a higher degree of cell granularity in the HaCaT and RAW cell line. Likewise, amino-functionalized particles (without dye) caused a higher SS mean value compared to unfunctionalized particles in the HaCaT cell line. This indicates that the amine ligand supports the adsorption on the cells and the particle uptake into cells. However, more replicates are needed for the flow cytometry since the results showed no explainable trend in the RAW cells, and the controls in the HaCaT cells partly showed a higher SS intensity than the samples.

The influence of silica coated UCNP with variable thickness and surface charge on their toxicity to HaCaT and RAW 264.7 cell lines was successfully investigated. Further studies that include more replicates in the flow cytometry measurements to characterize the uptake for both cell lines are however needed. Experiments to determine the degree of released fluoride and sodium ions should also be considered to relate the cytotoxicity of particles to the amounts released ions

5 Conclusions and Outlook

The main aim of this thesis was to investigate the changes of upconversion luminescence intensity of structured UCNP due to their resonant coupling with a plasmonic system such as a gold nanoshell. The structured UCNP consisted of a host structure of $NaYF_4$, which was doped with ytterbium as sensitizer and erbium as emitter, and consecutively coated with a silica and a gold shell. The changes in the emission intensity compared to particles without gold coating can occur in the form of enhancement, due to excitation or field enhancement, emission enhancement, or in the form emission quenching. Enhancement can be caused by the coupling of the excitation or emission energy to the plasmon resonance of the shell, which could be tuned by adjusting the core-shell ratio and adjusting the distance to the UCNP core (via adjustment of the thickness of the silica shell). Hence, finding a suitable core-shell structure was essential to reach upconversion enhancement. The particles were characterized by scanning transmission electron microscopy (STEM), X-ray diffraction spectrometry (XRD), dynamic light scattering (DLS), electrophoretic light scattering, inductively coupled plasma-optical emission spectroscopy (ICP-OES), UV-VIS-NIR spectroscopy and by upconversion fluorescence spectroscopy.

The optimal synthesis for UCNP with high monodispersity was first explored in chapter 4.1. UCNP consisting of $NaYF_4$ doped with 18 % Yb, and 2 % Er were synthesized by thermal decomposition method to yield monodisperse nanoparticles in the size range between 24-33 nm. The thermal decomposition with oleate precursors delivered the most consistent results regarding particle size and monodispersity, compared to other methods such as thermal decomposition with lanthanide chlorides or lanthanide trifluoroacetates as precursors. An undoped layer of $NaYF_4$ was coated onto the $NaYF_4$: Yb, Er cores through the thermal decomposition method using yttrium oleate as precursor. XRD measurements confirmed the formation of the undoped layer, which was shown by the weakening of cubic peaks that existed in the XRD diffractogram of the core, due to an increase of additional hexagonal peaks of the undoped layer. Through the undoped layer of 2±1 nm, the upconversion emission could be increased by a factor of 4.5 compared to the particles without such a layer, owing to surface passivation that prevents the interactions of the surface lanthanide ions with high vibrational energy sources such as organic ligands and solvents and the decrease of surface defects, which exist in the core and could lead to non-radiative decay processes.

Plasmon enhancement of UCNP consecutively coated with silica and gold was investigated in chapter 4.2. Calculations were done beforehand to determine which silica coated UCNP core-gold

shell size ratio was suitable for optimal upconversion emission enhancement. Two emission wavelengths were considered in the calculation: 540 nm (green) emission and 654 nm (red) emission for $NaYF_4$: Yb, Er cores. There were two limiting factors for emission enhancement of the structured UCNP: enhancement after dimmed pump excitation and enhancement after saturated pump excitation. In the case of a dimmed pump excitation, measurable enhancement of the green and red emission were expected for UCNP (d = 24 nm) with either thin silica shells (less than 30 nm) and thin gold shells (less than 10 nm) at dipole mode enhancement or with thicker silica shells between 110-120 nm and thick gold shells between 10-60 nm at cavity mode enhancement. In the case of saturated pump excitation, dipole mode, and higher order mode (quadrupole, hexapole) enhancements were possible. The focus was to coat UCNP cores with thick silica shells of more than 30 nm and gold shell with a thickness between 10-60 nm for optimal enhancement either in the higher order modes or in cavity mode, as the method for coating thick gold shell on large particles (d > 200 nm) is already well-established.

Thick silica shells were coated onto UCNP cores through a combination of the modified reverse microemulsion and Stöber methods, before coating them with gold nanoshells with a certain thickness for optimal plasmon enhancement based on the calculated core-shell ratios. First, thin silica shells were grown in the range of 7-44 nm on 24±2 nm diameter $NaYF_4$: Yb, Er through four growth steps in a modified reverse microemulsion. The fifth and further shells could be grown using the Stöber method, due to the increase of the colloidal stability along with the growth of the silica shell. The final silica shell thickness was 149±16 nm. An increase in green emission was observed, consistent with increasing silica shell thickness, since the UCNP core became better protected from the diffusion of ethanol or water into the silica shell, whose OH group will otherwise interfere with green emission.

Next, gold nanoclusters were bound onto surface functionalized silica coated UCNP, and gold nanoshells were grown consecutively on these clusters to investigate how plasmonic metal shells can modify upconversion emission resulting from changes due to local field enhancement, surface plasmon-coupled emission, or absorption of the excitation or emission light by the metal shell. The gold cluster deposition (d = 2±1 nm), which functioned as seeds for growing the gold shell, can be done in a one- or two-step deposition to ensure the growth of a smooth gold shell. For the growth of the gold shell, the one-step cluster deposition was proven to deliver a better homogenous shell.

The first successful experiment for coating closed gold shells was done on $NaYF_4$: Yb, Er particles (d = 24±2 nm) with a silica shell thickness of 44±4 nm and a gold shell thickness of 30±6 nm. A

medium-to-strong enhancement was expected at the 540 nm emission in the case of saturated pump excitation for these particles. Suppression of the emission at 540 nm and 654 nm emission was predicted in the case of dimmed pump excitation. The second sample of structured UCNP consisted of the same UCNP cores with a silica shell thickness of 149±8 nm, which were further coated with a thick complete gold shell with a thickness of 48±20 nm.

The measured extinction spectra of the gold shell particles were compared with theoretically modelled spectra to determine the correct core-shell size ratio, since silica particles could shrink in an electron microscope due to damage from the high energy electron beam and the high vacuum atmosphere. It turned out that the shrinking of the silica core in SEM was not as severe as reported in the literature for TEM, since the acceleration voltage used was much lower compared to TEM. Therefore, the measured extinction spectra were similar to the calculated spectra using the measured STEM diameter as the input size parameter for spectra modelling.

The investigation of possible enhancement in the upconversion luminescence intensity of samples with thinner than 30 nm and 48 nm gold shell compared to the silica-coated sample without gold shells was done with single particle measurements with a confocal setup under saturated pump excitation, since under this condition higher upconversion enhancement could theoretically be achieved than by dimmed pump excitation. In the single particle measurements, the green and red emission of the samples with thin gold shell were measured after application of 8000 and 16000 pulses, which represent lower and higher power density, respectively, with both being considered as saturated pump excitation. Based on calculations, an enhancement factor of 2.52 for the 540 nm emission and of 1.03 for the 655 nm emission was expected for the mentioned gold-shelled sample. However, the green emission intensity of the coated particles was 43±4 % lower than that of the uncoated ones, whereas the red emission intensity was 67±7 % lower than that of the non-gold shelled counterpart. The decay rate at all emission wavelengths in the single particle measurements decreased after coating with gold shell. The increase of the decay times was accompanied by emission quenching, which indicates an increase of the non-radiative decay rate at both emission wavelengths, either due to upconversion emission energy, absorption from excited Er^{3+} ions by the gold shell or by a non-radiative energy transfer of emission to the gold shell.

The emission intensities of the particles with the thick gold shell were also weaker than that of their respective non-shelled counterparts. The calculations predicted an enhancement factor of 0.19 at 540 nm emission, which indicates suppressed emission, and 2.3 at 654 nm emission, consistent with slight enhancement. The measured intensity of the green emission was 43±4 % lower, whereas

the red emission intensity was 67±7 % lower than that of the non-gold shelled counterpart. The decay times of the green and red emission of the gold-coated sample increased compared to those of uncoated particles. As in the case of samples with the thin gold shells, a thermal quenching effect, indicated by an increase of the lifetime at different excitation energies, should also be considered for high excitation power densities in the single particle measurements. A thick gold shell could further cause stronger cavity confinement, where the thick shell obstructed the excitation photons from reaching the UCNP and also prevented the emitted photons from being detected.

In future experiments, one could consider developing a method for coating silica coated UCNP cores with thinner gold shells to prevent excitation or emission absorption by thick gold shells. The same sized core may be coated first by a thin silica shell of 8 nm, and consecutively a gold shell of 10 nm thickness for optimal dipole mode enhancement under saturated pump excitation; or a silica shell with 20 nm thickness and gold shell thinner than 10 nm for dipole mode enhancement under dimmed pump excitation.

For the investigation of a possible fluorescence resonance energy transfer (FRET) effect from upconversion fluorescence emission to a nearby dye in chapter 4.3, rhodamine B isothiocyanate (RBITC) was coupled in the silica shells grown onto $NaYF_4$: Yb, Er nanoparticles (d = 24±2 nm) as core. RBITC was chosen, since its excitation energy is in the range of green upconversion emission of $NaYF_4$: Yb, Er nanoparticles. The average silica shell thickness of the five samples was 7±1 nm. The average dye coupling efficiency was 31±8 % and the coupled RBITC concentration was 0.71-1.99 mmol/L. The characterization of the upconversion fluorescence emission indicated excitation of the dye as a slight dye emission in the 580 nm range, originating either from FRET or reabsorption. The erbium ions on the surface transfered their energy mainly through the FRET process to the rhodamine dye, while the reabsorption process occurred between the erbium ions inside the UCNP sphere and the dye molecules in the silica. Although most dye molecules in the silica shell were within the Förster distance to the surface erbium ions, which could non-radiatively transfer their emission energy, stronger reabsorption effects between the erbium ions inside the UCNP sphere and the dye molecules in the silica dominated the energy transfer process. One could optimize the energy transfer efficiency by using $NaGdF_4$ as host crystal for resonant energy migration process, where the excitation energy is confined to the particle surface or by separating the sensitizer ytterbium and the emitter erbium in different layers since ytterbium is more sensitive to surface quenchers.

The cytotoxicity of silica coated UCNP on human keratinocytes (HaCaT cells), and murine macrophages (RAW 264.7 cells) were investigated with an MTT assay in chapter 4.4. Microporous silica shells with two different thicknesses: 7±1 nm for the thinly-coated silica and 21±2 nm for thickly-coated silica were coated onto the UCNP $NaYF_4$:Yb, Er (d = 33±2 nm) to increase the hydrophilicity of the particles, thus enabling them to be dispersed in cell culture medium for biological experiments. The particles were subsequently functionalized with N-(6-aminohexyl)-aminopropyltrimethoxysilane (AHAPS) that provided a positive charge on the nanoparticle surface to increase their uptake rate into cells. Experiments to quantify the amount of possible released lanthanide ions in the cell culture medium were performed to relate possible ion dissolution with their degree of cytotoxicity. The UCNP uptake potential was evaluated by flow cytometry through light side scattering measurement which was proportional to cell granularity or internal complexity. It was proven using ion release experiments that more lanthanide ions were released at a higher degree from thinner shelled samples and could possibly influence the degree of cytotoxicity of the particular samples.

The unfunctionalized particles generally had lower degrees of cytotoxicity in HaCaT compared to the amine-functionalized ones, due to a higher uptake of the positively functionalized particles resulting from a higher degree of initial interactions with the negatively charged membranes. The unfunctionalized particles caused lower changes in cell granularity compared to the amine-functionalized particles, which indicates that the degree of cytotoxicity correlated directly with the degree of cell granularity and that the amine ligand supported their adsorption on the cells and eventually their uptake.

By correlating MTT assay results with the flow cytometry measurements of the RAW 264.7 cells, a reduction in cell viability and an increase of cell granularity could be demonstrated after exposure, depending on the silica shell thickness of the particles. Thinner coated functionalized particles caused higher cytotoxicity than thicker coated particles, due to a higher degree of released lanthanide ions. In flow cytometry measurements the cells exposed to samples with thicker silica shells generally showed a higher degree of cell granularity in both the HaCaT and RAW 264.7 cell line. The unfunctionalized particles were more cytotoxic to the macrophage cells than the amine-functionalized particles. In future studies, experiments to determine the degree of released fluoride and sodium ions should also be considered to relate the particle cytotoxicity to the released or leached metal ions. The obtained results are important for future *in vivo* applications of UCNP as

bioimaging agents or in bioassays, as coating with a silica shells can be used to decrease the potential toxicity of UCNP.

Taken together a method for synthesizing UCNP with high upconversion emission intensity was optimized. The UCNP cores could be coated with a silica shell in the range from 7 to 149 nm, either for subsequent coating with a plasmon metal shell in plasmon-enhanced upconversion emission investigations or for increasing their hydrophilicity for further use in biological experiments. Furthermore, dye coupled in the silica shell on UCNP could be used in FRET-studies. Conclusively, UCNP shows great potential for the development of a wide-range future applications, either in optical electronics or in bioimaging. This thesis explored possibilities through which this can be possible, for example, by coupling these particles with various nanosystems or molecules.

6 Literature

1. Alemán, J.; Chadwick, A. V.; He, J., et al., Definitions of terms relating to the structure and processing of sols, gels, networks, and inorganic-organic hybrid materials (iupac recommendations 2007). Pure. Appl. Chem. **2007,** 79, 1801.

2. Burda, C.; Chen, X.; Narayanan, R., et al., Chemistry and properties of nanocrystals of different shapes. Chem. Rev. **2005,** 105, 1025.

3. Vollath, D., Nanomaterials: An introduction to synthesis, properties and application. Wiley-VCH Verlag GmbH & Co..KGaA: Weinheim, 2008.

4. Lead, J.; Wilkinson, K., Aquatic colloids and nanoparticles: Current knowledge and future trends. Environ. Chem. **2006,** 3, 159.

5. Lintern, M.; Anand, R.; Ryan, C., et al., Natural gold particles in eucalyptus leaves and their relevance to exploration for buried gold deposits. Nat. Comm. **2013,** 4, 2274.

6. Colomban, P.; Gouadec, G., The ideal ceramic-fibre/oxide-matrix composite: How to reconcile antagonist physical and chemical requirements?. Ann. Chim. Sci. Mater. **2005,** 30, 673.

7. Hashim, A. A., The delivery of nanoparticles. InTechOpen: Rijeka, Croatia, 2012.

8. Colomban, P., The use of metal nanoparticles to produce yellow, red and iridescent colour, from bronze age to present times in lustre pottery and glass: Solid state chemistry, spectroscopy and nanostructure. J. Nano Res. **2009,** 8, 109.

9. Salata, O. V., Applications of nanoparticles in biology and medicine. J. Nanobiotechnol. **2004,** 2, 3.

10. Pansare, V. J.; Hejazi, S.; Faenza, W. J., et al., Review of long-wavelength optical and NIR imaging materials: Contrast agents, fluorophores, and multifunctional nano carriers. Chem. Mater. **2012,** 24, 812.

11. Trofymchuk, K.; Reisch, A.; Shulov, I., et al., Tuning the colour and photostability of perylene diimides inside polymer nanoparticles: Towards biodegradable substitutes of quantum dots. Nanoscale **2014,** 6, 12934.

12. Soper, S. A.; Mattingly, Q. L., Steady-state and picosecond laser fluorescence studies of nonradiative pathways in tricarbocyanine dyes: Implications to the design of near-IR fluorochromes with high fluorescence efficiencies. J. Am. Chem. Soc. **1994,** 116, 3744.

13. Resch-Genger, U.; Grabolle, M.; Cavaliere-Jaricot, S., et al., Quantum dots versus organic dyes as fluorescent labels. Nat. Mater. **2008,** 5, 763.

14. Parak, W. J.; Pellegrino, T.; Plank, C., Labelling of cells with quantum dots. Nanotechnology **2005,** 16, R9.

15. Derfus, A. M.; Chan, W. C. W.; Bhatia, S. N., Probing the cytotoxicity of semiconductor quantum dots. Nano Lett. **2004,** 4, 11.

16. Kirchner, C.; Liedl, T.; Kudera, S., et al., Cytotoxicity of colloidal CdSe and CdSe/ZnS nanoparticles. Nano Lett. **2005,** 5, 331.

17. Efros, A. L.; Nesbitt, D. J., Origin and control of blinking in quantum dots. Nat. Nano. **2016,** 11, 661.

18. Chen, G.; Qiu, H.; Prasad, P. N., et al., Upconversion nanoparticles: Design, nanochemistry, and applications in theranostics. Chem. Rev. **2014,** 114, 5161.

19. Zhao, J.; Wu, J.; Xue, J., et al., Au/$NaYF_4$:Yb/Er binary superparticles: Synthesis and optical properties. Isr. J. Chem. **2016,** 56, 242.

20. Wang, Z.; Wang, C.; Han, Q., et al., Metal-enhanced upconversion luminescence of $NaYF_4$:Yb/Er with Ag nanoparticles. Mater. Res. Bull. **2017,** 88, 182.

21. Zhang, H.; Li, Y.; Ivanov, I. A., et al., Plasmonic modulation of the upconversion fluorescence in $NaYF_4$:Yb/Tm hexaplate nanocrystals using gold nanoparticles or nanoshells. Angew. Chem. Int. Edit. **2010,** 49, 2865.

22. Schietinger, S.; Aichele, T.; Wang, H.-Q., et al., Plasmon-enhanced upconversion in single $NaYF_4$:Yb^{3+}/Er^{3+} codoped nanocrystals. Nano Lett. **2010,** 10, 134.

23. Zhang, F.; Braun, G. B.; Shi, Y., et al., Fabrication of Ag@SiO_2@Y_2O_3:Er nanostructures for bioimaging: Tuning of the upconversion fluorescence with silver nanoparticles. J. Am. Chem. Soc. **2010,** 132, 2850.

24. Ge, W.; Zhang, X.; Liu, M., et al., Distance dependence of gold-enhanced upconversion luminescence in Au/SiO_2/ Y_2O_3: Yb^{3+}, Er^{3+} nanoparticles. Theranostics. **2013**; 3, 282.

25. Wei, D.; Sudheendra, L.; Jiangbo, Z., et al., Upconversion in $NaYF_4$:Yb/Er nanoparticles amplified by metal nanostructures. Nanotechnology **2011,** 22, 325604.

26. Esteban, R.; Laroche, M.; Greffet, J.-J., Influence of metallic nanoparticles on upconversion processes. J. Appl. Phys. **2009,** 105, 033107.

27. Wu, D. M.; García-Etxarri, A.; Salleo, A., et al., Plasmon-enhanced upconversion. J. Phys. Chem. Lett. **2014,** 5, 4020.

28. Amendola, V.; Bakr, O. M.; Stelacci, F., A study of the surface plasmon resonance of silver nanoparticles by the discrete dipole approximation method: Effect of shape, size, structure, and assembly. Plasmonics **2010,** 5, 85.

29. Qian, L. P.; Zhou, L. H.; Too, H.-P., et al., Gold decorated $NaYF_4$:Yb/Er/$NaYF_4$/silica (core/shell/shell) upconversion nanoparticles for photothermal destruction of BE(2)-C neuroblastoma cells. J. Nanopart. Res. **2011,** 13, 499.

30. Fujii, M.; Nakano, T.; Imakita, K., et al., Upconversion luminescence of Er and Yb codoped $NaYF_4$ nanoparticles with metal shells. J. Phys. Chem. C **2013,** 117, 1113.

31. Priyam, A.; Idris, N. M.; Zhang, Y., Gold nanoshell coated $NaYF_4$ nanoparticles for simultaneously enhanced upconversion fluorescence and darkfield imaging. J. Mater. Chem.**2012,** 22, 960.

32. Dousti, M. R.; Amjad, R. J.; Mahraz, Z. A. S., Enhanced green and red upconversion emissions in Er^{3+}-doped boro-tellurite glass containing gold nanoparticles. J. Mol. Struct. **2015,** 1079, 347.

33. Greybush, N. J.; Saboktakin, M.; Ye, X., et al., Plasmon-enhanced upconversion luminescence in single nanophosphor–nanorod heterodimers formed through template-assisted self-assembly. ACS Nano **2014,** 8, 9482.

34. Zhang, W.; Ding, F.; Chou, S. Y., Large enhancement of upconversion luminescence of $NaYF_4$:Yb^{3+}/Er^{3+} nanocrystal by 3D plasmonic nano-antennas. Adv. Mater. **2012,** 24, OP236.

35. Kannan, P.; Abdul Rahim, F.; Chen, R., et al., Au nanorod decoration on $NaYF_4$:Yb/Tm nanoparticles for enhanced emission and wavelength-dependent biomolecular sensing. ACS Appl. Mater. Inter. **2013,** 5, 3508.

36. Feng, A. L.; Lin, M.; Tian, L., et al., Selective enhancement of red emission from upconversion nanoparticles via surface plasmon-coupled emission. RSC Adv. **2015,** 5, 76825.

37. Fischer, S.; Hallermann, F.; Eichelkraut, T., et al., Plasmon enhanced upconversion luminescence near gold nanoparticles–simulation and analysis of the interactions. Opt. Express **2012,** 20, 271.

38. Park, W.; Lu, D.; Ahn, S., Plasmon enhancement of luminescence upconversion. Chem. Soc. Rev. **2015,** 44, 2940.

39. Abdul Jalil, R.; Zhang, Y., Biocompatibility of silica coated $NaYF_4$ upconversion fluorescent nanocrystals. Biomaterials **2008,** 29, 4122.

40. Chen, J.; Zhao, J. X., Upconversion nanomaterials: Synthesis, mechanism, and applications in sensing. Sensors **2012,** 12, 2414.

41. Guller, A. E.; Generalova, A. N.; Petersen, E. V., et al., Cytotoxicity and non-specific cellular uptake of bare and surface-modified upconversion nanoparticles in human skin cells. Nano Res. **2015,** 8, 1546.

42. Li, R.; Ji, Z.; Dong, J., et al., Enhancing the imaging and biosafety of upconversion nanoparticles through phosphonate coating. ACS Nano **2015,** 9, 3293.

43. Wang, F.; Banerjee, D.; Liu, Y., et al., Upconversion nanoparticles in biological labeling, imaging, and therapy. Analyst **2010,** 135, 1839.

44. Wang, M.; Abbineni, G.; Clevenger, A., et al., Upconversion nanoparticles: Synthesis, surface modification and biological applications. Nanomed-Nanotechnol. **2011,** 7, 710.

45. Wang, Y.; Liu, K.; Liu, X., et al., Critical shell thickness of core/shell upconversion luminescence nanoplatform for FRET application. J. Phys. Chem. Lett. **2011,** 2, 2083.

46. Chang, H.; Xie, J.; Zhao, B., et al., Rare earth ion-doped upconversion nanocrystals: Synthesis and surface modification. Nanomaterials **2015,** 5, 1.

47. Muhr, V.; Würth, C.; Kraft, M., et al., Particle-size-dependent Förster resonance energy transfer from upconversion nanoparticles to organic dyes. Anal. Chem. **2017,** 89, 4868.

48. Mattsson, L.; Wegner, K. D.; Hildebrandt, N., et al., Upconverting nanoparticle to quantum dot FRET for homogeneous double-nano biosensors. RSC Adv. **2015,** 5, 13270.

49. Arbeloa, F. L.; Ojeda, P. R.; Arbeloa, I. L., Fluorescence self-quenching of the molecular forms of rhodamine B in aqueous and ethanolic solutions. J. Lumin. **1989,** 44, 105.

50. Sun, L.-D.; Wang, Y.-F.; Yan, C.-H., Paradigms and challenges for bioapplication of rare earth upconversion luminescent nanoparticles: Small size and tunable emission/excitation spectra. Acc. Chem. Res. **2014,** 47, 1001.

51. Dong, H.; Du, S.-R.; Zheng, X.-Y., et al., Lanthanide nanoparticles: From design toward bioimaging and therapy. Chem. Rev. **2015,** 115, 10725.

52. Liu, S.; Chen, G.; Ohulchanskyy, T. Y., et al., Facile synthesis and potential bioimaging applications of hybrid upconverting and plasmonic $NaGdF_4:Yb^{3+}$, Er^{3+} /silica/gold nanoparticles. Theranostics **2013,** 3, 275.

53. Li, R.; Ji, Z.; Dong, J., et al., Cytotoxicity, tumor targeting and pet imaging of sub-5 nm $KGdF_4$ multifunctional rare earth nanoparticles. ACS Nano **2015,** 9, 3293.

54. Graf, C.; Gao, Q.; Schütz, I., et al., Surface functionalization of silica nanoparticles supports colloidal stability in physiological media and facilitates internalization in cells. Langmuir **2012,** 28, 7598.

55. Rancan, F.; Gao, Q.; Graf, C., et al., Skin penetration and cellular uptake of amorphous silica nanoparticles with variable size, surface functionalization, and colloidal stability. ACS Nano **2012,** 6, 6829.

56. Kuhn, D. A.; Vanhecke, D.; Michen, B., et al., Different endocytotic uptake mechanisms for nanoparticles in epithelial cells and macrophages. Beilstein J Nanotech. **2014,** 5, 1625.

57. Schmid, G., Principles and fundamentals. Wiley VCH: Weinheim, 2008.

58. Iravani, S., Green synthesis of metal nanoparticles using plants. Green Chem. **2011,** 13, 2638.

59. Wilbur, J. L.; Whitesides, G. M., Self-assembly and self-assembled monolayers in micro- and nanofabrication. In Nanotechnology, Timp, G., Ed. Springer New York: New York, NY, 1999; pp 331.

60. Ventra, M. D.; Evoy, S.; Haflin, J. R., Introduction to nanoscale science and technology. Springer US: Boston, USA, 2004.

61. Alvarez, M. M.; Khoury, J. T.; Schaaff, T. G., et al., Optical absorption spectra of nanocrystal gold molecules. J. Phys. Chem. B **1997,** 101, 3706.

62. Khlebtsov, N.; Dykman, L., Biodistribution and toxicity of engineered gold nanoparticles: A review of *in vitro* and *in vivo* studies. Chem. Soc. Rev. **2011,** 40, 1647.

63. Hammond, J.; Bhalla, N.; Rafiee, S., et al., Localized surface plasmon resonance as a biosensing platform for developing countries. Biosensors **2014**, 4, 172.

64. Dykman, L. A.; Khlebtsov, N. G., Gold nanoparticles in biology and medicine: Recent advances and prospects. Acta Naturae **2011,** 3, 34.

65. Ge, L.; Li, Q.; Wang, M., et al., Nanosilver particles in medical applications: Synthesis, performance, and toxicity. Int. J. Nanomed. **2014,** 9, 2399.

66. Medintz, I. L.; Mattoussi, H.; Clapp, A. R., Potential clinical applications of quantum dots. Int. J. Nanomed. **2008,** 3, 151.

67. Fang, W.; Wei, Y., Upconversion nanoparticle as a theranostic agent for tumor imaging and therapy. J.Innov. Opt. Heal. Sci. **2016,** 09, 1630006.

68. Haase, M.; Schafer, H., Upconverting nanoparticles. Angew. Chem. Int. Ed. Engl. **2011,** 50, 5808.

69. Wang, F.; Liu, X., Recent advances in the chemistry of lanthanide-doped upconversion nanocrystals. Chem. Soc. Rev. **2009,** 38, 976.

70. Heer, S.; Kömpe, K.; Güdel, H. U., et al., Highly efficient multicolour upconversion emission in transparent colloids of lanthanide-doped $NaYF_4$ nanocrystals. Adv. Mater. **2004,** 16, 2102.

71. Stouwdam, J. W.; Van Veggel, F. C. J. M., Near-infrared emission of redispersible Er^{3+}, Nd^{3+}, and Ho^{3+} doped LaF_3 nanoparticles. Nano Lett. **2002,** 2, 733.

72. Yi, G.; Lu, H.; Zhao, S., et al., Synthesis, characterization, and biological application of size-controlled nanocrystalline $NaYF_4$:Yb, Er infrared-to-visible up-conversion phosphors. Nano Lett. **2004,** 4, 2191.

73. Zhang, Y.-W.; Sun, X.; Si, R., et al., Single-crystalline and monodisperse LaF_3 triangular nanoplates from a single-source precursor. J. Am. Chem. Soc. **2005,** 127, 3260.

74. Mai, H.-X.; Zhang, Y.-W.; Si, R., et al., High-quality sodium rare-earth fluoride nanocrystals: Controlled synthesis and optical properties. J. Am. Chem. Soc. **2006,** 128, 6426.

75. Mai, H.-X.; Zhang, Y.-W.; Sun, L.-D., et al., Size- and phase-controlled synthesis of monodisperse $NaYF_4$:Yb, Er nanocrystals from a unique delayed nucleation pathway monitored with upconversion spectroscopy. J. Phys. Chem. C **2007,** 111, 13730.

76. Boyer, J.-C.; Cuccia, L. A.; Capobianco, J. A., Synthesis of colloidal upconverting $NaYF_4$: Er^{3+}/Yb^{3+} and Tm^{3+}/Yb^{3+} monodisperse nanocrystals. Nano Lett. **2007,** 7, 847.

77. Jingning, S.; Xiao, Q.; Nan, Y., et al., Synthesis of monodisperse hexagonal $NaYF_4$: Yb, Ln (Ln = Er, Ho and Tm) upconversion nanocrystals in TOPO. Nanotechnology **2007,** 18, 445607.

78. Jingning, S.; Yiguang, J., A single-step synthesis and the kinetic mechanism for monodisperse and hexagonal-phase $NaYF_4$: Yb, Er upconversion nanophosphors. Nanotechnology **2009,** 20, 275603.

79. Wang, F.; Chatterjee, D. K.; Li, Z., et al., Synthesis of polyethylenimine/$NaYF_4$ nanoparticles with upconversion fluorescence. Nanotechnology **2006,** 17, 5786.

80. Wang, F.; Liu, X., Upconversion multi colour fine-tuning: Visible to near-infrared emission from lanthanide-doped $NaYF_4$ nanoparticles. J. Am. Chem. Soc. **2008,** 130, 5642.

81. Wang, M.; Mi, C.-C.; Liu, J.-L., et al., One-step synthesis and characterization of water-soluble $NaYF_4$:Yb,Er/polymer nanoparticles with efficient up-conversion fluorescence. J. Alloy Compd. **2009,** 485, L24.

82. Park, J.; An, K.; Hwang, Y., et al., Ultra-large-scale syntheses of monodisperse nanocrystals. Nat. Mater. **2004,** 3, 891.

83. Stöber, W.; Fink, A.; Bohn, E., Controlled growth of monodisperse silica spheres in the micron size range. J.Coll. Interface Sci. **1968,** 26, 62.

84. Arriagada, F. J.; Osseo-Asare, K., Synthesis of nanometer-sized silica by controlled hydrolysis in reverse micellar systems. In The colloid chemistry of silica, American Chemical Society: 1994; Vol. 234, p 113.

85. Arriagada, F. J.; Osseo-Asare, K., Synthesis of nanosize silica in a nonionic water-in-oil microemulsion: Effects of the water/surfactant molar ratio and ammonia concentration. J. Coll. Interface Sci. **1999,** 211, 210.

86. Luca, R.; Stefano, B.; Barbara, C., et al., Immobilization of proteins in silica gel: Biochemical and biophysical properties. Curr. Org. Chem. **2015,** 19, 1653.

87. Li, Z.; Zhang, Y., Monodisperse silica-coated polyvinylpyrrolidone/$NaYF_4$ nanocrystals with multi colour upconversion fluorescence emission. Angew. Chem. Int. Ed. **2006,** 45, 7732.

88. Shan, J.; Ju, Y., Controlled synthesis of lanthanide-doped $NaYF_4$ upconversion nanocrystals via ligand induced crystal phase transition and silica coating. Appl. Phys. Lett.**2007,** 91, 123103.

89. Johnson, N. J. J.; Sangeetha, N. M.; Boyer, J.-C., et al., Facile ligand-exchange with polyvinylpyrrolidone and subsequent silica coating of hydrophobic upconverting [small beta]-$NaYF_4$:Yb^{3+}/Er^{3+} nanoparticles. Nanoscale **2010,** 2, 771.

90. Ding, H. L.; Zhang, Y. X.; Wang, S., et al., Fe_3O_4@SiO_2 core/shell nanoparticles: The silica coating regulations with a single core for different core sizes and shell thicknesses. Chem. Mater. **2012,** 24, 4572.

91. Khan, M. A.; Idriss, H., Advances in plasmon-enhanced upconversion luminescence phenomena and their possible effect on light harvesting for energy applications. Wires. Energy Environ. **2017,** 6.

92. Ghosh, P.; Oliva, J.; Rosa, E. D. L., et al., Enhancement of upconversion emission of $LaPO_4$:Er@Yb core−shell nanoparticles/nanorods. J Phys. Chem. C **2008,** 112, 9650.

93. Wei, X. Z.; Mulvaney, P., Chapter 3 - optical properties of strongly coupled plasmonic nanoparticle clusters. In Handbook of surface science, Richardson, N. V.; Holloway, S., Eds. North-Holland: 2014; Vol. 4, pp 75.

94. Hugall, J.; Singh, A.; Hulst, N. V., Plasmonic cavity coupling. ACS Photonics **2018,** 5, 43.

95. Naik, G.; Kim, J.; Kinsey, N., et al., Chapter 6 - alternative plasmonic materials. In Handbook of surface science, Richardson, N. V.; Holloway, S., Eds. North-Holland: 2014; Vol. 4, p 189.

96. Garcia, M. A., Surface plasmons in metallic nanoparticles: Fundamentals and applications. J. Phys. D: Appl. Phys. **2011,** 44, 283001.

97. Anger, P.; Bharadwaj, P.; Novotny, L., Enhancement and quenching of single-molecule fluorescence. Phys. Rev. Lett. **2006,** 96, 113002.

98. Moroz, A., A recursive transfer-matrix solution for a dipole radiating inside and outside a stratified sphere. Ann. Phys.-New York **2005,** 315, 352.

99. Zhou, F.; Li, Z.-Y.; Liu, Y., et al., Quantitative analysis of dipole and quadrupole excitation in the surface plasmon resonance of metal nanoparticles. J. Phys.Chem. C **2008,** 112, 20233.

100. Kumbhar, A. S.; Kinnan, M. K.; Chumanov, G., Multipole plasmon resonances of submicron silver particles. J. Am. Chem. Soc. **2005,** 127, 12444.

101. Prodan, E.; Radloff, C.; Halas, N. J., et al., A hybridization model for the plasmon response of complex nanostructures. Science **2003,** 302, 419.

102. Halas, N., Playing with plasmons: Tuning the optical resonant properties of metallic nanoshells. MRS Bulletin **2011,** 30, 362.

103. Lal, S.; Westcott, S. L.; Taylor, R. N., et al., Light interaction between gold nanoshells plasmon resonance and planar optical waveguides. J. Phys. Chem. B **2002,** 106, 5609.

104. Oldenburg, S. J.; Jackson, J. B.; Westcott, S. L., et al., Infrared extinction properties of gold nanoshells. Appl. Phys. Lett. **1999,** 75, 2897.

105. Penninkhof, J. J.; Sweatlock, L. A.; Moroz, A., et al., Optical cavity modes in gold shell colloids. J. Appl. Phys. **2008,** 103, 123105.

106. Meer, B. W. V. D., FRET – Förster resonance energy transfer: From theory to applications, first edition. Wiley-VCH Verlag GmbH & Co. KGaA: Weinheim, 2014.

107. Riuttamäki, T.; Hyppänen, I.; Kankare, J., et al., Decrease in luminescence lifetime indicating nonradiative energy transfer from upconverting phosphors to fluorescent acceptors in aqueous suspensions. J. Phys. Chem.C **2011,** 115, 17736.

108. Wu, P. G.; Brand, L., Resonance energy transfer: Methods and applications. Anal. Biochem. **1994,** 218, 1.

109. Marin, R.; Labrador-Paéz, L.; Skripka, A., et al., Upconverting nanoparticle to quantum dot förster resonance energy transfer: Increasing the efficiency through donor design. ACS Photonics **2018**.

110. Soukka, T.; Rantanen, T.; Kuningas, K., Photon upconversion in homogeneous fluorescence-based bioanalytical assays. Ann. NY Acad. Sci. **2008,** 1130, 188.

111. Wang, X.; Valiev, R. R.; Ohulchanskyy, T. Y., et al., Dye-sensitized lanthanide-doped upconversion nanoparticles. Chem. Soc. Rev. **2017,** 46, 4150.

112. Hu, J.; Wu, X.; Liu, X., et al., Modulating upconversion luminescence through fluorescent dyes. J. Solid State Chem. **2017,** 255, 139.

113. Williams, D. B.; Carter, C. B., Transmission electron microscopy. Lenum Press: New York, London, 1996.

114. Erni, R.; Rossell, M. D.; Kisielowski, C., et al., Atomic-resolution imaging with a sub-50-pm electron probe. Phys. Rev. Lett. **2009,** 102, 096101.

115. Hitachi launches world's highest resolution FE-SEM. http://www.nanotech-now.com/news.cgi?story_id=42612. (accessed 26.04.2019)

116. Zhou, W.; Wang, Z. L., Scanning microscopy for nanotechnology: Techniques and applications. Springer Science & Business Media: New York, 2007.

117. Kalantar-Zadeh, K.; Fry, B., Nanotechnology-enabled sensor. Springer US: New York, 2008.

118. Stetefeld, J.; Mckenna, S. A.; Patel, T. R., Dynamic light scattering: A practical guide and applications in biomedical sciences. Biophys. Rev. **2016,** 8, 409.

119. Berne, B. J.; Pecora, R., Dynamic light scattering: With applications to chemistry, biology, and physics. John Wiley & Sons: New York, 1976.

120. Siegert, A. J. F., On the fluctuations in signals returned by many independently moving scatterers. Massachusets Institute of Technology Ed.: Cambridge, 1949.

121. Hunter, R. J., Zeta potential in colloid science: Principles and applications. Academic Press: London, 1988.

122. Varenne, F.; Botton, J.; Merlet, C., et al., Standardization and validation of a protocol of zeta potential measurements by electrophoretic light scattering for nanomaterial characterization. Colloid. Surface. A **2015,** 486, 218.

123. Xu, R., Particle characterization: Light scattering methods. Springer Science & Business Media: Dordrecht, 2006.

124. Lakowicz, J. R., Principles of fluorescence spectroscopy. Springer Science+Business Media: New York, 2010.

125. Albani, J. R., Fluorescence spectroscopy principles. In Principles and applications of fluorescence spectroscopy, Blackwell Publishing Ltd: Hoboke, 2008; p 88.

126. Bennett, R. G., Instrument to measure fluorescence lifetimes in the millimicrosecond region. Rev. Sci. Instrum. **1960,** 31, 1275.

127. Matthews, D.; Summers, H.; Njoh, K., et al. Novel Optical Instrumentation for Biomedical Applications II. In Time-resolved measurements using stroboscopic excitation, Optical Society of America: Munich, 2005; p MD3.

128. Badea, M. G.; Brand, L., Time-resolved fluorescence measurements. In Methods in enzymology, Academic Press: Cambridge, 1979; Vol. 61, p 378.

129. Dominik, A.; Steinhilber, D.; Wurglics, M., Instrumentelle analytik kompakt. Wissenschaftliche Verlagsgesellschaft mbH: Stuttgart, 2013.

130. Marcum, S. D.; Yarrison-Rice, J. M. Bragg diffraction of X-rays and of electrons. http://www.cas.miamioh.edu/~marcumsd/p293/lab3/lab3.htm. (accessed: 26.04.2019)

131. Borchardt-Ott, W., Crystallographie an introduction. Springer Science+Business Media: Berlin, 2011.

132. Miller, C. X-ray spectroscopy goniometer. https://commons.wikimedia.org/wiki/File:X-ray_spectroscopy_Goniometer.jpg. (accessed: 26.04.2019)

133. Evans Analytical group. ICP-MS and ICP-MS detection limit guidance. http://www.nanoscience.co.jp/surface_analysis/pdf/icp-oes-ms-detection-limit-guidance-BR023.pdf. (accessed: 26.04.2019)

134. Boss, C. B.; Fredeen, K. J., Concept, instrumentation and techniques in inductively coupled plasma optical emission spectrometry. Perkin Elmer, Inc.: Shelton, USA, 2004.

135. Dean, J. R., Practical inductively coupled plasma spectroscopy. John Wiley & Sons, Ltd.: Kent, 2005.

136. Li, C.; Dongmei, Y.; Lin, J. Multifunctional upconversion mesoporous silica nanostructures for dual modal imaging and *in vivo* drug delivery. Small **2013**, 4150.

137. Lewinski, N.; Colvin, V.; Drezek, R., Cytotoxicity of nanoparticles. Small **2008,** 4, 26.

138. Haslam, G.; Wyatt, D.; Kitos, P. A., Estimating the number of viable animal cells in multi-well cultures based on their lactate dehydrogenase activities. Cytotechnology **2000,** 32, 63.

139. Cytoselect MTT cell proliferation assay kit. https://www.mybiosource.com/prods/Assay-Kit/CytoSelect-MTT-Cell-Proliferation-Assay/datasheet.php?products_id=168154. (accessed: 26.04.2019)

140. Conner, S. D.; Schmid, S. L., Regulated portals of entry into the cell. Nature **2003,** 422, 37.

141. Verma, A.; Stellacci, F., Effect of surface properties on nanoparticle–cell interactions. Small **2010,** 6, 12.

142. Zhang, J.; Liu, F.; Li, T., et al., Surface charge effect on the cellular interaction and cytotoxicity of $NaYF_4$:Yb^{3+}, Er^{3+} @SiO_2 nanoparticles. RSC Adv. **2015,** 5, 7773.

143. Gnach, A.; Lipinski, T.; Bednarkiewicz, A.; Rybka, J.; Capobianco, J. A., Upconverting nanoparticles: assessing the toxicity. Chem. Soc. Rev. **2015**, 1561.

144. Jin, J.; Gu, Y.-J.; Man, C. W.-Y., et al., Polymer-coated $NaYF_4$: Yb^{3+}, Er^{3+} upconversion nanoparticles for charge-dependent cellular imaging. ACS Nano **2011,** 5, 7838.

145. Xia, A.; Gao, Y.; Zhou, J., et al., Core–shell $NaYF_4$: Yb^{3+}, Tm^{3+}@Fe_xO_y nanocrystals for dual-modality T2-enhanced magnetic resonance and NIR-to-NIR upconversion luminescent imaging of small-animal lymphatic node. Biomaterials **2011,** 32, 7200.

146. Gulzar, A.; Xu, J.; Yang, P., et al., Upconversion processes: Versatile biological applications and biosafety. Nanoscale **2017,** 9, 12248.

147. Wysokińska, E.; Cichos, J.; Zioło, E., et al., Cytotoxic interactions of bare and coated $NaGdF_4$: Yb^{3+}, Er^{3+} nanoparticles with macrophage and fibroblast cells. Toxicol. *in vitro* **2016,** 32, 16.

148. Dickinson, B., Introduction to flow cytometry: A learning guide. B. D. Biosciences: San Jose, USA, 2002.

149. Brown, M.; Wittwer, C., Flow cytometry: Principles and clinical applications in hematology. Clin. Chem. **2000,** 46, 1221.

150. Lu, P., Confocal scanning optical microscopy and nanotechnology. In Handbook of Microscopy for Nanotechnology, Springer: San Diego, 2005; p 3.

151. Wang, J.; Yang, M.; Yang, L., et al., A confocal endoscope for cellular imaging. Engineering **2015,** 1, 351.

152. Bastos, V.; Ferreira De Oliveira, J. M. P.; Brown, D., et al., The influence of citrate or PEG coating on silver nanoparticle toxicity to a human keratinocyte cell line. Toxicol. Lett. **2016,** 249, 29.

153. Yi, G.; Peng, Y.; Gao, Z., Strong red-emitting near-infrared-to-visible upconversion fluorescent nanoparticles. Chem. Mater. **2011,** 23, 2729.

154. Wei, Y.; Lu, F.; Zhang, X., et al., Synthesis of oil-dispersible hexagonal-phase and hexagonal-shaped $NaYF_4$:Yb, Er nanoplates. Chem. Mater. **2006,** 18, 5733.

155. Zhengquan, L.; Zhang, Y., An efficient and user-friendly method for the synthesis of hexagonal-phase $NaYF_4$:Yb, Er/Tm nanocrystals with controllable shape and upconversion fluorescence. Nanotechnology **2008,** 19, 345606.

156. Na, H.; Woo, K.; Lim, K., et al., Rational morphology control of [small beta]- $NaYF_4$: Yb, Er upconversion nanophosphors using a ligand, an additive, and lanthanide doping. Nanoscale **2013,** 5, 4242.

157. Wang, J.; Shah, Z. H.; Zhang, S., et al., Silica-based nanocomposites via reverse microemulsions: Classifications, preparations, and applications. Nanoscale **2014,** 6, 4418.

158. Van Blaaderen, A.; Vrij, A., Synthesis and characterization of colloidal dispersions of fluorescent, monodisperse silica spheres. Langmuir **1992,** 8, 2921.

159. Graf, C.; Van Blaaderen, A., Metallodielectric colloidal core−shell particles for photonic applications. Langmuir **2002,** 18, 524.

160. Zhang, X.; Guo, L.; Luo, J., et al., Metallic nanoshells with sub-10 nm thickness and their performance as surface-enhanced spectroscopy substrate. ACS Appl. Mater.Inter. **2016,** 8, 9889.

161. Rahman, P.; Green, M., The synthesis of rare earthfluoride based nanoparticles. Nanoscale **2009,** 1, 214.

162. Auzel, F., Upconversion and anti-Stokes processes with f and d ions in solids. Chem. Rev.**2004,** 104, 139.

163. Yu, M.; Li, F.; Chen, Z., et al., Laser scanning up-conversion luminescence microscopy for imaging cells labeled with rare-earth nanophosphors. Analytical Chemistry **2009,** 81, 930.

164. Nyk, M.; Kumar, R.; Ohulchanskyy, T. Y., et al., High contrast *in vitro* and *in vivo* photoluminescence bioimaging using near infrared to near infrared up-conversion in Tm^{3+} and Yb^{3+} doped fluoride nanophosphors. Nano Lett. **2008,** 8, 3834.

165. Wang, L.; Yan, R.; Huo, Z., et al., Fluorescence resonant energy transfer biosensor based on upconversion-luminescent nanoparticles. Angew. Chem. Int. Edit. **2005,** 44, 6054.

166. Liu, Q.; Sun, Y.; Yang, T., et al., Sub-10 nm hexagonal lanthanide-doped $NaLuF_4$ upconversion nanocrystals for sensitive bioimaging *in vivo*. J. Am. Chem. Soc. **2011,** 133, 17122.

167. Suyver, J. F.; Grimm, J.; Van Veen, M. K., et al., Upconversion spectroscopy and properties of $NaYF_4$ doped with Er^{3+}, Tm^{3+} and/or Yb^{3+}. J. Lumin. **2006,** 117, 1.

168. Yan, R. X.; Li, Y. D., Down/up conversion in Ln^{3+}-doped YF_3 nanocrystals. Adv. Funct. Mater. **2005,** 15, 763.

169. Krämer, K. W.; Biner, D.; Frei, G., et al., Hexagonal sodium yttrium fluoride based green and blue emitting upconversion phosphors. Chem. Mater. **2004,** 16, 1244.

170. Fu, J.; H. Fu, X.; Wang, C., et al., Controlled growth and up-conversion improvement of sodium yttrium fluoride crystals. Eur. J. Inorg. Chem. **2013**, 2013, 1269.

171. Oldenburg, S. J.; Hale, G. D.; Jackson, J. B., et al., Light scattering from dipole and quadrupole nanoshell antennas. Appl. Phys. Lett. **1999,** 75, 1063.

172. Wang, F.; Han, Y.; Lim, C. S., et al., Simultaneous phase and size control of upconversion nanocrystals through lanthanide doping. Nature **2010,** 463, 1061.

173. Pokhrel, M.; Valdes, C.; Mao, Y., Ultraviolet upconversion enhancement in triply doped $NaYF_4$: Tm^{3+},Yb^{3+} particles: The role of Nd^{3+} or Gd^{3+} co-doping. Opt. Mater. **2016,** 58, 67.

174. Manurung, R. V.; Wu, C. T.; Roy, P. K., et al., A plasmon-tuned 'gold sandwich' for metal enhanced fluorescence in silica coated $NaYF_4$: Yb, Er upconversion nanoparticles. RSC Adv. **2016,** 6, 87088.

175. Green, K. ; Wirth, J.; Lim, S. F., Optical investigation of gold shell enhanced 25 nm diameter upconverted fluorescence emission. Nanotechnology **2016,** 27, 135201.

176. Ling, L.; Kory, G.; Hans, H., et al., Enhancement of single particle rare earth doped $NaYF_4$: Yb, Er emission with a gold shell. Nanotechnology **2015,** 26, 025101.

177. Li, Z.; Wang, L.; Wang, Z., et al., Modification of $NaYF_4$: Yb, Er@SiO_2 nanoparticles with gold nanocrystals for tunable green-to-red upconversion emissions. J. Phys. Chem. C **2011,** 115, 3291.

178. Zhang, J; Liu, F.; Li, T.; He, X.; Wang, Z., Surface charge effect on the cellular interaction and cytotoxicity of $NaYF_4$:Yb^{3+}, Er^{3+}@SiO_2 nanoparticles. RSC Adv. **2015,** 5, 7773.

179. Kowalik, P.; Elbaum, D.; Mikulski, J., et al., Upconversion fluorescence imaging of Hela cells using ros generating SiO_2-coated lanthanide-doped $NaYF_4$ nanoconstructs. RSC Adv. **2017,** 7, 30262.

180. Shi, F.; Wang, J.; Zhai, X., et al., Facile synthesis of [small beta]-$NaLuF_4$: Yb/Tm hexagonal nanoplates with intense ultraviolet upconversion luminescence. Cryst. Eng. Comm. **2011,** 13, 3782.

181. Ostrowski, A. D.; Chan, E. M.; Gargas, D. J., et al., Controlled synthesis and single-particle imaging of bright, sub-10 nm lanthanide-doped upconverting nanocrystals. ACS Nano **2012,** 6, 2686.

182. Shi, F.; Wang, J.; Zhang, D., et al., Greatly enhanced size-tunable ultraviolet upconversion luminescence of monodisperse [small beta]-$NaYF_4$:Yb, Tm nanocrystals. J. Mater.Chem. **2011,** 21, 13413.

183. Haase, M., Surface treatment method for nanoparticles. WO 2008/074869 Al, 2008.

184. Som, T.; Karmakar, B., Efficient green and red fluorescence upconversion in erbium doped new low phonon antimony glasses. Opt. Mater. **2009**, 31, 609.

185. Zervas, M. N.; Codemard, C. A., High power fiber lasers: A review. IEEE J. Sel.Top. Quant. .**2014,** 20, 219.

186. Steinkemper, H.; Fischer, S.; Hermle, M., et al., Stark level analysis of the spectral line shape of electronic transitions in rare earth ions embedded in host crystals. New J. Phys. **2013,** 15, 053033.

187. Barker, A. J.; Cage, B.; Russek, S., et al., Ripening during magnetite nanoparticle synthesis: Resulting interfacial defects and magnetic properties. J. Appl. Phys. **2005,** 98, 063528.

188. Voss, L. F.; Bazerbashi, M. F.; Beekman, C. P., et al., Oxidation of oleic acid at air/liquid interfaces. J. Geophys. Res. **2007,** 112.

189. Klemperer, W.; Pimentel, G. C., Hydrogen bonding in sodium trifluoroacetate-trifluoroacetic acid compounds. J. Phys. Chem. **1954,** 22.

190. Puri, M.; Verma, R. D., Trinuclear metal(III) trifluoroacetates. Monatsheft. Chem. **1984,** 115, 533.

191. Fuson, N.; Josien, M.-L.; Jones, E. A., et al., Infrared and raman spectroscopy studies of light and heavy trifluoroacetic acids. J. Phys. Chem. **1952,** 20, 1627.

192. Mularczyk, E.; Drzymala, J., Removal of decomposition products from sodium oleate. Ind. Eng. Chem. Res. **1996,** 35, 788.

193. Palo, E.; Tuomisto, M.; Hyppänen, I., et al., Highly uniform up-converting nanoparticles: Why you should control your synthesis even more. J. Lumin. **2017,** 185, 125.

194. Liu, C.; Wang, H.; Zhang, X., et al., Morphology- and phase-controlled synthesis of monodisperse lanthanide-doped $NaGdF_4$ anocrystals with multi colour photoluminescence. J. Mater. Chem. **2009,** 19, 489.

195. Yi, G.-S.; Chow, G.-M., Water-soluble $NaYF_4$: Yb, Er (Tm)/ $NaYF_4$ /polymer core/shell/shell nanoparticles with significant enhancement of upconversion fluorescence. Chem. Mater. **2007,** 19, 341.

196. Schäfer, H.; Ptacek, P.; Zerzouf, O., et al., Synthesis and optical properties of KYF_4/Yb, Er nanocrystals, and their surface modification with undoped KYF_4. Adv. Funct. Mater. **2008,** 18, 2913.

197. Lehmann, O.; Kömpe, K.; Haase, M., Synthesis of Eu^{3+}-doped core and core/shell nanoparticles and direct spectroscopic identification of dopant sites at the surface and in the interior of the particles. J.Am. Chem. Soc. **2004,** 126, 14935.

198. Mai, H.-X.; Zhang, Y.-W.; Sun, L.-D., et al., Highly efficient multi colour up-conversion emissions and their mechanisms of monodisperse $NaYF_4$: Yb, Er core and core/shell-structured nanocrystals. J. Phys. Chem. C **2007,** 111, 13721.

199. Li, X.; Shen, D.; Yang, J., et al., Successive layer-by-layer strategy for multi-shell epitaxial growth: Shell thickness and doping position dependence in upconverting optical properties. Chem. Mater. **2013,** 25, 106.

200. Abel, K. A.; Boyer, J.-C.; Veggel, F. V., Hard proof of the $NaYF_4$/$NaGdF_4$ nanocrystal core/shell structure. J. Am. Chem. Soc. **2009,** 131, 14644.

201. Qian, L. P.; Yuan, D.; Shun Yi, G., et al., Critical shell thickness and emission enhancement of $NaYF_4$: Yb, Er/$NaYF_4$/silica core/shell/shell nanoparticles. J. Mater. Res. **2011,** 24, 3559.

202. Vetrone, F.; Naccache, R.; Mahalingam, V., et al., The active-core/active-shell approach: A strategy to enhance the upconversion luminescence in lanthanide-doped nanoparticles. Adv. Funct. Mater. **2009,** 19, 2924.

203. Xu, W.; Chen, X.; Song, H., Upconversion manipulation by local electromagnetic field. Nano Today **2017,** 17, 54.

204. Meng, L. Thermal and optical-gain effects in nanophotonics with applications to sensing and perfect absorption. Ph.D Dissertation, Institut de Ciencies Fotoniques, Universitat Politecnica de Catalunya, Barcelona, 2018.

205. Khlebtsov, B. N.; Khanadeev, V. A.; Khlebtsov, N. G., Determination of the size, concentration, and refractive index of silica nanoparticles from turbidity spectra. Langmuir **2008,** 24, 8964.

206. Thoma, R. E.; Hebert, G. M.; Insley, H., et al., Phase equilibria in the system sodium fluoride-yttrium fluoride. Inorg. Chem. **1963,** 2, 1005.

207. Kwadrin, A.; Koenderink, A. F., Probing the electrodynamic local density of states with magnetoelectric point scatterers. Phys. Rev. B **2013,** 87, 125123.

208. Suyver, J. F.; Aebischer, A.; García-Revilla, S., et al., Anomalous power dependence of sensitized upconversion luminescence. Phys. Rev. B **2005,** 71, 125123.

209. Gu, Z.; Yan, L.; Tian, G., et al., Recent advances in design and fabrication of upconversion nanoparticles and their safe theranostic applications. Adv. Mater. **2013,** 25, 3758.

210. Fan, W.; Bu, W.; Shi, J., On the latest three-stage development of nanomedicines based on upconversion nanoparticles. Adv. Mater. **2016,** 28, 3987.

211. Deng, R.; Wang, J.; Chen, R., et al., Enabling Förster resonance energy transfer from large nanocrystals through energy migration. J. Am. Chem. Soc. **2016,** 138, 15972.

212. Lahtinen, S.; Lyytikainen, A.; Pakkila, H., et al., Disintegration of hexagonal $NaYF_4$: Yb^{3+}, Er^{3+} upconverting nanoparticles in aqueous media: The role of fluoride in solubility equilibrium. J. Phys. Chem. C **2017,** 121, 656.

213. Katagiri, K.; Narahara, M.; Sako, K., et al., SiO_2 shell formation mechanism and enlargement on hydrophobized nanoparticles via a reverse microemulsion process. J Sol-Gel Sci. Tech. **2017,** 84, 110.

214. Koole, R.; Van Schooneveld, M. M.; Hilhorst, J., et al., On the incorporation mechanism of hydrophobic quantum dots in silica spheres by a reverse microemulsion method. Chem. Mater. **2008,** 20, 2503.

215. Wolcott, A.; Gerion, D.; Visconte, M., et al., Silica-coated CdTe quantum dots functionalized with thiols for bioconjugation to IGG proteins. J. Phys.Chem. B **2006,** 110, 5779.

216. Kobayashi, Y.; Katakami, H.; Mine, E., et al., Silica coating of silver nanoparticles using a modified Stöber method. J. Coll. Interface Sci. **2005,** 283, 392.

217. Lemyre, J. L.; Lamarre, S.; Beaupre, A., et al., A new approach for the characterization of reverse micellar systems by dynamic light scattering. Langmuir **2010,** 26, 10524.

218. Fenn, E. E.; Wong, D. B.; Giammanco, C. H., et al., Dynamics of water at the interface in reverse micelles: Measurements of spectral diffusion with two-dimensional infrared vibrational echoes. J. Phys. Chem. B **2011,** 115, 11658.

219. Zhang, M.; Cushing, B. L.; O'connor, C. J., Synthesis and characterization of monodisperse ultra-thin silica-coated magnetic nanoparticles. Nanotechnology **2008,** 19, 085601.

220. Mer, V. K. L., Nucleation in phase transitions. Ind. Eng. Chem. **1952,** 44, 1270.

221. Hlavacek, A.; Sedlmeier, A.; Skladal, P., et al., Electrophoretic characterization and purification of silica-coated photon-upconverting nanoparticles and their bioconjugates. ACS Appl. Mater. Inter. **2014,** 6, 6930.

222. Jana, N. R.; Earhart, C.; Ying, J. Y., Synthesis of water-soluble and functionalized nanoparticles by silica coating. Chem. Mater. **2007,** 19, 5074.

223. Liu, F. Y.; Zhao, Q.; You, H. P., et al., Synthesis of stable carboxy-terminated $NaYF_4$: Yb^{3+}, Er^{3+} @SiO_2 nanoparticles with ultrathin shell for biolabeling applications. Nanoscale **2013,** 5, 1047.

224. Bergmann, O. Synthese und Charakterisierung von Upconversion-Nanopartikeln. MSc. Dissertation, Hochschule Darmstadt-University of Applied Science, Darmstadt, 2018.

225. Reculusa, S.; Poncet-Legrand, C.; Ravaine, S., et al., Syntheses of raspberry like silica/polystyrene materials. Chem. Mater. **2002,** 14, 2354.

226. Ramsay, D. A.; Sutherland, The vibration spectrum and molecular configuration of cyclohexane. Proc. R Soc. Lon. A Mat. **1947,** 190, 245.

227. Cong, T.; Ding, Y.; Xin, S., et al., Solvent-induced luminescence variation of upconversion nanoparticles. Langmuir **2016,** 32, 13200.

228. Liu, N.; Qin, W.; Qin, G., et al., Highly plasmon-enhanced upconversion emissions from Au@[small beta]- $NaYF_4$: Yb, Tm hybrid nanostructures. Chem. Comm. **2011,** 47, 7671.

229. Duff, D. G.; Baiker, A.; Edwards, P. P., A new hydrosol of gold clusters. 1. Formation and particle size variation. Langmuir **1993,** 9, 2301.

230. Westcott, S. L.; Oldenburg, S. J.; Lee, T. R., et al., Formation and adsorption of clusters of gold nanoparticles onto functionalized silica nanoparticle surfaces. Langmuir **1998,** 14, 5396.

231. Ultra-high resolution scanning electron microscope. https://www.hitachi-hightech.com/file/ca/pdf/library/literature/SU8000FamilyBrochure.pdf. (accessed 05.12.2018)

232. Sauerbeck, C.; Haderlein, M.; Schürer, B., et al., Shedding light on the growth of gold nanoshells. ACS Nano **2014,** 8, 3088.

233. Tharion, J.; Satija, J.; Mukherji, S., Glucose mediated synthesis of gold nanoshells: A facile and eco-friendly approach conferring high colloidal stability. RSC Adv. **2014,** 4, 3984.

234. Van Blaaderen, A.; Kentgens, A. P. M., Particle morphology and chemical microstructure of colloidal silica spheres made from alkoxysilanes. J. Non-Cryst. Solids **1992,** 149, 161.

235. Bohren, C. F.; Huffman, D. R., Absorption and scattering by a sphere. In Absorption and scattering of light by small particles, Wiley-VCH Verlag GmbH: Weinheim 2007; p 82.

236. Mie, G., Beiträge zur optik trüber medien, speziell kolloidaler metallösungen. Ann. Phys. **1908,** 330, 377.

237. Zhang, X.; Ye, S.; Zhang, X., et al., Optical properties of SiO_2@M (M = Au, Pd, Pt) core-shell nanoparticles: Material dependence and damping mechanisms. J. Mater. Chem. C **2015,** 3, 2282.

238. Green, K. K.; Wirth, J.; Lim, S. F., Nanoplasmonic upconverting nanoparticles as orientation sensors for single particle microscopy. Sci. Rep.-UK **2017,** 7, 762.

239. Würth, C.; Kaiser, M.; Wilhelm, S., et al., Excitation power dependent population pathways and absolute quantum yields of upconversion nanoparticles in different solvents. Nanoscale **2017,** 9, 4283.

240. Feng, A. L.; You, M. L.; Tian, L., et al., Distance-dependent plasmon-enhanced fluorescence of upconversion nanoparticles using polyelectrolyte multilayers as tunable spacers. Sci. Rep.-UK **2015,** 5, 7779.

241. Li, Z.; Zhang, Y.; Jiang, S., Multi colour core/shell-structured upconversion fluorescent nanoparticles. Adv. Mater. **2008,** 20, 4765.

242. Wolfbeis, O. S., An overview of nanoparticles commonly used in fluorescent bioimaging. Chem. Soc. Rev. **2015,** 44, 4743.

243. Duan, C.; Liang, L.; Li, L., et al., Recent progress in upconversion luminescence nanomaterials for biomedical applications. J. Mater. Chem. B **2018,** 6, 192.

244. Cheng, L.; Yang, K.; Zhang, S., et al., Highly-sensitive multiplexed *in vivo* imaging using PEGylated upconversion nanoparticles. Nano Res. **2010,** 3, 722.

245. Verhaegh, N. A. M.; Blaaderen, A. V., Dispersions of rhodamine-labeled silica spheres: Synthesis, characterization, and fluorescence confocal scanning laser microscopy. Langmuir **1994,** 10, 1427.

246. Wang, Y.; Tu, L.; Zhao, J., et al., Upconversion luminescence of β- $NaYF_4$: Yb^{3+}, Er^{3+}@β-$NaYF_4$ core/shell nanoparticles: Excitation power density and surface dependence. J. Phys. Chem. C **2009,** 113, 7164.

247. Tan, W.; Wang, K.; He, X., et al., Bionanotechnology based on silica nanoparticles. Med. Res. Rev. **2004,** 24, 621.

248. Ow, H.; Larson, D. R.; Srivastava, M., et al., Bright and stable core−shell fluorescent silica nanoparticles. Nano Lett. **2005,** 5, 113.

249. Canning, J.; Huyang, G.; Ma, M., et al., Percolation diffusion into self-assembled mesoporous silica microfibres. Nanomaterials **2014,** 4, 157.

250. Blaaderen, A. V.; Vrij, A., Synthesis and characterization of monodisperse colloidal organo-silica spheres. J. Coll. Interface Sci. **1993,** 1, 18.

251. Imhof, A.; Megens, M.; Engelberts, J. J., et al., Spectroscopy of fluorescein (FITC) dyed colloidal silica spheres. J. Phys. Chem. B **1999,** 103, 1408.

252. Gunawardana, K. B.; Green, N. S.; Bumm, L. A., et al., Metal-enhanced fluorescence of dye-doped silica nano particles. J. Fluoresc. **2015,** 25, 311.

253. Liang, J.; Xue, Z.; Xu, J., et al., Highly efficient incorporation of amino-reactive dyes into silica particles by a multi-step approach. Colloids Surface A **2013,** 426, 33.

254. Widmer, S.; Reber, M. J.; Müller, P., et al., Incorporation of a FRET dye pair into mesoporous materials: A comparison of fluorescence spectra, FRET activity and dye accessibility. Analyst **2015,** 140, 5324.

255. Bogush, G. H.; Zukoski, C. F., Studies of the kinetics of the precipitation of uniform silica particles through the hydrolysis and condensation of silicon alkoxides. J. Coll. Interface Sci.**1991,** 142, 1.

256. Liang, S.; Shephard, K.; Pierce, D. T., et al., Effects of a nanoscale silica matrix on the fluorescence quantum yield of encapsulated dye molecules. Nanoscale **2013,** 5, 9365.

257. Martins Estevão, B.; Miletto, I.; Marchese, L., et al., Optimized rhodamine B labeled mesoporous silica nanoparticles as fluorescent scaffolds for the immobilization of photosensitizers: A theranostic platform for optical imaging and photodynamic therapy. Phys. Chem. Chem. Phys. **2016,** 18, 9042.

258. Becker, W., Advanced time-correlated single photon counting techniques. Springer Science & Business Media: Berlin, 2005.

259. Kristoffersen, A. S.; Erga, S. R.; Hamre, B., et al., Testing fluorescence lifetime standards using two-photon excitation and time-domain instrumentation: Rhodamine B, coumarin 6 and lucifer yellow. J. Fluoresc. **2014,** 24, 1015.

260. Hong Nhung, T.; Thi Ha Lien, N.; Thi Thuy Duong, V., et al., Dye-doped silica-based nanoparticles for bioapplications. Adv. Nat. Sci. Nanosci. **2013,** 4, 043001.

261. Sun, L.; Gu, J.; Zhang, S., et al., Luminescence resonance energy transfer based on β-$NaYF_4$: Yb, Er nanoparticles and TRITC dye. Sci. China B Chem. **2009,** 52, 1590.

262. Wang, J.; Deng, R., Energy transfer in dye-coupled lanthanide-doped nanoparticles: From design to application. Chem. Asian J. **2018,** 13, 614.

263. Kuningas, K.; Rantanen, T.; Ukonaho, T., et al., Homogeneous assay technology based on upconverting phosphors. Anal. Chem. **2005,** 77, 7348.

264. Forster, T., 10th spiers memorial lecture. Transfer mechanisms of electronic excitation. Discuss. Faraday Soc. **1959,** 27, 7.

265. Morgan, C. G.; Dad, S.; Mitchell, A. C., Present status of, and future prospects for, upconverting phosphors in proximity-based bioassay. J. Alloy Comp. **2008,** 451, 526.

266. Bednarkiewicz, A.; Nyk, M.; Samoc, M., et al., Up-conversion FRET from Er^{3+}/Yb^{3+}:$NaYF_4$ nanophosphor to CdSe quantum dots. J. Phys. Chem. C **2010,** 114, 17535.

267. Huang, K.; Liu, H.; Kraft, M., et al., A protected excitation-energy reservoir for efficient upconversion luminescence. Nanoscale **2018,** 10, 250.

268. Gnach, A.; Bednarkiewicz, A.; Rybka, J.; Capobianco, A., Upconverting nanoparticles: Assessing the toxicity. Chem. Soc. Rev. **2015**, 1561.

269. Asenath Smith, E.; Chen, W., How to prevent the loss of surface functionality derived from aminosilanes. Langmuir **2008,** 24, 12405.

270. Wang, Y.; Zhao, Q.; Han, N., et al., Mesoporous silica nanoparticles in drug delivery and biomedical applications. Nanomedicine **2015,** 11, 313.

271. Izak-Nau, E.; Voetz, M.; Eiden, S., et al., Altered characteristics of silica nanoparticles in bovine and human serum: The importance of nanomaterial characterization prior to its toxicological evaluation. Part. Fibre Toxicol. **2013,** 10, 56.

272. Monopoli, M. P.; Walczyk, D.; Campbell, A., et al., Physical−chemical aspects of protein corona: Relevance to *in vitro* and *in vivo* biological impacts of nanoparticles. J. Am. Chem. Soc. **2011,** 133, 2525.

273. Pisani, C.; Rascol, E.; Dorandeu, C., et al., The species origin of the serum in the culture medium influences the *in vitro* toxicity of silica nanoparticles to HepG2 cells. PLOS ONE **2017,** 12, e0182906.

274. Hofmann, A.; Thierbach, S.; Semisch, A., et al., Highly monodisperse water-dispersable iron oxide nanoparticles for biomedical applications. J. Mater. Chem. **2010,** 20, 7842.

275. Kurtz-Chalot, A.; Villiers, C.; Pourchez, J., et al., Impact of silica nanoparticle surface chemistry on protein corona formation and consequential interactions with biological cells. Mater. Sci. Eng. C **2017,** 75, 16.

276. Lisjak, D.; Plohl, O.; Vidmar, J., et al., Dissolution mechanism of upconverting AYF_4: Yb,Tm (A = Na or K) nanoparticles in aqueous media. Langmuir **2016,** 32, 8222.

277. Merck, S.-A. Dulbecco's modified eagle's medium (DME) formulation. https://www.sigmaaldrich.com/life-science/cell-culture/learning-center/media-formulations/dme.html. (accessed 01.11.2018).

278. Dukhno, O.; Przybilla, F.; Muhr, V., et al., Time-dependent luminescence loss for individual upconversion nanoparticles upon dilution in aqueous solution. Nanoscale **2018,** 10, 15904.

279. Yoon, S.-H., Membrane bioreactor processes principles and applications. CRC Press: Boca Raton, 2015.

280. Vibe, C. B.; Fenaroli, F.; Pires, D., et al., Thioridazine in PLGA nanoparticles reduces toxicity and improves rifampicin therapy against mycobacterial infection in zebrafish. Nanotoxicology **2016,** 10, 680.

281. Johnsen, E.; Brandtzaeg, O. K.; Vehus, T., et al., A critical evaluation of amicon ultra centrifugal filters for separating proteins, drugs and nanoparticles in biosamples. J. Pharmaceut. Biomed. Anal. **2016,** 120, 106.

282. Nel, A. E.; Mädler, L.; Velegol, D., et al., Understanding biophysicochemical interactions at the nano–bio interface. Nat. Mater. **2009,** 8, 543.

283. Leroueil, P. R.; Berry, S. A.; Duthie, K., et al., Wide varieties of cationic nanoparticles induce defects in supported lipid bilayers. Nano Lett. **2008,** 8, 420.

284. Xia, T.; Kovochich, M.; Liong, M., et al., Cationic polystyrene nanosphere toxicity depends on cell-specific endocytic and mitochondrial injury pathways. ACS Nano **2008,** 2, 85.

285. Sonawane, N. D.; Thiagarajah, J. R.; Verkman, A. S., Chloride concentration in endosomes measured using a ratioable fluorescent Cl− indicator: Evidence for chloride accumulation during acidification. J. Bio. Chem. **2002,** 277, 5506.

286. Liang, H.; Jin, C.; Tang, Y., et al., Cytotoxicity of silica nanoparticles on HaCaT cells. J. Appl. Toxicol. **2014,** 34, 367.

287. Wilhelm, C.; Gazeau, F.; Roger, J., et al., Interaction of anionic superparamagnetic nanoparticles with cells: Kinetic analyses of membrane adsorption and subsequent internalization. Langmuir **2002,** 18, 8148.

288. Pan, Y.; Neuss, S.; Leifert, A., et al., Size-dependent cytotoxicity of gold nanoparticles. Small **2007,** 3, 1941.

289. Jeong, Y.; Lim, D. W.; Choi, J., Assessment of size-dependent antimicrobial and cytotoxic properties of silver nanoparticles. Adv. Mater. Sci. Eng. **2014,** 2014, 6.

290. Mu, Q.; Hondow, N. S.; Krzemiński, Ł., et al., Mechanism of cellular uptake of genotoxic silica nanoparticles. Part. Fibre Toxicol. **2012,** 9, 29.

291. Jochums, A.; Friehs, E.; Sambale, F., et al., Revelation of different nanoparticle-uptake behavior in two standard cell lines NIH/3T3 and A549 by flow cytometry and time-lapse imaging. Toxics **2017,** 5, 15.

292. Schrade, A.; Mailänder, V.; Ritz, S., et al., Surface roughness and charge influence the uptake of nanoparticles: Fluorescently labeled pickering-type versus surfactant-stabilized nanoparticles. Macromol. Biosci. **2012,** 12, 1459.

293. Kumar, A.; Pandey, A. K.; Singh, S. S., et al., A flow cytometric method to assess nanoparticle uptake in bacteria. Cytometry Part A **2011,** 79A, 707.

294. Zamai, L.; Falcieri, E.; Zauli, G., et al., Optimal detection of apoptosis by flow cytometry depends on cell morphology. Cytometry **1993,** 14, 891.

295. Liu, C.; Hou, Y.; Gao, M., Are rare-earth nanoparticles suitable for *in vivo* applications? Adv. Mater. **2014,** 26, 6922.

296. Adding, L. C.; Bannenberg, G. L.; Gustafsson, L. E., Basic experimental studies and clinical aspects of gadolinium salts and chelates. Cardiovasc. Drug. Rev. **2001,** 19, 41.

297. Palasz, A.; Czekaj, P., Toxicological and cytophysiological aspects of lanthanides action. Acta. Biochim. Pol. **2000,** 47, 1107.

298. Agalakova, N. I.; Gusev, G. P., Molecular mechanisms of cytotoxicity and apoptosis induced by inorganic fluoride. ISRN Cell Biology **2012,** 2012, 16.

299. Nabeshi, H.; Yoshikawa, T.; Arimori, A., et al., Effect of surface properties of silica nanoparticles on their cytotoxicity and cellular distribution in murine macrophages. Nanoscale Res. Lett. **2011,** 6, 93.

300. Sohaebuddin, S. K.; Thevenot, P. T.; Baker, D., et al., Nanomaterial cytotoxicity is composition, size, and cell type dependent. Part. Fibre Toxicol. **2010,** 7.

301. Ibuki, Y.; Toyooka, T., Nanoparticle uptake measured by flow cytometry. In Nanotoxicity: Methods and protocols, Reineke, J., Ed. Humana Press: Totowa, 2012; p 157.

7 Scientific posters

1. **C. Kembuan,** M. Saleh, A. Beqiraj, U. Resch-Genger, C. Graf. 1st conference and spring school on properties, design and applications of upconverting nanomaterials 23rd – 27rd May 2016. "Structured metal nanoshell particles for controlled enhancement of photon up-conversion and Cu detection" Wroclow (Poland).

2. **C. Kembuan,** M. Saleh, U. Resch-Genger, C. Graf. IACIS 2015 and 47th Conference of the German Colloid Society, May 24 – 28, 2015. "Structured metal nanoshell particles for controlled enhancement of photon upconversion and Cu detection", Mainz (Germany).

3. M. Saleh, Y. Shen, **C. Kembuan,** A. Beqiraj, F. Frenzel, U. Resch-Genger, C. Graf. 1st conference and spring school on properties, design and applications of upconverting nanomaterials 23rd – 27rd May 2016. "Optimization of the coating procedure of upconversion nanoparticles with silica", Wroclow (Poland).

8 Attachments

Attachment A: Calculations of TEOS for a growth of 7 nm silica shell on UCNP core

UCNP core: UC_Er_4 (core average diameter (d_{TEM}) = 24±1 nm; c = 25 mg/mL)
Dispersion volume = 1.3 mL (m_{UCNP} = 32.5 mg)
UCNP particle density = 4.21 g/cm^3; SiO_2 density = 2 g/cm^3.

$$\text{Total amount of UCNP core} = \frac{1}{6} \cdot (d_{UCNP})^3 \cdot \pi \cdot \left(\frac{m_{UCNP}}{4.21 \cdot 10^{18}}\right) \text{ particles} \quad (8.1)$$

Total amount of UCNP cores = 1.07×10^{15} particles.
The volume of SiO_2 for one UCNP core (V_{SiO2}), when the core is coated by 7 nm SiO_2, was calculated by substracting the volume of the UCNP core (V_{UCNP}) from the total volume of the UCNP core with the shell ($V_{UCNP+SiO2}$) with

$$V_{SiO2} = V_{UCNP+SiO2} - V_{UCNP} \quad (8.2)$$

V_{SiO2} = 28 × 10^3 nm^3 7 × 10^3 nm^3 = 21 × 10^3 nm^3
The mass of silica (m SiO_2) was determined by:

$$m\ SiO_2 = V_{SiO2} \cdot 2 \times 10^{-21} \quad (8.3)$$

m SiO_2 = 4.2×10^{-18} g.
The total mass of SiO_2 (m total SiO_2) for the coating was calculated by multiplying the silica mass on one particle with the total number of particles:

$$m\ total\ SiO_2 = m\ SiO_2 \cdot n \quad (8.4)$$

This gave a total mass of 3.21 mg SiO_2. The corresponding amount of TEOS was calculated by the following equation (with molar masses M_r TEOS = 208.32 g/mol; Mr SiO_2 = 60.08 g/mol):

$$\text{TEOS (mL)} = \frac{m_{total\ SiO2} \cdot 208.32\ \frac{g}{mL} \cdot 0.001}{60.08 \frac{g}{mol} * 0 \cdot 94 \frac{g}{mL}} \quad (8.5)$$

Hence, 0.159 mL of TEOS was needed to coat 32.5 mg UC_Er_4 with 7 nm silica shell.

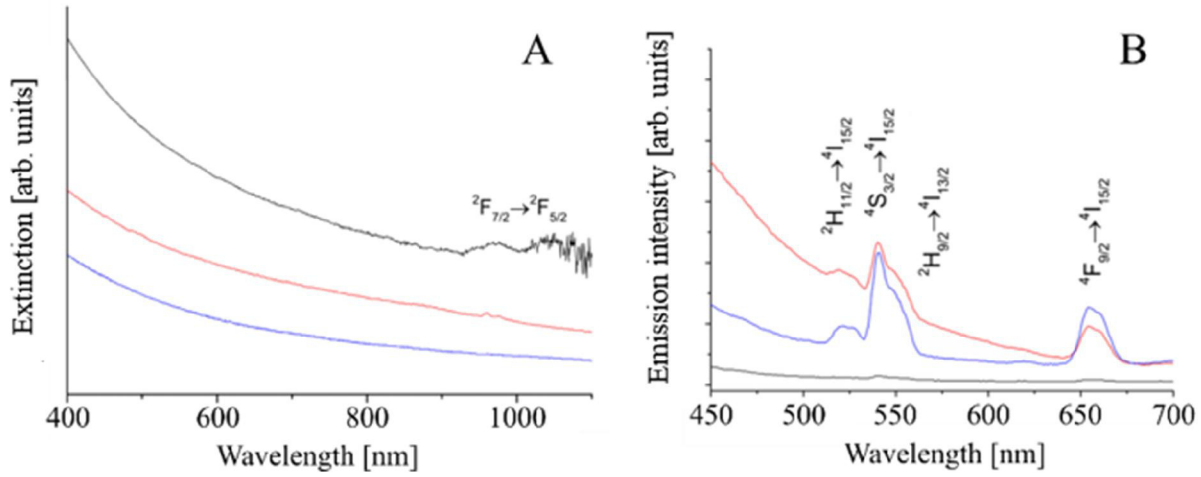

Attachment B A: extinction spectra and B: fluorescence spectra of UC_Er_2 (black line), UC_Er_2@1 (red line), and UC_Er_2@2 (blue line)

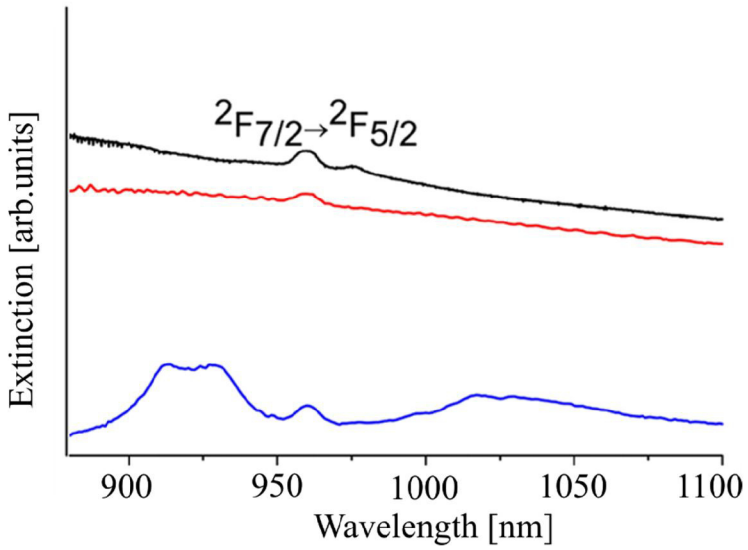

Attachment C: Extinction spectra of UC_Tm_1 (black line), UC_Tm_1@1 (blue line), and UC_Tm_1@5 (red line)

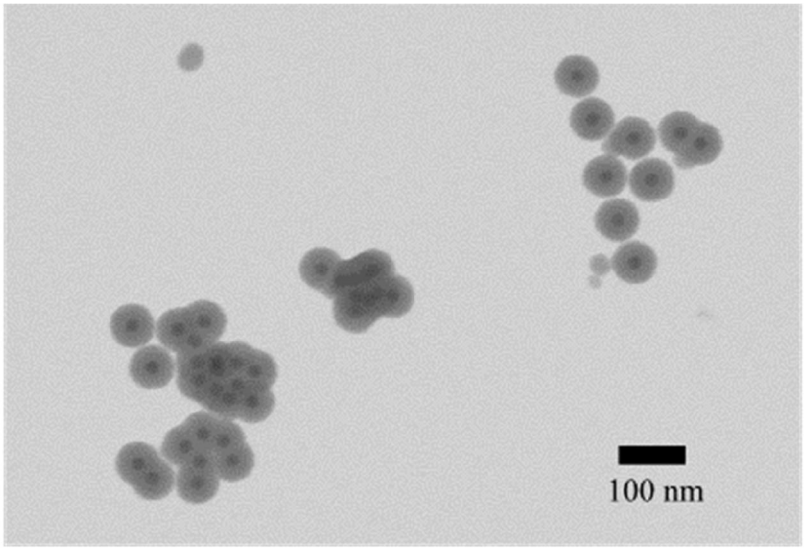

Attachment D: STEM image of UCNP cores ($NaYF_4$: Yb,Er, 20 ± 2 nm diameter) after silica coating by a Stöber-like method after a first silica shell coating (11±1 nm) through the reverse microemulsion method

In the following are the absorption spectra of RBITC calibration standard solutions and RBITC calibration curve:

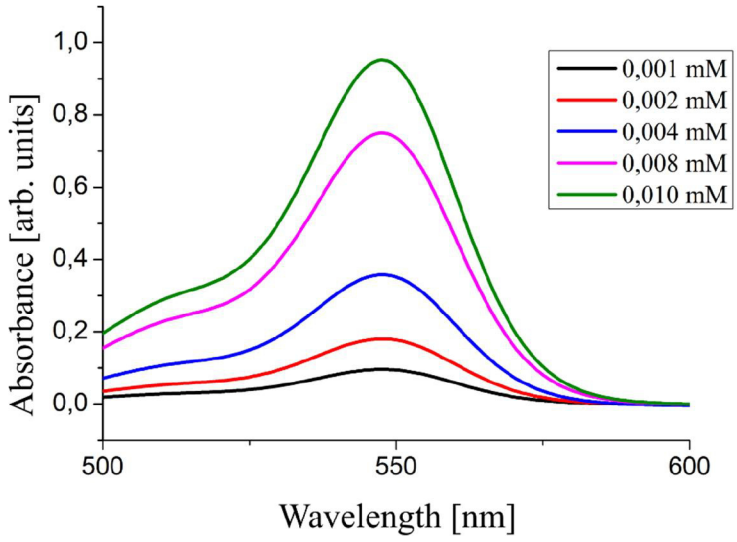

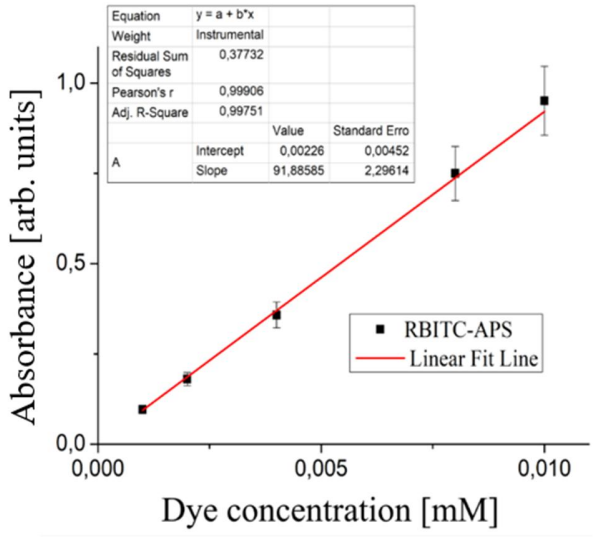

Attachment E: Absorption spectra of absorption at 547 nm (upper image) and calibration curve of RBITC absorption at 547 nm (bottom image) at various dye concentration

In the following are the absorption spectra of RBITC-doped silica-coated UCNP samples and calculation example of RBITC concentration coupled in the shell in each samples:

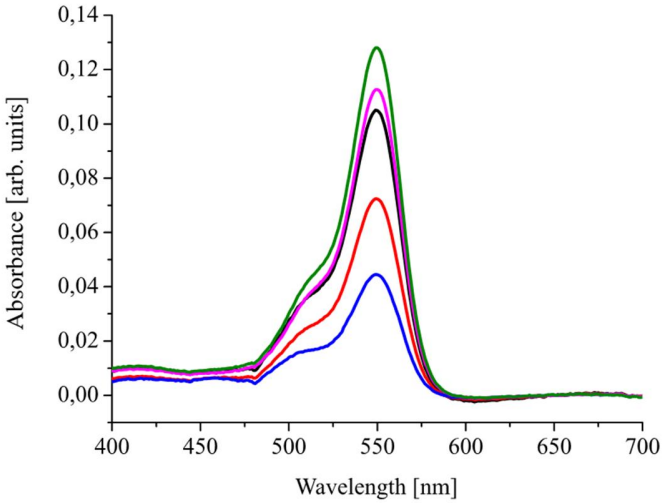

Attachment F: Absorption spectra of dye-doped silica coated UC_Er_4 samples after their treatment with 0.43 M NaOH: pink line (UC_Er_4@RBITC_5); green line (UC_Er_4@RBITC_4); red line (UC_Er_4@RBITC_3); black line (UC_Er_4@RBITC_2) and blue line (UC_Er_4@RBITC_1) and below is the calculation example of RBITC concentration in silica.

For the calculation of RBITC dye concentration silica shell (mmol RBITC per litre SiO_2), the absorption intensity of UC_Er_4@RBITC_1 was determined to be 0.04285± 0.0004 (see Table 4-8) based on the absorption spectrum of the sample, which corresponds to a dye concentration of [4.67±0.15] $\times \cdot 10^{-3}$ mmol/L.

For the absorption measurement, a 1:1 equimolar volume of the sample and 0.43 M NaOH were mixed, hence the real dye concentration (c_{dye}) was [9.33±0.3] $\times \cdot 10^{-4}$ mmol/L. The sample concentration was weighted to be 4.5±0.5 mg/mL. This result meant, that in 1 mL solution that was diluted with 0.43 M NaOH for the measurement, the volume of silica coated UCNP was 0.00176 cm^3 silica coated UCNP and volume of silica was 0.00132 cm^3 (particle density was 2 g/cm^3). Hence, the molar amount of dye per L SiO_2 was 0.71±0.02 mmol/L SiO_2 (see Table 4-8).

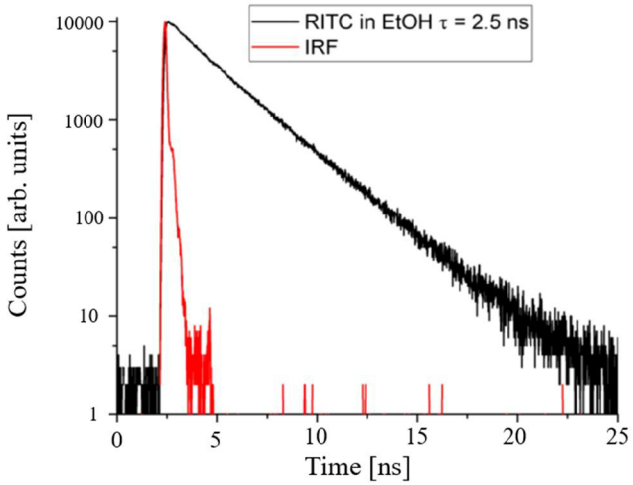

Attachment G: Lifetime of pure rhodamine B isothiocyanate in EtOH. Dye excitation at 540 nm